Integrating 4D seismic data into dynamic characterisation of an HPHT reservoir

Lu Ji

Submitted for the degree of Doctor of Philosophy

Heriot-Watt University

Institute of Petroleum Engineering

School of Energy, Geoscience, Infrastructure and Society

November 2017

Abstract

During the production of a high-pressure and high-temperature reservoir, massive pressure depletion happens giving rise to geomechanical changes which can lead to dangerous events for field development, such as fault reactivations and well failures. Therefore dynamic reservoir characterisation and monitoring is very important for this type of reservoirs. In this thesis, I use time-lapse time-shifts observed between 4D seismic surveys for the integrated study on dynamic characterisation of the Shearwater field which is a high-pressure and high-temperature field in Central North Sea.

This thesis consists of two parts. Before using time-shifts for reservoir characterisation, they need to be accurately calculated. In the first part, I present a critical comparison of three different types of methods (DHFCC, CLM, and NLI). With applications to a set of synthetic and real time-lapse seismic data of various quality and time-shift magnitudes, the advantages and disadvantages of each method have been revealed. I have found that all the time-shift methods can successfully measure time-shifts. Among them, NLI is the most outstanding method as it gives smooth time-shifts with relatively good accuracy and the time-strains derived from there are more stable and interpretable.

In the second part, I perform the dynamic reservoir characterisation. Firstly, time-shifts are generated using the three methods and are then interpreted by linking them with geology and production patterns. The measured time-shifts essentially have the same distribution and magnitude. They can be generally correlated with field geology and production volumes. Furthermore, by taking derivation, four time-strain anomalies are identified in some overburden and underburden formations. In the following work, I perform the geomechanical modelling and the evaluation of overburden gas and geomechanical effects, trying to understand the physics behind these anomalies. I have found that most of the anomalies can be modelled by closely linked with geological patterns. The large overburden time-strain is mainly due to geomechanical effects rather than fluid changes. Apart from that, the constructed geomechanical model has also been calibrated and updated using time-lapse time-shifts, and is useful for analysing the evolution of stress and strain fields in order to predict potential failure events.

Overall, my PhD research has successfully measured, interpreted and applied time-lapse time-shift, and has demonstrated its good value in dynamic reservoir characterisation.

Dedication

This thesis is dedicated to my husband Yiqun Zhang

&

our parents

Acknowledgements

First of all, I would like to thank my supervisor, Professor Colin MacBeth, with my deepest gratitude for giving me the opportunity to pursue a PhD degree in the ETLP group, and for providing me the chance to study the Reservoir Evaluation and Management MSc course when I was struggling at the beginning of my Ph.D. My study and research work would not have been completed without his wonderful guidance, constant encouragement and continuous support. More than that, I would like to thank him for guiding me to be a more confident, courageous, and persistent person.

I thank Dr. Asghar Shams for co-supervising this research. Thanks to Dr. Reza Falahat, and Dhiman Mondal for providing software demonstrations at the beginning of my PhD study. Thanks to Dr. Hamed Amini, Dr. Zhen Yin, Dr. Ricardo Rangel, Dr. Mingyi Wong, Dr. Veronica Omofoma, and Dr. Angel Bricerno for useful discussions on this project. Special thanks to Dr. Maria Mangriotis for giving me constructive suggestions and for helping me with programming.

I thank the sponsors of ETLP Phase V and VI (BG, BP, CGG, Chevron, ConocoPhilips, Eni, ExxonMobil, Hess, Ikon, Landmark, Maersk, Nexen, Norsar, OMV, Petoro, Petrobras, RSI, Shell, Statoil, Suncor, TAQA, TGS and Total) for funding my PhD research. Thanks to Shell, BP, ConocoPhilips, and Chevron for providing the data used in this thesis.

I would like to show my appreciation to all my ETLP colleagues for their friendship and support during these years: Colin MacBeth, Maria-Daphne Mangriotis, Hamed Amini, Romain Chassagne, Asghar Shams, Lee-Jean Wong, Zhen Yin, Mingyi Wong, Angel Briceno, Ricardo Rangel, Veronica Omofoma, Qi Zhang, Chong Geng, Niki Obiwulu, Phung Nguyen, Dennis Obidegwu, Miguel Alfonzo, Gustavo Corte, Alejandro Jaramillo, Ilya Fursov, Anders Matheson, Dhiman Mondal, Mathieu Chamberfort, Reza Falahat, Danil Khakimov, Olarinre Salako, Erick Alvarez, Shuzhe Tian, Juliana Santos, Ilona Dvorak, and Sergey Kurelenkov. Special thanks to Lee-Jean for providing me the place to stay and giving me all the kind help during my last period of study. These meant a lot to me, I am really grateful.

I also would like to thank all the support staff in EGIS, especially to Debbie, Tom and Alan, for helping me solve registration and IT problems whenever I requested. I thank all my friends for social interactions and care for making me always feel like at home.

Finally, I am very grateful to my husband, my parents, and my parents in law for their firm support, selfless love and continuous encouragement. Thanks for always being there for me.

Lu Ji, November 2017, Edinburgh

Declaration Statement

ACADEMIC REGISTRY

Research Thesis Submission

Name*:*	Lu Ji		
School:	Energy, Geoscience, Infrastructure and Society		
Version:	Final	Degree Sought:	PhD, Petroleum Engineering

Declaration

In accordance with the appropriate regulations I hereby submit my thesis and I declare that:

1) the thesis embodies the results of my own work and has been composed by myself
2) where appropriate, I have made acknowledgement of the work of others and have made reference to work carried out in collaboration with other persons
3) the thesis is the correct version of the thesis for submission and is the same version as any electronic versions submitted*.
4) my thesis for the award referred to, deposited in the Heriot-Watt University Library, should be made available for loan or photocopying and be available via the Institutional Repository, subject to such conditions as the Librarian may require
5) I understand that as a student of the University I am required to abide by the Regulations of the University and to conform to its discipline.
6) I confirm that the thesis has been verified against plagiarism via an approved plagiarism detection application e.g. Turnitin.

* *Please note that it is the responsibility of the candidate to ensure that the correct version of the thesis is submitted.*

Signature of Candidate*:*		Date:	

Submission

Submitted By	LU JI
Signature of Individual Submitting:	
Date Submitted:	

For Completion in the Student Service Centre (SSC)

Received in the SSC by			
Method of Submission			
E-thesis Submitted			
Signature:		Date:	

Contents

List of Figures

List of Tables

List of Abbreviations and Symbols

Symbols

t	Two-way traveltime of seismic wave
Δt	Time-lapse time-shift
A	Seismic amplitude
ΔA	Seismic amplitude change
CO2	Carbon dioxide
ρ	Density
∅	Porosity
pp	Pore pressure
σ	Total stress
σ_{eff}	Effective stress
R	factor relating change in velocity to change in vertical strain
ε_{zz}	Physical strain / vertical strain
α	The Biot's coefficient
E	The Young's modulus
υ	The Poisson's ratio
V_P	P-wave velocity
V_S	S-wave velocity
Z	Depth-thickness
K	Bulk modulus

Abbreviations

1D	One-dimensional
2D	Two-dimensional
3D	Three-dimensional
4D	Four-dimensional, also known as time-lapse
CLM	Correlated leakage method
DHFCC	Dave Hale's fast cross-correlation
ETLP	Edinburgh time-lapse project
HPHT	High-pressure, high temperature
LoFS	Life-of-field seismic
NLI	Non-linear inversion
NRMS	Normalized root mean square
PRM	Permanent reservoir monitoring
RG	Reservoir geomechanics
RMS	Root mean square
RMSD	Root mean square deviation
TWT	Two-way traveltime
FD	Finite-difference

Chapter 1
Introduction

This chapter lays the foundation and provides the structure for this thesis. It starts with a brief discussion on the current global energy landscape, the reason why dynamic reservoir characterisation is important, and the tools generally applied for this purpose. It then gives an insight into the time-lapse (4D) seismic and its role in dynamic reservoir characterisation. It also introduces the concept and applications of time-lapse time-shifts. Next, it identifies the main challenges faced by this study of dynamic characterisation of HPHT reservoirs, and sets up the main objectives for this research. At the end, it provides a general outline of each chapter of this thesis.

1.1 Background

1.1.1 The changing landscape of global energy

Nowadays, the landscape of global energy is undergoing significant changes with the rapid technological developments in the energy industry and the ever-increasing global attention on 'decarbonisation' to fight against climate change. A recent statistical review of the world energy released by BP has shown a shift of the global energy dependency from the traditional fossil energy (coal and oil) towards gas and the fast-growing renewables (such as wind, solar, and geothermal) (BP, 2017). The tendency of this shift can be visualized in the diagram of Figure 1.1a, in which the share of oil and coal will continue to decrease whilst other relatively new forms of energy keep on increasing in the near term.

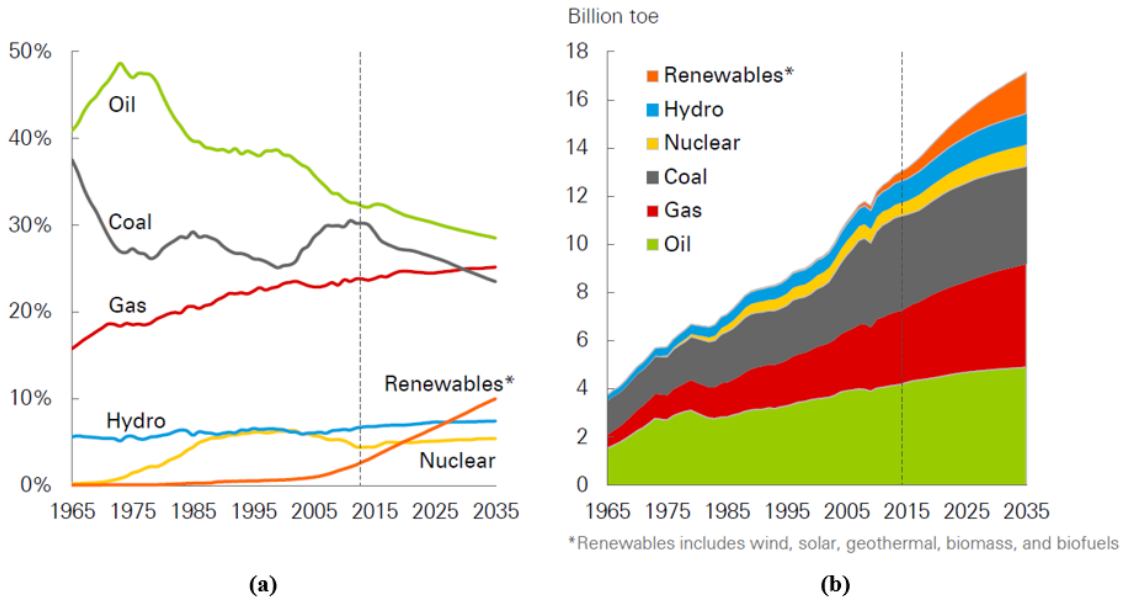

Figure 1.1: Diagrams showing the gradual transition in the fuel mix: (a) the share of primary energy from 1965 to 2035; (b) the primary energy consumption by fuel from 1965 to 2035 (BP, 2017).

However, despite these changes, the total demand for traditional hydrocarbon energy is still expanding (Figure 1.1b), bringing more and more challenges to the petroleum industry. Moreover, in view of the low oil price at the time of writing ($48/bbl), it is now crucial more than ever for the petroleum industry in taking actions to adapt itself in order

to stand firm and meet the needs of this changing world. Therefore, in the current situation, the optimization of hydrocarbon production has become increasingly essential and needs to be carried out in a more efficient, economic and environmental friendly way. To fulfil this purpose, the main focus of this thesis – dynamic reservoir characterisation and monitoring, can make a significant contribution.

1.1.2 Reservoir characterisation

In the area of field exploration and development, diverse sources of data are acquired and used to interpret various properties of a hydrocarbon reservoir which is located thousands of metres underneath the earth's surface. These information are generally divided into two categories – hard data and soft data in the form of direct or indirect measurements, which are then put together to build a computer based reservoir model used for the purpose of reservoir characterisation and monitoring (Hodgson, 2009). Hard data normally refers to the direct measurements from subsurface, however, each one of them only reveal specific information at a specific location. For example, well production data provide information about reservoir quality, well pressure data provide information about reservoir connectivity, and core data provides information about the level of heterogeneity in the reservoir. In fact, these kinds of information are always localized (usually at well location), therefore to combine them together for reservoir characterisation would introduce a large amount of uncertainty.

Having this in mind, it is very important to obtain various information in the space between wells to complete the picture of reservoir characterisation. Seismic data, as one form of soft data, can be a powerful tool to fill in the gap. During the past decades, seismic techniques have evolved significantly from the early 1D seismic trace and 2D seismic lines to the later 3D and dedicated 4D seismic volumes. The dramatic revolution in seismic acquisition and processing has not only improved the absolute spatial resolution and relative accuracy in image positioning compared to previous datasets (Yilmaz and Doherty, 2001), but also has provided better seismic imaging with reduced noise level. The concept of time-lapse seismic data (4D) is fairly straightforward, in that it is a set of repeated 1D, 2D or 3D seismic data acquired at different calendar times over the same area to assess changes in the subsurface with time, such as fluids-contact movement, un-swept area and by-passed oil, to help improve the knowledge of geology settings and

structure, and to give information for infill drilling deployment, etc. Since it was first introduced in the 1980's, it has been widely used and regarded as one of the most important tools for dynamic reservoir characterisation.

In the practice of reservoir modelling, 3D seismic datasets are used together with well log data at the beginning to condition the geological model by providing both the structural framework and property variations. The geological model is then up-scaled to a coarser grid as the simulation model to model dynamic properties such as fluid saturation and pressure, and the modelled results will be history matched to field production data if they are available. Uncertainties within the static model (geological model) and the dynamic model (simulation model) can be further constrained by 4D seismic data (Johnston, 2013).

1.2 Time-lapse seismic and its role in dynamic reservoir characterisation

1.2.1 Application of 4D seismic in dynamic reservoir monitoring

4D seismic has evolved during the past decades from a series of geophysical field experiments to a practical reservoir monitoring tool which can add significant value to the reservoir management process (Lumley, 2004).

The earliest 4D seismic examples can be traced back to the 1980's in the US, where 4D was successfully used for the monitoring of steam injection projects (Greaves and Fulp, 1987). These early 4D examples were conducted for onshore shallow reservoirs located less than thousand meters in depth. A few years later, the first offshore 4D seismic reservoir monitoring was introduced to the Oseberg field in the North Sea in 1991 to monitor changes of saturation and gas-oil contact, as well as to refine reservoir model parameters (Johnstad *et al.,* 1993). These early 4D seismic data were mainly conducted in a qualitative manner (Pedersen *et al.*, 1996; Marsh *et al.*, 2001) . In the meantime, in academia, the pioneering work done by Amos Nur and his group at Stanford University, provided a good insight into the rock physics basis for 4D seismic, and this shed a light on 4D quantitative analysis (Nur *et al.*, 1998). Although several pilot projects were conducted in the North Sea, 4D seismic had a slow start at the beginning because those projects turned out to have less economic impact on reservoir management (Carstens, 2009). However, the turning point quickly appeared after the commercial and technical

success of the Gullfaks 4D project since 1995. Its success clearly demonstrated the value of 4D in monitoring fluid and pressure changes in a complex reservoir during production (Sønneland *et al.*, 1997).

The quality of time-lapse seismic was then significantly enhanced thanks to the technical improvements in seismic acquisition and processing, which has enabled the applications of time-lapse seismic data towards a more quantitative way, such as estimating fluid saturation or pore pressure changes in the reservoir (Tura and Lumley, 1999; Meadows, 2001; Landrø, 2001; Corzo *et al.*, 2013; Calvert *et al.*, 2014; Landa *et al.*, 2015), evaluating geomechanical changes such as subsidence, reservoir compaction, and overburden / underburden stretching (Nickel *et al.*, 2001; Olden *et al.*, 2001; Guilbot and Smith, 2002; Hatchell *et al.*, 2003; Herwanger and Horne, 2009; Onaisi *et al.*, 2015).

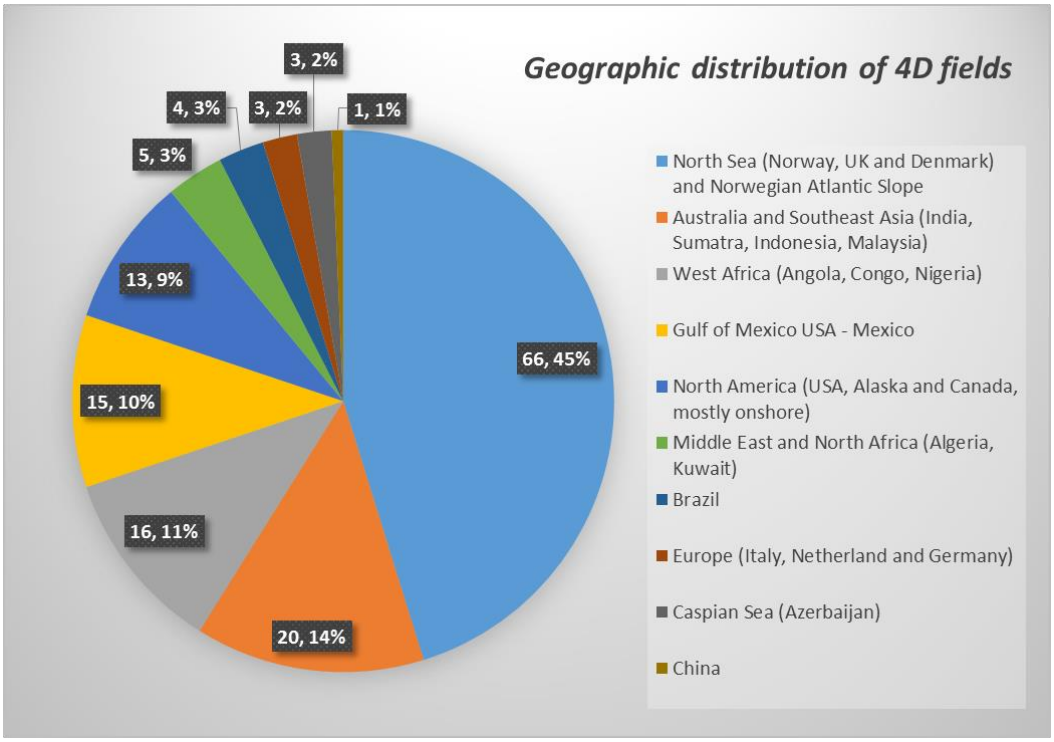

Figure 1.2: A pie chart showing the geographic distribution of 4D fields throughout the world (modified after Rangel (2016)). The number of 4D fields in each area and its percentage of total 4D fields are displayed on the pie chart.

4D seismic has now been widely deployed across the world as shown in Figure 1.2. According to a database summarized by Rangel (2016), the recorded number of hydrocarbon fields all around the world under time-lapse seismic monitoring had reached

146 in 2014, among which the majority are distributed over the area of North Sea (45%), Australia and South-east Asia (14%), West Africa (11%), Gulf of Mexico (10%), and North America (9%). Applications in the rest of the world (such as Middle East and North Africa, Brazil, Europe, Caspian Sea, and China) are also catching up. 4D seismic monitoring has been intensively applied to reservoirs of various geologic types (such as Turbidites, fluvial, deltaic, shallow marine, carbonate shelf, and Aeolian), and of a varying depth from several hundred meters to over 5000 meters subsurface (Rangel, 2016).

With the continuing improvements in marine 4D repeatability (such as the normalised RMS difference of some dedicated PRMs can now be reduced down to a level as low as 4% (Bertrand *et al.*, 2014)), and all the intense efforts put onto seismic history matching and geomechanical modeling, time-lapse seismic has now become a standard tool for field characterisation and management at different stages of a field life cycle, starting from field exploration, to development, and to production and optimization stage (Figure 1.3). Now, the main roles of 4D seismic are to map out bypassed / residual oil for new drilling opportunities (Koster *et al.*, 2000), to evaluate displacement efficiency and to detect water front to avoid the costly mistake of drilling new wells into swept zones (Kloosterman *et al.*, 2003), to characterise reservoir quality (such as reservoir geometry, compartmentalization, faults and fault transmissibility, intra-reservoir connectivity, communication between fields), to accurately separate the effect of pressure changes and saturation changes (Landrø, 2001), to predict geomechanical effects, and to monitor the performance of wells . The maturity for most of the 4D applications is shown in Figure 1.4.

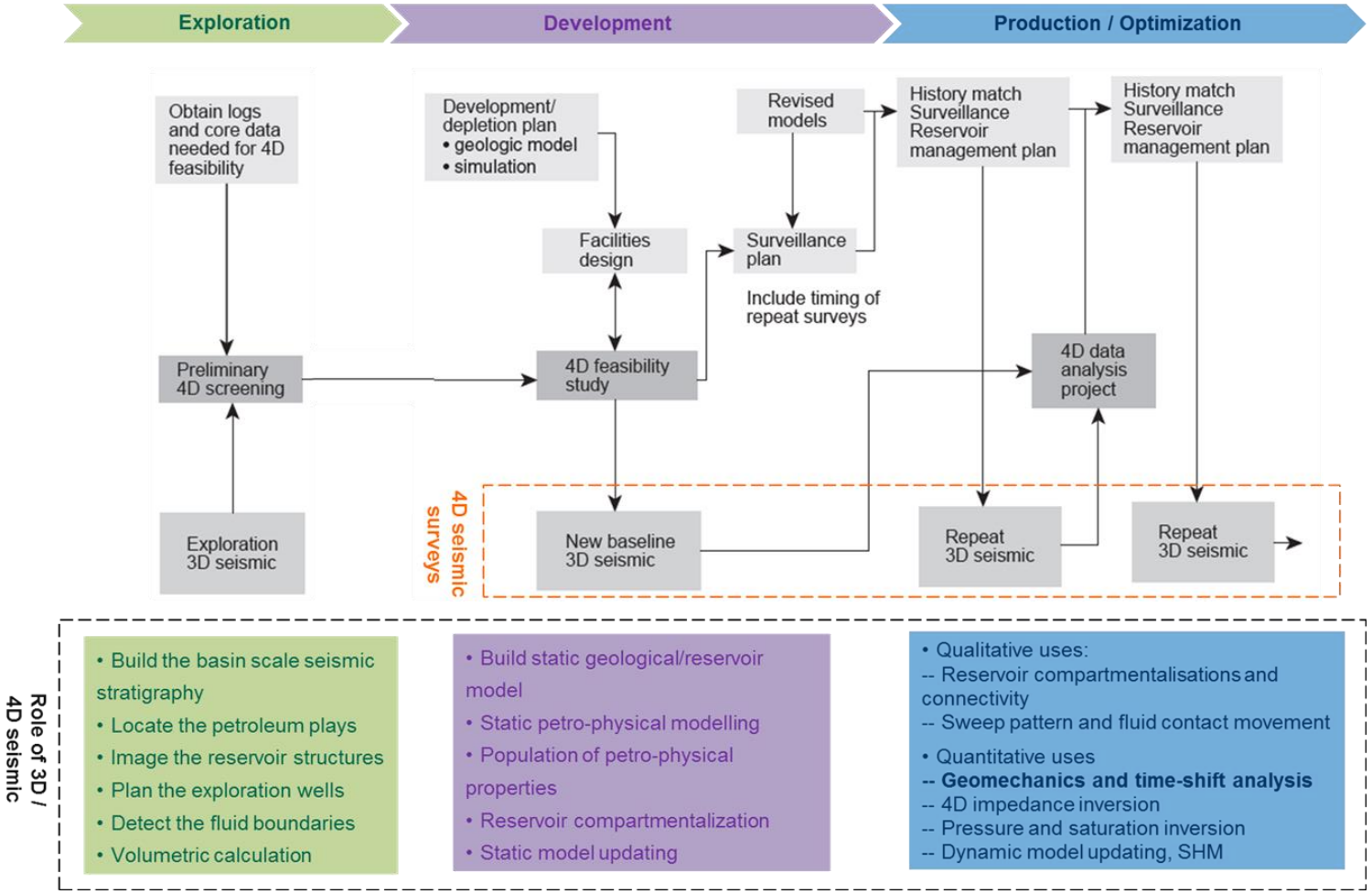

Figure 1.3: 4D activities and its role at different stages of a field life cycle, starting from field exploration, to development, and to production and optimization (modified after Johnston (2013) and Tian (2014)).

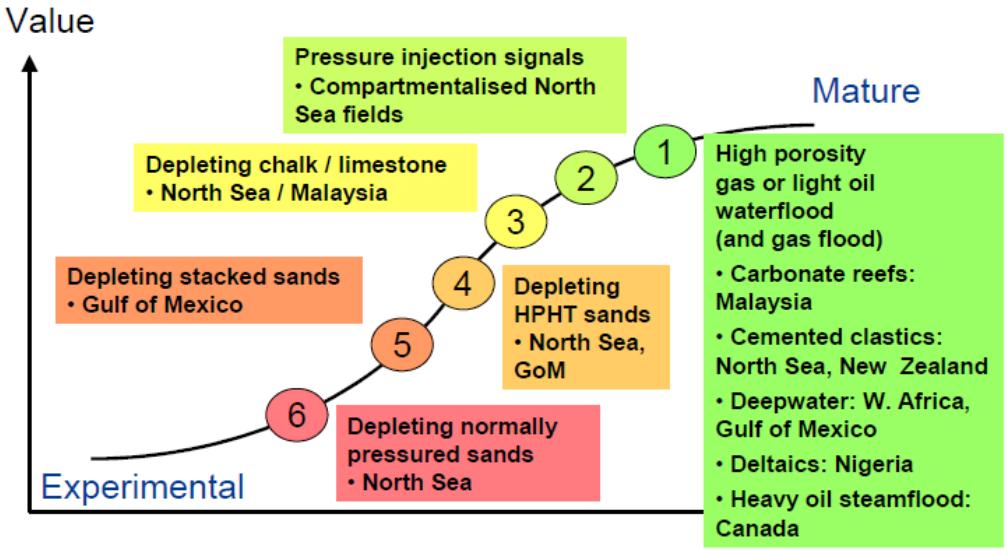

Figure 1.4: A maturity S-curve for different 4D applications. The waterflood / gasflood only include high porosity reservoirs. For low porosity reservoirs (e.g. Ø<22%), it would sit further down the curve due to the smaller 4D signal (Staples *et al.*, 2006).

1.2.2 Time-lapse time-shift and its application

Time-lapse time-shift (Δt) is one of the most popular time-lapse seismic attributes used in dynamic reservoir characterisation. It represents the two-way traveltime (TWT) difference between time-lapse seismic surveys both inside and outside the reservoir. For example, during the hydrocarbon production of a reservoir under pressure depletion drive, the decrease of pore pressure will happen inside the reservoir, and this will lead to changes in the stress and strain fields of the rock formations both inside and outside the reservoir (Hatchell and Bourne, 2005b). This will cause a certain degree of deformation (thickness change) as well as seismic velocity change in these formations (Figure 1.5). According to the rock-physics study, changes in fluid saturation will also induce velocity change, however it is usually not as significant as the change caused by deformation, and more details will be discussed in Chapter 6. As a result, seismic waves propagating through these rocks will have different traveltime before and after production which can be measured from time-lapse seismic surveys, and these TWT differences are referred to as time-lapse time-shifts. Due to the cumulative nature of the seismic TWT, the time-lapse time-shift accumulates along seismic ray path, which means, at a particular point, time-shift represents the sum of traveltime differences of all the layers above.

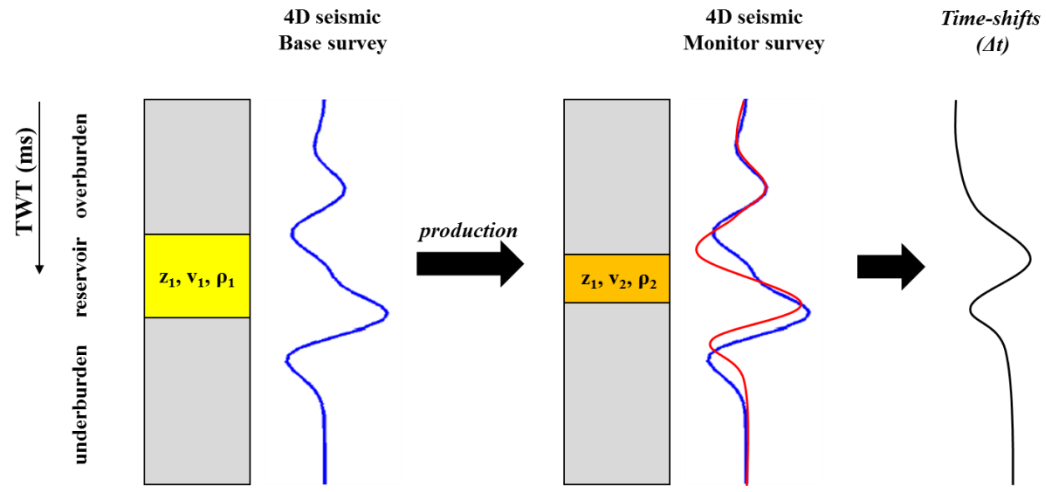

Figure 1.5: A schematic representation of physical principles of time-lapse seismic and time-shift between seismic base survey (left) and monitor survey (middle), and time-shifts between them (right) (adapted after Hodgson (2009)). Changes due to production cause changes in the thickness and elastic properties of the reservoir, therefore changing the traveltime and amplitude of the reflected seismic pulse.

Normally, the time-lapse time-shift used for 4D analysis is extracted from migrated full-stack (zero-offset) 4D seismic data, and sometimes, it comes from restricted offset stacks in order to provide an indication of offset dependency (Landrø and Janssen, 2002; Landrø and Stammeijer, 2004; Fuck *et al.*, 2007, 2009; Ghaderi and Landrø, 2009; Herwanger and Horne, 2009; Kudarova *et al.*, 2016). Rarely are such measurements performed on raw pre-stack data, although some examples do exist in the literature (Røste *et al.*, 2006, 2007; Hawkins, 2008). Clearly all such time shifts carry an interpretational benefit to some degree, but post-stack time-shift results are of more practical value for reservoir interpretation and characterisation. Overburden time-lapse time shifts can be used as an input to a linear inversion for reservoir pressure, and can add more confidence in the estimation of stress changes (Hodgson *et al.*, 2007; Garcia *et al.*, 2010; Smith *et al.*, 2012; Wong *et al.*, 2015).

In the past, large time-shifts (10ms and above) in the overburden were observed and interpreted as the result of reservoir compaction. But for small time-shifts, they were usually considered as artefacts of acquisition or processing non-repeatability. It was not until 2003, Hatchell et al. published a revelatory work that very small time-shifts can be measurable from 4D seismic data and can be interpretable as changes inside reservoirs (Hatchell *et al.*, 2003). Small time-shifts often represent small-scale geomechanical

effects, and have an average magnitude ranging from 1 to 2ms (Hatchell *et al.*, 2003). Figure 1.6 shows field examples where small and large time-shifts have been observed.

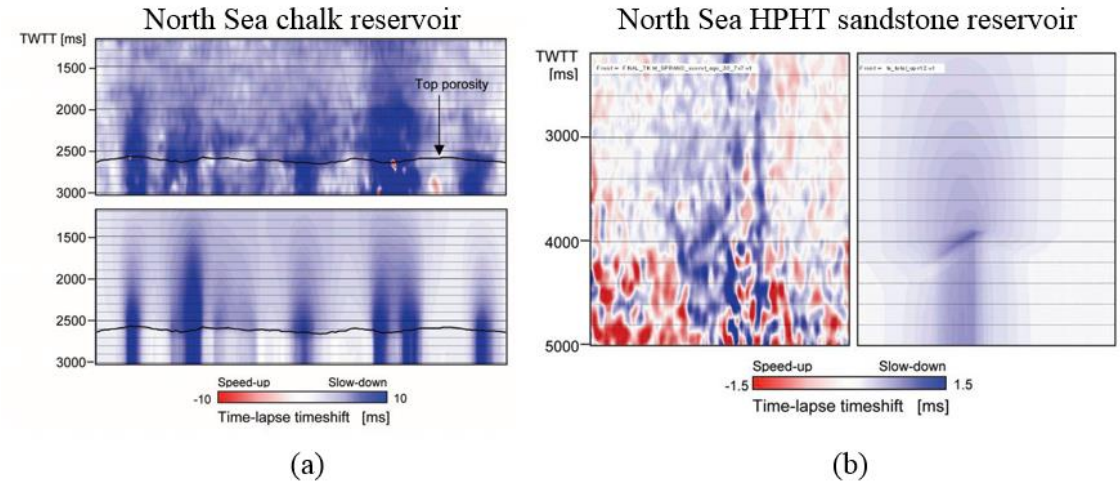

Figure 1.6: The magnitude of observed time-lapse time-shift for different type of fields: (a) time-lapse time-shift of up to 10 ms was observed in a North Sea chalk reservoir; (b) time-lapse time-shift of as small as 1.5 ms was observed in a North Sea HPHT sandstone reservoir (Hatchell and Bourne, 2005b).

Now, time-shift of a wide range of magnitude (from 0.2 ms to 40 ms) in distinct seismic reflectors over elapsed time can be measured properly, and its magnitude is dependent on field property (such as lithology, thickness, and depth), production and recovery mechanisms, and elapsed period. The measurement accuracy is quoted at 0.1 ms for streamer surveys and 50 microseconds for PRMs (MacBeth *et al.*, 2012; MacBeth and Mangriotis, 2017). Excellent results are observed from PRMS datasets (such as the Ekofisk LoFS) due to their distinctive signal to noise ratio (Bertrand *et al.*, 2013; Wong *et al.*, 2015).

Figure 1.7 shows time-shifts for different types of fields and various production or optimization mechanisms, values are as small as 0.5 ms to as large as 40 ms. In the overburden, time-shifts of 2 to 40 ms have been observed and are mainly related to extension which are caused by reservoir compaction. There are many good examples of overburden time-shift measurements in the literature, among which the extension-related time-shifts can be quite large for HPHT or compacting chalk fields (Guilbot and Smith, 2002; Hatchell and Bourne, 2005b; Garcia, 2011). The opposite effect of reservoir

extension due to pressurisation cause by an injector, and time-shifts from overburden depletion (speed-up) do exist, but are quoted less often because they are more difficult to observe on the seismic data, and also perhaps down-weighted due to a natural asymmetry of the stress/strain response (e.g. R factor of 2 for reservoir rock and 5 for non-reservoir rock (Hatchell and Bourne, 2005b)). Time-shifts are also generated in the underburden but are rarely discussed. A typical underburden example is shown in Figure 1.8, approximately 4 to 7 ms underburden time-shift were observed from Norne field between 2001 and 2006, which is most likely attributed to a 4D velocity decrease within the sandstone due to pore pressure increase after water and gas injection in the reservoir (Aarre, 2006, 2007).

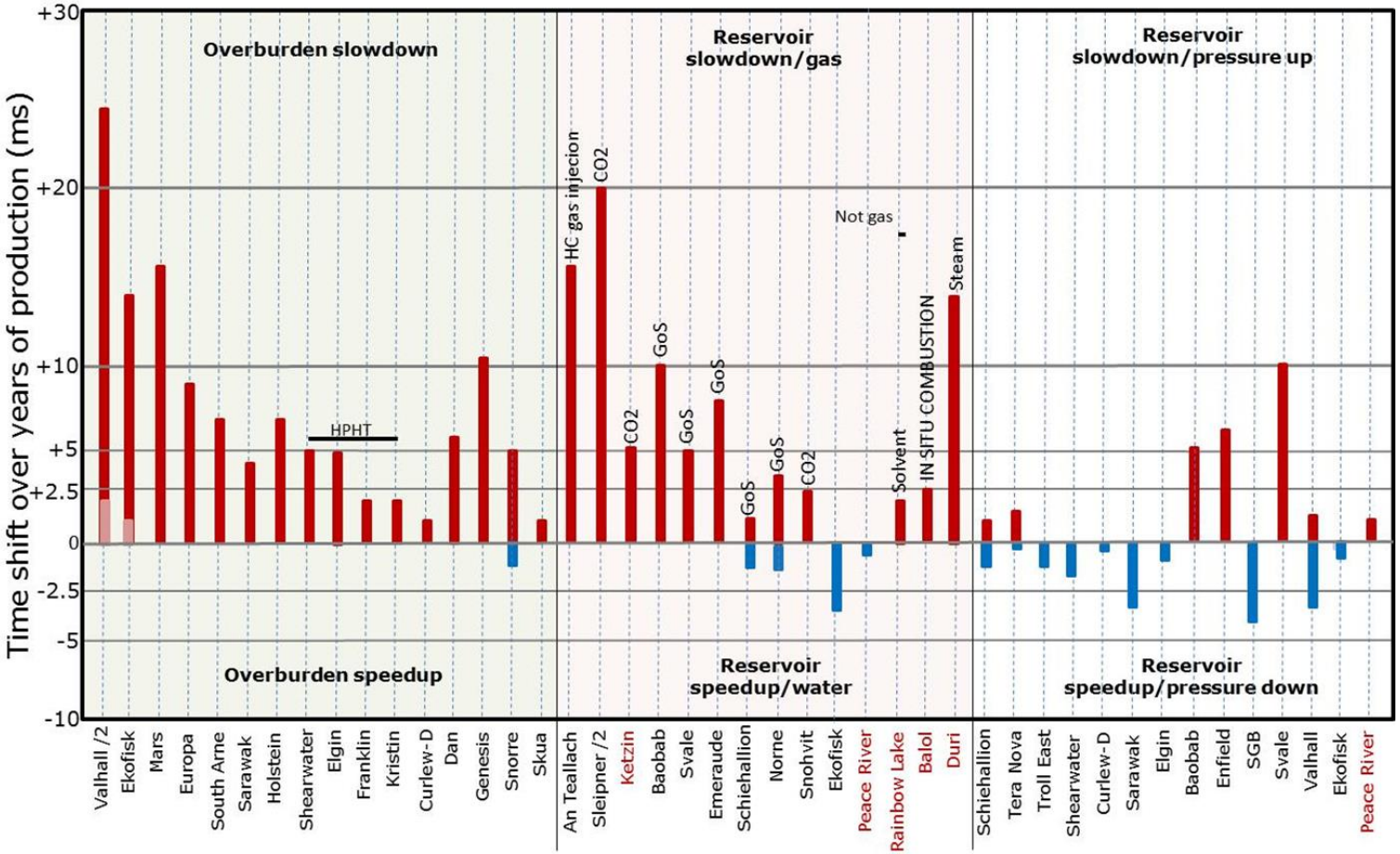

Figure 1.7: Ball-park time-shift magnitude for different types of fields and various production / recovery mechanisms. Time-shift magnitude varies from as small as 0.5 ms to as large as 40 ms. In the overburden, time-shifts of 2 to 40 ms have been observed from strong geomechanical effects (MacBeth *et al.*, 2016)

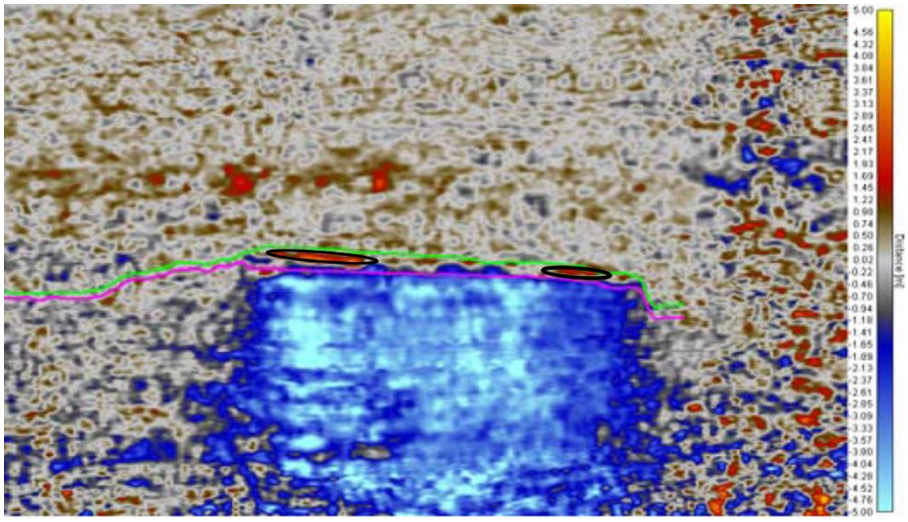

Figure 1.8: The large underburden time-shift (approx. 4-7 ms) observed from Norne field between 2001 and 2006 due to fluid changes rather than geomechanical effects, black circles highlighted the upward fluid contact movements (Aarre, 2007).

However, the time-shift story becomes complicated inside the reservoir due to the competition between the effects of geomechanics and those due to water or gas saturation changes. And these time shifts are generally smaller than those associated with the overburden extension. Nevertheless, there are cases when one effect may dominate, such as for gas or the case of pressure up due to an injector (Aarre, 2007; Alsos *et al.*, 2009). The effect of fluid contact movements should also be noted such as the upward movement signals (red) inside the reservoir as highlighted by black circle in Figure 1.8 (Aarre, 2007).

Although there is a large number of time-shift observations published so far, the number of methods that apply time-shift for dynamic reservoir characterisation and management is limited. Apart from qualitative time-shift analysis, quantitative time-shift analysis mainly focuses on the relationship between velocity and stress / strain. The approaches used for solving the non-uniqueness in this relationship differ for various cases, with R-factor being the most commonly used approach (Hatchell and Bourne, 2005b, 2005a; Hatchell *et al.*, 2005; Tigrek and Hatchell, 2006; Hatchell *et al.*, 2007; Staples *et al.*, 2007b). The R-factor is a constant which represents the ratio between the fractional change in vertical P-wave velocities and the fractional changes in path length as in Eq. 2-7 (Hatchell and Bourne, 2005b). This approach compares observed overburden time-shifts with those calculated from geomechanical modelling using the equation proposed

by Hatchell and Bourne (2005b), and uses the resulted mismatch to update reservoir compaction model. Similar to this approach, an anisotropic model of velocity changes with stress and strain is brought up by Herwanger and Horne (2005). Instead of using post-stack time-shifts, Røste *et al.* (2005) and Hawkins *et al.* (2007) adopt pre-stack seismic information for estimating reservoir compaction and stress changes. Furthermore, the approach suggested in Bourne and Hatchell (2007) uses geomechanical concepts to pose a linear relationship that directly links reservoir compaction to the strain (derived from time-shift using R factor) in the overburden, so that a linear inversion can be performed for the estimation of reservoir compaction. Similar approaches based on this have been developed and extended the inversion for reservoir compaction to the inversion of pressure change and saturation change (Hodgson *et al.*, 2007; Garcia *et al.*, 2010; Corzo *et al.*, 2013; Wong *et al.*, 2015).

1.3 Main challenges and research motivation

Although the topic of integrating 4D seismic into dynamic reservoir characterisation has been researched over the past decades, there are still a wide range of practical challenges remaining to be solved. These challenges are confronted at different stages of the integration work, and usually vary a lot across different types of reservoirs. For the type of high-pressure and high-temperature (HPHT) reservoirs, the main challenges in dynamic characterisation and monitoring are widely considered to be the production-related geomechanical issues due to their initial reservoir conditions, geological settings, and developing strategies.

1.3.1 The definition and classification of HPHT reservoirs

High-pressure high-temperature fields broadly exist in Gulf of Mexico, North Sea, South East Asia, Africa, China and Middle East (Shadravan and Amani, 2012). The original definition of HPHT was first introduced by the Department of Trade Industry (DTI) for the United Kingdom continental shelf (UKCS) as "Where the undisturbed bottom hole temperature at prospective reservoir depth is greater than 300 °F and the maximum anticipated pore pressure of any porous formation to be drilled through exceeds 10,000 psi (Maldonado *et al.*, 2006). However, to help identify HPHT operating environments, safe operating envelopes and technology gaps, a new terminology has been developed (as

in Table 1.1) to segment HPHT reservoirs into three tiers. As seen in Figure 1.10, most HPHT operations to date have taken place under Tier I conditions with pressures up to 15,000 psi (1034 bar) and temperatures up to 350 ºF (177 ºC).

Table 1.1: The industry HPHT Tier classification (Glass, 2005; Maldonado *et al.*, 2006)

	Pressure		Temperature	
	Kpsi	bar	degC	degF
Tier I (HPHT)	10-15	689-1034	149-177	300-350
Tier II (Extreme-HPHT)	15-20	1034-1379	177-204	350-400
Tier III (Ultra-HPHT)	20-30	1379-2068	204-260	400-500

Knowing how the fluid behave during production is also important for an HPHT gas-condensate reservoir. Figure 1.9 shows a common phase diagram of a gas-condensate reservoir. Its initial reservoir condition is in the single-phase area to the right of the critical point. As reservoir pressure declines, the fluid passes through the dew point and a liquid phase drops out of the gas (Fan *et al.*, 2006).A gas condensate reservoir can choke on its heavy components. Condensate liquid saturation can build up near a well because of drawdown below the dew point pressure, this will ultimately restrict the flow of gas (Fan et al., 2006). All of these will have an impact on 4D signals.

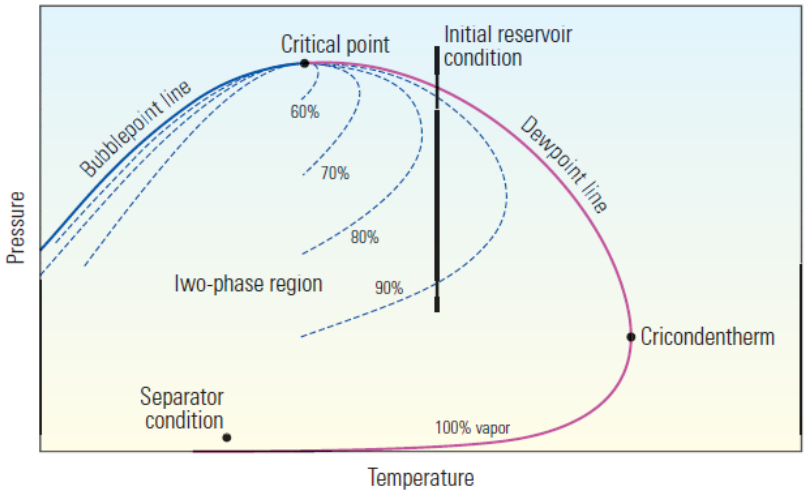

Figure 1.9: Phase diagram of a gas-condensate reservoir(Fan *et al.*, 2006).

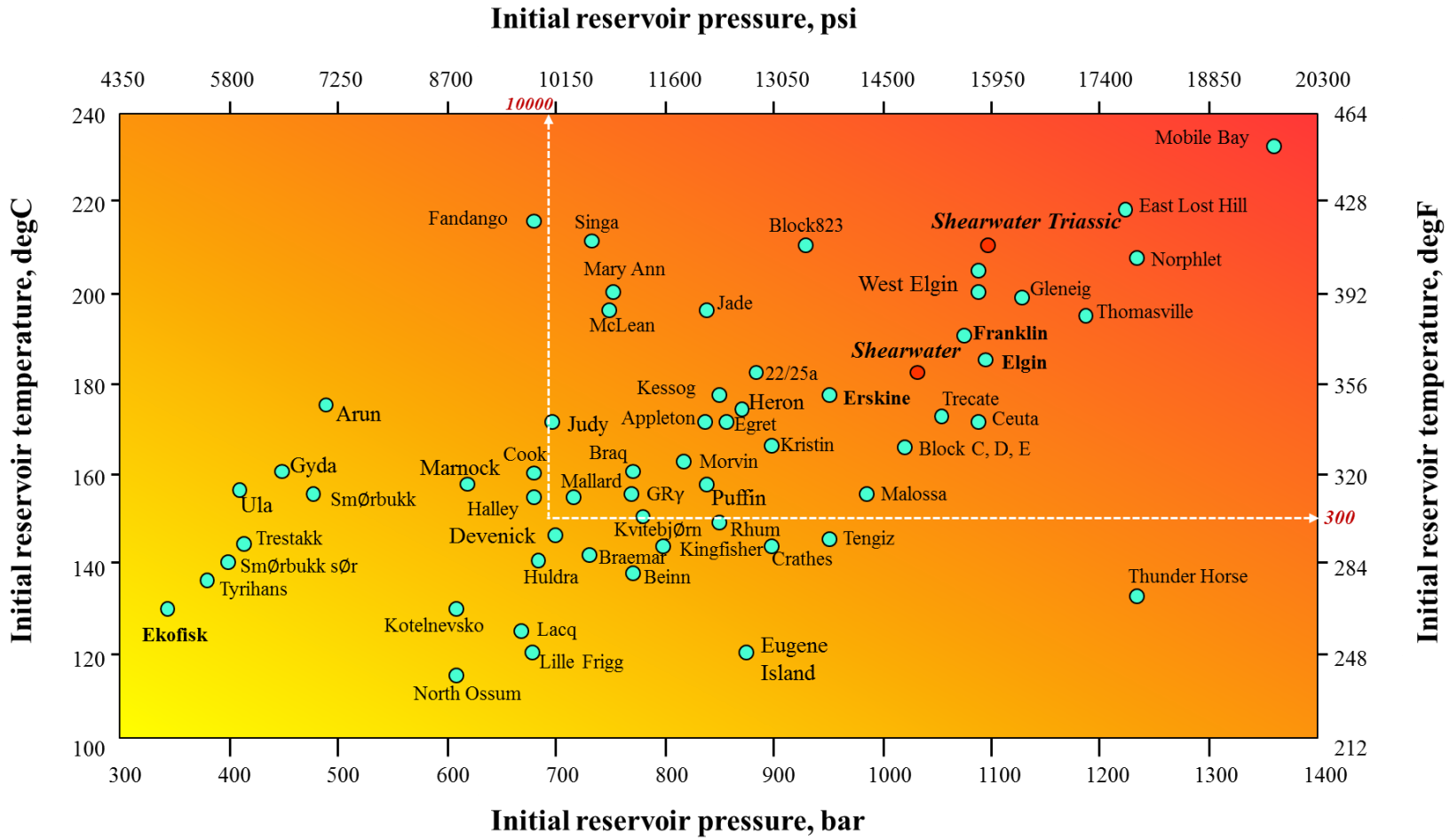

Figure 1.10: Fields across the world with high/extreme/ultra pressure / temperature (adapted after Baird et al., 1998; DeBruijn et al., 2008; Kfoury, 2012). White dashed lines indicate the minimum pressure and minimum temperature for the classification of HPHT fields.

1.3.2 Reservoir compaction and potential effects

Throughout the entire life of a HPHT field, challenges have been acknowledged from a wide range, covering aspects from physical and economic technologies to regulatory (Shadravan and Amani, 2012). Among these risks, reservoir compaction has always be a major concern as resultant deformations may lead to severe well damage and huge economic loss.

The deeply buried and geomechanically sensitive HPHT reservoirs are generally developed under pressure depletion drive rather than any external drive mechanisms. From previous experiences of operating most HPHT wells, considerable pressure depletion usually happens three to four years after the production initiated (Glass, 2005). As a result, part of the weight of the overburden originally supported by the highly pressured pore fluids will be transferred to the rock matrix of the reservoir, resulting in a change of the in-situ stress state, causing the reservoir to compact. However, for a sand reservoir this may not lead to significant rock failure. As shown by Vaziri *et al.* (2006), rock compaction may lead to increased resistance to rock break-up owing to the increased friction between the sand grains and arching around the perforations. Therefore, it is more likely that the compaction will result in deformations and rock failures in the overburden (Li *et al.*, 2003), such as the collapse of overlying seals, overburden fault reactivation, bedding movement, and surface subsidence as seen in Figure 1.11 (Herwanger and Horne, 2009).

The presence of faults and other form of deformations, in turn, will lead to severe damages of the existing wells, such as the fault-slip-induced casing breach. Since considerable volumes of gas still remain in place, a good characterisation of the subsurface stress and strain fields is vital for future infill drilling operations. However, due to the extreme conditions of HPHT fields, hard data measurements are always insufficient and even absent, which makes the analysis hard to process. Fortunately this could now be achieved with the help of repeated and high quality 4D seismic data and the derived seismic attributes such as the time-lapse time-shifts.

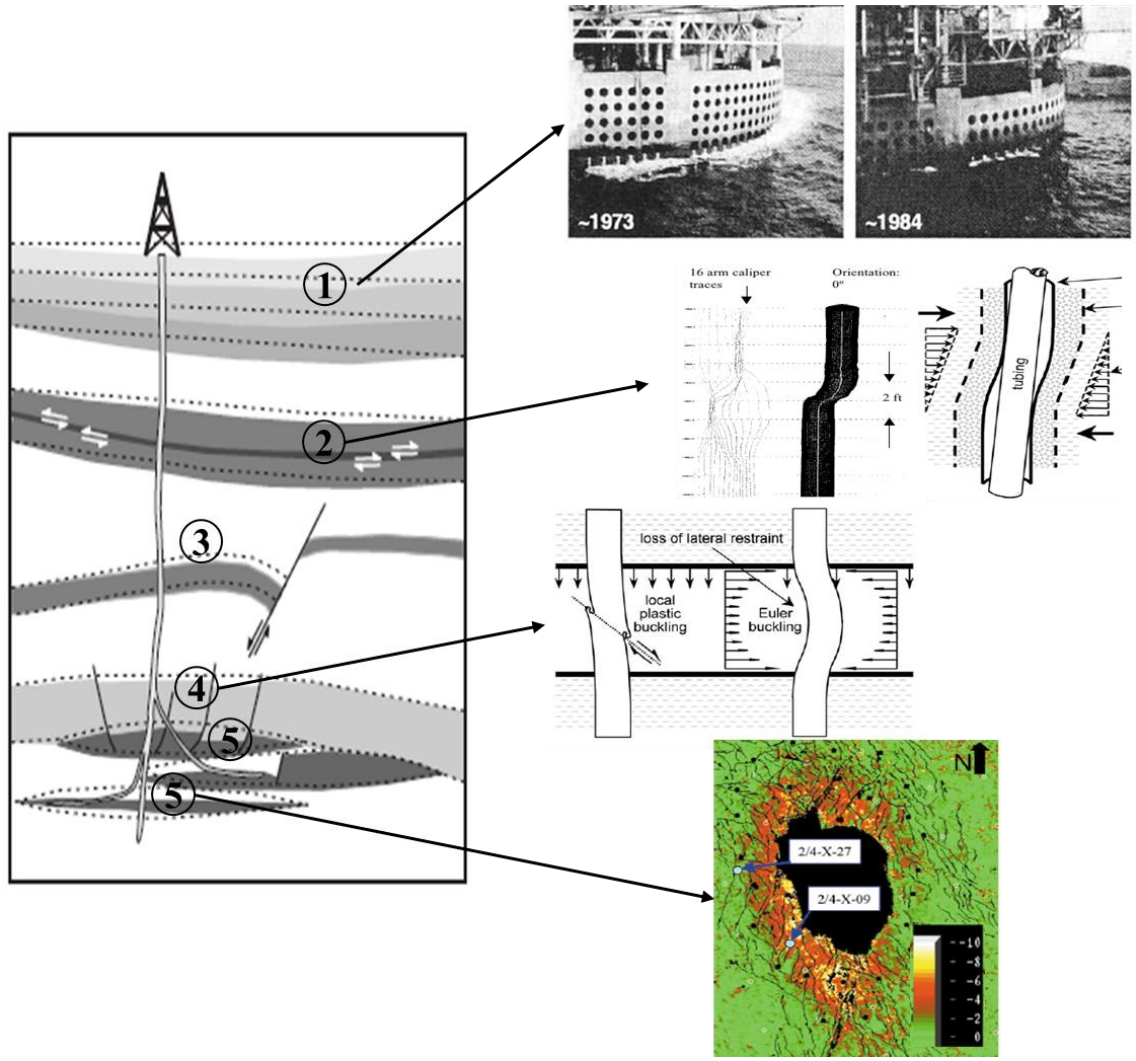

Figure 1.11: The left is a sketch of potential subsurface deformations during reservoir production, dotted lines represent preproduction state, and solid lines indicate post-production state. Subsurface deformations can occur as 1 surface subsidence, 2 bedding parallel slip, 3 fault reactivation, 4 breach of seal integrity, and 5 reservoir compaction (Herwanger and Horne, 2009). Right figures give examples of different subsurface deformations (Nagel, 2001; Bruno, 2002; Dusseault *et al.*, 2001; Guilbot and Smith, 2002).

Since the first application in Ekofisk (Guilbot and Smith, 2002) studying the overburden stretching related time-lapse time-shifts, the use of 4D seismic attributes in geomechanical characterisation and monitoring has been successfully demonstrated and widely applied across different types of fields to study the subsurface stress and strain evolutions. This kind of application covers the use of 4D seismic observations to validate geomechanical models (Hatchell *et al.*, 2005; Hatchell and Bourne, 2005a, 2005b), to derive reservoir compaction maps (Hatchell and Bourne, 2005a; Herwanger and Horne,

2009), and to detect vertical and lateral reservoir compartmentalization (Staples *et al.*, 2007b). However, before using time-lapse time-shifts for reservoir geomechanical monitoring, it is essential to obtain them in a more efficient and accurate way. However, from the past experiences, it is not trivial to be achieved, and is influenced by a lot of factors.

1.3.3 The challenge of measuring time-lapse time-shifts

Theoretically, time-shifts can be measured very accurately in discrete, regularly sampled 4D seismic data, with the only limitation being the signal-to-noise ratio of the data. As a general concern, improper acquisition and processing can affect the time-shift measurements. For example, the false time-shifts of HPHT field - Curlew-D as shown in Figure 1.12a were partly due to systematic errors caused by a relative miss-positioning error of 6m between the two surveys, and was further exacerbated by steep dips (Fehmers *et al.*, 2007). However, with the latest development in 4D seismic acquisition and processing, non-repeatability is no longer a big issue especially for dedicated PRMs. However, for low-repeatability 4D datasets, pre-processing and pre-conditioning of the datasets are needed before moving to the time-shift measurement step.

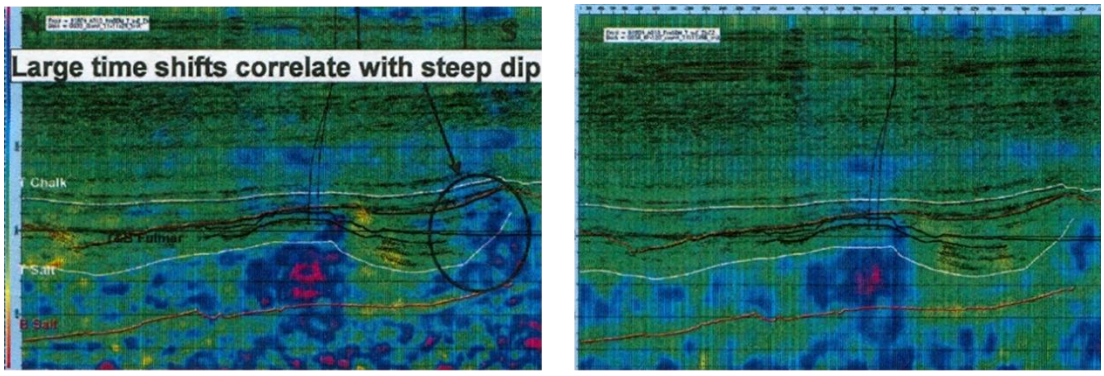

Figure 1.12: Acquisition related time-shifts, an example from Curlew-D; (a)time-shift profile before correction, (b) time-shift profile after correction (Fehmers *et al.*, 2007).

In practice, the accuracy also depends on the measurement algorithms. Since the concept of time-lapse time-shift was introduced, a large number of measurement techniques have been published. However, there are inherent limitations within each method, and the accuracy of recovering various magnitudes of time-shifts from various quality of 4D

seismic data needs to be evaluated. Unsuitable calculation methods in some cases will give unstable results and can even introduce artificial noise, and as a result this will bias the interpretation (Kanu *et al.*, 2016). Therefore, selecting a proper time-shift calculation method for different application scenarios is a big challenge to be tackled at the beginning.

1.3.4 The gas bearing chalk formation

Apart from the challenges presented above, there is also an overburden issue which exists in some of the HPHT fields in the Central North Sea. It is related to a gas bearing chalk formation (mainly within Hod) that is causing additional well engineering problems. Cementations across the zone – as part of the intermediate/production casing string installation have so far been rarely successful in obtaining a full shut off (Glass, 2005). As a result, the B-annulus (the annulus between the production casing and next outer casing) in these wells is permanently pressurized although it may take as long as two years after the start of production before the Hod pressures are seen(Glass, 2005). Therefore, effectively isolating the over-pressured gas bearing formation is important, and this will require a good identification of the occurrence of these formations and where they are gas filled with the help of 4D seismic. Apart from that, a geomechanical analysis of this formation is also important.

1.4 Objectives of this research

Based on the main challenges described above, the main objective of this thesis is set to integrate 4D seismic data, geology, geomechanics and rock physics into dynamic reservoir characterisation of a high-pressure and high-temperature field. This project cannot aim to integrate effectively as neither the simulation model nor the full geomechanical model is provided, however it does aim to understand how best 4D seismic can be linked with geomechanics and depletion patterns. Apart from that, the time-shift distributions outside of the reservoir are believed to carry important information that should not be ignored. In this work, I will break away from just vertical time-shifts, to determine more information on how to measure deformation and stress using the 4D seismic.

This work will be progressed in 4 stages:

In the first stage, I will conduct an extensive study of the published time-lapse time-shift calculation methods, and based on the knowledge built from there, I will make an in-depth analysis of three selected techniques and evaluate their performance in cases of various seismic quality and time-shift magnitude.

In the second stage, I will perform a general characterisation of the HPHT reservoir, interpret the observed 4D seismic attributes (time-shift and amplitude) with integration of geology and production information. I will use not only the zero-offset time-shifts but also the angle-stack time-shifts for reservoir characterisation.

In the third stage, I will address geomechanical issues, conduct a simplified geomechanical model and calibrated it with the help of 4D seismic information. I will analyse the evolution of stress and strain fields and predict potential future well failure events.

In the last stage, I will model the overburden time-shift anomaly, based on various assumptions of gas and geomechanical effects.

1.5 Thesis outline

To tackle the challenges and to achieve the objectives stated above, this thesis will develop the idea of integrating 4D seismic data (mainly the observed 4D time-shifts) into dynamic reservoir characterisation of an HPHT field. The structure of this thesis is outlined in Figure 1.13, and it was followed by a brief description of the remaining chapters.

Chapter 2 provides a brief overview of fundamental theories applied in this study. The main part of this chapter starts with a general literature review of different methods for time-lapse time-shift calculation, and discussions on the advantages and limitations of various methods. It then moves to the fundamentals of geomechanics, and linking it with 4D seismic. And finally, it touches on the study of rock physics for modelling effects of physical changes on seismic properties.

Chapter 3 presents a critical comparison of three different time-shift measurement techniques (DHFCC, CLM, and NLI) introduced in Chapter 2. The three methods are

compared through applications to both synthetic and real 4D seismic datasets. The synthetic datasets include both idealised noise-free and noise-added (with the range selected in accordance with the general noise level of North Sea fields) scenarios. In the meantime, the magnitude of time-shift imposed on these synthetic monitors is made to vary from small to large. For synthetic tests, results calculated by the three methods are compared by determining their NRMS deviation from the input values. For field data tests, results are compared in a more qualitative way. At the end, each of the time-shift methods is evaluated considering different aspects, and the most appropriate method is suggested for the following study.

Chapter 4 builds on chapters 2 and 3 to show a general reservoir characterisation of the Shearwater field using 4D seismic attributes as well as geology and production information. Time-shift volumes are measured from Shearwater time-lapse seismic vintages by the three time-shift methods discussed in chapters 2 and 3, and then the best result is converted into time-strain to understand the instantaneous changes within each interval. Discussions on 4D amplitude changes as well as the time-shift variations with offset are also provided. After that, the focus is moved onto the interpretation of the calculated time-shift and time-strain distributions, and linking them with field geological and production information. In addition, synthetic test is conducted to give an insight into the cause of the Heather shale anomaly.

Chapter 5 aims to understand how best the 4D seismic can be linked with the geomechanics in terms of stress and strain evolution in the subsurface, and also how the 4D seismic is responding to the depletion patterns within the reservoir. During the study, a simplified reservoir geomechanical model has been constructed to match the time-shift distribution observed from Chapter 4, with the help of reservoir simulation, geology and rock mechanics studies. This current study evolves towards a deeper assessment of mechanical failures, and thus the predictions of well stability during drilling and production.

Chapter 6 addresses the abnormal overburden time-shift and time-strain distributions, and aims to explore the potential reasons causing this large amount of time-shift increase. The prevailing hypotheses include the gas effect and the geomechanical effect. Both effects are modelled for time-shift behaviour and compared to the observations. To model the

4D gas effect, different initial gas saturations are considered, as well as separate scenarios with and without solution gas. With respect to the geomechanical effect, the magnitude of R factor is incorporated into the discussion, and an extra velocity-stress/strain sensitivity linked to the opening of cracks is considered for heightened R factors.

Chapter 7 summarizes the thesis with conclusions, and in addition, recommendations are provided for future research in dynamic reservoir characterisation using 4D seismic data.

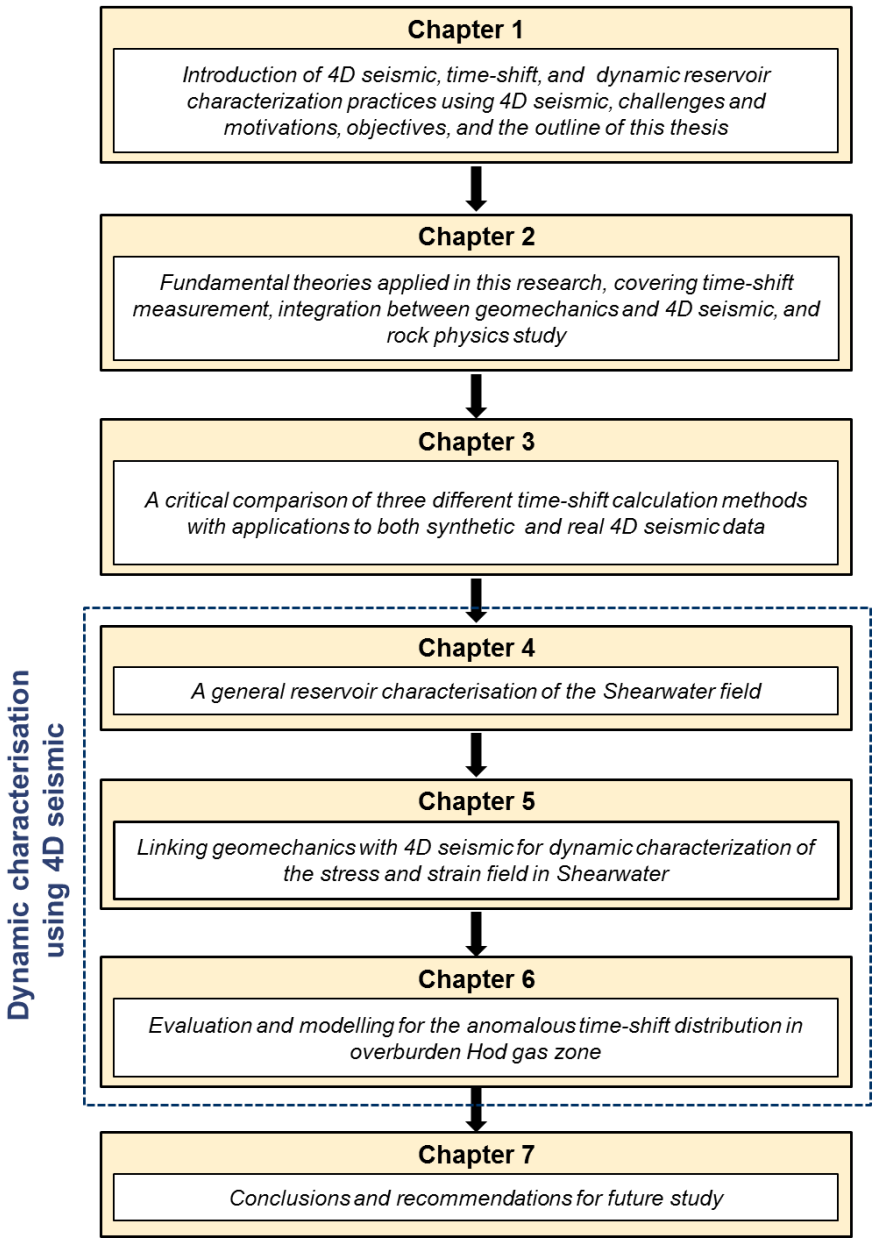

Figure 1.13: The general development and structure of this thesis

Chapter 2

Fundamental theories in this research

This chapter provides an overview of fundamental theories applied in this research. As this research has been developed in a close relation with time-lapse time-shift, the measurement techniques for this attribute are of great importance. In the first part, I review different methods for time-lapse time-shift calculation published so far, and discuss their advantages and limitations in application. In this research the time-lapse time-shift is used for reservoir characterisation in both qualitative and quantitative ways with the integration of geomechanical modelling. In the second part, I give an overview of reservoir geomechanics, time-lapse time-strain, and the link between 4D seismic and geomechanics. At the end, I talk about the effect of changes in elastic properties on 4D seismic and the Gassmann model for rock physics study in this research.

2.1 Introduction

Based on the motivations and objectives stated in Chapter 1, this PhD research is closely developed around the star attribute of the time-lapse seismic – the time-lapse time-shift. Unlike other theory-developing kind of research, this is more inclined to use 4D seismic in a practical way, where the measurement, interpretation, and application of this intriguing seismic attribute are fully researched. In each part of this research, theories in different aspects have been used and integrated. Therefore, in this chapter I present an overview of the fundamental theories applied in this study, including time-shift measurement techniques, integration of geomechanics and 4D seismic, and rock physics study on fluid effects.

2.2 Different techniques for time-shift calculation

2.2.1 Cross-correlation based techniques

Over the past two decades, there have been a variety of developments for the measurement of time-lapse time-shifts; among them, the most commonly used technique is cross-correlation. This technique is a measure of the similarity between two datasets as a function of the lag, and its function is often normalised as written in Eq. 2-1:

$$NCC_j = \frac{\sum_i a_i \, b_{i+j}}{\sqrt{\sum_i a_i^2 \sum_i b_i^2}} \ , \qquad \text{Eq. 2-1}$$

where NCC is the correlation coefficient, and j is the lag.

It should be noted that $\left|NCC_j\right| \leq 1$, and that NCC_j only equals to 1 when the two series are perfectly identical (Gubbins, 2004). By finding the maximum correlation coefficient, the time-shift is returned in proportion to the lag. Because of the discrete sampling of the time series, sub-sample resolution can be tackled by fitting a function in the vicinity of the maximum cross-correlation value. If we chose the two points at either side of this maximum value, then it is trivial to fit a parabola to these three points and calculate the lag and cross-correlation value associated with the peak.

The cross-correlation of two seismic datasets is carried out with a sliding window to capture the localised spatial and vertical variation of time-shifts (Hodgson, 2009). A commonly used window function is the boxcar window; other types like the Hanning window and the Gaussian window are also quite often applied to help reduce the edge effect caused by strong events. In the following sub-sections, I choose three typical cross-correlation-based methods and generally review their advantages and disadvantages in application.

The 3D warping approach: Hall et al. (2002)

The 3D warping approach described in Hall et al. (2002) provides as a way to align two time-lapse seismic data sets as part of a full cross-matching scheme. Before 3D warping, the two seismic data sets are processed through a cross-equalisation scheme, which is similar to that used by Rickett and Lumley (2001), to account for general variations in phase and amplitudes. The 3D warp derivation procedure used here is based on cross-correlation of small data volumes from the two data sets at nodes positioned on picked horizons but distributed evenly in x and y. For each node location, a warp vector is defined by the shift-vector that gives the best correlation coefficient. The derived nodal warps are subsequently interpolated, first in time then horizontally, to provide a warp vector for each sample (Hall *et al.*, 2005). The best warp parameters in three directions (in-line, cross-line and vertical time) are determined through testing a range of values and assessing the stability of the results. Coarse node spacing can be used when running the first-pass warping, and the general static shifts determined from this step will be removed before re-assessing the warp. This technique also implements a local grid refinement at the locations of main events, to tackle the issues with sub-sample resolution (Figure 2.1).

Time-shifts calculated using this warping technique are generally stable, as they are calculated along horizons. However, it is quite time consuming to find the best 3D warp parameters (in-line, cross-line and time ranges) through trial and error optimisations. In addition, it requires identification of a number of stable reflectors to ensure an accurate vertical warp calculation.

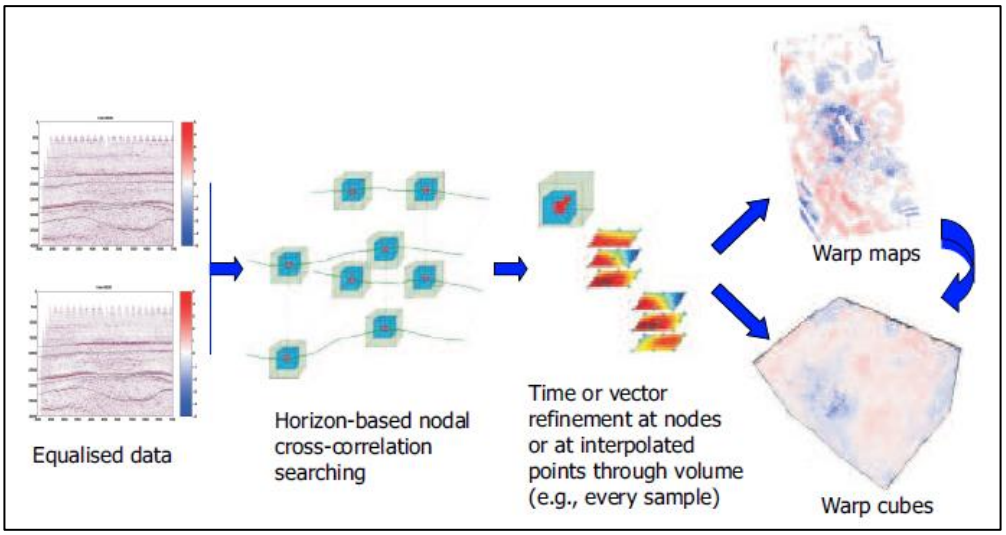

Figure 2.1: The workflow of the 3D warping method (Hall et al., 2005).

The fast cross-correlation method: Rickett et al. (2006)

To reduce the long computational time of cross-correlation and extend the time-shift calculation to the entire volume of seismic data, an improved cross-correlation method was developed by Rickett et al. in 2006. This method assumes that a time-shift can be estimated by picking the maxima of local cross-correlations to align two seismic datasets. Rather than computing a single cross-correlation function for the entire trace, they compute local cross-correlations in running windows to allow for non-stationarity in the variability between the two time series. The original computation cost used to be $N_C \times N_l \times N_s$, where N_C denotes the total number of local correlations, N_l is the number of lags in each local correlation, and N_s is the number of samples in each local window. They then suggest just cross-correlating for the sample at the centre of the window (Rickett *et al.*, 2006), and writing the cross-correlation for the next sample as a function of this (Eq. 2-2). By applying this formula recursively, the computing cost can be condensed to $N_C \times N_l$.

$$C_{l,k+1} = C_{l,k} - a_{k-\frac{N_s}{2}} b_{k-\frac{N_s}{2}+l} + a_{k+1+\frac{N_s}{2}} b_{k+1+\frac{N_s}{2}+l} \quad , \qquad \text{Eq. 2-2}$$

where k denotes the location of the centre of each window.

Beyond trace-to-trace cross-correlations, they also suggest that more robust time-shifts can be estimated by cross-correlating small patches of data (Rickett and Lumley, 2001). Like other cross-correlation based methods, this also gives very noisy time-shifts; thus,

in order to make the derivatives interpretable, smoothing needs to be applied. However, the amount of smoothing needs to be watched carefully, in order to retain the subtle details which may be caused by geomechanical changes (Rickett *et al.*, 2006). They suggest a smoothing approach using an adaptive filter, based on the magnitude of the cross-correlation peak. This produces less smoothing in areas of strong signal and high repeatability, and more smoothing in noisy areas (Rickett and Lumley, 2001).

The 3D cross-correlation technique: Hale (2007)

Like Rickett's fast cross-correlation, Hale's cross-correlation method finds the maximum cross-correlation in a 3D sense and reduces the calculation time to $N_C \times N_l$. However, these methods differ in the type of sliding window selected, in that, unlike the boxcar window in Rickett et al. (2006), Hale (2007) chooses the Gaussian window, so that 3D 'blobs' of data are cross-correlated. Moreover, instead of just recovering for time-shift, Dave Hale's method calculates three displacement components (vertical time-shifts, inline lateral shifts and cross-line lateral shifts) simultaneously.

The local cross-correlation in this method consists of a cyclical search, whereby a sequence of correlations and shifts along each spatial dimension are applied to the seismic cubes. So, at a given iteration step, the shifts found in the previous step are applied to one of the cubes before the next correlation. A new set of shifts are then calculated - first vertically, and then in the horizontal direction. This process is repeated until all shifts become negligible, and it has been found that 4 iterations are enough for time-shift calculation (Hale, 2009). In addition, to improve the spatial resolution, whitening and smoothing filters are applied to both seismic vintages before correlation.

2.2.2 Problems with the cross-correlation-based calculations

Although the cross-correlation-based techniques have been commonly used, they are not without problems. Their windowed nature means that there are inherent limitations of resolution and accuracy. Increasing the window length for calculation gives smooth images, as this stabilizes the time-shift estimation, but at the cost of reducing the resolution. In contrast, a short window can give more details in the time-shift profile, but this faces risks of miscorrelating events if one of the events being correlated is outside the window, and losing the value of the event in future time-strain derivation, as it is too

noisy. For these reasons, a good window parameter needs to be decided before performing the calculation and this is usually done through trial and error.

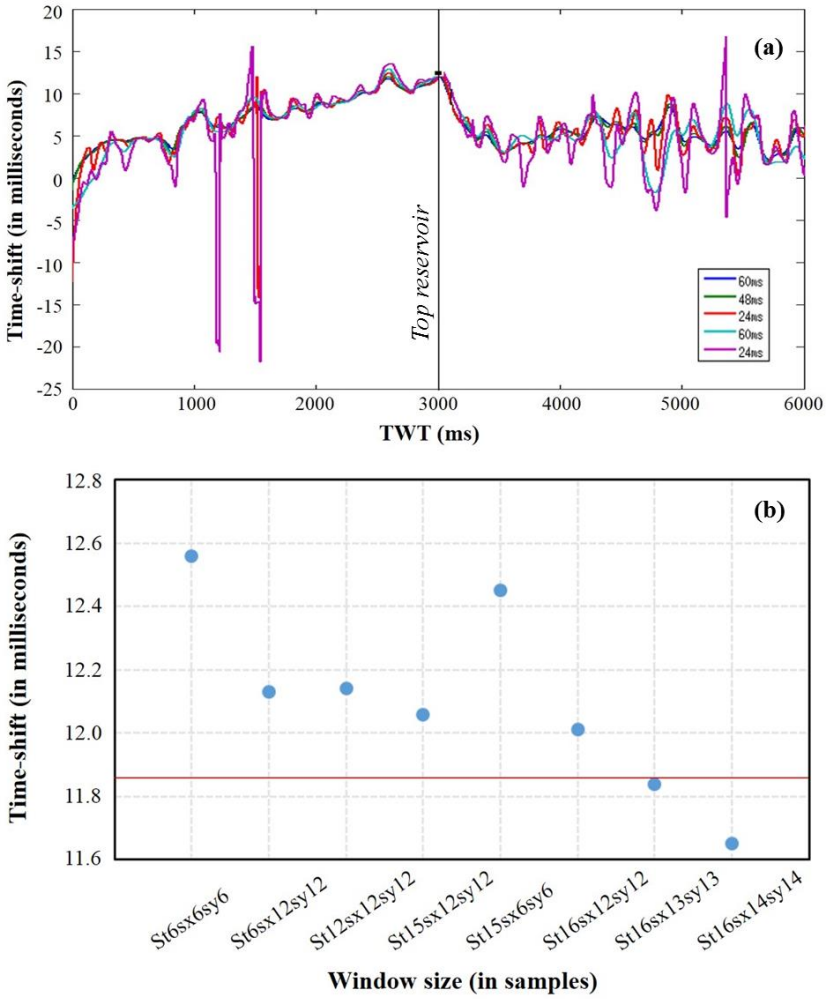

Figure 2.2: The optimization of window size for cross-correlation based time-shift measurements, (a) shows the vertical profile of time-shift for each window, and (b) shows the time-shift magnitude at the top of reservoir for different window sizes (st, sx and sy are vertical time window and two spatial windows respectively and they are in number of samples), the true time-shift value is also plotted with the red line.

An example for window optimisation is shown in Figure 2.2. Time-shift results are extracted from time-shift cubes of a North Sea field, which are estimated using 8 different window sizes (st6sx6sy6, st6sx12sy12, st12sx12sy12, st15sx12sy12, st15sx6sy6, st16sx12sy12, st16sx13sy13, st16sx14sy14). The st, sx and sy represent vertical time window and two spatial windows respectively in number of samples, and they can be converted into milliseconds and metres by multiplying each with vertical time-sampling rate or lateral grid sizes. The estimated time-shift profiles display very similar tendencies,

as they increase through the overburden, reaching a maximum point at top reservoir before reducing inside the reservoir, and they start to increase again in the overburden (Figure 2.2a). The stability of time-shifts in the overburden and underburden is quite poor for small windows, and improvements start to show with an increase in the size. The top reservoir is not well resolved within the long-window results, as the window smears this rapid change. When the magnitude at the top of the reservoir location is compared by plotting with the true value of the time-shift, the error reaches up to 1ms for some window sizes (Figure 2.2b).

Another issue is with the tapers used in some techniques (e.g. Gaussian tapers in DHFCC). Although they help to stabilize the time-shift estimation and reduce spectral leakage when properly used (Gubbins, 2004), they may bias predictions if the length of each taper is too short (Hodgson, 2009). Figure 2.3 illustrates the bias caused by a Gaussian taper, where s2 is a time-shifted version of s1. After applying the Gaussian taper, the location of the peak in s2 is shifted towards s1, and this will reduce the time-shift value to be recovered in cross-correlation.

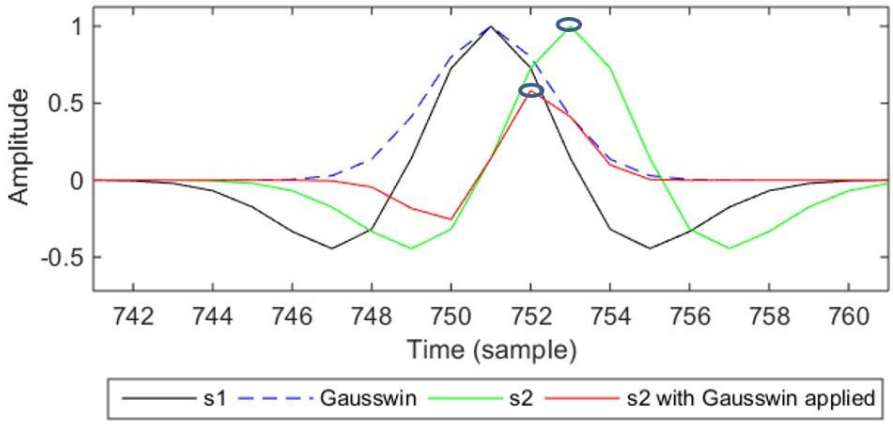

Figure 2.3: An illustration of the bias caused by a Gaussian window. After applying the Gaussian taper, the peak event in s2 is shifted towards s1 and this will make recovered time-shift smaller than the true value.

2.2.3 Non-cross-correlation-based techniques

Non-cross correlation techniques have also been developed in recent years, among these are inversion-based approaches such as the non-rigid matching developed by Nickel and Sønneland (1999) and the non-linear inversion method by Rickett *et al.* (2007), and Taylor-expansion-based approaches such as the one by Hatchell *et al.* (2003) and the

correlated leakage method proposed by Whitcombe *et al.* (2010). In addition, there are some interesting techniques have been considered to recover time-shift in the time-time domain (Zabihi Naeini, 2013), or by going to the pre-stack domain (e.g. Li et al., 2004; Fuck et al., 2007). In the following sub-sections, I choose only a few representative techniques for this review; to see a more comprehensive summary of different time-shift techniques, please refer to Table 2.2.

The non-linear inversion method by Rickett et al. (2007)

The non-linear inversion (NLI) method aims to find the time-shift that, once applied, will minimize the misfit between base and monitor seismic volumes. The least-squares objective function is formed as in Eq. 2-3:

$$E = |d - f(m)|^2 + \alpha|\nabla_x m|^2 + \beta\left|\nabla_y m\right|^2 + \gamma|\nabla_t^2 m|^2 \quad , \qquad \text{Eq. 2-3}$$

where the data vector, *d*, contains the baseline seismic data volume; the model vector, *m*, represents the time-shift volume; and the nonlinear function *f(m)* applies these time-shifts to the monitor survey. There are various options for solving nonlinear least-square problems. Rickett chooses the Gauss-Newton method, which works by linearizing the non-linear operator around the current model, solving the resulting linear problem, updating the model and iterating (Hodgson, 2009).

At the same time, the stability of time-shift and its first order derivative (named as time-strain) is built into the objective function, with three smoothness constraints. Two spatial constraints, ∇x and ∇y, are imposed for smoothing in the inline and cross-line directions, to obtain consistent time-shifts from trace to trace, and the vertical constraint, ∇t^2, is for stable estimates of time strains. The weighted second derivative of time-shift needs to be continuous to ensure a smooth time-strain result. The three weights control the relative weighting of the three smoothing constraints. Before performing the NLI method, three smoothing weights need to be chosen, usually through trial and error until they give the most satisfactory result from an interpretation perspective.

The new warping approach: Williamson et al. (2007) and the modified version proposed by Grandi et al. (2009)

Instead of warping for time-shifts, which in general provides insufficient resolution and stability, Williamson et al. (2007) recast the warping as a non-linear inverse problem. This method inverts for velocity perturbations only, assuming the physical strain of the overburden to be negligible, and trying to match both the time-shifts and reflectivity change. It was further modified by Grandi et al. (2009) to invert for time strains instead of velocity perturbations. However, this method is difficult to use and the amplitudes may not be trusted.

The correlated leakage method: Whitcombe et al. (2010)

The correlated leakage method (CLM) devised by Whitcombe *et al.* (2010) finds an innovative way to calculate the time-shifts. In this approach, time-shifts are measured from the gradient of a line fitted to a cross plot, in which, the *y*-axis contains the amplitude difference between the baseline and monitor (Eq. 2-4), and the *x*-axis contains the amplitude difference between the baseline and monitor average and a time-shifted version of this average (Eq. 2-5) (Whitcombe *et al.*, 2010). The Taylor expansion functions for the *x* and *y* axes are expressed as follows:

$$Y = M - B = f(t+a) - f(t) \approx [f(t) + af'(t)] - f(t) = af'(t) \quad , \qquad \text{Eq. 2-4}$$

$$\begin{aligned} X &= \frac{[(B+M)_{i+1} - (B+M)_i]}{2} \\ &= \frac{[f(t+\Delta t) + f(t+\Delta t+a)] - [f(t) + f(t+a)]}{2} \\ &\approx \frac{\{[f(t) + \Delta t f'(t) + f(t+a) + \Delta t f'(t+a)] - [f(t) + f(t+a)]\}}{2} \\ &= \frac{\Delta t f'(t) + \Delta t f'(t+a)}{2} \approx \frac{\{\Delta t f'(t) + [\Delta t f'(t) + a\Delta t f''(t)]\}}{2} \\ &\approx \Delta t f'(t) \quad , \end{aligned} \qquad \text{Eq. 2-5}$$

where Δt is a user defined time-shift, $f''(t)$ is the second derivative of $f(t)$, and a is the time-shift to be estimated.

The least-square approach is used for finding the best gradient of each line fitted to the cross-plot. And this method is expanded to the 3D domain by cross-plots of 3D patches of data within a sliding window.

The workflow for this method is illustrated in Figure 2.4. Compared to another approach, by Hatchell *et al.* (2003), which also uses the Taylor expansion, the correlated leakage method works better, as it avoids performing derivations on the original seismic traces, and instead it uses seismic traces directly for the calculation. As the approximations made in Taylor expansion calculation, this method works well in small time-shift scenarios, and should be carefully applied if large time-shifts are expected.

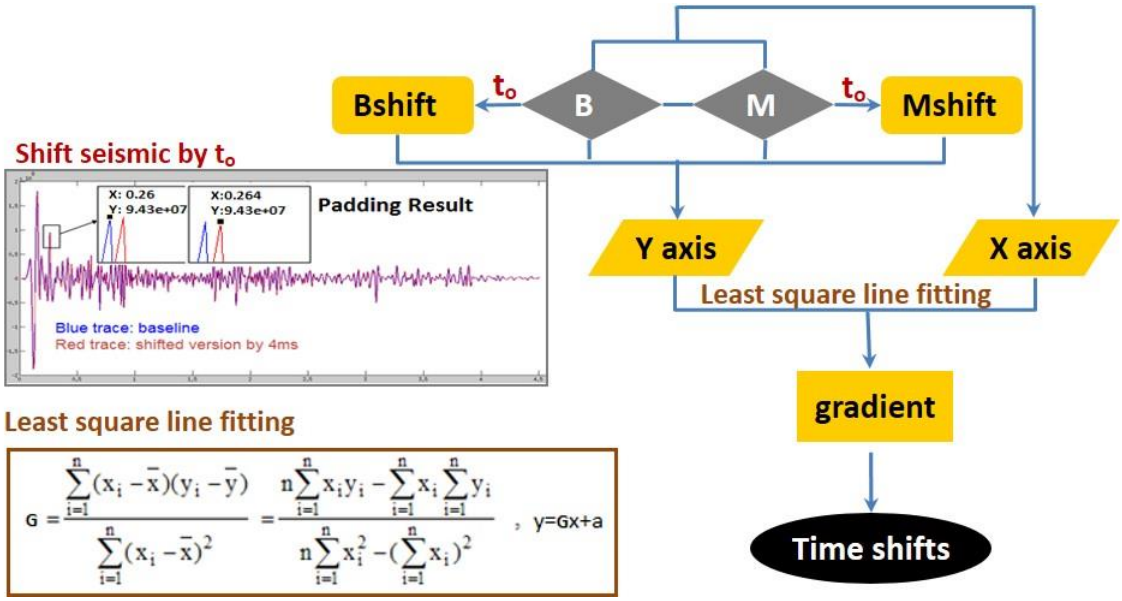

Figure 2.4: The workflow of the Correlated Leakage Method (CLM)

So far, there have been some work done by others to compare different time-shift methods and discuss their pros and cons, such as the latest one by Kanu *et al.* (2016), he compares both cross-correlation and non-cross correlation methods by applying to synthetic datasets (Figure 2.5).

However, most of these methods comparisons are based on synthetic tests or single field case, in chapter 3, I am going to show a detailed comparison for three different types of time-shift methods (DHFCC, CLM and NLI) with application to both synthetic and real data applications, among which the synthetic tests are well tailed to account for dataset noise and time-shift magnitude.

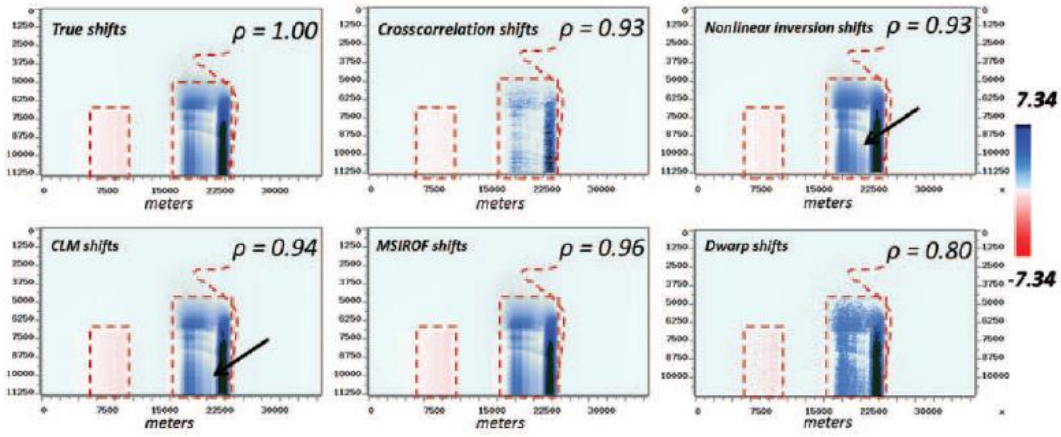

Figure 2.5 Comparison of estimated time shifts from the time-shift extraction methods with the true zero-offset shift imposed in the zero-offset case. Spearman rank correlation coefficient (ρ) compares the similarity of the estimated shifts with the true shifts (Kanu *et al.*, 2016).

2.3 Geomechanics and 4D seismic

2.3.1 The stress arching phenomenon

Production of an HPHT reservoir always leads to massive pore pressure depletion, resulting in changes in the stress inside and outside of the reservoir (Sayers and Schutjens, 2007). Within the reservoir, pressure depletion causes an increase of the effective vertical stress acting on the reservoir rock and therefore gives rise to reservoir compaction. In the overburden, the effective vertical stress is reduced above the compacting reservoir, causing overburden stretching. As the reservoir has a finite extension, compaction is smaller at the edges than in the centre because of the constraining effect of the side-burden acting as supporting pillars. This phenomenon is called stress arching as displayed in Figure 2.6 (Staples *et al.*, 2007b; Hodgson, 2009). Within the arching zone, the top of the arch does not move significantly, but the lowermost part of the overburden falls along with the top reservoir, resulting in vertical extension within the arching zone. If the moduli of the overburden and underburden rocks are relatively similar, stress arching can also occur in the underburden (Staples *et al.*, 2007b).

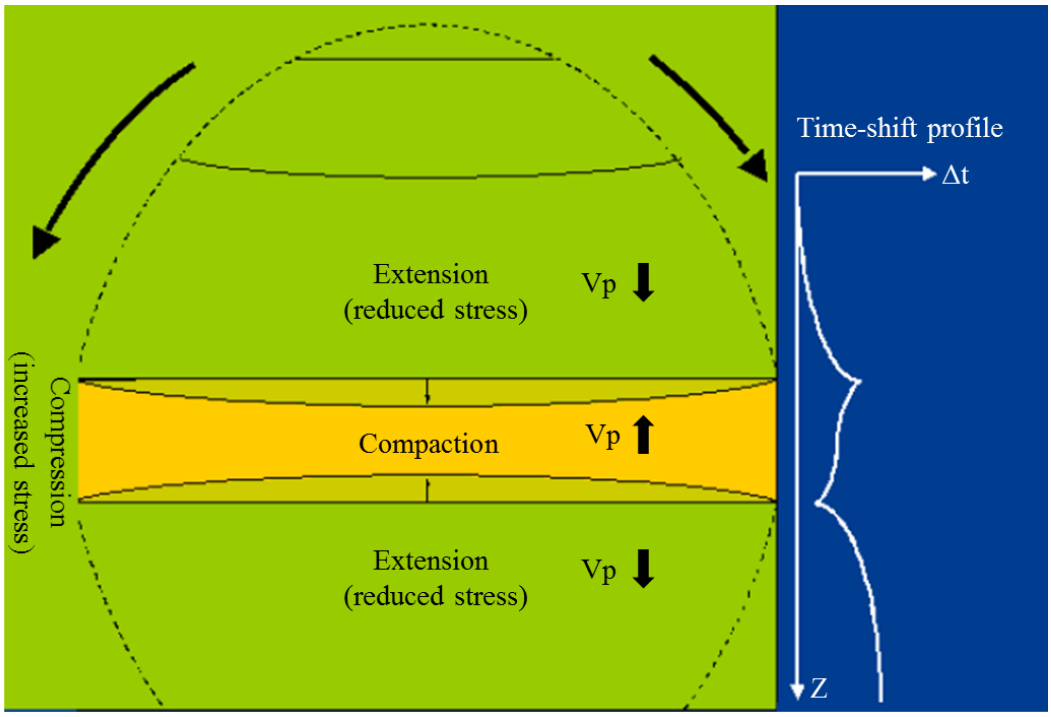

Figure 2.6: A schematic diagram showing reservoir compaction and the surrounding rock extension with associated seismic velocity variations (Staples *et al.*, 2007b).

In the overburden towards the centre, the velocity is reduced giving rise to a time delay for seismic ray passing through it. On the contrary, in the pillars to either side of the reservoir where compression is occurring, the velocity is increased leading to a time advance. Therefore, the arching phenomenon could be viewed from the time-lapse time-shift / time-strain profiles (Staples *et al.*, 2007b).

2.3.2 Time-lapse time-strain

Due to the cumulative nature of the time-lapse time-shifts, it's not straightforward to assess changes at a particular location. Therefore, a differentiation is needed to derive the fractional change in traveltime at that location. This vertical derivative of time-shift is referred to as time-strain. Figure 2.7 shows an example about the different abilities of time-shift and time-strain to interpret the interval changes inside and outside the reservoir.

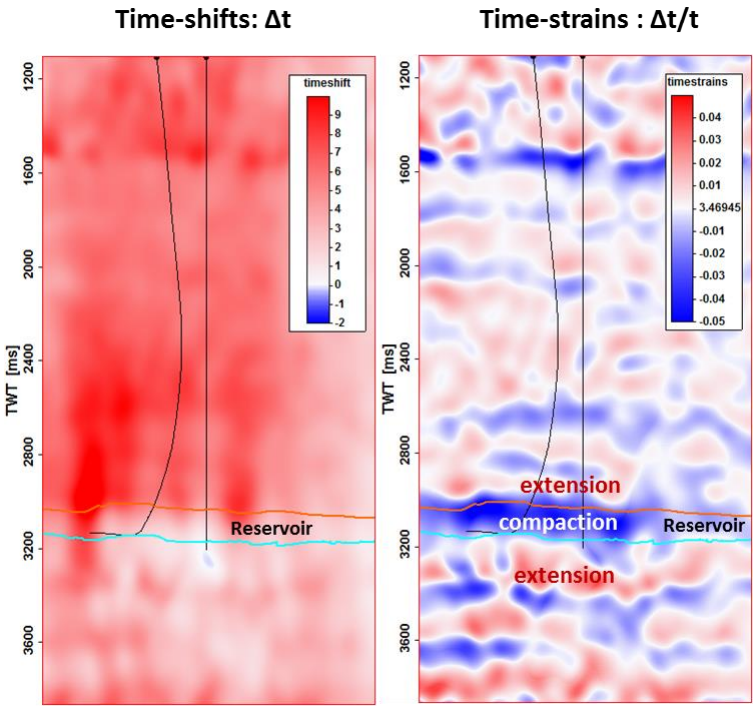

Figure 2.7: An illustration of the differences between time-shifts and time-strains in revealing interval changes both inside and outside of the reservoir.

By converting time-shift into time-strain, the compression and extension signals in each interval are distinguished in different polarity and the value of traveltime fractional change is obtained. First suggested by Landrø and Janssen (2002), this fractional change in traveltime is further decomposed into a vertical strain component and a fractional change in velocity as follows Landrø and Stammeijer (2004):

$$\frac{\Delta t}{t} \approx \frac{\Delta z}{z} - \frac{\Delta v}{v} \qquad \text{Eq. 2-6}$$

2.3.3 Linking geomechanics with 4D seismic – the R factor and beyond

Built on the observations and concepts in time-lapse time-shifts, Hatchell et al. made the key progress in 2003 in introducing the integration between geomechanics and 4D seismic, where they predict the distribution and magnitude of the 4D time shifts using geomechanical modelling (Hatchell *et al.*, 2003). In contrast to the simple 1D (uniaxial) approach of Guilbot and Smith (2002) and Landrø and Janssen (2002), Hatchell et al. point out that the strain is not uniformly distributed above the reservoir, but spatially variable in a manner that is dependent on a number of factors, such as the shape of the

reservoir or the mechanical properties of the rocks for example. And this idea was emphasized by Stammeijer *et al.*, (2004) working on the same dataset.

In 2005, the integration was brought one step further by Røste et al. (Eq. 2-7) and Hatchell et al (Eq. 2-8) respectively but similar in the concept of introducing a linear relationship between velocity and strain to solve the non-uniqueness in Eq. 2-6. Different symbols and conventions are used in their equations as in Eq. 2-7 and 2-8, with the R factor being more widely used afterwards.

$$\frac{\Delta v}{v} = -R\frac{\Delta z}{z} \qquad \text{Eq. 2-7}$$

$$\frac{\Delta v}{v} = \alpha\frac{\Delta z}{z} \qquad \text{Eq. 2-8}$$

Based on this relation, time-shifts inside and outside of the reservoir are now lined with vertical strains straightforward. As the vertical strain is one of the output from geomechanical modelling, this relation has made 4D seismic as a very efficient tool in the calibration of geomechanical models (Staples et al., 2007; Herwanger and Koutsabeloulis, 2011; Herwanger et al., 2013).

Since then, a lot of work have been done trying to measure and model the R factors. A table is given below showing a summary of the published analysis on R factors (Table 2.1). Field examples show the R-value for non-reservoir rocks (unloading) are higher than reservoir rocks (loading). While laboratory test show the magnitude of R factors could vary a lot and could be dependent on lithology, cracks, stress applied, and so on.

For a porous material that undergoes uniaxial compaction (and where the compaction of the grain material is ignored), the relative change in the thickness is related to the change in porosity. The work presented in Hatchell and Bourne (2005) assumes the seismic velocity as a function of porosity, V(φ), so velocity change can be written as a function of vertical strain and porosity. With R factor, these equations can be reorganised and R becomes a function of porosity and velocity. Take relation between velocity and porosity for Chalk formations from sonic and neutron logs, the equation can be further simplified as a function of porosity only. Porosity varies with depth, so the R factors varies with depth. In most cases the R-values predicted from these velocity-porosity models are more

or less consistent with what is observed for reservoir rock (loading) while much smaller for non-reservoir rock (unloading). This method will be used as one of the resources of R factors in Shearwater field and will be presented in Chapter 6. Apart from that, another controversial method for deriving R factors will also be shown in that chapter which utilises angle-stack seismic datasets to discriminate the fractional changes in thickness and velocity changes (Landrø and Stammeijer, 2004).

Table 2.1: Values of R factor from published papers

Source	R factor	references
Valhall	$R^+ = 5$ $R^+ = 4 - 9$ $R^+ = 5 – 7$	Hatchell 2005 Hatchell and Bourne 2005 Van Gestel et al 2008
Ekofisk	$R^+ = 6$	Byerley et al. 2006
Elgin and Franklin	$R^+ = 7$	Hawkins et al 2007
Shearwater	$R^- = 1, R^+ = 5$ $R^- = 1- 3 , R^+ = 4 - 6$ **$R^+ = 20 – 35$** (chalk group)	Cox and Hatchell 2008 Hatchell et al. 2005 Staples et al. 2007
Rock-physics models in Mavko's book	Depends on porosity (better match in reservoir rock): R = 1-3 (from empirical velocity-porosity trends)	(Hatchell et al. 2005)
	Depends on opening of cracks, crack density, aspect ratio, and orientation (for stretching): R=2-10 (estimated using microcracks model by Sayers and Kachanov, 1995) R=4-6 (observed in overburden above different compacting reservoirs)	(Hatchell et al. 2005)
Shearwater Elgin and Franklin Snorre	Depends on lithology (integrating geomechanical model and observed timeshifts) **R^+=20-35** (Hod chalk in **shearwater**) **R^+=20-100** (chalk formation in **Elgin and Franklin**) R^+=20 (overburden in Snorre)	Staples et al. 2007 De Gennaro et al. 2008 Roste et al. 2015
Laboratory test	Depends on stress path, sorting: A North Sea field shale core from 2.5km depth, with 10% porosity and 80%clay content: $R^- = 6$ for compacting shale, $R^+ = 13$ for stretching shale	(Holt et al. 2008)
Laboratory test for Berea sandstone and Foxhill sandstone	Depends on magnitude of applied stress, deformation mechanism and fluid saturation. R=10-100 (R as a function of hydrostatic pressure changes between 10 and 60 Mpa) R=5-30 (as a function of uniaxial stress changes between 10 and 45 Mpa) R=0-20 (for brine saturated sandstone) R=20-60 (for dry sandstone)	(Pal-Bathija and Batzle 2007)

2.4 Rock physics studies in the overburden

Overburden pressure changes and the Skempton B-coefficient

It is widely known that pore fluids strongly influence the seismic properties of rocks, and consequently velocity, and this is quite common in the reservoir. What about things in the overburden especially when there is gas initially dissolved in the connate water or exist in the pore space?

Normally, it is assumed that the overburden only suffers shear deformation as a result of depletion, hence there is no change in the pore volume and no change in the pore pressure there (Fjaer *et al.*, 2008). However, this only works for homogeneous overburden. If the formation around the reservoir is not homogeneous, the "no change of volume" statement is less valid, even if linear elasticity still is. In this situation, stress changes arising from reservoir production will impact on the pore space and reduce the pressure sufficiently for some gas to be released. Since the permeability in overburden rocks is usually low, any variation in stiffness – even on a small scale – may result in corresponding variations in pore pressure due to variations in volumetric strain. Hence, there may be pockets of released gas even if the average pore pressure on a larger scale is above the threshold for gas release. Within linear elasticity, the formula of the Skempton B-coefficient (Eq. 2-9) is applicable for estimating the pore pressure change given the volumetric deformation.

$$B = \frac{\Delta p_f}{\Delta \bar{\sigma}} = \frac{\frac{K_{fl}}{\emptyset}\left(1 - \frac{K_{\mathrm{dry}}}{K_0}\right)}{\frac{K_{fl}}{\emptyset}\left(1 - \frac{K_{\mathrm{dry}}}{K_0}\right) + K_{\mathrm{dry}}\left(1 - \frac{K_{fl}}{K_0}\right)} \qquad \text{Eq. 2-9}$$

Where K_{fl} is the bulk modulus of fluid, K_{dry} is the bulk modulus of the dry rock frame, K_0 is the bulk modulus of the matrix, $\Delta\bar{\sigma}$ is the mean total stress change, and can be determined from triaxial test or geomechanical modeling via the following equation:

$$\Delta\bar{\sigma} = \frac{1}{3}(\Delta\sigma_1 + 2\Delta\sigma_3) \qquad \text{Eq. 2-10}$$

Combing the two, the pore pressure change can be calculated as:

$$\Delta p_f = B\Delta\bar{\sigma} \qquad \text{Eq. 2-11}$$

The amount of gas come out of solution can then be calculated incorporating the gas solubility concept.

To study the changes of gas saturation on the seismic properties, a rock physics model is used. So far, a lot of rock physics models have been applied for the study of chalk formations, such as the Kuster and Toksöz model, the self-consistent model, the Differential Effective Medium model. However, these are usually applied for reservoir chalk and require information such as shape of pore space. For the analysis in the overburden rock, limited well logs and cores are available for obtaining these information,

and also to make an easier and practical start, the Gassmann rock physics model is used in this research. A more detailed work will be present in Chapter 6.

2.5 Summary

This chapter presented an overview of the fundamental theories to be applied in this research. As this research has been developed in a close relation with time-lapse time-shift, the measurement techniques for this attribute are of great importance. In the first part, the background theory as well as the advantages and disadvantages of the different time-shift measurement methods have been reviewed. A summary of these time-shift methods is listed in Table 2.2. In the second part, an overview of reservoir geomechanics, time-lapse time-strain, and the link between 4D seismic and geomechanics has been provided. At the end, an introduction of the rock physics study to be done for the overburden was given.

Table 2.2: Summary of published methods for measuring time-lapse time-shifts

Category	Name	Method	Comments	Lateral shifts	Thesis applied
Cross-correlation based methods	ETLP 3D warping (Hall *et al.*, 2002, 2005)	Event cross-correlation	Local grid refinement and warp vectors	Yes	
	Fast cross-correlation (Rickett *et al.*, 2006)	Fast local cross-correlation using boxcar window (no taper)	Previous average cross-correlation functions	No	
	Hale 3D warping (Hale, 2007, 2009)	Fast local cross-correlation using Gaussian window (taper)	Pre-whitening to improve lateral resolution	Yes	√
Non-cross correlation based methods	NLI (Rickett *et al.*, 2007)	Nonlinear inversion for full traces	Time-shift slowly varying	Maybe	√
	Williamson warping (Williamson *et al.*, 2007)	Warping with both time-shift and reflectivity change	Time-shift and amplitude inverted together, vertical strain neglected	No	
	Grandi's refinement (Grandi *et al.*, 2009)	Warping with time-strain	Amplitude changes excluded, re-formulated Williamson equation	No	
	CLM (Whitcombe *et al.*, 2010)	Cross-plotting	Taylor expansion	Yes	√
	Lie (2011)	Inversion for smooth time-shifts	Inversion with smoothing functions for smooth time-shifts	No	
	Chu *et al.* (2012)	Cross-correlation followed by time-strain estimation	Use offset seismic data, time-shifts constrained to fit a linear function	No	

Chapter 3

A critical comparison of three methods for time-lapse time-shift calculation

This chapter provides a critical comparison of three different measurement techniques (DHFCC, CLM, and NLI). The three methods are compared through applications to a set of synthetic tests that are designed for a comprehensive examination of the performance of three selected time-shift methods, as well as four real time-lapse seismic datasets from three North Sea fields. The results are compared to the input and the real observations respectively. At the end, each of the time-shift methods is evaluated from different aspects, and the most appropriate method is selected for the following study.

3.1 Introduction

In Chapter 1, I talked about the definition of the time-lapse time-shift and reviewed its role in dynamic reservoir characterisation. In chapter 2, a variety of time-shift calculation methods published so far were reviewed as well as the inherent shortcomings for some methods. Based on this, I select Hale's fast cross-correlation (2007), Rickett's non-linear inversion (2007), and Whitcombe's correlated leakage method (2010) for the analysis in this chapter, and they are referred to as DHFCC, NLI, and CLM respectively in the following description. Java code for DHFCC is provided by the author and has been compiled into MATLAB in my test. The MATLAB code for NLI was originally written by Hodgson (Hodgson, 2009), and the MATLAB code for CLM is written by myself with the help of a previous ETLP student Chambefort (Chambefort, 2013). During the method comparison, firstly, a set of synthetic tests are conducted to evaluate the efficiency of each method on recovering time-shifts from both ideal and noisy datasets. The three methods are then applied to the real 4D seismic data from three North Sea fields (the Ekofisk field, the Erskine field and the Schiehallion field), and finally, the calculated time-shifts and derived time strains are compared to give some insights into the most suitable method for future study.

3.2 Comparison of methods with application to synthetic data

Now we are aware that several time-shift calculation methods have been developed so far, the next question is how well they can work for our fields? In order to test the applicability of these time-shift measurement techniques, a series of synthetic tests have been carried out and followed by application of real data.

3.2.1 Description of synthetic tests

To prepare for the synthetic datasets, a 2D section was extracted from the 1989 Ekofisk survey as the baseline seismic (Figure 3.1c), then the synthetic monitor was created (Figure 3.1d) by applying an already known, smoothly time-spatial-varying time-shift function to the base. This synthetic time-shift had a maximum magnitude of 8ms, and was designed to mimic the distribution of that around a heavily compacted reservoir, with

positive and negative values indicating slowdown (extension) and speedup (compaction) respectively (Figure 3.8a).

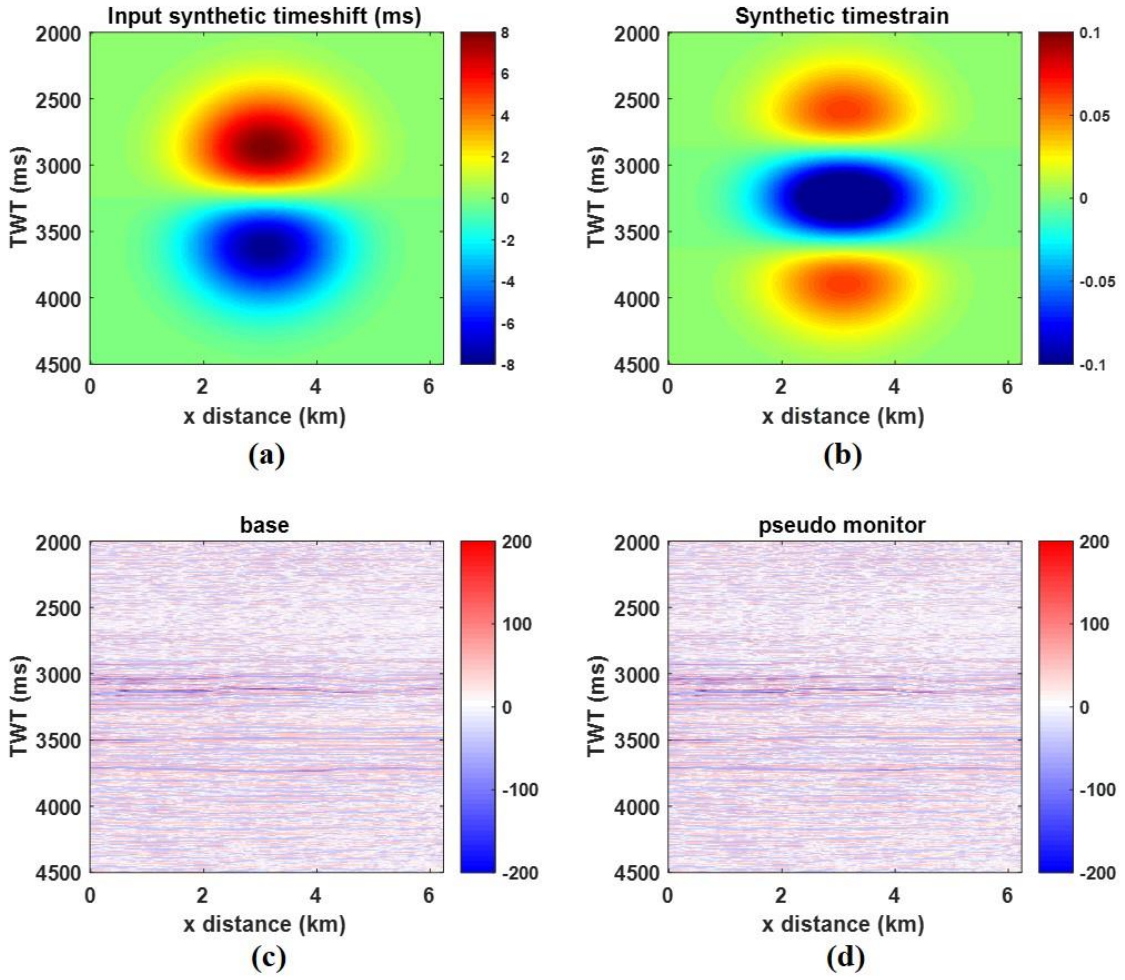

Figure 3.1: (a) The input synthetic time-shift profile for creating the pseudo monitor survey. (b) The synthetic timestrain derived from the input time-shift. (c) The base seismic extracted from the 1989 Ekofisk seismic survey. (d) The pseudo monitor after applying the input synthetic time-shift to the base seismic.

3.2.2 Results of the idealised synthetic time-shift tests

Figure 3.2 shows the results of the time-shifts calculated using DHFCC, CLM and NLI respectively, and the derived time strains. To ensure an unbiased comparison, the two window-based methods, DHFCC and CLM, were performed using the same size of sliding window. It is noted that the CLM method does not have a smoothing filter initially implemented; therefore, a Gaussian smoothing was applied in order to stabilize the final

result. All three methods managed to recover the distribution pattern and magnitude of time-shift very close to the input. When moving on to compare the derived time strains, the disparities become more obvious. Apart from the inherent noise caused by the derivation process, it can still be very clearly seen that the CLM result fails to recover the sharp change at the overburden/reservoir and reservoir/under-burden interfaces (Figure 3.2d), while NLI gives the best results (Figure 3.2f) by taking difference between the estimated results and the inputs, a clearer qualitative comparison is obtained between the synthetic and estimated time-shift and time-strain (Figure 3.3).

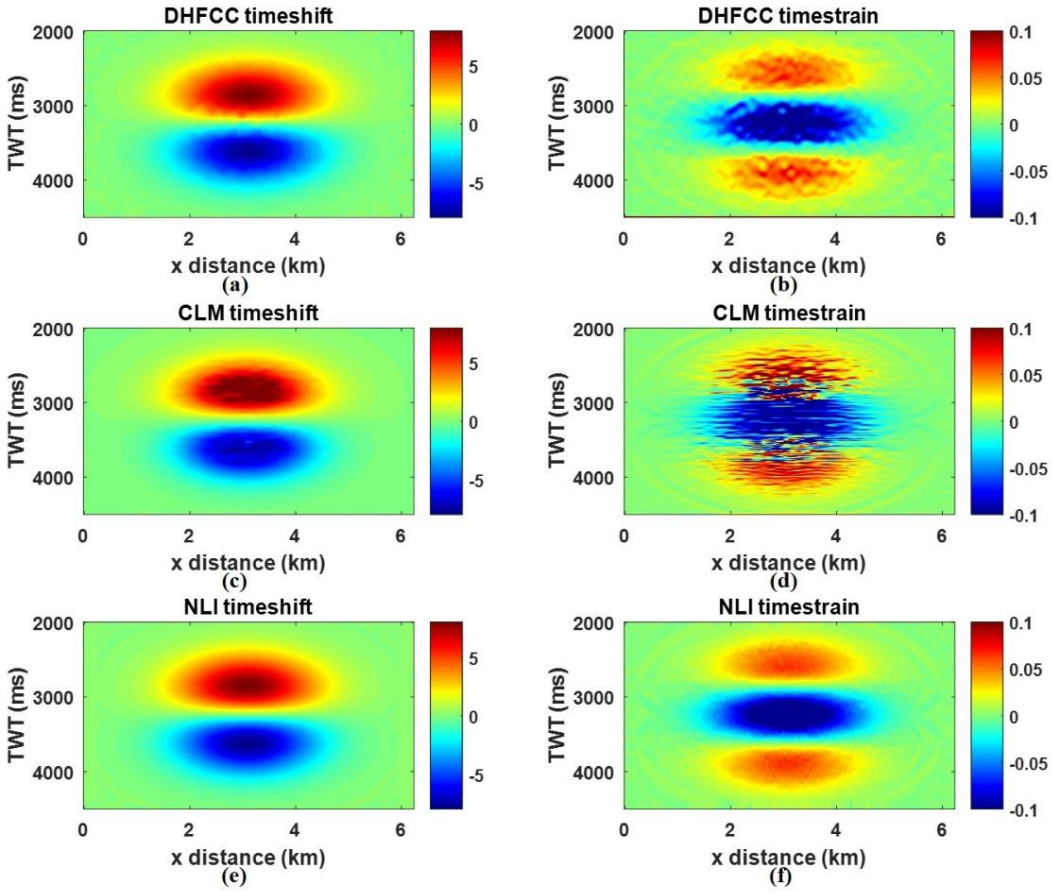

Figure 3.2: (a) Time-shift calculated from DHFCC method, and (b) derived time-strain. (c) Time-shift calculated from the CLM, and (d) derived time-strain. (e) Time-shift calculated from NLI method, and (f) derived time-strain.

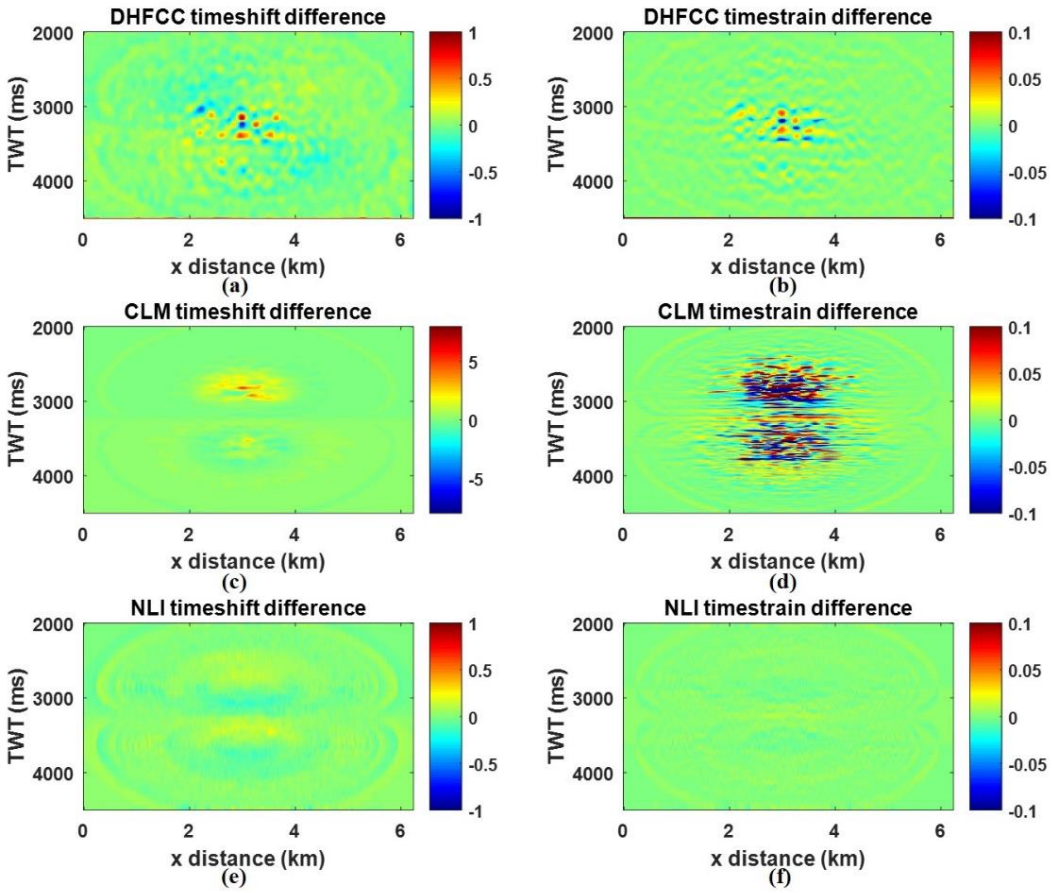

Figure 3.3: Difference between synthetic time-shifts and estimated time-shifts using the DHFCC, CLM and NLI respectively. Note the different colour scales used in (a), (c) and (e).

To quantify the calculation error for each method, the normalized-root-mean-squared-deviation (NRMSD) was calculated for each result Eq. 3-1.

$$NRMSD = \frac{\sqrt{\frac{1}{N}\sum(X_{syn} - X_{est})^2}}{\max(X_{syn}) - \min(X_{syn})} \quad , \qquad \text{Eq. 3-1}$$

where *Xsyn* is the synthetic input, *Xes*t is the calculation result, and *N* is the number of samples.

The higher the value of NRMSD, the lower the degree of matching between the two parameters under comparison; the NRMSD values for each method are displayed in Table 3.1. Clearly, the NLI method recovers the most accurate time-shift and time-strain, which is best matched with the synthetic inputs, and the DHFCC results rank just after this. The residual variance of the CLM results is the highest compared to the other two methods,

especially for the time-strain estimation. This synthetic test shows that for even the best scenario with smoothly varying synthetic shifts and no noise or reflectivity changes between baseline and monitor, post-calculation smoothing is still required for the CLM result to approach the accuracy of the NLI result.

Table 3.1: The normalized root-mean-square deviation (NRMSD) of time-shift and time-strain results from all three methods compared to input synthetic time-shift and time-strain.

Normalized root-mean-square deviation (NRMSD)			
	DHFCC	**CLM**	**NLI**
Time-shift	0.34%	1.89%	0.26%
Time-strain	8.06%	16.88%	1.11%

3.2.3 Noise tests

The synthetic test above is an idealised scenario, which contains no additional noise; however, in the real world this situation never exists, as seismic data are always accompanied by noise. To facilitate these tests, different levels of random noise were applied to the previous synthetic datasets. It is important to note that random noise is only one source of noise within seismic data; other forms of noise also exist, but these are not the concern of the present topic. Here the imposed noise is in a range between 0 and 40% to make it in favour of the seismic repeatability close to the real data (e.g. NRMS is usually under 40% for North Sea fields).

Seismic repeatability can be calculated by the ratio of the root-mean-square of amplitude difference divided by the average RMS amplitude of the original surveys, as stated in Eq. 3-2 (Behrens *et al.*, 2001).

$$NRMS = {}^{2\sqrt{\sum(A-B)^2}}\Big/_{\sqrt{A^2}+\sqrt{B^2}} \quad . \qquad \text{Eq. 3-2}$$

The range of values of this particular metric is between zero for perfectly matched data and 2 for uncorrelated data.

The signal-to-noise ratio between the two surveys (SNR) can also be estimated from the NRMS, as stated in Eq. 3-3 (Behrens *et al.*, 2001). The range of values for SNR is zero to infinity and provides a comparison to the synthetic baseline and monitor before and after adding a different noise level.

$$SNR = \sqrt{2 - NRMS^2}/NRMS \qquad \text{Eq. 3-3}$$

Figure 3.4 shows the calculated NRMS and SNR for different levels of random noise inserted in this synthetic test. The NRMS values in scenarios where noise level varies between 5% and 20% are very close to some North Sea examples with large time-shifts.

Noise %	NRMS	SNR
0.1	0.14	1411.52
1	0.93	215.88
5	5.62	35.53
10	11.69	17.00
15	23.69	8.20
20	28.90	6.63
25	34.93	5.38
30	39.02	4.74
40	56.87	2.95

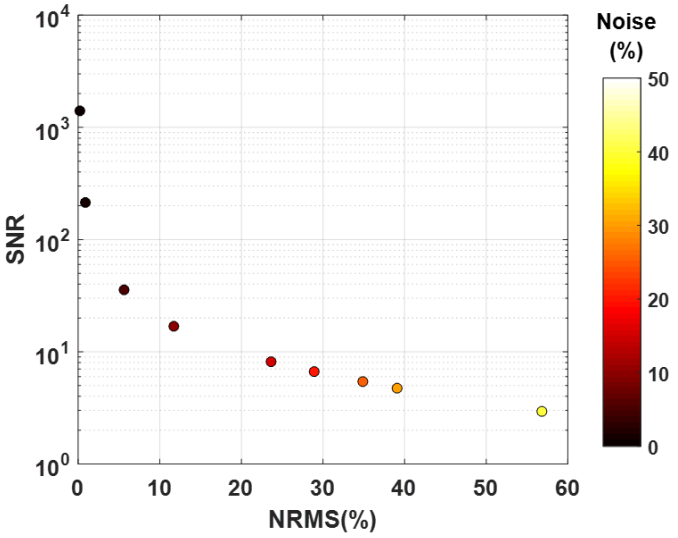

Figure 3.4: Relationship among noise level, NRMS and SNR for synthetic test.

As shown in Figure 3.5, the NRMSD of both the CLM and NLI results increases with the increase of noise level in the seismic data. When the noise level is less than 20%, the time-shift calculation errors from NLI and DHFCC are quite similar, and NLI is even better than DHFCC in recovering a good time-strain profile. However, when the noise level is higher than the threshold of 20%, the behaviour of two methods flips. Clearly, the DHFCC method does a very good job in dealing with very noisy data. To overcome the weakness of the NLI method in noisy datasets, we may need to apply a higher weight of smoothness constraints in the objective function, but this should be done in an appropriate way as over-smoothing may bias the results.

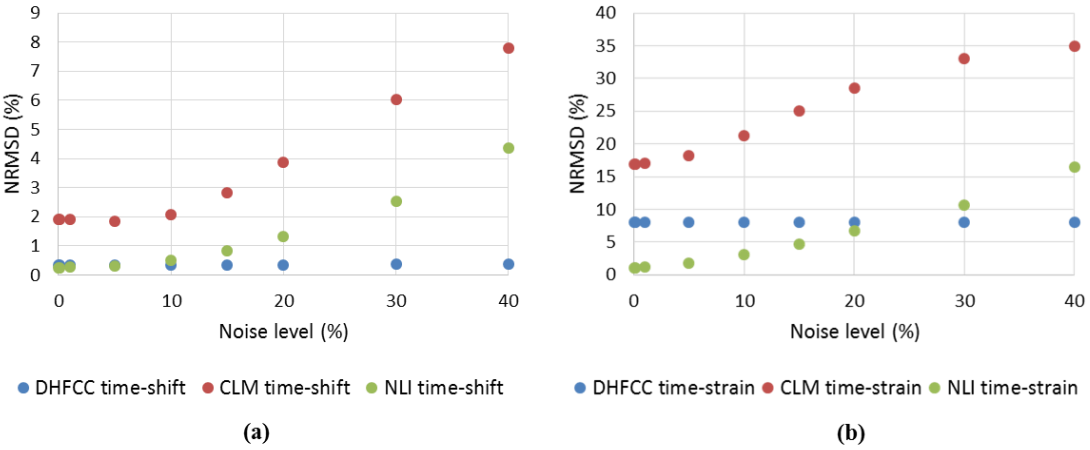

Figure 3.5: Normalized root-mean-square deviation (NRMSD) of the calculated time-shift and time-strain results for seismic with different noise levels, using the three methods.

3.2.4 Small time-shift tests

In reality, the magnitude of observed time-shifts varies quite a lot depending on field production and recovery mechanisms, reservoir thickness, depth, and elapse period, with a range from as small as 0.2 ms to as large as 20 ms+ (MacBeth and Mangriotis, 2017). The following synthetic tests are designed to account for small time-shift scenarios with various levels of background noise. Similarly to the previous work in section 3.2.1, a smoothly varying time-shift is created, but with a maximum magnitude of 1ms, then inputted to the base data, together with noise functions to create a set of monitors. After time-shift calculation using the three methods, the results were compared with input time-shift data, as shown in Figure 3.6. Compared to results from previous large time-shift scenarios (Figure 3.5), it can be seen that the NLI results are more stable in small time-shift scenarios, even when the noise level is high; the CLM results are fairly close, apart from a small improvement in time-strain results. However, the DH technique does not appear to work very well for small time-shift scenarios especially for subsequent time-strain derivation. The reason for this is that the smoothing process in the DH method has over-smoothed the time-shift signal, and has seen the real time-shift signal as noise, as both of them are in the same range.

We should notice that, although it may seem to be straightforward, random noise is unrealistic. In reality, different noise models should be applied according to the overburden noise of the field (Wong, 2016). Moreover, the noise test is the best-case

scenario; only time-shift is included without any reflectivity changes and no displacements in the lateral dimensions, which is not true for a real case. So, in the following sections, I am going to explore the feasibility of each method when applied to real seismic datasets in the North Sea.

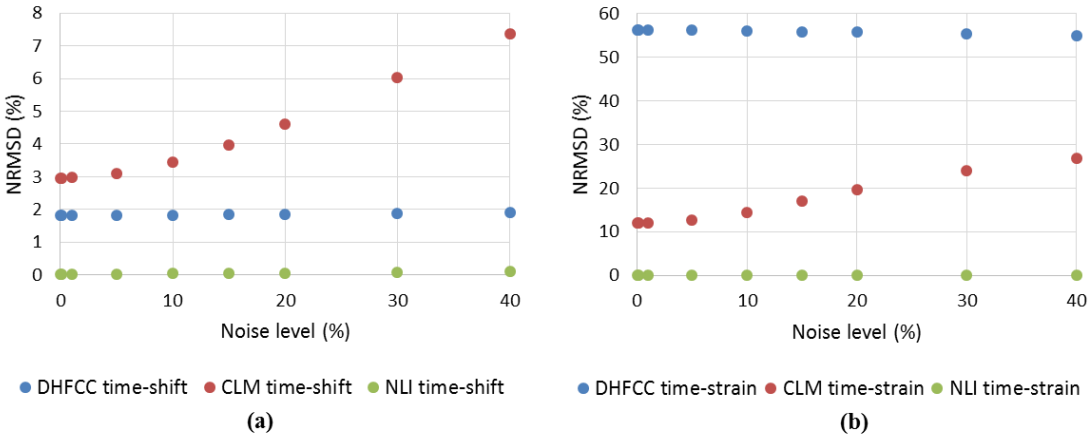

Figure 3.6: Cross-plots of normalized root-mean-square deviation (NRMSD) against noise level for the three time-shift measurement approaches; all data come from small time-shift tests.

3.3 Comparison of methods with application to field data

In this section, the three time-shift measurement techniques are applied to four North Sea datasets. Calculated time-shift results for each field will be compared laterally and will also be compared with published results, if they are available.

3.3.1 Application to the Ekofisk field – highly compacting reservoir

The first field for application is the Ekofisk field, which is situated in the southwestern part of the Norwegian North Sea (Figure 3.7a) with a water depth of about 72 m. The reservoir has an elongated anticlinal structure with the long axis in the north/south direction, and the thickness of the overlying sediments is 2840 m at the crest (Sulak and Danielsen, 1989). The reservoir consists of two fine-grained very high porosity and low matrix permeability limestone formations - the Danian Age Ekofisk formation and the Maastrichtian Age Tor formation, which are separated by a thin and impermeable Tight Zone (Figure 3.7b). Since it was brought on stream in 1971, massive compaction has happened due to reservoir production, and this caused a 2.5m subsidence at seabed

between 1973 and 1985 (Haller, 2012). Full field water injection started in 1987, since due to the water weakening nature of the formation chalk, reservoir compaction was not stopped.

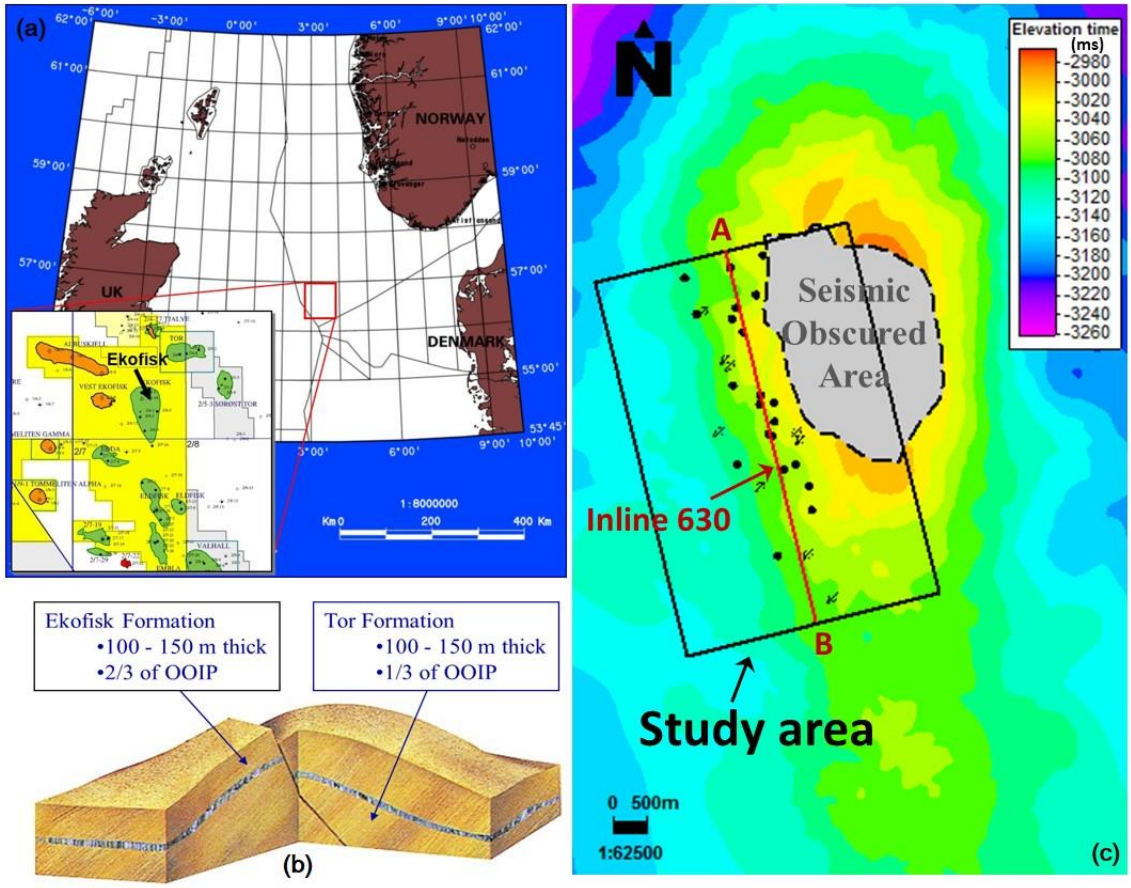

Figure 3.7: (a) The location of the Ekofisk field (Tolstukhin *et al.*, 2012). (b) A general illustration of the formation composition of the reservoir: above is the Ekofisk formation, below is the Tor formation, and they are separated by a thin impermeable zone (Haller, 2012). (c) Time map at Top Reservoir: the grey coloured area is the Seismic Obscured Area caused by a gas cap. The study area is in the south-west part of this field, as illustrated by the black rectangle and the red line inside shows the location of the cross-section which is used in the following analysis.

A seismic monitoring programme has been established at Ekofisk, with marine streamer 4D seismic surveys that were acquired over the field in 1989, 1999, 2003, 2006 and 2008. The NRMS values of seismic repeatability calculated using Kragh and Christie (2002) equation are in a range between 25 and 175, with an average of 80. In 2010, the Ekofisk Life of Field Seismic project (referred to as LoFS) was installed, aiming to frequently acquire 4D seismic data of very high repeatability. The LoFS project has since been

delivering outstanding seismic repeatability (NRMS of 3-5%), with clean, well-resolvable 4D signals and low residual 4D noise (Buizard *et al.*, 2013). Compaction-induced geomechanical changes in the overburden have resulted in 4D time-shifts as large as 20 ms (Folstad, 2010).

For comparison of the methods, time-shifts are calculated from one set of towed streamer surveys (1989 and 2003) and one set of LoFS surveys (lofs1 and lofs 2) for the area outlined in the black rectangle as shown in Figure 3.7c. Through trial and error tests, a search window of 15 samples in the vertical axis and 12 traces by 12 traces in the x- and y-axes is used in the DHFCC and CLM calculations.

As shown in Figure 3.8, the time-shift magnitude between the two towed streamer surveys is up to 10ms; this is comparable with published values (Folstad, 2010). The three time-shift maps are extracted at the Top Reservoir to represent the cumulative time-shift throughout the overburden interval. The blank area that appears in every map is caused by a gas cloud which obscured seismic signals. By plotting using the same colour bar each time, the similarity in time-shift distribution can be clearly seen, with a large positive time-shift in active production areas. However, a certain number of disparities in magnitude and distribution are also visible: for example in the two areas in the south of the time-shift maps (Figure 3.8a, b, and c). Negative time-shifts are observed in these areas on both the CLM and NLI maps, but not on the DHFCC map. There are no wells in the controversial area, so the disparate time-shift distribution can hardly to be genuine unless due to strong geomechanical changes. Going through seismic sections in those areas reveals that these are actually calculation errors due to seismic noise and an inappropriate interpolation process. As mentioned in section 3.2.3, the smoothing procedure in DHFCC is very efficient in suppressing noise for moderately repeated seismic surveys during large time-shift calculations.

Time-shift sections provide another perspective (Figure 3.8d, e, f). They are extracted from inline 630, which is located in an intensive producing area. The orange horizon refers to the top reservoir and the blue one refers to the base reservoir. Time-shifts can be seen in all sections, which are increasing continuously through the overburden, and decreasing inside the reservoir. In contrast to the small compaction signal in the upper reservoir around well P1, a stronger negative time-shift signal is picked up by both the

CLM and NLI results. The strong reduction in time-shift is correlated with the fact that the lower Ekofisk and Tor formations compacted more than the Top Ekofisk during production. This signal is weakened in the DHFCC result, due to the tapering process, as mentioned in previous chapter. There is a noise burst in the CLM result especially in the under-burden interval.

As the two LoFS datasets were recorded 6 months apart, the estimated time-shift magnitude is relatively small, just around 1ms. Again, time-shift maps were extracted at the Top Reservoir (Figure 3.9); all three methods successfully brought out extension signals in the central producing area and confirmed each other at the southeast corner. However, the DH method did not suppress noise very well in the west area. The time-shift sections in Figure 3.9 demonstrate roughly the same patterns. However, the extension signals picked up by CLM and NLI in both left and right corners were attenuated by the DHFCC method, moreover, the slowdown signal around P1 just below base reservoir was lost in the DH result. Noise is very well suppressed in the NLI result, while the CLM result seems to have the best resolution, as its distribution pattern reflects the geology, to some degree.

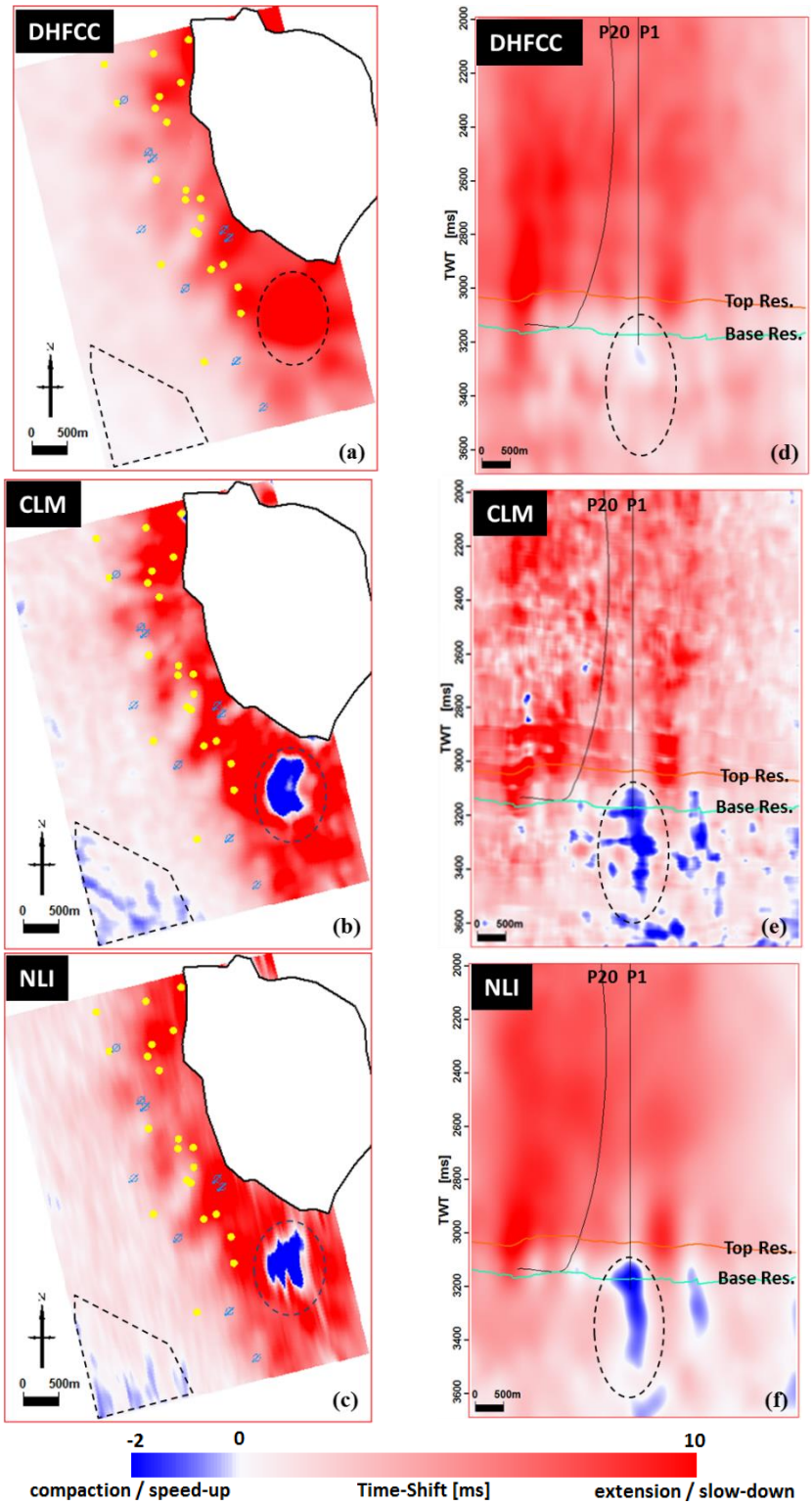

Figure 3.8: Ekofisk time-shift results by DHFCC, CLM and NLI between 1989 and 2003. Calculation errors are pointed out by dashed lines; (a), (b), (c) are time-shift maps at the Top Reservoir, and (d), (e), (f) are time-shift sections of inline 630, as indicated by the red line AB in Figure 3.7c.

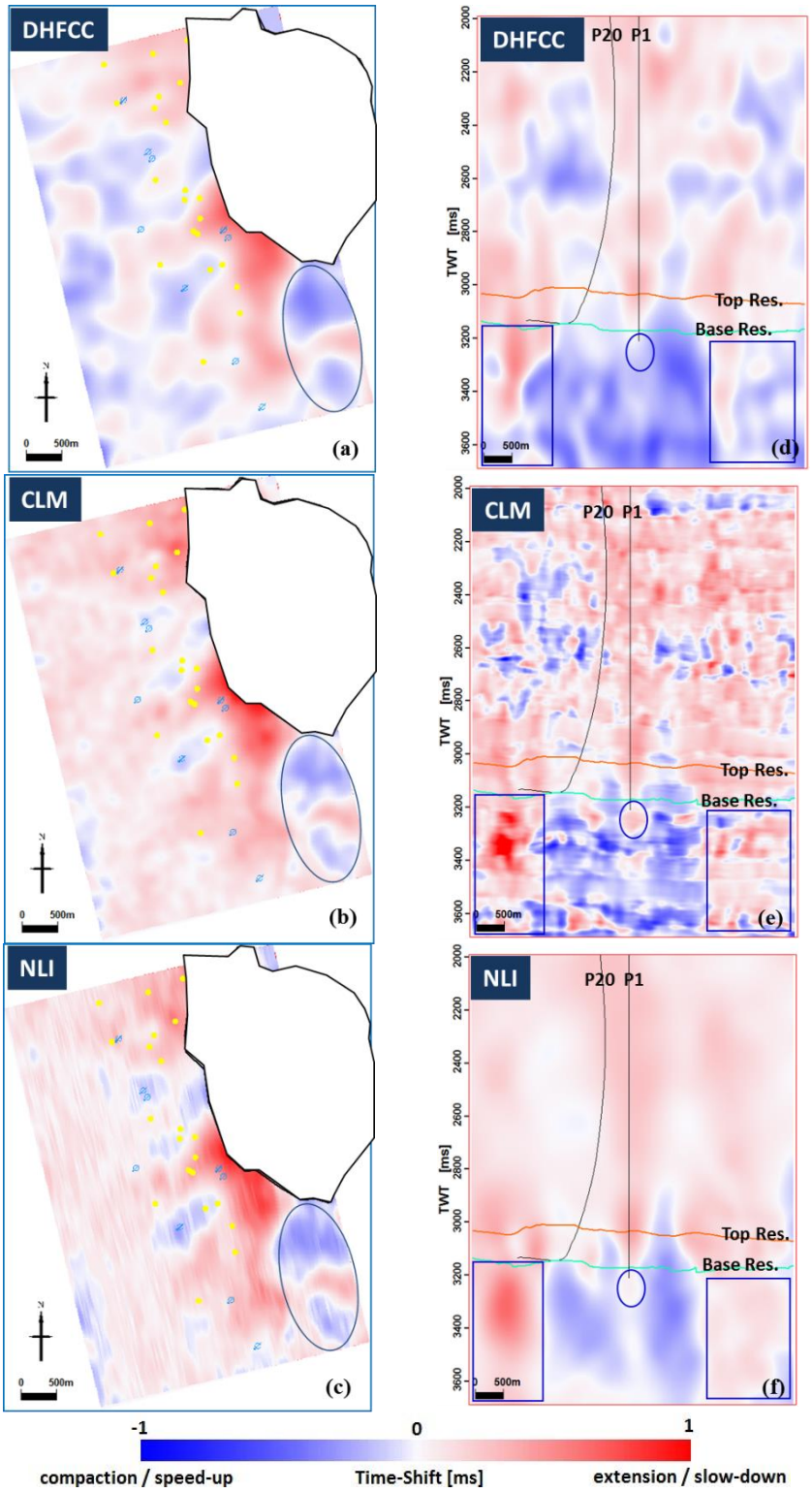

Figure 3.9: Ekofisk time-shifts between lofs1 and lofs2 calculated by DHFCC (a and d), CLM (b and e), and NLI (c and f).

3.3.2 Application to the Erskine field – an HPHT gas condensate reservoir

The Erskine field is a high-temperature (340° F) and high-pressure (14000psi) gas condensate field, which is located on the western margin of the East Central Graben (HajNasser, 2012). Main reservoirs in this field are the Pentland, Erskine and Heather formations, all of which were deposited in the Jurassic age. Massive pressure depletion happened during the production period, which caused strong geomechanical changes. 4D seismic surveys available in this field are the 1989 pre-production survey and the 2001 monitor seismic survey. The 4D amplitude map from HajNasser (2012) shows strong negative amplitude change concentrated around the producers in the eastern part, which matches the time-shift distribution reported by Fletcher (2004) (Figure 3.10).

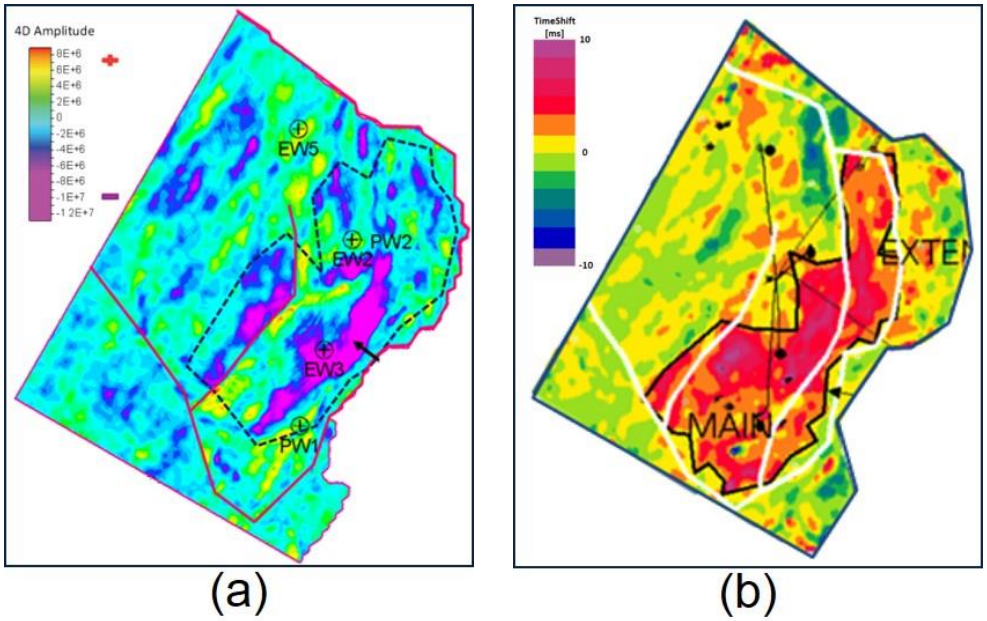

Figure 3.10: (a) 4D amplitude change across the reservoir (HajNasser, 2012). (b) time-shift map (Fletcher, 2004). Extension pattern corresponds very well with field depletion pattern.

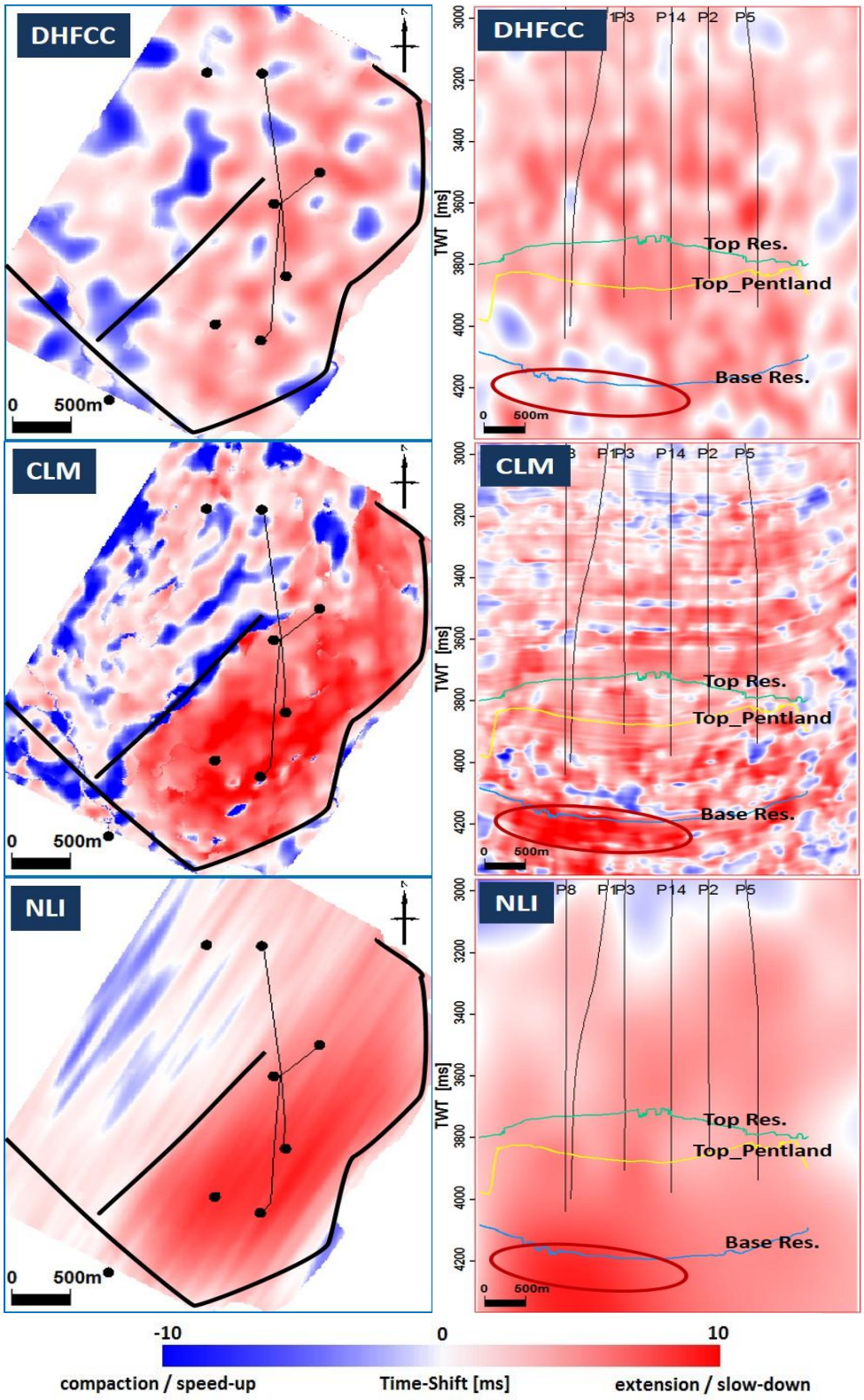

Figure 3.11: Erskine time-shifts between 1989 and 2001 calculated by the three methods

Figure 3.11 shows the time-shift results calculated by the DHFCC, CLM and NLI techniques; as suggested in HajNasser (2012), a calculating window of size st9sx11sy11

was applied in the DHFCC and CLM. Time-shift maps were extracted at Base Reservoir with the main faults and producing wells plotted together. Compared with Fletcher's time-shift map in Figure 3.10b, the present time-shift estimations match very well in terms of magnitude and distribution pattern. Both the CLM and NLI results clearly recover the positive time-shift distribution in the eastern area caused by shale activation, while DHFCC attenuates this character. Moreover, the distribution of the CLM result corresponds with the fault location quite well, as it breaks along these faults, especially in the centre.

Among the three time-shift sections, the CLM has the best resolution, as it matches the depositional character of formations in this field. The NLI result is too smooth to reflect those features. Nevertheless, it is good to see that both of them pick up the same strong under-burden time-shifts in the left side, which may correspond to a combined effect of both geomechanical changes and production.

3.3.3 Application to the Schiehallion field – a thin and multiple-stacked reservoir

The final field for application is the Schiehallion field, which is situated on the United Kingdom continental shelf about 200 km to the west of the Shetland Islands and lies at a water depth of about 450 m (Martin and Macdonald, 2010). Deposited in a deep water continental slope environment (Figure 3.12a), the reservoir of the Schiehallion field comprises a complex Lower Tertiary sequence of amalgamated turbidite channel sands, which generally run in the direction from southeast to northwest, as shown in Figure 3.12b (Martin and Macdonald, 2010). A series of east-west trending normal faults segregate the field and divide the reservoir into five distinct segments with limited or no lateral communication (Falahat, 2012). Because of the character of this field, a single segment (segment 1) is selected for this study. The reservoir quality of this field varies in character from poor quality thinly inter-bedded sands and shale to high quality massive sands with high porosity and permeability. Figure 3.12c shows the distribution of seismically recoverable geobodies that reveals the strong reservoir heterogeneity.

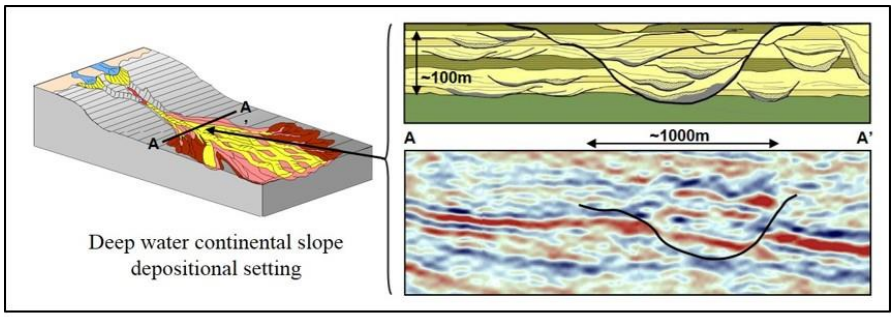

(a)

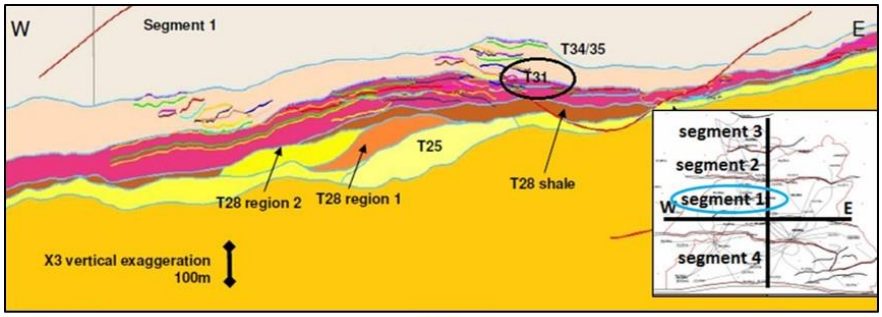

(b)

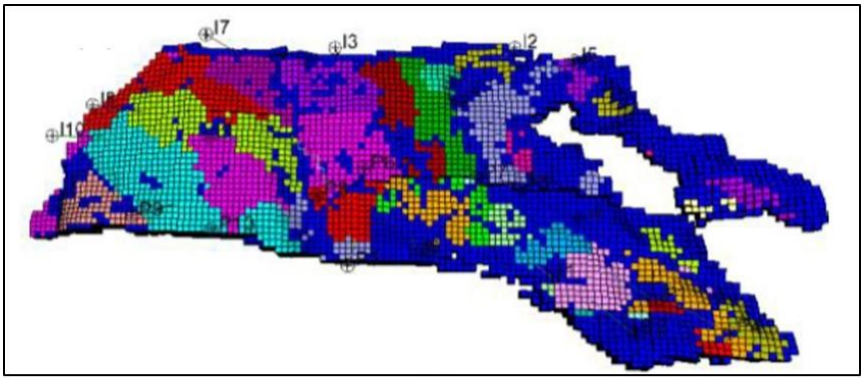

(c)

Figure 3.12: General geological information of the Schiehallion reservoir: (a) depositional environment and channelised structure of the sediments (Martin and Macdonald, 2010). (b) geological cross-section (west to east) in Schiehallion segment 1 (Martin and Macdonald, 2010). (c) The geological model of the Schiehallion reservoir in segment 1. These geobodies control the connectivity and fluid flow in the reservoir (Falahat, 2012).

Multi-vintages of 4D seismic data have been shot in this field, among which the 1996 (pre-production) and 2002 (four years after production start-up) datasets were provided for these time-shift calculation tests. Previous work from others has seen a low magnitude of time-shifts (around 1 ms) between this period (Falahat, 2012). These time-shifts were estimated either by subtracting time differences of interpreted horizons or by modelling the effect from pressure and saturation changes respectively. An NRMS map was

generated for an interval of 300ms to 600ms above the reservoir of 1996-2002, using equations proposed by (Kragh and Christie, 2002), showing the poor repeatability in seismic datasets (Figure 3.13).

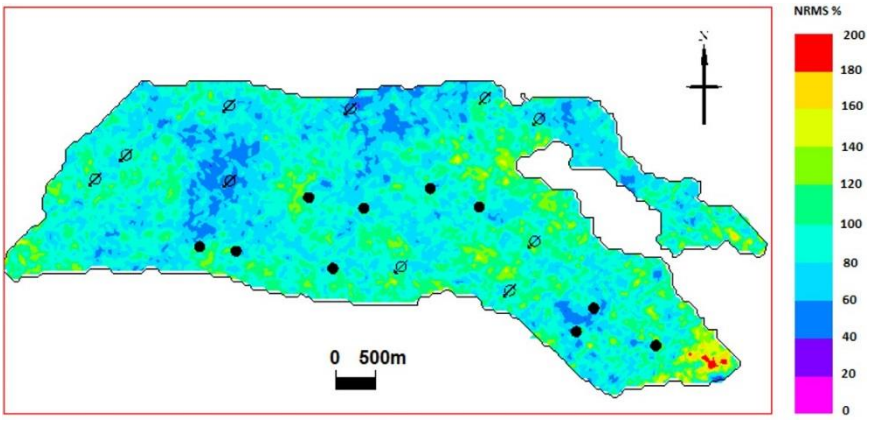

Figure 3.13: Seismic repeatability (NRMS) in the overburden (calculated by the method proposed by Kragh & Christie, 2002).

Instantaneous time-shift maps were extracted at the Base Reservoir (Figure 3.15). Despite the high noise level, they show similar character of positive time-shift distribution, as indicated. The distribution also correlates with the softening signals showed in the RMS amplitude map in some areas (Figure 3.14).

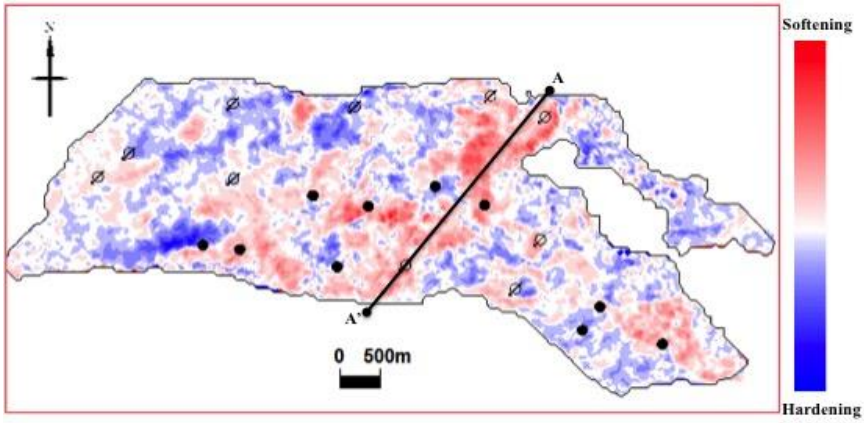

Figure 3.14: 4D map of the sum of negative amplitude between the Top and Base Reservoir (between 1998 and 2002).

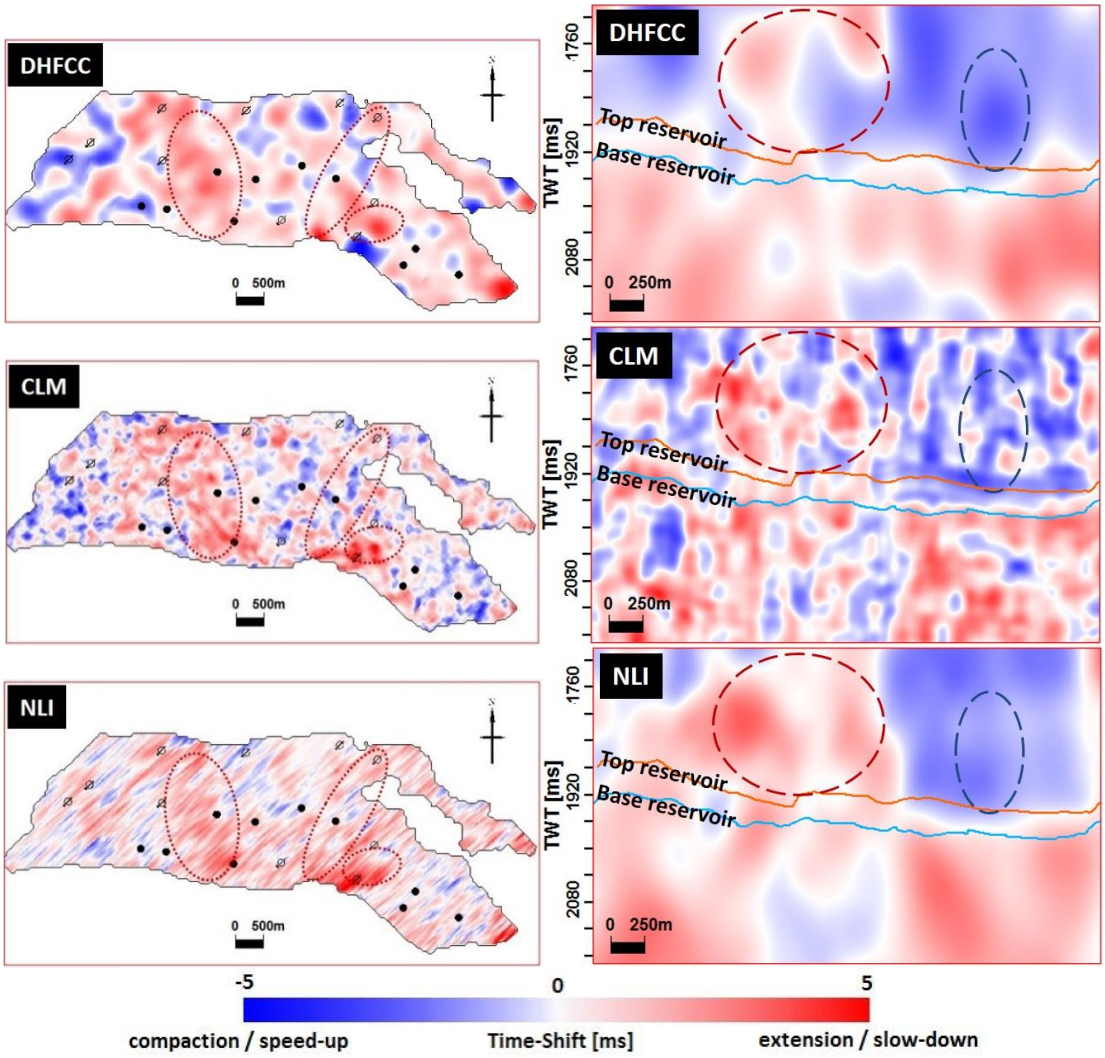

Figure 3.15: Schiehallion time-shifts between 1996 and 2002 calculated by three methods

The three time-shift sections displayed in Figure 3.15 are extracted from line AA'. All of them manage to show extension signals in the under-burden that are mainly due to geomechanical effects. Central over-burden extension is observed in all three results, but the positive time-shift on the left side caused by a producing well is lost in the DHFCC result. In terms of noise level, NLI behaves much better than the DHFCC and CLM methods.

3.3.4 Which is the best method?

All the time-shift and time-strain results from the previous analysis are summarized in Figure 3.16, Figure 3.17 and Figure 3.18. A marking scheme is introduced here for

comparing the efficiency of the three time-shift measurement techniques. Scores of between 0 and 10 are given for each field application, to account for aspects such as result noise, resolution, and time-strain quality. High marks will be given to low values of the first two aspects, but high values of the last two aspects.

In terms of time-shift quality, taking Erskine as an example, DHFCC generates the worst result among the three, so it is assigned a score of 6 (3 for resolution and 3 for noise level). NLI suppressed noise better than CLM in the western part, whereas the pattern of the CLM time-shift map coincides well with the distribution of the two main faults, so NLI scores 15 (5 for resolution and 10 for noise level), and CLM scores 16 (9 for resolution and 7 for noise level).

In terms of time-strain quality, taking the Ekofisk towed streamer results, for example, they all show relatively good resolution, as they reveal the strong compaction signal inside the reservoir and extension signals above top reservoir and under base reservoir. Because of the nature of the derivation process, all the time-strain results are high in noise level, but DHFCC and NLI are relatively better than CLM, as they already involve smoothing techniques when generating time-shifts. So in this aspect, scores of 7, 9 and 5 are allocated to DHFCC, NLI and CLM respectively.

In terms of the computational cost, currently under the condition of ETLP's cluster and when dealing with seismic datasets less than 1 gigabyte, it takes about 1 hour for DHFCC, and 6 hours for CLM, 4 hours for NLI. Of course, time will be reduced with smaller size of seismic data and a more powerful cluster as well, therefore, this will not be included into my marking criteria.

Finally, after summing up all the marks in each aspect, NLI is regarded as the best method for this research, as it generates both good time-shifts and stable time strains. The marking detail is shown in Table 3.2. For generating better maps, this technique needs to be extended from 2D to 3D. The traditional cross-correlation based method is still good for time-shift calculation in many cases. In terms of good resolution, CLM is the best. However, as none of those smoothing techniques are imposed, further tricks for suppressing noise are needed to make it a robust technique.

Table 3.2: Marks for each method applied, based on time-shift and time-strain quality

Fields	Methods	Time-shift quality		time-strain quality (0-10)	Total mark (0-30)
		Noise level (0-10)	Resolution (0-10)		
Ekofisk (03-89)	DHFCC	8	6	7	21
	CLM	6	8	5	19
	NLI	9	6	9	24
Ekofisk (lofs2-1)	DHFCC	6	6	5	15
	CLM	4	7	4	15
	NLI	7	6	6	19
Erskine (01-89)	DHFCC	3	3	3	9
	CLM	7	9	3	19
	NLI	10	5	4	19
Schiehallion (02-96)	DHFCC	8	5	5	18
	CLM	6	6	7	19
	NLI	9	5	6	20

3.4 Summary

This chapter has provided a critical review of three time-shift calculation methods. In the first part, the three methods were applied to a set of synthetic tests that were designed to evaluate the accuracy in recovering time-shifts. It was found that in the case of large time-shifts, the DHFCC method did a very good job in recovering a stable time-shift profile, even when dealing with very noisy seismic data. However, the accuracy of the CLM and NLI methods decreased with the increase of noise level in seismic data. In the case of recovering small time-shifts, despite still giving a stable result, DHFCC lost its accuracy, while, in contrast, NLI and CLM tended to give better results. In the second part, the three time-shift measurement techniques were applied to four North Sea datasets, of which the seismic quality and time-shift magnitude varies. A marking scheme was used for method comparison in terms of computational cost, time-shift and time-strain quality. It was found that NLI is the best method for this research, as it both generates good time-shifts and stable time strains. The resolution of the DHFCC method and the ability of noise suppression of the CLM method need to be improved if they are to be considered for future use. In the following chapters, I am going to use the time-shift techniques discussed here for time-shift measurement of the Shearwater field, and try to interpret them for dynamic reservoir characterisation.

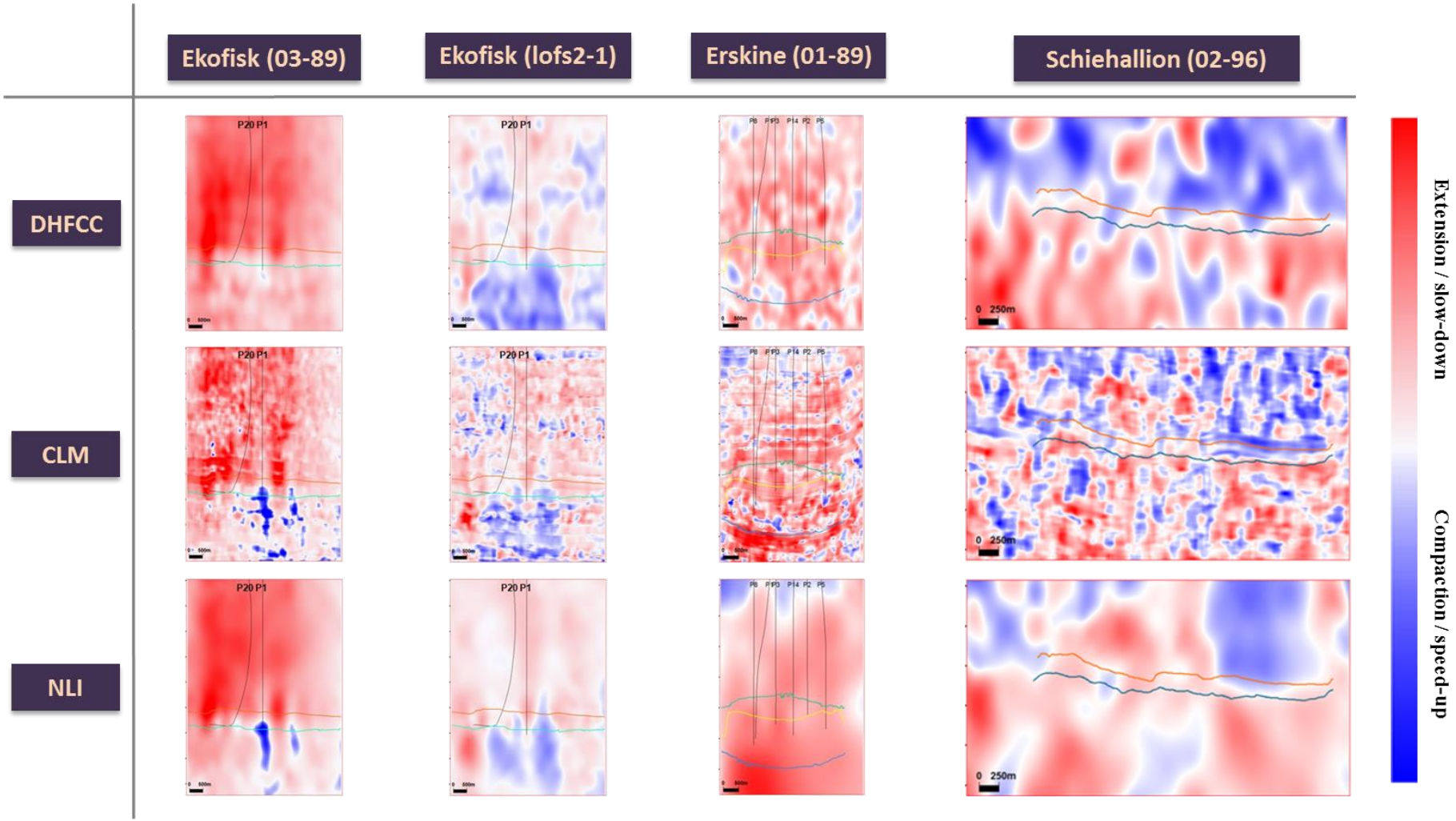

Figure 3.16: Time-shift method comparison – section view of time-shift results from DHFCC, CLM, NLI for four North Sea datasets.

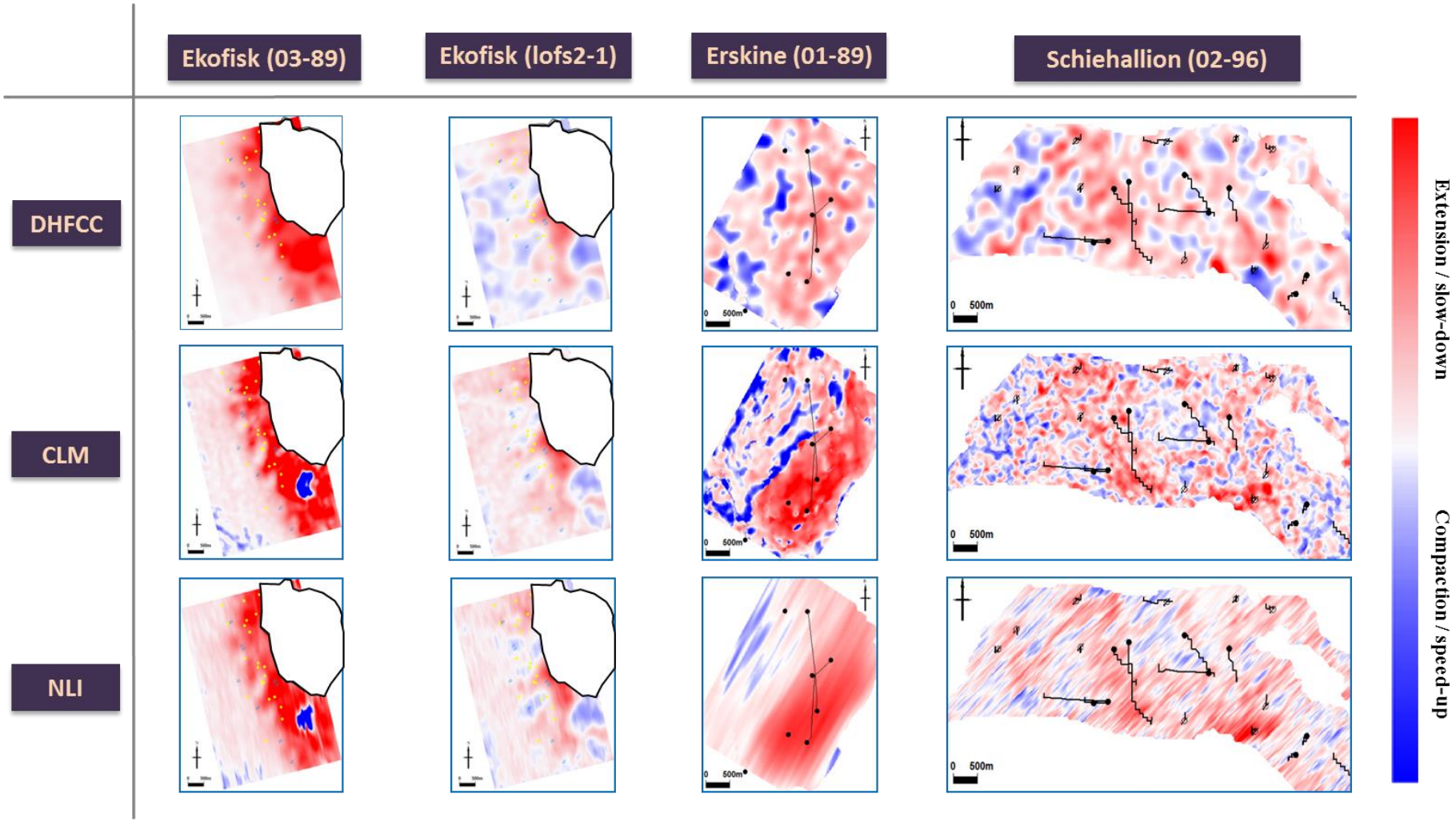

Figure 3.17: Time-shift method comparison – map view of time-shift results from DHFCC, CLM, NLI for four North Sea datasets

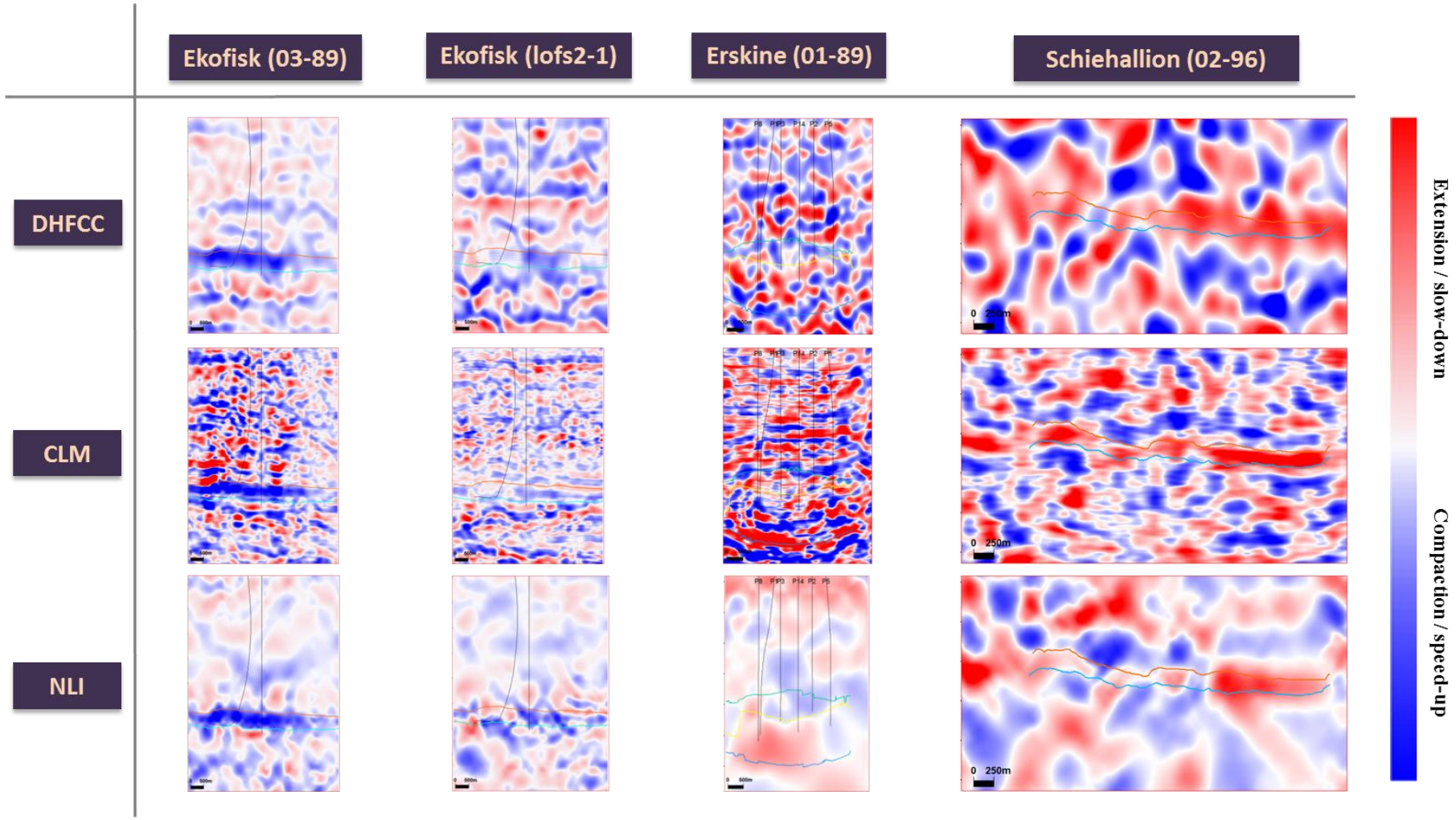

Figure 3.18: Time-shift method comparison – section view of derived time-strain results from DHFCC, CLM, NLI for four North Sea datasets

Chapter 4

General reservoir characterisation of Shearwater field

This chapter provides a general reservoir characterisation of the Shearwater field. Shearwater is a high-pressure and high-temperature gas condensate field, which is located in the Central Graben Area of the Central North Sea. In the first part, a description of the field is provided, covering the field's key facts, geological and production information. Next, time-shift volumes are measured from Shearwater time-lapse seismic vintages by the three different time-shift measurement algorithms discussed in chapter 3, and then the best result is converted into time-strain to understand the instantaneous changes within each interval. Discussions on 4D amplitude changes as well as the time-shift variations with offset are also provided. After that, the focus is moved onto the interpretation of the calculated time-shift and time-strain distributions, and linking them with field geological and production information. In addition, synthetic test is conducted to give an insight into the cause of the Heather shale anomaly. Remaining problems to be solved in the following chapters are also mentioned at the end.

4.1 Description of the Shearwater field

4.1.1 Field key facts

The Shearwater field is a high-pressure and high-temperature (HPHT) gas condensate field, which is located offshore in the UK Block 22/30b within the Central Graben Area of the Central North Sea (Figure 4.1) and was the first offshore HPHT field in production in the North Sea. It has an average water depth of 90 m (295 ft) and is approximately 225 km (140 miles) to the east of Aberdeen (Shell, 2015). As seen in Figure 4.1, the Shearwater field is geographically close to some well-studied HPHT fields such as the Elgin-Franklin fields to its west and the Erskine field to its east. Discovered in 1988, this field was further explored by appraisal wells drilled in 1991, 1992 and 1996, and finally the first production was initiated in September 2000 (Beck, 2015). Condensate and gas were produced under pressure depletion drive from two separate reservoirs of Jurassic age - the Upper Fulmar and the Lower Fulmar sandstone formations. The initial reservoir pressure was around 15,400 psi (1062 bar), above the estimated pressure dew point of 6,800 psi (469 bar), and the reservoir temperature was at 360 degF (182 degC). After four years of production, a pressure depletion of over 8,000 psi was recorded and this gave rise to many geomechanical hazards which will be described in Chapter 5. The current licence of the Shearwater Field is co-held by Shell (28%), Esso E&P (44.5%), and Arco (27.5%), with Shell being the operator (Beck, 2015).

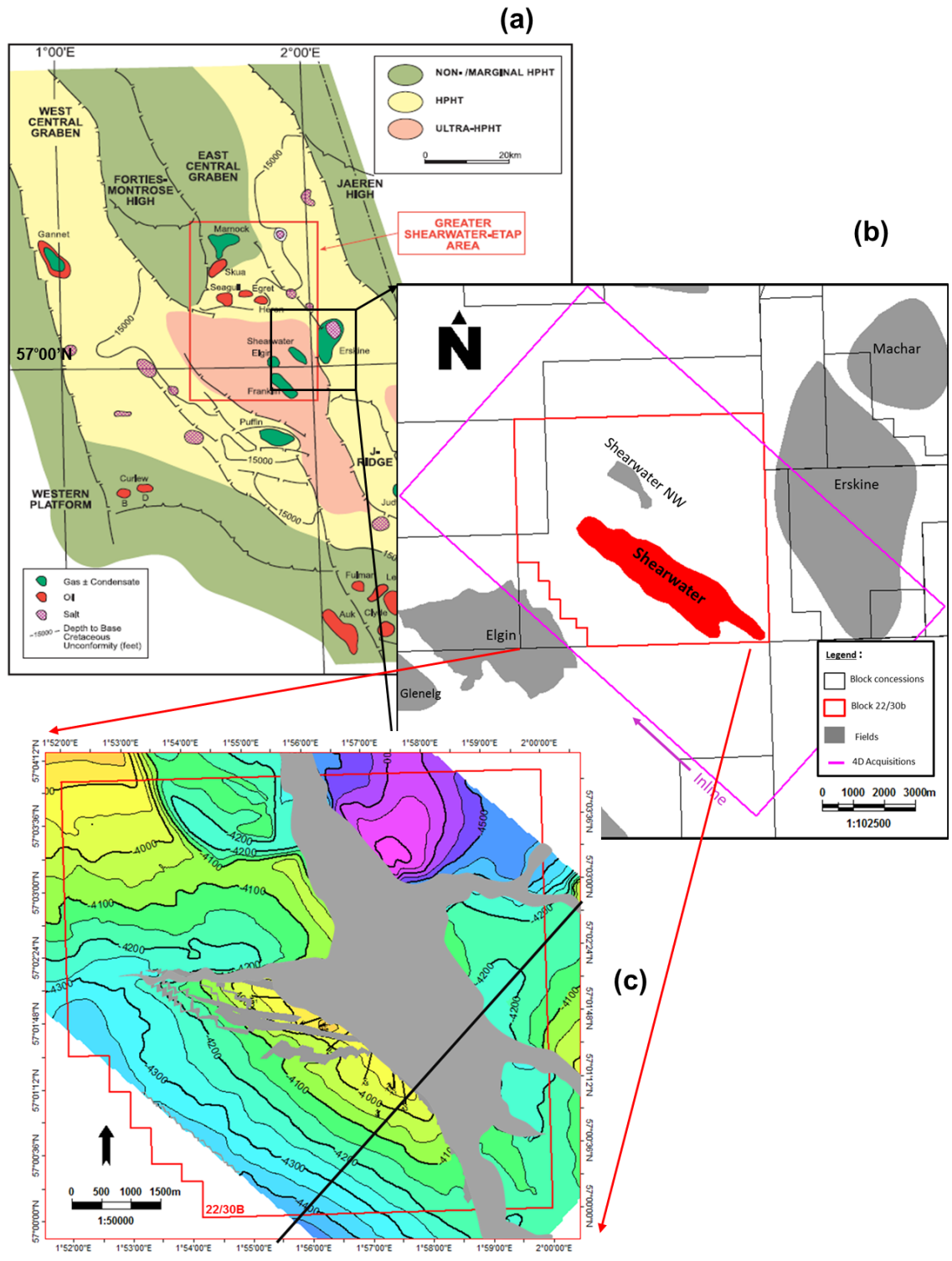

Figure 4.1: (a) The geographical location of the Shearwater field (Winefield *et al.*, 2005), and (b) a closer view of the field with neighbouring HPHT fields and its 4D seismic acquisition area plotted. (c) Time structure map of the Top Fulmar Reservoir. The faults are coloured in grey (modified after Gilham *et al.* (2005)). Black line shows the location of the cross-section in Figure 4.2.

4.1.2 Geological information

The stratigraphic and structural setting of the Shearwater field was revealed based on penetrated formations from exploration wells, observed seismic events, regional deposition background, and information from adjacent fields (Lasocki et al., 1999; Gilham et al., 2005; Erratt et al., 2010). The trap of this field consists of a tilted fault block of Triassic, Middle Jurassic (Pentland Formation) and Upper Jurassic (Fulmar and Heather formations) stratigraphy, with two major near-vertical faults defining the northern and eastern boundaries of the trap (Figure 4.1c) (Gilham et al., 2005). This structural setting is a result of the evolution of the rift system in the Central North Sea Basin between the Permian and the Late Jurassic period, and the regional thermal uplift from the Late Kimmeridgian producing Zechstein salt diaper structures (Rattey and Hayward, n.d.; Erratt et al., 1999; Winefield et al., 2005; Erratt et al., 2010). These distorted sediments then underwent truncation and erosion, which created the so-called 'Base Cretaceous Unconformity', also known as the 'Late Cimmerian Unconformity' (Rawson and Riley, 1982). This event can be clearly marked from seismic data (Figure 4.2), and is usually used as a regional reflection marker representing the transition from the syn-rift to the post-rift stage (Gabrielsen, 1984; Nottvedt et al., 1995). Thereafter, the deposition process stabilized and resulted into relatively flat formations.

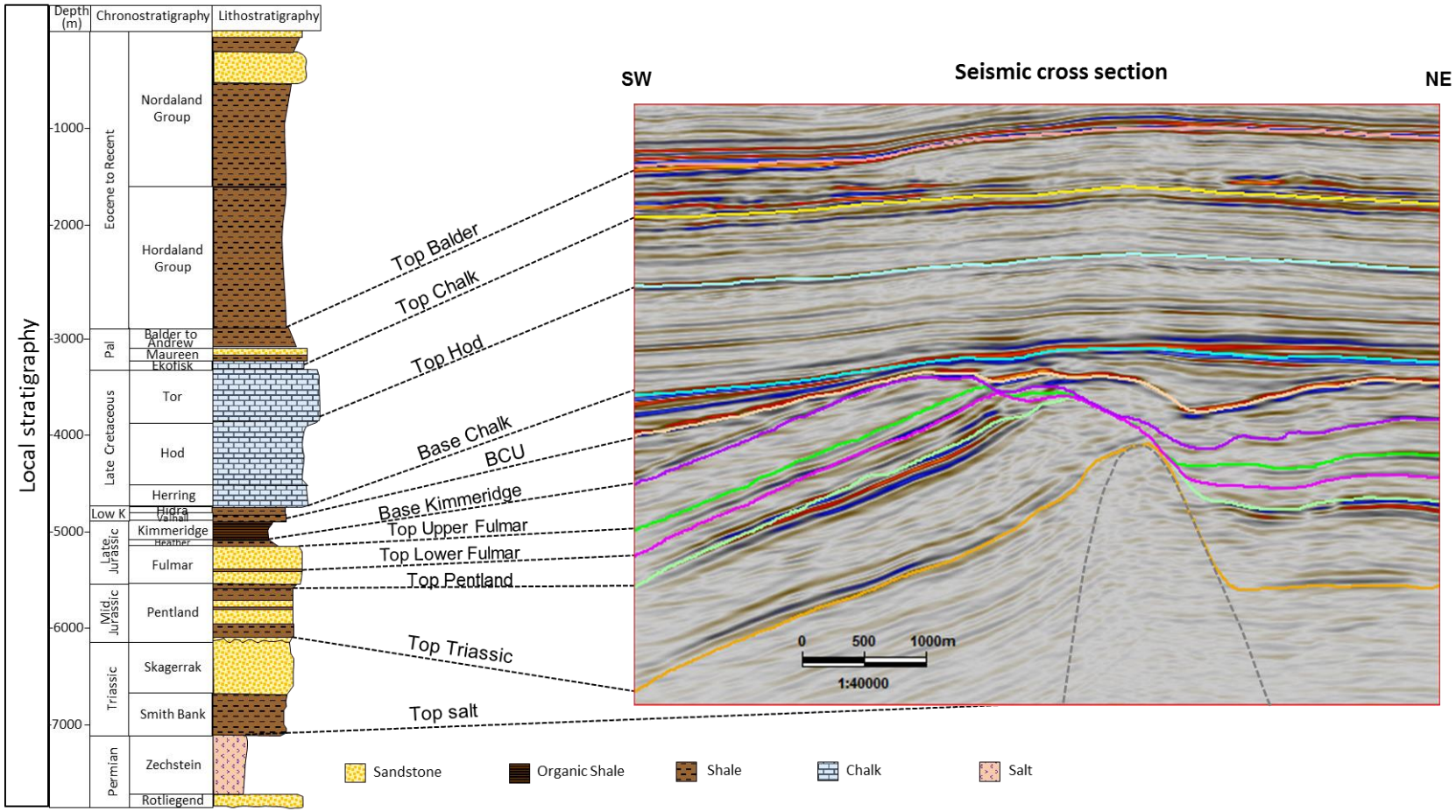

Figure 4.2: (left) The stratigraphic succession of the Shearwater field (Lasocki *et al.*, 1999; Rangel, 2016). (Right) X-Line seismic cross section across the Shearwater Field from the 2001 baseline seismic survey. Main geologic horizons in the overburden, reservoir and under-burden are interpreted in the seismic section and linked with the stratigraphic succession.

The main reservoir under production is the Upper Jurassic Fulmar formation, which is comprised of 700 ft stacked shoreface sandstones with high NetSand-To-Gross ratio and porosity up to 24% (Gowland, 1996; Gilham *et al.*, 2005). The gas-condensate and water contact is detected at 16900 ft tvdss (Gilham *et al.*, 2005). Based on the interpretations of core and well-log data (Figure 4.3) and a strong seismic mid-Fulmar signal (Figure 4.2), the Fulmar formation is divided into the Upper (high porosity) and the Lower (low to moderate porosity) Fulmar. From well-correlation as shown in Figure 4.4, both of the two units correlate very well between wells with a relatively uniform thickness. Regionally, they are comparable with the lower Fulmar and mid-Fulmar of the Elgin and Franklin fields, while only the Lower Fulmar can be correlated with the one of the Erskine field. Previous core and log characterisations by Gowland (1996); Gilham *et al.* (2005) show a further subdivision of the Fulmar formation into 13 depositional cycles, which can be grouped into 4 geological units (Figure 4.3). From bottom to top, it reveals a continuous middle to upper shore-face depositional setting.

Apart from the Fulmar formation, Winefield *et al.* (2005) suggest that other potential reservoirs could be found in the fluvial sandstones of the Middle Jurassic Pentland formation as well as the Aeolian sandstones of the Triassic Skagarrak formation.

The main hydrocarbon source rock is the Upper Jurassic Kimmeridge Clay, with a secondary source rock from the Upper Jurassic Heather shale and Middle Jurassic Pentland shale (Cayley, 1987). The hydrocarbon accumulation is sealed by the overburden Heather, Kimmeridge Clay, Cromer Knoll and Lower Chalk formations (Figure 4.2) (Winefield *et al.*, 2005).

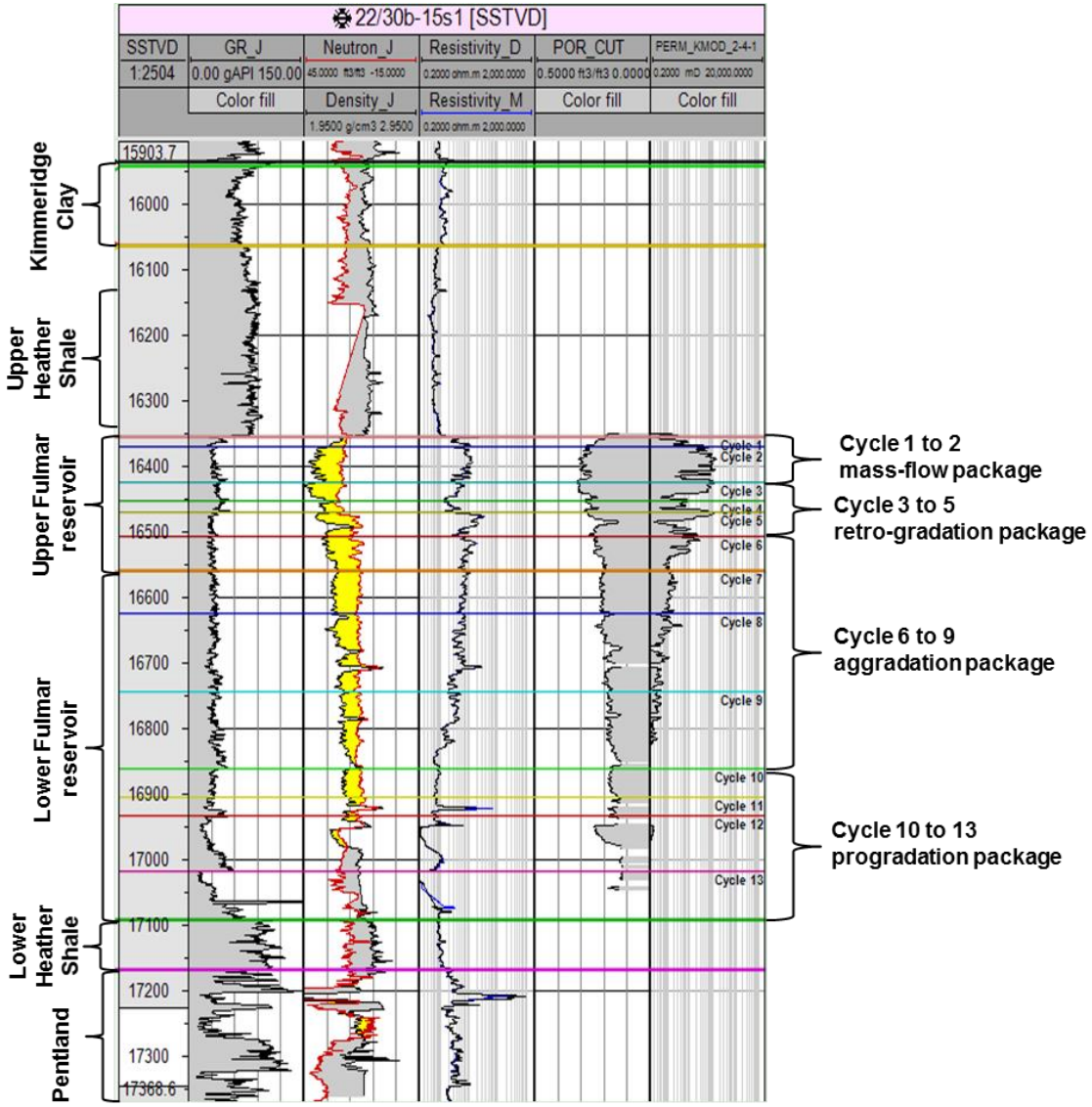

Figure 4.3: The Fulmar formation evaluation and zonation at a well location (figure and description adapted after Gowland (1996); Gilham *et al.* (2005)). This formation can be further subdivided into 13 depositional cycles, and grouped into 4 geological units. Cycle10 to 13 represent a progressive expansion of the shoreface environment across the greater Shearwater area. Cycle 6 to 9 show a thick sequence of sand-rich inner shoreface facies. Cycle 3 to 5 display a retrogradational sequence that probably marks the initial backstepping of the Fulmar shoreface. Cycle 1 to 2 include distinct mass-flow events following the de-stabilization and collapse of the shoreface in the north and western shoreline.

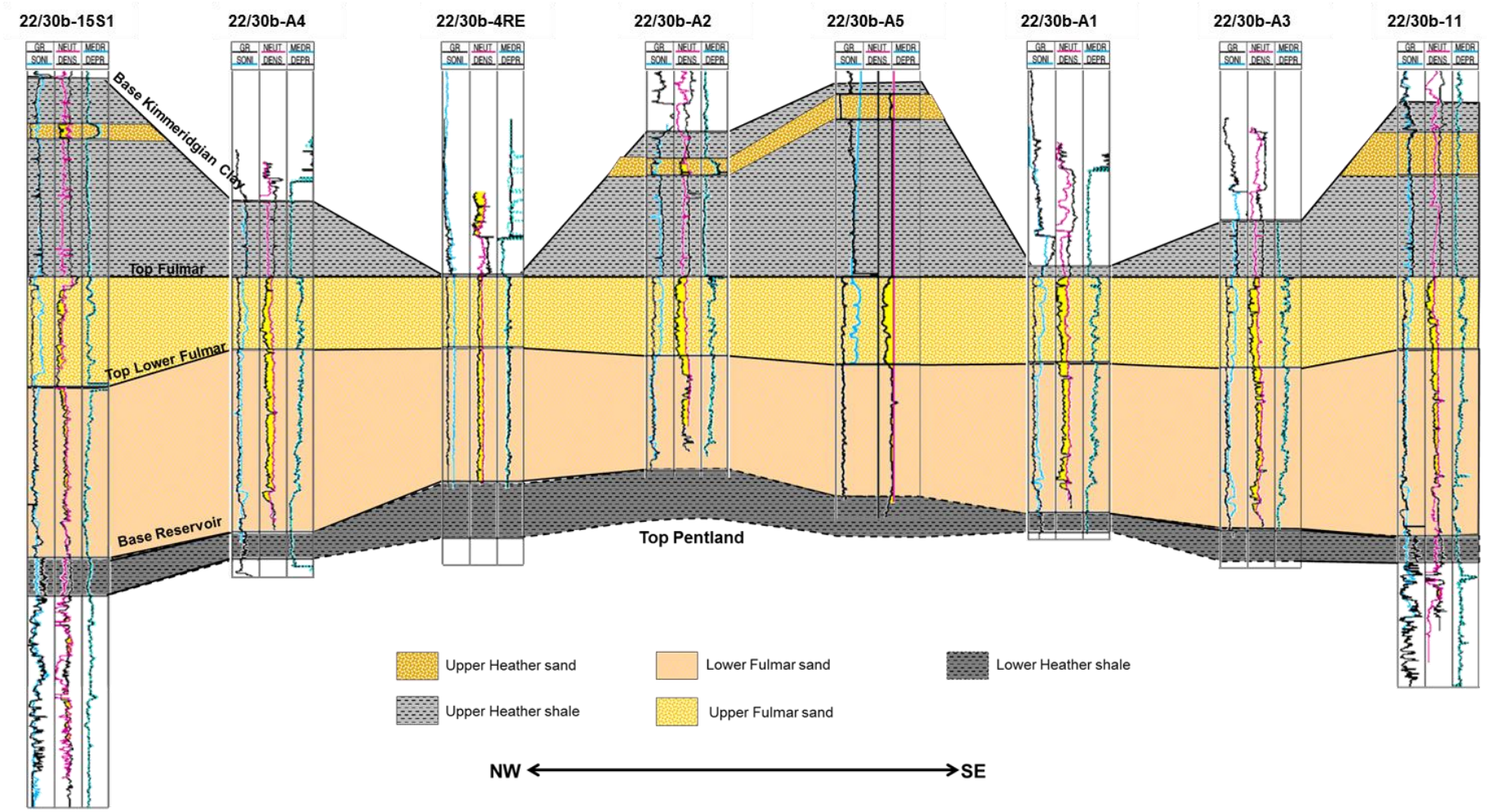

Figure 4.4: Well correlation of the main intervals of the Shearwater Field (adapted after Gilham et al., 2005)

4.1.3 Overpressure in the Central North Sea

It is widely known that the central graben area of the Central North Sea is highly over-pressured. As stated by Gaarenstroom *et al.* (1993), the overpressure is the amount of pore pressure exceeding the hydrostatic pressure, and the main factors contributing to that are the depth, disequilibrium compaction, kerogen transformation and oil cracking. Holm (1998) shows the typical pore pressure profile for Central Graben area: the upper part of the Tertiary succession is normally pressured, and is separated from the over-pressured pre-Cretaceous Jurassic and Triassic reservoirs by a pressure transition zone formed by the Upper Cretaceous Chalk and Lower Cretaceous Cromer Knoll groups. Apart from the deep depth, Winefield *et al.* (2005) pointed out that the overpressure development in this area is also influenced by lateral changes in reservoir or aquifer connectivity and the presence of significant lateral structural barriers to the migration of formation fluids and pressure. They also indicated that the early oil charge in the Late Cretaceous preserved part of the primary intergranular porosity, and this also contributed to the overpressure (Rangel, 2016).

4.1.4 Production history

The field came on stream in 2000 with four wells targeting Jurassic Fulmar formation (SW 01, 07, 08, and 09), and one targeting the Pentland formation (SW05). Side-track well SW08s1 and SW04 were drilled in 2002. SW06 well was drilled in the unconnected northwest block in 2004. Figure 4.5 shows Shearwater reservoir pressure measured from SW08s1, SW09, SW07, SW04 and SW01, respectively with the timing of 4D seismic surveys, and well failure events plotted. Approximately 2000 and 8000 psi of pressure depletion were observed up to the time of the first monitor and the second monitor seismic surveys respectively. Geomechanical hazards induced by the pressure depletion and reservoir compaction have led to several well failure events through the production period as plotted in Figure 4.5. By 2010, only SW06 was producing intermittently. The cumulative gas production up to 2012 is about 450 Bcf with 35% recovery factor. New wells are being planned for the significant remaining gas condensate volumes, among which the SW09S3 well was successfully delivered on-stream in 2015 (Beck, 2015).

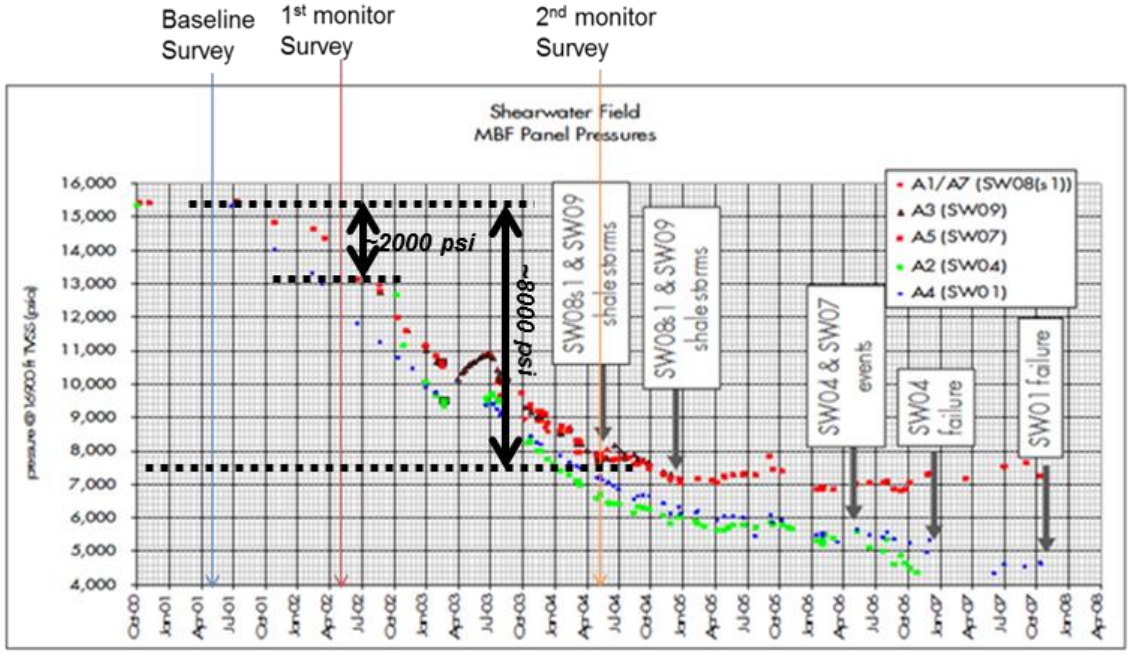

Figure 4.5: Shearwater reservoir pressure measured from SW08s1, SW09, SW07, SW04 and SW01, respectively with the timing of 4D seismic surveys, and well failure events plotted. Approximately 2000 and 8000 psi pressure depletion were observed respectively up to the time of the first monitor and the second monitor seismic surveys (Shell internal report).

4.2 Shearwater time-lapse seismic and time-shift estimation

4.2.1 4D seismic surveys

Time-lapse seismic surveys have been acquired over Shearwater field in the strike direction running from southeast to northwest (Figure 4.1). The baseline survey was acquired in 2001 about half a year after the field came on stream with very low pressure depletion during that period. It was followed by the first monitor survey in 2002, and the second monitor survey in 2004, with maximum pressure depletion of around 3000 psi and 9000 psi observed until the acquisition time of each survey respectively. The three 4D seismic surveys were first co-processed in 2004, and later re-processed in 2011 including pre-processing and migration with an updated velocity model which was derived using data from 3 different azimuths (96, 01 and CGG speculative survey) (Guzman, 2011). The re-processing improved data quality and the seismic non-repeatability of full-stack datasets was estimated to be less than 10%, with the exception of the area associated with boundary faults (Figure 4.6). Both angle-stacks and full-stacks of 2011 re-processed datasets were provided by Shell and were used for the computation of 4D seismic signals in this study. Offset ranges used for angle-stacks are 300-1100m, 1200-2000m, 2100-2900m, and 3900-4700m respectively (Shell, 2013).

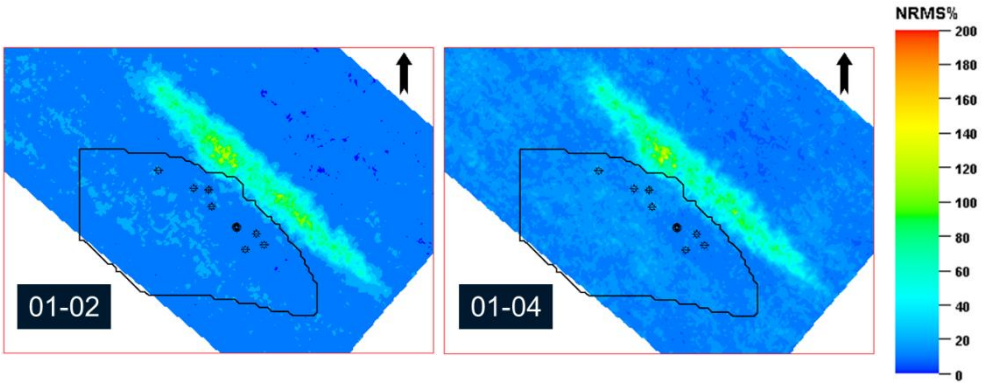

Figure 4.6: NRMS maps extracted in the overburden show very good seismic repeatability of 2001, 2002 and 2004.

In 2013, a new monitor survey was acquired for this field following the same acquisition parameters of vintage 2002 (CGG, 2013). In the same year, the previous three seismic vintages together with the new survey were co-processed by CGG. Details of acquisition parameters for all seismic surveys are listed in Table 4.1.

Table 4.1: A summary of acquisition parameters of seismic surveys in 2001, 2002, 2004 and 2013 (CGG, 2013).

Parameter	2001	2002	2004	2013
Shot By	Veritas	PGS	PGS	Dolphin Geophysical
Main Vessel	M/V SeisQuest	M/V Ramform Viking	M/V Ramform Valiant	
Source				
Number of sources	2	2	2	2
Source Separation	50m	50m	50m	50m
Volume	3450 cu. in.	3090 cu. in.	3090 cu. in.	
Depth	6m	6m	6m	M/V 6m
Shot Interval	25m	25m	25m	25m
Streamers				
Number	8	10	10	10
Active Length	6000m	4500m	6000m	4500m
Depth	8m	8m	8m	8m
Group Interval	12.5m	12.5m	12.5m	12.5m
Groups	480	360	360	480
Separation	100m	100m	100m	100m
Nominal Near Offset	214m	314m	314m	110m
Recording				
Sample Rate	2ms	2ms	2ms	2ms
Record Length	8192ms	8000ms	8172ms	8000ms
Undershoot				
Acquired	Yes	Yes	No	Yes

4.2.2 Shearwater time-shift and time-strain

During the production of the Fulmar reservoir, massive pressure drop has been observed due to the field drive mechanism. Hence, as discussed in Chapter 2, changes in stress and strain fields both inside and outside of the reservoir rocks influenced the formation integrity and well production (Addis, 1997; Hettema *et al.*, 1998; Hatchell *et al.*, 2003; Sayers and Schutjens, 2007). Since these changes can be qualitatively visualised and quantitatively measured in terms of time-lapse time-shifts (Segall, 1989; Hatchell *et al.*, 2003; Tura *et al.*, 2005), it is very important to measure them accurately for the benefit of the following reservoir characterisation. For this purpose, all the three methods (DHFCC, CLM, NLI) evaluated in chapter 3 are applied to recover Shearwater time-lapse time-shifts from both full-stack and angle-stack 4D seismic datasets.

In order to find a balance between the noise level and resolution for the two window based methods (DHFCC and CLM), the size of the window has been optimized by testing different options ranging from 2 to 15 samples both vertically and laterally. Finally the result using a window size of st8sx10sy10 is considered to be optimum and realistic (among all the options) and therefore, this window size is used for all window based time-shift calculations for this field.

In Figure 4.7, the vertical TWT sections from left to right displays the time-shift results measured by DHFCC, CLM and NLI. Results from DHFCC and NLI are quite smooth and the one from CLM has better resolution. The magnitudes of different time-shift results are very close to the maximum value of about 5ms, and the distribution patterns are also comparable as they accumulated through the overburden, reduced through the reservoir and increased again in the underburden, reaching a maximum in the lower Pentland formation. The vertical variation surrounding the reservoir is expected according to the reservoir compaction effect. However, the dramatic increase in the deeper underburden is not expected, and the magnitude is even bigger than that in the overburden, which cannot be explained by the arching effect.

Figure 4.9 provides a coarse understanding of the time-shift distribution by taking a vertical profile and converting it into time-strain. Time-shift and time-strain at a well site, and a typical lithology column in this area are also plotted in this figure.

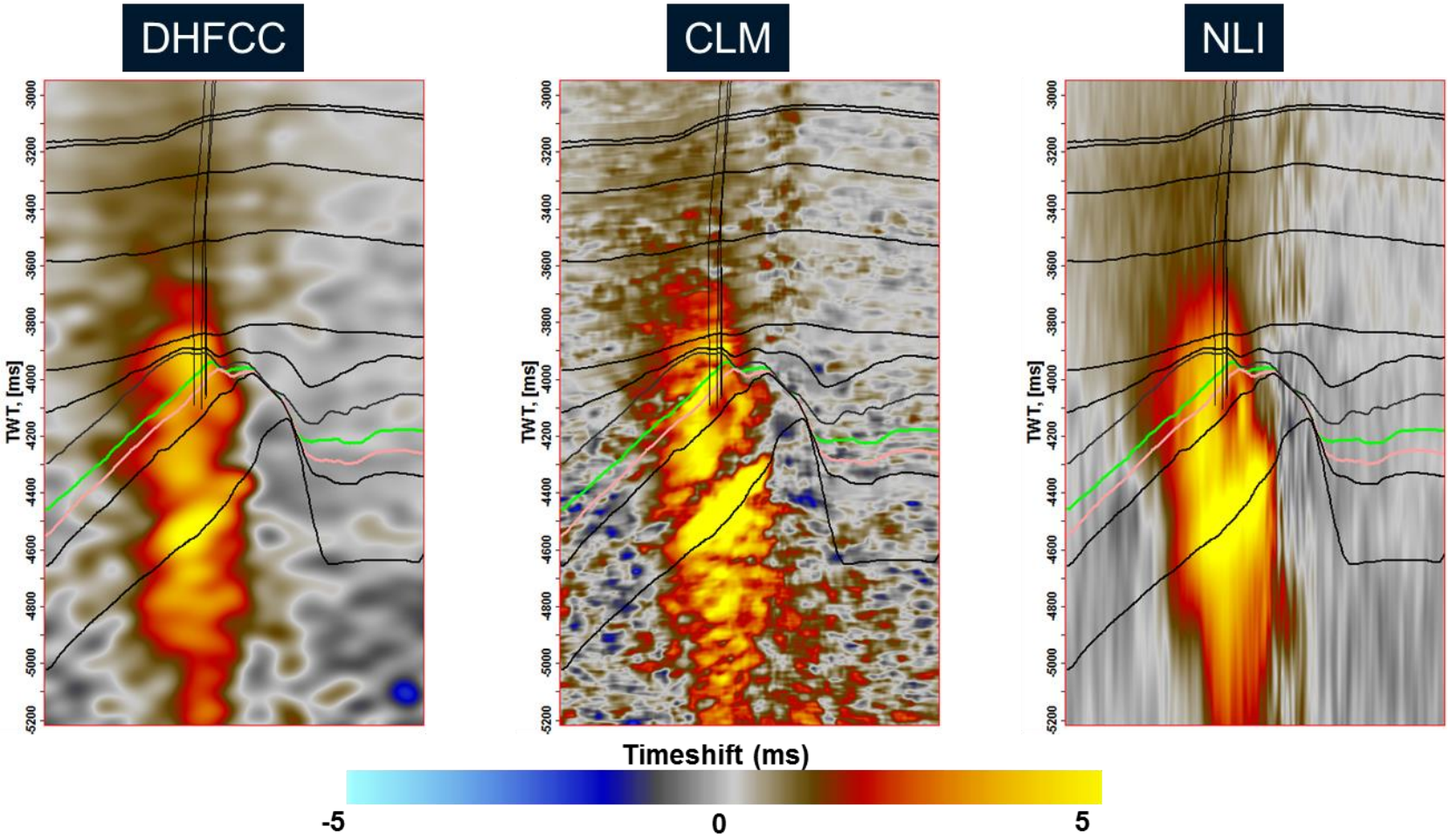

Figure 4.7: Shearwater time-shift results measured from DHFCC, CLM and NLI. The green and pink horizons represent the Top Upper Fulmar Formation and the Top Lower Fulmar Formation respectively.

Four main time-strain anomalies are then observed: a strong extension signal at the base of the chalk, a compression signal in shales immediately above the reservoir, various extension signals inside the Pentland, and another compaction signal within the Top Triassic. It should be noted that there is only production in Fulmar formation, and since Lower Fulmar has lower porosity, production is mainly in the upper part of this formation. The localisation of the base chalk anomaly is surprising, which may arise due to a change of mechanical properties or possible fluid effect. The flip polarity of the time-strain in the immediate caprock is also unexpected as these shales usually undergo significant stretching as a consequence of the reservoir compaction. A recent study by Rangel (2016) suggests there might be a pressure diffusion from the underlying Fulmar reservoir into this thin shale layer that is causing this negative time-strain. However, a closer look at the shape of the anomaly (Figure 4.8) shows it is just smearing around the top of the reservoir rather than filling a large area of the shale layer, which may also be caused by time-shift calculation errors.

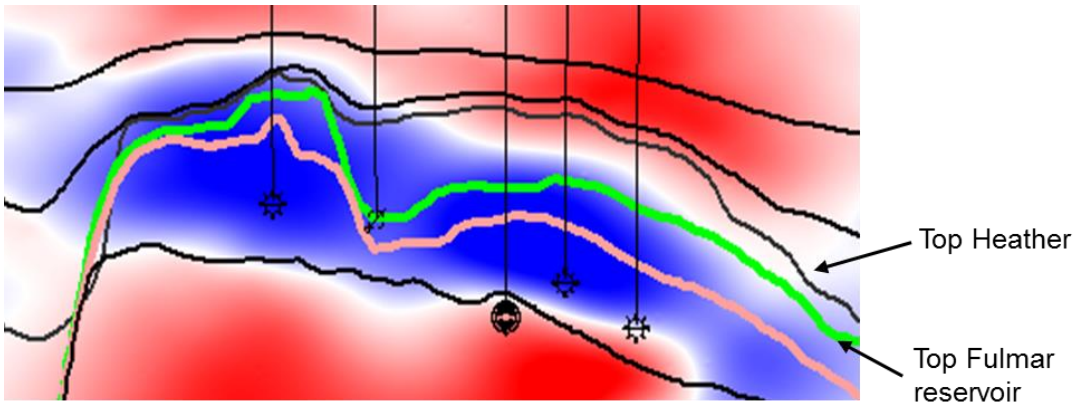

Figure 4.8: A closer look at the negative time-strain anomaly in the overburden shale. This section is extracted from inline veiw, the green horizon is the top Fulmar reservoir.

The two large time-strains in the underburden are more complicated. According to Eq. 2-6, large time-strains are usually related to high physical strains or strong velocity sensitivity to the resultant physical strain (big R factors). Underburden time-strain anomalies could be due to salt movement, residual multiples, ray bending/ ray tracing effects, lateral shifts, or similar active shale issue like the one in Rangel (2016). In the following chapters, I am going to address most of the anomalies by means of geomechanical analysis and rock physics study. More explanations and suggestions will be presented in the last chapter as well.

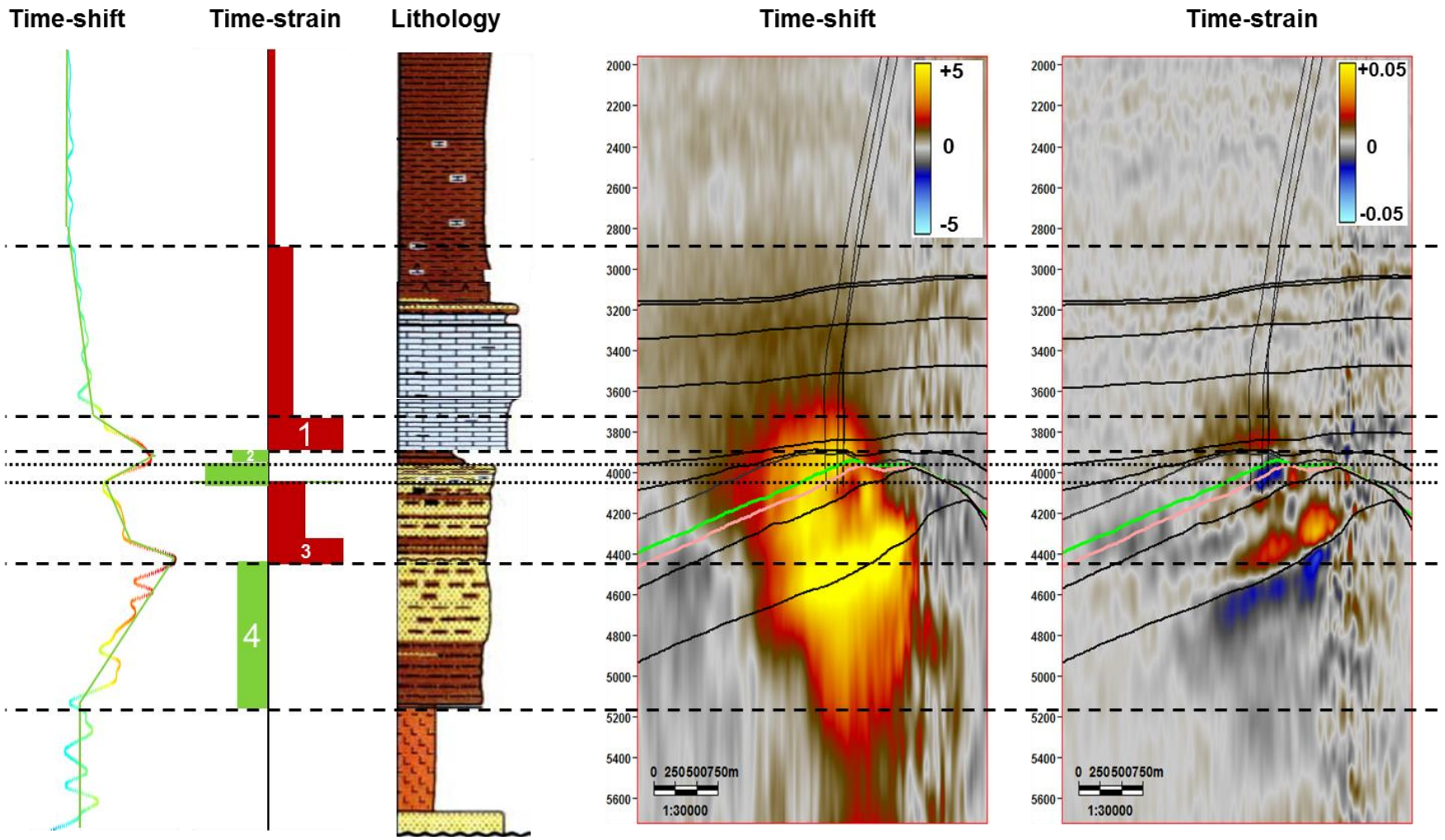

Figure 4.9: Time-shift composite plot – a coarse scale view

4.2.3 Time-shift correction and 4D amplitude analysis

4D amplitude difference (ΔA) between time-lapse seismic surveys are commonly used as a qualitative approach to show saturation and pressure changes, to indicate reservoir connectivity and fluids contact movement. Before, it was calculated by subtracting base from monitor without time-alignment as follow:

$$\Delta A = RMS_{t_2}^{t_1}(Monitor) - RMS_{t_2}^{t_1}(Baseline) \ . \qquad \text{Eq. 4-1}$$

where RMS is the root mean square, and is measured through a window with the top and bottom defined by t_1 and t_2.

This usually works fine with the absence of large time-shifts. However, large travel-time differences are present at seismic reflectors in Shearwater as seen from the measured time-shift profiles (Figure 4.7), therefore they cannot be ignored when generating amplitude difference between base and monitor seismic surveys. Figure 4.10 shows the impact of time-shift by extracting 4D amplitude difference using time-shift corrected seismic data, and compared to the one without time-alignment. Time-shift volume used for time-alignment is the one calculated by NLI method. Most of the highlighted artificial events in Figure 4.10a are removed in Figure 4.10b after time-shift correction, which reflects that existing time-shift will have a significant impact on seismic amplitudes.

Theoretically, after time-shift correction, the 4D amplitude differences should only appear inside the producing reservoir. However as seen in Figure 4.10b, there are still residual changes in the overburden and below the reservoir. As these are not producing intervals, amplitude changes appear in these layers could either be residual artefacts due to inadequate time-shift correction, or real signals due to some unknown changes happening there. As there have been quite a lot of work done on time-shift calculation to increase the confidence in its reliability, the following study will be focused on the latter. Some hypotheses are residual gas in overburden chalk layers, dipping structure and geomechanical effects, which will be discussed in the following chapters.

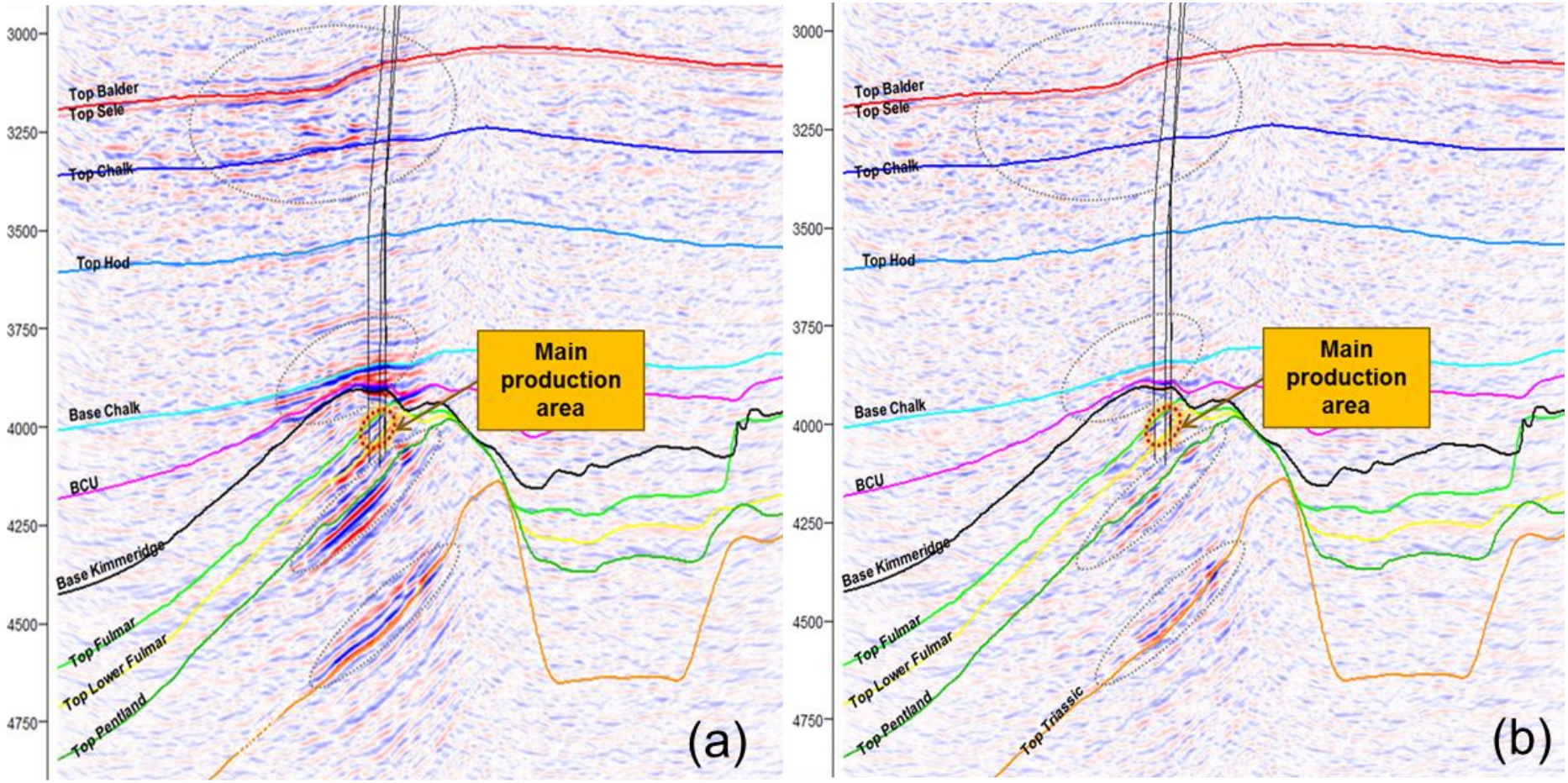

Figure 4.10: Amplitude difference between base and monitor seismic surveys: (a) before and (b) after time-shift correction. Black dashed circles point out the artificial signals caused by time-shifts.

After time-shift correction, the 4D RMS amplitude map is extracted using a 30 ms window around the Top Fulmar

Figure 4.11. It displays a combination of pressure, fluid saturation, and stress-strain induced effects.

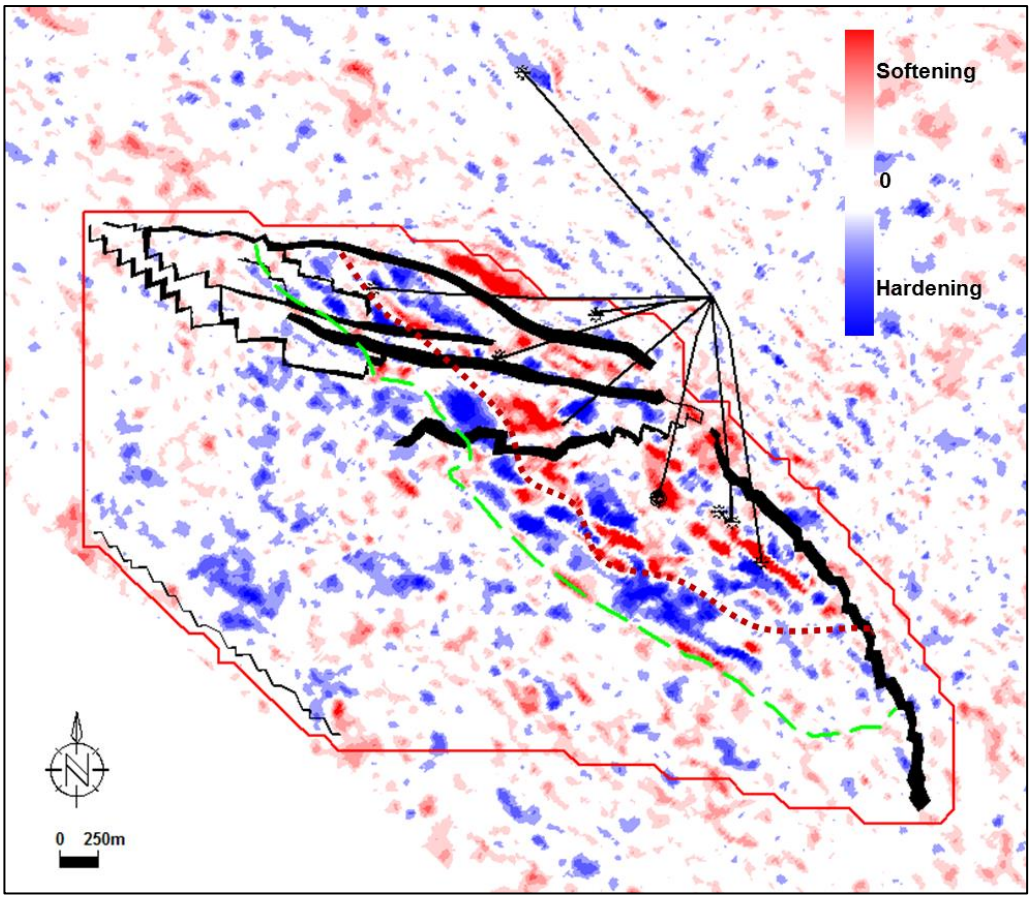

Figure 4.11: 4D RMS amplitude map at reservoir level, the green dashed line is the original gas and water contact, and the red one is the possible new GWC interpreted from this map.

Table 4.2: 4D amplitude changes due to various reservoir changes, and their 4D convention.

Reservoir changes	4D amplitude changes	4D convention
Reservoir compaction	Hardening	↑
Saturation change	Hardening	↑

Table 4.2 summarizes seismic amplitude changes in response to reservoir rock and fluid changes: the saturation changes in the swept zone by water replacing gas increases fluid density and causes hardening; rock frame stiffening due to reservoir compaction also causes hardening and usually is concentrated in the crest area of the structure. This is also used for the interpretation of the GWC movement as displayed in

Figure 4.11 in green and red dashed curves. Although with hardening being the dominant 4D amplitude changes, there are also some softening areas as seen in

Figure 4.11, this might due to the decrease of pore-pressure that reduces the acoustic moduli of gas leg, gas come of solution from condensate liquid, or improper horizon interpretation.

4.2.4 Time-shift variations with offsets

In this study, five sets of offset stacks for seismic vintages of 2001 and 2004 are provided by Shell. The offset ranges used for each set of angle-stacks are 300 - 1100 m, 1200 - 2000 m, 2100 - 2900 m, 3000 - 3800 m, and 3900 - 4700 m respectively, with each set covering an offset range of 800 m. Time-shifts and time-strains measured from them generally display an increase with offset trend (Figure 4.12). Time-shift maps at Top Fulmar (Figure 4.13) show that the increase of time-shift with offset is mainly concentrated in the gas leg around the producing area.

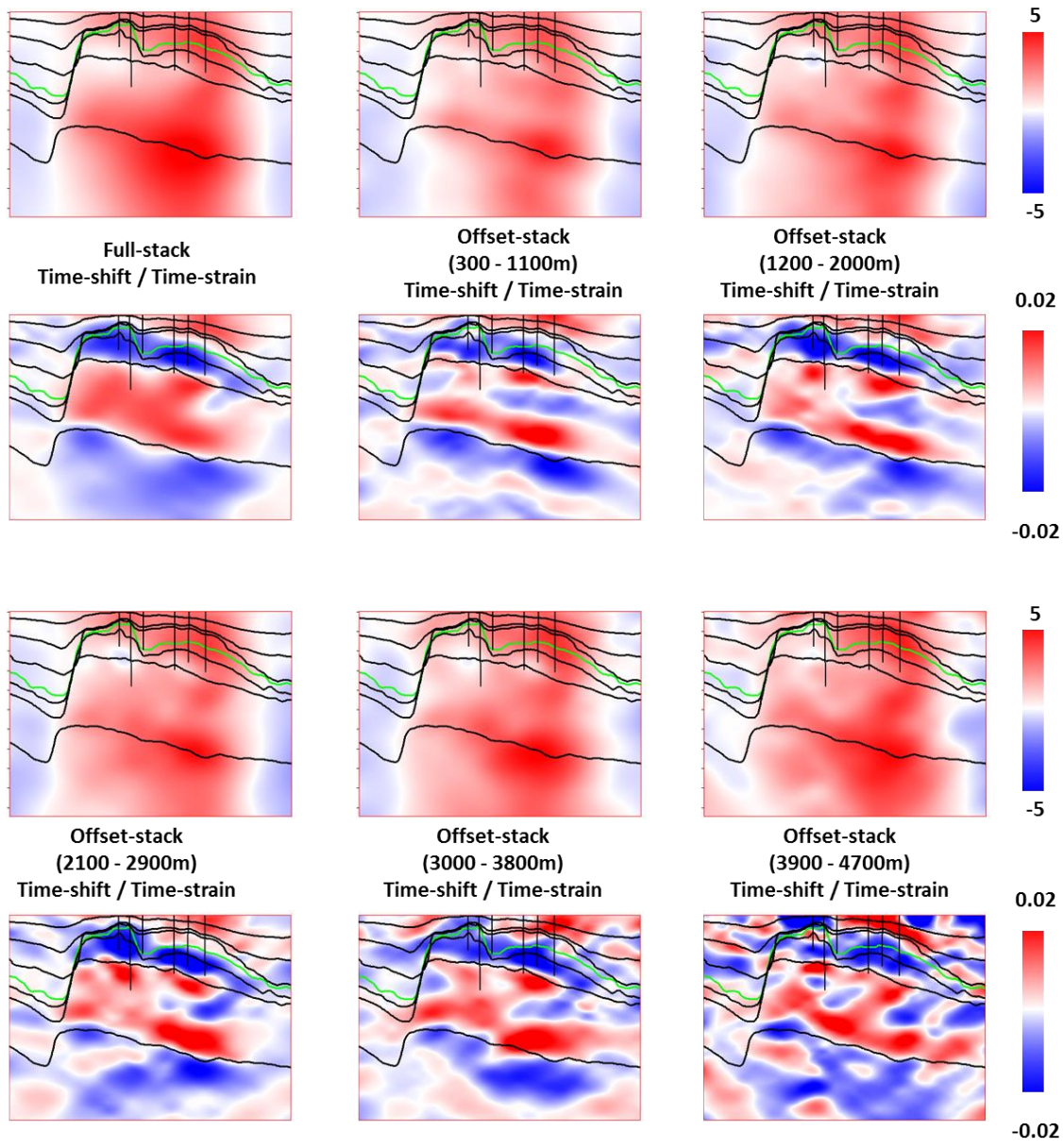

Figure 4.12: Time-shift and time-strain results for full-stack and offset-stack datasets between 2001 and 2004, sections are generated from inline 1489.

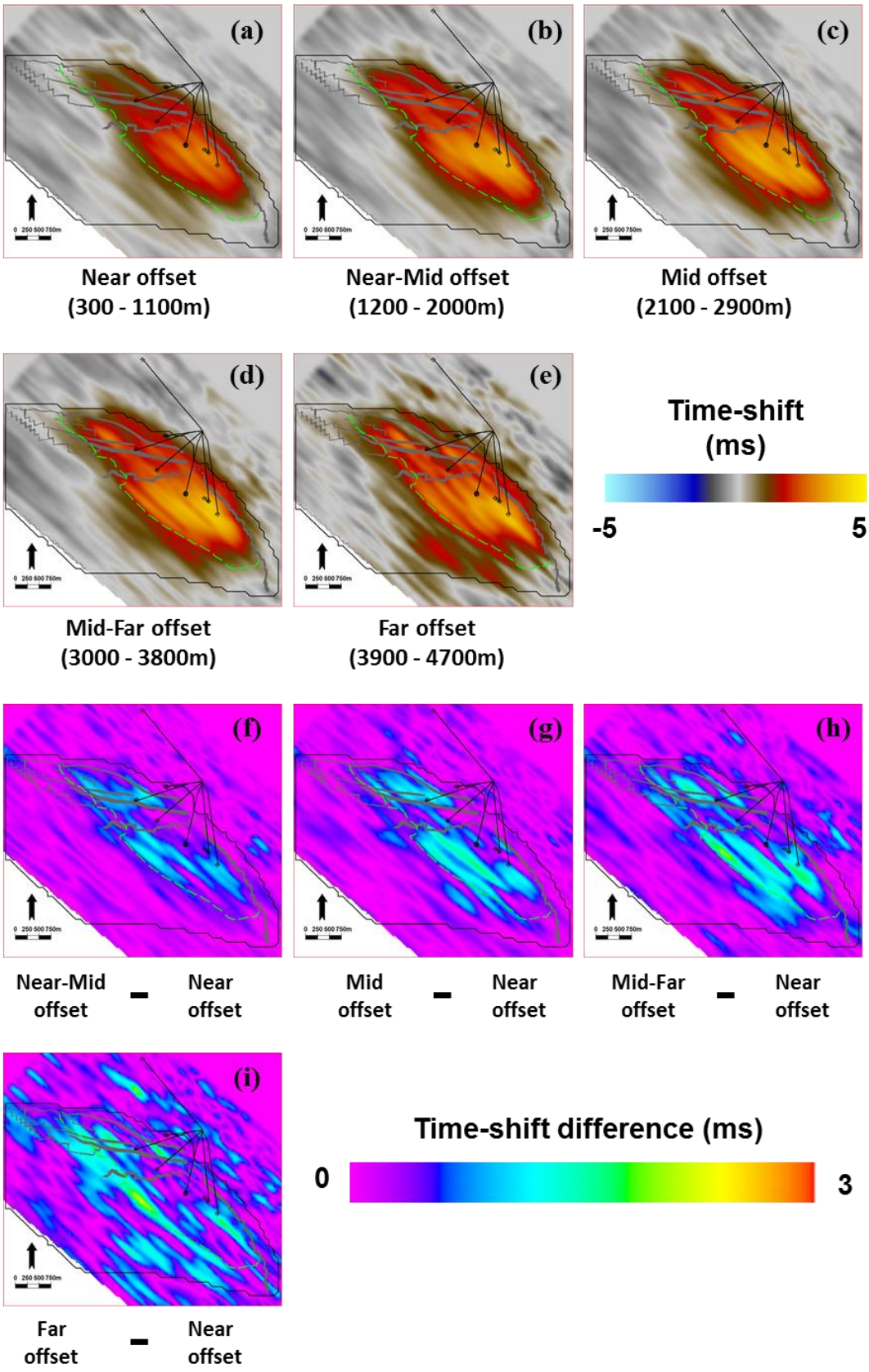

Figure 4.13: (a) to (e) are time-shift maps extracted at Top Fulmar for five different offset ranges. (f) to (i) are time-shift differences between near and far offsets. These display a general increase of time-shift magnitude around the producing area.

The far-offset measurement in Figure 4.13 clearly captures the time-shift signal at the southwestern boundary of the reservoir, while it is not present in neither near-offset nor mid-offset measurements. This phenomenon is explained by sketches in Figure 4.14, due to the arching effect, overburden velocity changes are mainly concentrated above the crest area of the reservoir, therefore, at the boundary of the reservoir only the far-offset ray paths are able to catch information of the overburden changes. Meanwhile, a wide angle also includes more overburden noise into the seismic data, causing the time-shift measurement to be much noisier than the other measurements.

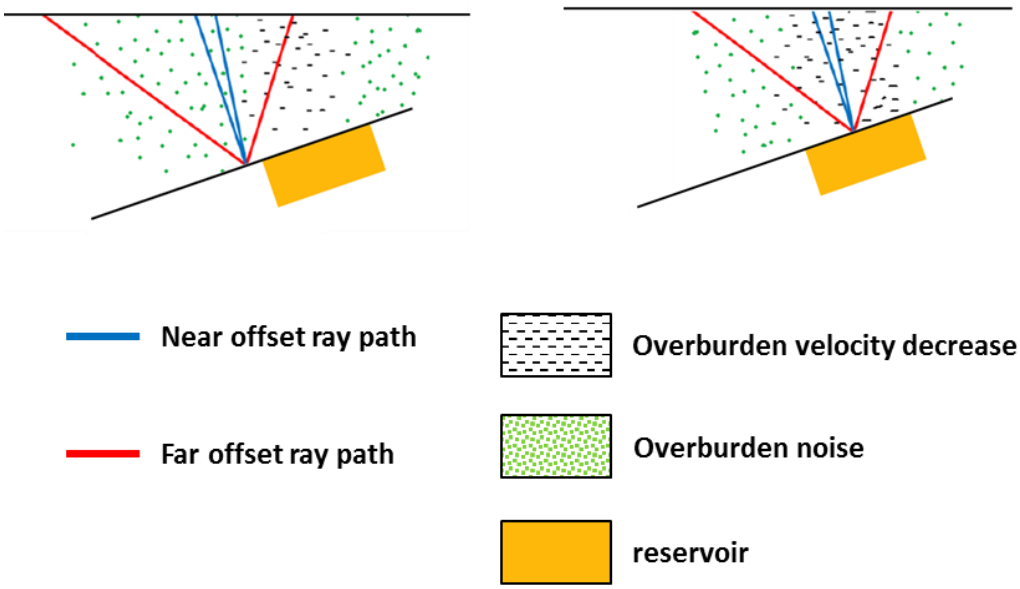

Figure 4.14: Near and far offset ray paths indicating that only the far offset ray paths experience the overburden slowdown at the reservoir boundary (adapted after Guzman (2011).

A study by Landrø and Stammeijer (2004) presents a method to distinguish velocity and thickness changes using different offset time-shifts. In Chapter 5, I will show a study for calculating R factors by combing the R factor equation proposed by Hatchell and Bourne (2005b).

4.3 Time-shift interpretation

After the calculation of different time-lapse time-shifts from full-stack and angle-stack seismic datasets, I am going to interpret these attributes by honouring production and geology information. A synthetic test on the abnormal time-shift behaviour in the Heather shale is also performed in order to show the errors brought in by time-shift calculations.

4.3.1 Interval time-shift versus production

Figure 4.15 displays the interval time-shift changes within the Upper Fulmar formation. Time-shift maps are generated from the difference between the time-shift at the top Lower Fulmar and the time-shift at the top Upper Fulmar. For the period between 2001 and 2002, very limited gas and condensate had been produced as seen in Table 4.3, so the calculated time-shift is as expected to be relatively small (about 1.2 ms). Above 3 ms of time-shift is observed in Figure 4.15a, and mostly distributed around the producing wells. In the southeast part, compaction signals spread into a large area, indicating a very good lateral and vertical reservoir connectivity in that area, which agrees with the study on fluid flow baffles and barriers by Gilham *et al.* (2005). Meanwhile the time-shift distribution shows a partial communication between the central and eastern blocks, which is consistent with the lateral connectivity linked with the boundary fault. Some evidences of this connectivity and isolation of west block are also found in the residual salt and gas composition fingerprint data (Gilham *et al.*, 2005), where the two sources of data are identical in the central and eastern blocks, and differs from the ones in western block (Figure 4.16).

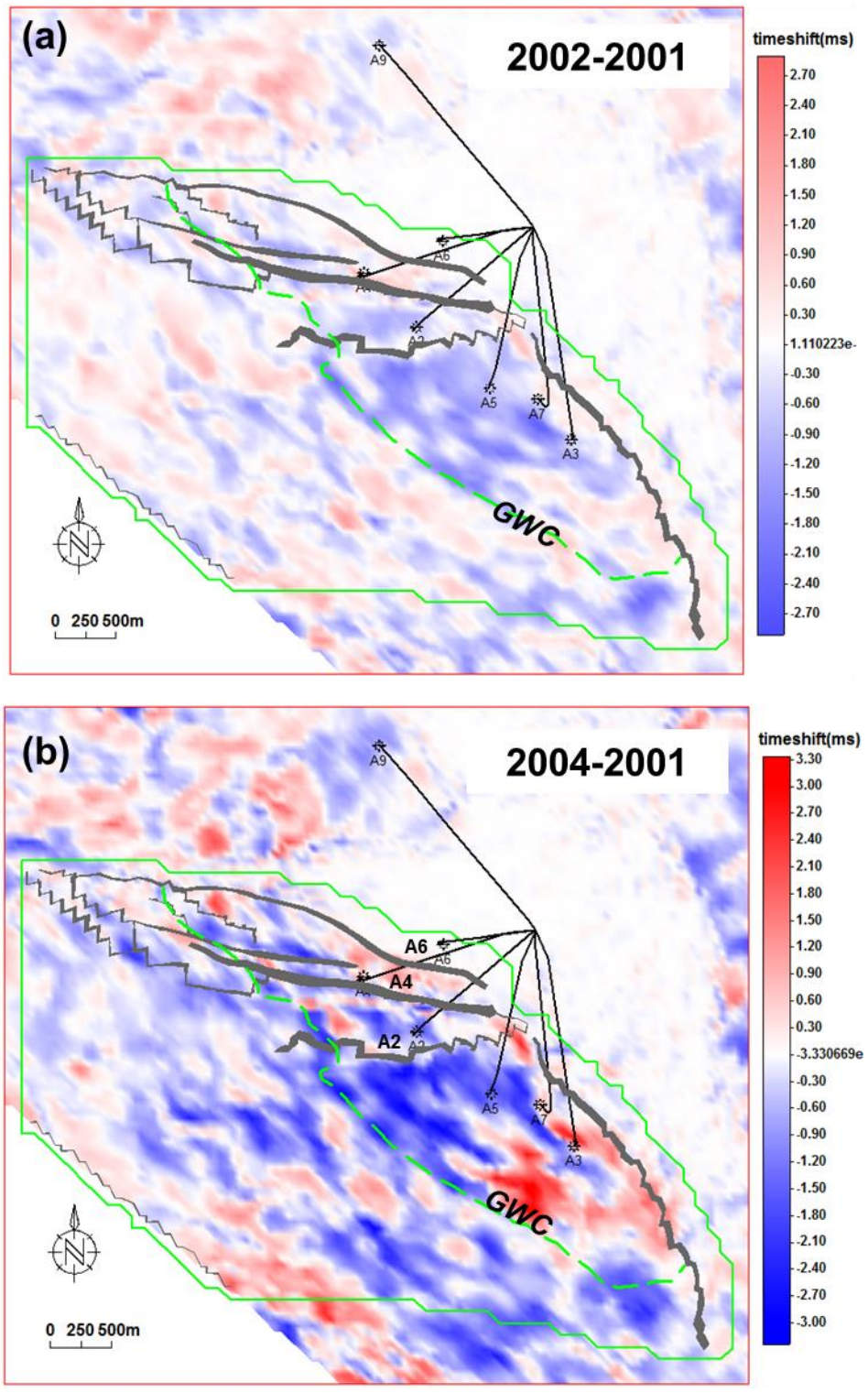

Figure 4.15: Time-shift changes within the Upper Fulmar interval (a) between 2001 and 2002, (b) between 2001 and 2004. Green dashed line represent the gas and water contact. faults are plotted and coloured in grey.

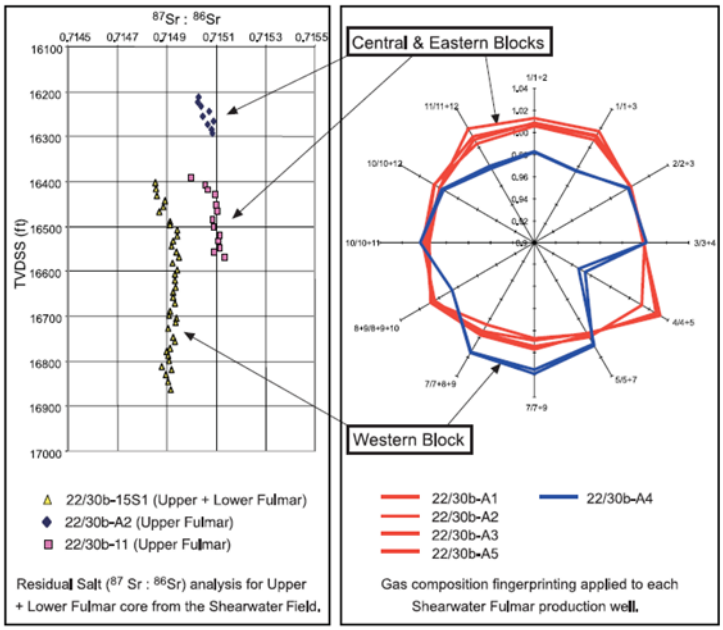

Figure 4.16: Residual salt (87Sr:86Sr) and gas composition fingerprinting data from the Shearwater Fulmar reservoir (Gilham *et al.*, 2005). Both of the two plots show a good lateral connection between central and eastern block, while the western block appears to be isolated.

Table 4.3: Cumulative production volumes of each well for the periods from 2001 to 2002, and from 2001 to 2004. The cumulative production volumes are calculated from surface production rate, and then converted into reservoir condition through material balance.

Well	Produced Fluid Volume (ft^3*10^6)	
	2001 to 2002	2001 to 2004
A2	0	550
A3	0	1190
A4	580	2090
A5	490	1400
A7	10	1000
A9	0	20

Until the time of the second monitor survey in 2004, all of the wells started production with significant volumes produced from A4, A5, and A3 (Table 4.3). Most of the time-shift pattern and magnitude shown in Figure 4.15b are consistent with production. The sand body distributions are illustrated on the sweet spot map (Figure 4.17a), bright yellow in the producing area corresponds to good quality sandbodies. There are quite high

correlations between 4D signals and geology. Extension signals in time-shift map could be related to shale expansion in response to adjacent sandbodies production. The comparison between simulated pressure change (Figure 4.17b) and observed 4D changes are not very consistent in terms of magnitude if we only consider pressure effect. This indicates that additional fluid effect such as gas saturation changes also plays a role in influencing 4D signals, thus it needs to be incorporated into the interpretation.

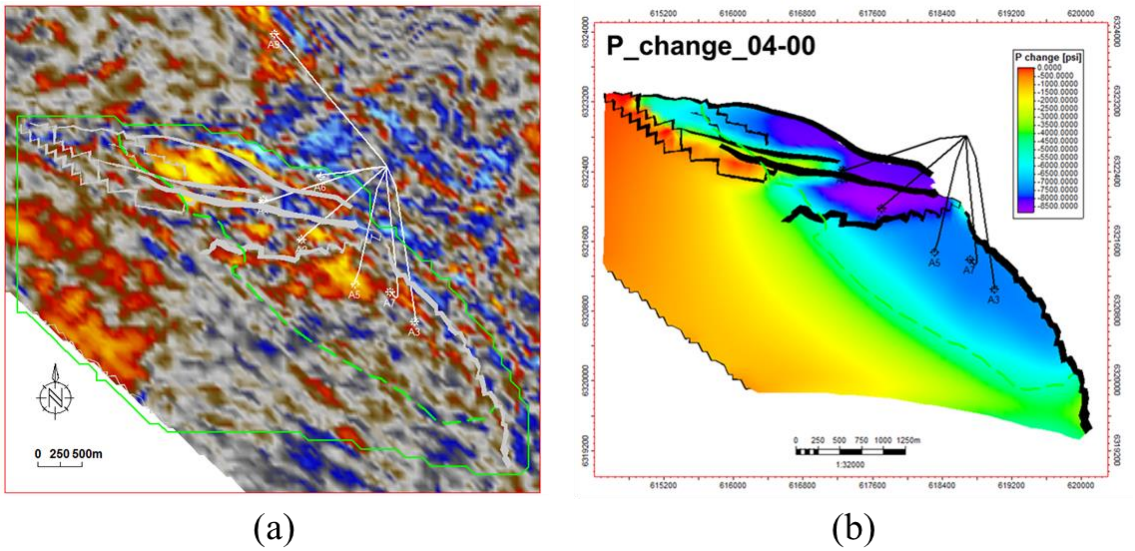

Figure 4.17: (a) Sweet-spot in the sand bodies of Upper Fulmar interval; (b) reservoir pressure change from 2000 until 2004 (map output from simulator)

4.3.2 Synthetic test on time-shift and time-strain calculation

As mentioned earlier in this chapter, an abnormal negative time-strain distribution is observed in the immediate shale layer above reservoir. Rangel (2016) has shown some evidences of the pressure diffusion in the shale layer. Therefore, this is not repeated here, instead, a synthetic test on the calculation error is performed. To prepare for the synthetic baseline and monitor seismic data, a time-strain is modelled incorporating R factors and physical strains output from a geomechanical model before it is integrated for computing the input time-shift. The geomechanical model is simplified to represent similar lithology and structures of the Shearwater case. The resultant time-shift is then applied to the baseline survey to create a synthetic monitor survey. In this case, only time difference exists between two surveys, with no amplitude difference at present. After that, time-shift and time-strain calculation are performed using the same method for calculating the time-shift and time-strain displayed in Figure 4.9.

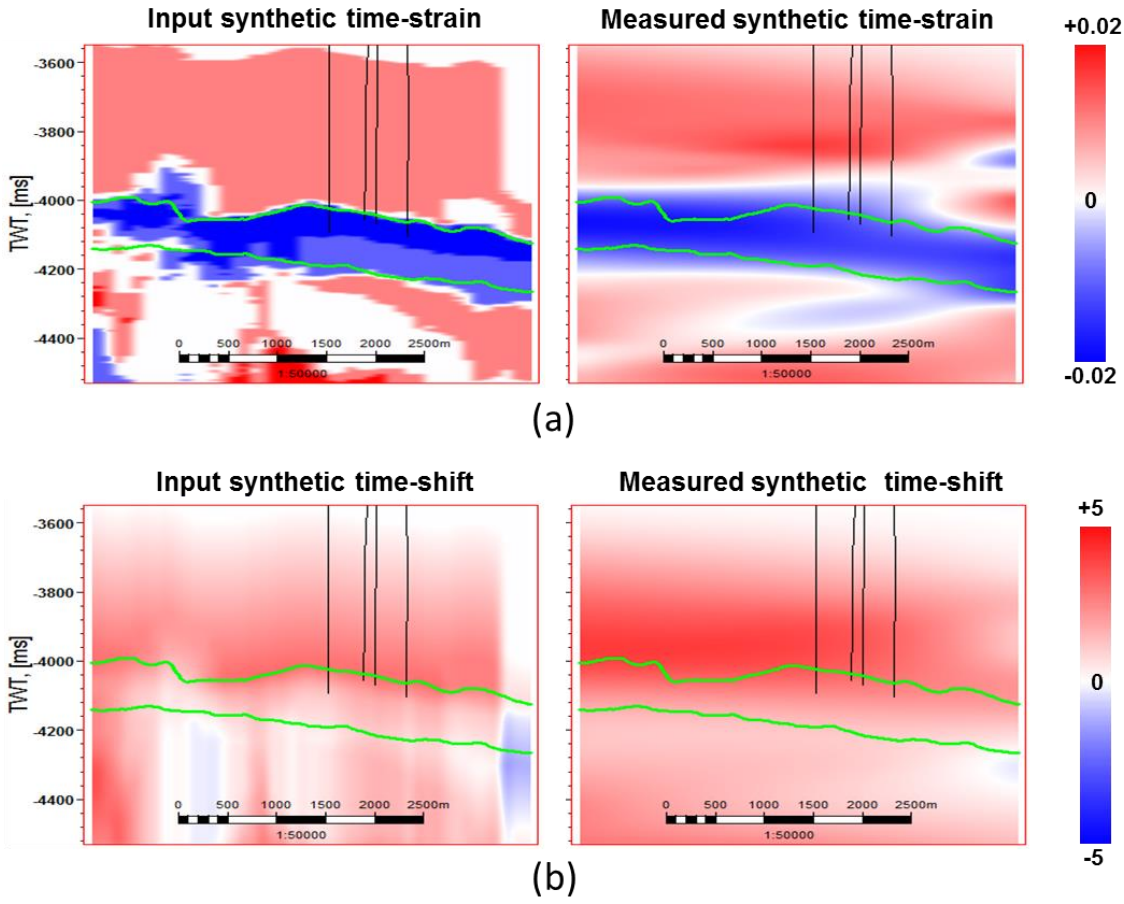

Figure 4.18: Synthetic test on time-shift and time-strain calculation

The comparison results are displayed in Figure 4.18. Smearing of time-strain is also observed in the synthetic result, however, the distribution pattern is not very comparable with the real observation which appears in a good accordance with the top structure of the reservoir. Thus the smearing effect of the calculation algorithm may only reveal half of the truth. Additional effects apart from that should also be considered, such as the pressure diffusion in shales proposed by (Rangel, 2016). Similar work is presented in (Hajnasser, 2012) for Erskine field, where a pore pressure decrease in the Heather shale triggers an increase of effective stress and vertical compressional strain.

4.4 Summary

This chapter has provided a general reservoir characterisation of the Shearwater field. In the first part, various information from literature were walked through to understand the geology background, overpressure, and the production history of the Shearwater field. In the second part, Shearwater 4D seismic data quality and acquisition parameters were

reviewed, followed by time-shift measurements using the three different algorithms discussed in chapter 2. Time-strain was derived from the calculated time-shift volumes, and was used to identify four anomalous zones. It also briefly displayed the effect of time-shift on the calculation of 4D amplitude changes. After that, time-shift variations with offset was explored by comparing the measured time-shifts and time-strains from different offset seismic data. Time-strains calculated from these angle-stack data also provided confirmation of the four anomalies. The final part of this thesis focused on the interpretation of the measured vertical time-shifts from previous part, and linked them with field geology and production information. The abnormal time-strain signal in the Heather shale was modelled to test my doubt on calculation error. This appears to have partially resolved the problem. Deviations from this calculation could be due to other effects such as shale diffusion.

One of the major issues which exists in HPHT fields is the geomechanical effects. For the benefit of Shearwater dynamic reservoir characterisation, I am going to explore the geomechanical problems with the integration of 4D seismic data.

Chapter 5

Linking geomechanics with 4D seismic on Shearwater

This chapter continues the story of dynamic characterisation of the Shearwater field by integrating time-lapse seismic analysis with geomechanical modelling. It aims to understand how best the 4D seismic can be linked with the geomechanics in terms of stress and strain evolution in the subsurface. During the study, it focuses on the construction and calibration of a simplified reservoir geomechanical model with the help of reservoir simulation, geology and rock mechanics studies. Based on that, this study evolves towards a deeper assessment of mechanical failures, and thus the predictions of well stability during drilling and production.

5.1 Introduction to the geomechanical issue

Reservoir production-induced geomechanical issues have been widely observed in different types of hydrocarbon fields across the world. Different reservoirs are experiencing different magnitudes of reservoir compaction, which enhances overburden stretching and subsidence, giving rise to fault re-activation, influencing the integrity of the weak formations and the wells drilled through them. Table 5.1 lists the geomechanical effects observed from three types of reservoirs, together with their production and 4D seismic information.

Table 5.1: Geomechanical characteristics for different types of reservoirs

Field	Reservoir Type	Pressure	4D Seismic	Geomechanical Effects
Shearwater	• HPHT gas condensate (4700-5000 m subsea)	• Initial pore pressure at 106 MPa • 58 MPa depletion after 3 years production	• Time-shift 5 ms 2001-2004 • Time-strain up to 0.02	• Reservoir compaction • Seabed subsidence • Well shear failure
Ekofisk	• Fractured Chalk (2900-3300 m subsea, 300 m thick)	• Initial above bubble point 38 MPa • Depletion + water injection	• Time-shift 10-20 ms between 1989 to 1999 • 1.5 ms time-shift for LOFS	• Significant seabed subsidence • Reservoir compaction due to production and injection • Water weakening • Fault reactivation, fracture of seal, gas clouds in overburden • Permeability reduction
Genesis	• Deepwater turbidite (unconsolidated)	• Initial pore pressure at 55-60 MPa • Bubble point at 40 MPa • 20-30 MPa depletion after 3 years production	• Time-shift up to 10 ms at the top of producing interval • Time-strain up to 0.025 within 0.5 s region above top reservoir, no further extension	• Significant production-related reservoir compaction • Overburden subsidence and dilation • 80%-95% permeability loss • 4 wells lost due to compaction-related shear failure • Loss of sand control in completed interval

It is found that geomechanical effects in these fields are all accompanied with large time-shifts. The examples in Figure 5.1 show good correlations in the locations where large time-shift and intense well failure events have been observed, suggesting that reservoir compaction contributed significantly to their failure (Hudson *et al.*, 2006).

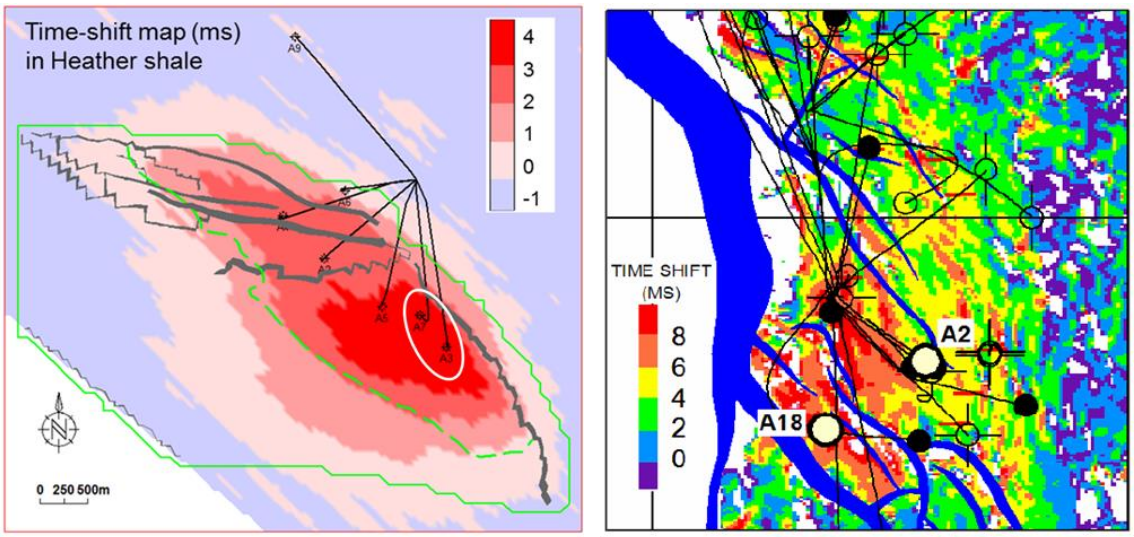

Figure 5.1: Time-shift maps (top) in the Heather shale formation of the Shearwater field, and (bottom) at the top of the N1 Sand of the Genesis field (Hudson *et al.*, 2006). In both fields, locations of failed wells (A3, A7 in Shearwater, and A2, A8 in Genesis) correspond very well to areas with high time-shifts, suggesting that reservoir compaction contributed significantly to their failure.

In Shearwater, the majority of the previously producing wells have failed due to shale influx (Figure 5.2). These shale influx events are linked with large geomechanical deformations such as fault reactivation or interface slip, according to the simultaneous well failures and the size of debris produced from there. It would be useful if these weak areas could be recognized in the seismic profile before failures were initiated; however they are usually of a sub-seismic scale that could not be visualized directly from seismic data. Since significant volumes of gas condensate still remain in place, new wells are being planned to access these volumes, either by side-tracking existing damaged wells or by drilling infill wells. Therefore, a better characterisation of the field (especially where the failure happened previously) is essential for future field development. The time-shift examples shown in Figure 5.1 seem to be quite useful, as they can image the stress concentrations and directly indicate the well failure zones. However, this only works after the problem happens. A good forecast is of more importance for future well deployment (such as well trajectories, casing and mud weight selections), and this could be gained from a well construct and calibrated geomechanical model.

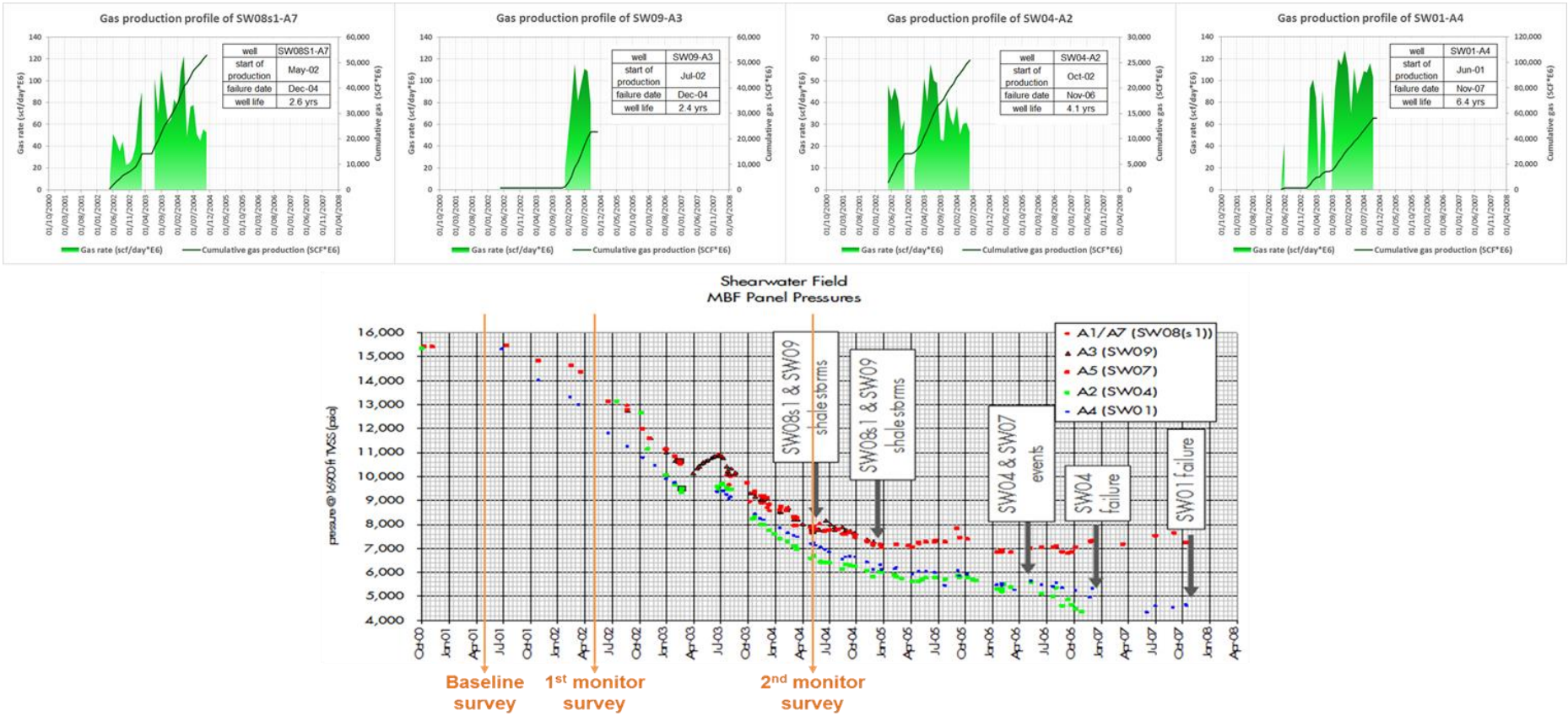

Figure 5.2: Well production and pressure profiles along with seismic timing and well failure events and timing

So far, many finite element techniques and software (e.g. VISAGE, ANSYS, DIANA, GEOSIM, SAFEM, and ABAQUS) have been developed to gain quantitative insights into the development of stress and strain fields inside and outside of reservoirs, in response to the hydrocarbon production activities. In this study, the software 'Petrel Reservoir Geomechanical modeller' (also named as VISAGE) is used for the construction and simulation of the Shearwater geomechanical model. As displayed in Figure 5.3, the entire workflow of the Shearwater geomechanical study contains four main stages. The first stage requires various inputs for the construction of the geomechanical model, such as the geomechanical grid, mechanical properties, distributions of pressure, saturation and temperature, boundary conditions and an optional discontinuity model. In the second stage, the geomechanical simulation is run to model for the stress and strain changes in response to reservoir production. The resulting vertical strain (ε_{zz}) is then converted into time-strain by multiplying with different R factors for each layer. The third stage is the geomechanical model calibration step, where the time-strain predicted from the geomechanical model in previous stage is compared with the real one derived from the observed time-lapse time-shift. Other information from field measurements and observations, such as the platform subsidence, and reservoir compaction, are also used for the model calibration. If there are mismatches detected, it will go back to the first stage and start the geomechanical modelling again. Finally, in the last stage, the calibrated geomechanical model is put forward to model the evolution of stress and strain in the future production and optimization period, and therefore help to forecast the stability of wellbores during and after drilling, predict the potential deformation inside and outside of the reservoir, and provide advice on the drilling window and blowout risk. Next, I will explain the work of each stage in more detail.

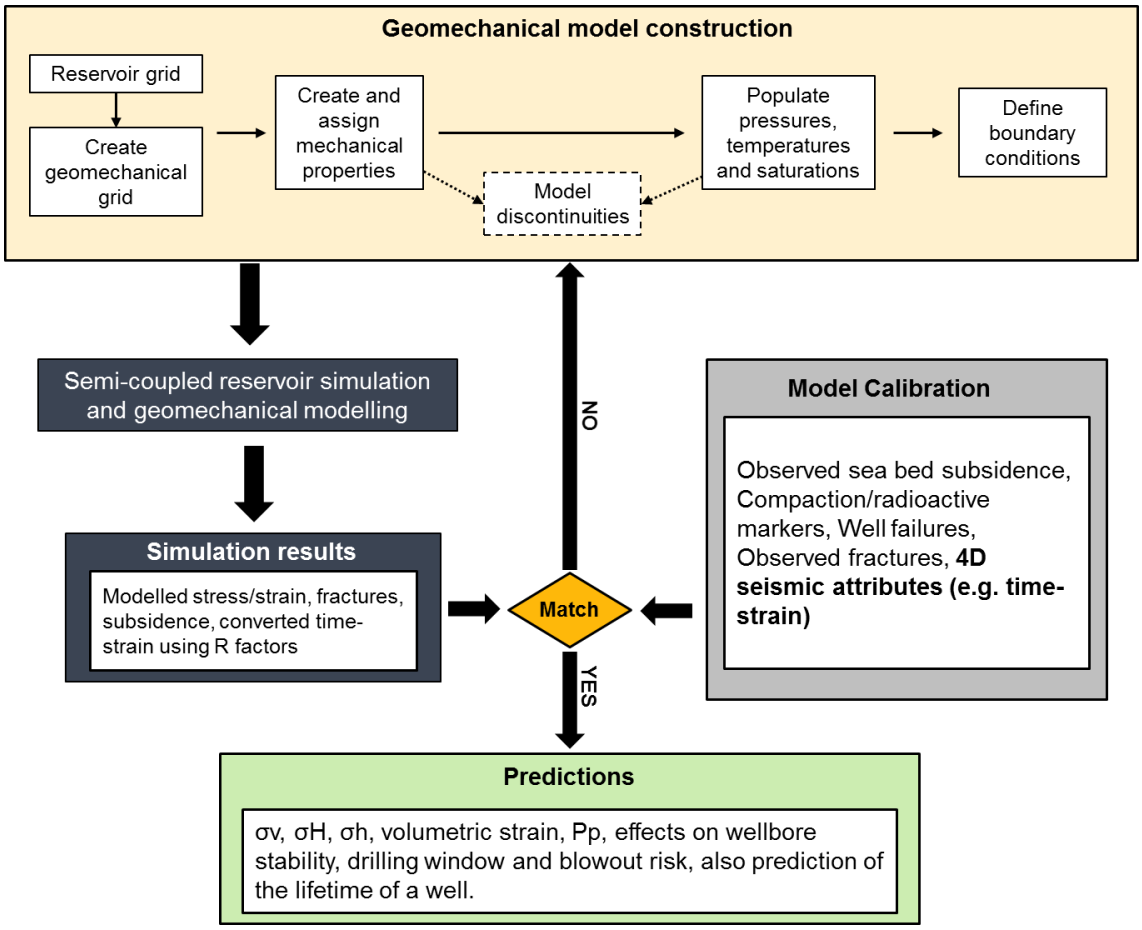

Figure 5.3: The workflow of Shearwater geomechanical modelling, calibration and application by linking these with 4D seismic. The calculated time-lapse time-strains are compared with those simulated from the geomechanical modelling.

5.2 Constructing the Shearwater geomechanical model

5.2.1 Geomechanical model grid

The reservoir grid required for constructing the geomechanical model is taken from the simulation results provided by Shell. It contains the upper and lower Fulmar and is subdivided into 13 layers based on the geology. The reservoir grid is then embedded in all directions, both laterally and vertically, to create the new geomechanical model. As the requirement of the reservoir geomechanics module of Petrel, this reservoir grid has to be simplified to avoid bad cells during the embedding process. Above the reservoir, 6 overburden layers were added, along with a water column, extending the model upwards to the sea level. Below the reservoir, 4 layers were added to serve as the under-burden and extend it downwards to 25500ft depth. Laterally in each direction, 9 grid cells with sizes increasing by a factor of 1.5 were added as sideburdens, in order to minimize the

effect of the numerical dispersion associated with the numerical simulation. The final geomechanical model grid of the Shearwater field as displayed in Figure 5.4 contains 73x56x24 grid cells in total.

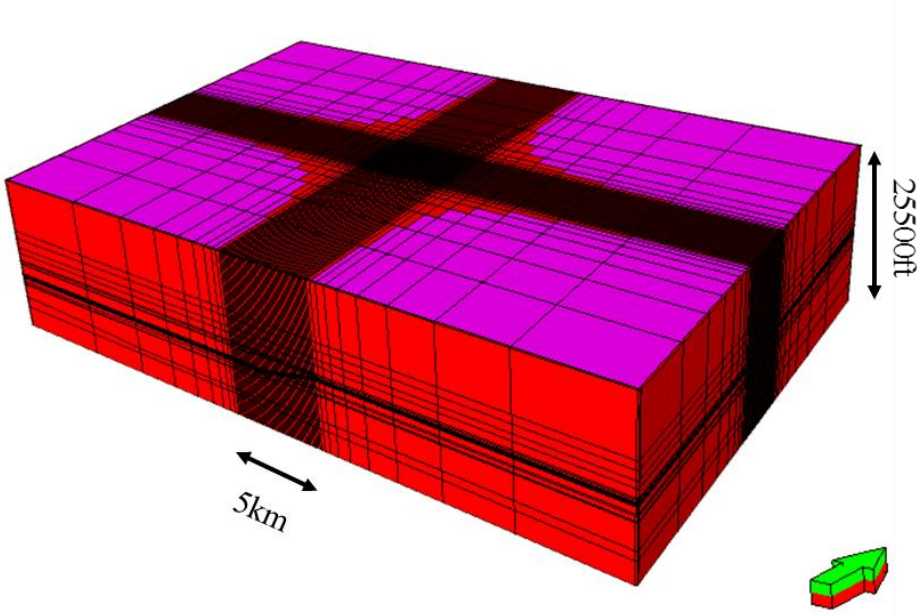

Figure 5.4: The geomechanical grid of the Shearwater field. The model has 73x56x24 grid cells.

5.2.2 Material modelling

The second step is material modelling, where a material library is created for populating mechanical properties into each layer, according to the main lithology. The mechanical behaviour of each lithology is considered to be elastic, isotropic, and homogeneous.

Theoretically, the rock mechanical properties required here should be static moduli, which are usually derived from laboratory rock mechanical tests. These differ from the dynamic moduli which are calculated from the elastic wave properties (e.g. velocity, density, and porosity) from well logs or seismic waves based on empirical or experimental correlations. The truth is that the static and dynamic moduli of the same rock could differ considerably, especially for the weak rock (Zimmer, 2003). The main reasons for that are likely to be the differences in strain amplitude and the heterogeneous nature of the rock microstructure (Fjaer *et al.*, 2008; Hodgson, 2009). The strain amplitudes for seismic waves are of the order of 10^{-6} to 10^{-7}, while in a rock mechanical test they are typically 10^{-2} to 10^{-3} (Fjaer *et al.*, 2008). The relation between the two varies a great deal for different cases, and, so far, there have not been very clear scaling factors between them.

In this study, due to the shortage of information from rock mechanical tests, a combination of static and dynamic moduli and values from the literature are used, which may introduce uncertainties to the modeling results.

There have been many studies working on generating empirical correlations between mechanical properties (e.g. the Young's modulus and the Poisson's ratio) and well-log measurements. Table 5.2 lists the correlations used in this study to determine the lower and upper bounds of the mechanical properties. Together with published values for this field and adjacent HPHT fields (Staples *et al.*, 2007a; De Gennaro *et al.*, 2010; Hajnasser, 2012), a table of material properties was generated as shown in Table 5.3.

Table 5.2: Correlations of mechanical properties from the literature, where E is the Young's modulus, in GPa, ν is the Poisson's ratio, G is the shear modulus, in GPa, ∅ is porosity, in %, and Δtp is the P-wave interval transit time, in μs/ft.

Lithology	Correlations	reference
Sandstone	$E = 48.09 - 1.0185\phi$	Edlmann (2001)
	$\upsilon = 0.0923 + 0.0032\phi$	
Shale	$E = 0.076*(304.8/\Delta t_p)^{3.23}$	Horsrud (2001)
	$G = 0.03*(304.8/\Delta t_p)^{3.30}$	
	$\upsilon = E/2G - 1$	
Chalk	$E = 0.0225e^{-11.2\phi}$	Fjaer et al. (2008)

Table 5.3: Mechanical properties and layering in the Shearwater geomechanical BASE model

Layer No.	Formation	Young's Modulus (GPa)			Poisson's Ratio			Bulk Density (g/cm	Porosity
		Low	High	Figure 5.6	Low	High	Figure 5.6		
1	Nordland and Hordland Group	2	7	5	0.25	0.33	0.31	2.05	0.3
3	Tor chalk	26.4	53.3	40	0.25	0.33	0.31	2.636	0.1
4	Hod chalk	11.5	42.6	35	0.25	0.33	0.31	2.583	0.15
5	Chalk and Marl - base Creta	3	35	30	0.25	0.33	0.31	2.535	0.12
6	Organic Claystone and Marl	3	12	8	0.25	0.33	0.31	2.506	0.2
7 to 13	Sandstone - Upper Fulmar - Reservoir	4.3	8	6	0.15	0.2	0.16	2.147	0.26
14 to 19	Sandstone - Lower Fulmar - Reservoir	15	16	15	0.2	0.25	0.22	2.355	0.18
20	Lower Heather shale	2	18	10	0.25	0.33	0.3	2.5	0.1
21	Pentland	18.9	37	30	0.1	0.2	0.1	2.4	0.1
22	Triassic	20	36	28	0.25	0.33	0.3	2.4	0.1
23	Salt	25.3	36.5	26	0.25	0.25	0.25	1.09	0

5.2.3 Defining the pore pressure and the boundary condition

In a typical geomechanical analysis, various effective stresses are used as the main parameters to study subsurface deformations. The effective stress is calculated by subtracting pore pressure from the total stress (Eq. 5-1).

$$\sigma_{eff} = \sigma - \alpha P_P \quad , \qquad \text{Eq. 5-1}$$

where σ is total stress, Pp is pore pressure, α is stress-sensitivity coefficient, and σ_{eff} is effective stress.

In this geomechanical model, the pore pressure results from the reservoir simulation model at the time steps of 2001, 2004 and 2013 are coupled to estimate the evolution of the effective stresses as they diverge from the initial status.

Before initiating the geomechanical simulation, a boundary condition needs to be well-defined, and in this case the simplest stress initialisation is used. Wellbore data collected from CNS fields have indicated vertical stress as the maximum principal stress (Kwakwa *et al.*, 1991); hence the CNS generally displays a normal faulting stress regime, where $\sigma_V > \sigma_H > \sigma_h$, or $\sigma_V > \sigma_H \approx \sigma_h$. However, in the overpressure area of CNS, due to the coupling of pore pressure and horizontal stresses, the minimum and maximum horizontal stresses approach the magnitude of the vertical stress, and the state of stress tends towards isotropic (Hillis and Nelson, 2005). A number of measurements have been undertaken to generate the world stress map, as shown in

Figure 5.5, from which the direction of maximum horizontal stress in this field is measured at NW50° from the map and the vertical stress inclination is set to 90°.

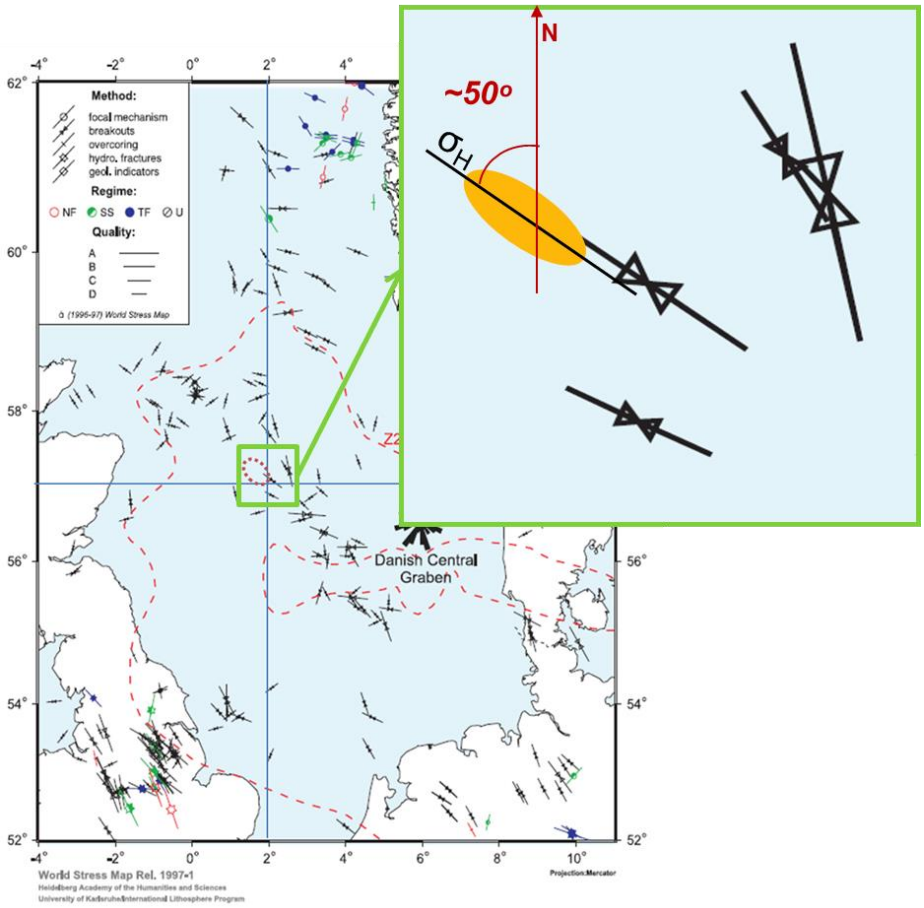

Figure 5.5: The direction of the in-situ maximum horizontal stress (σ_H) at the Shearwater field location from the World Stress Map. The World Stress Map data come from Reinecker et al. (2003).

5.3 Model calibration and update

To increase the accuracy of the stress and strain predictions simulated from the constructed geomechanical model, a comprehensive calibration has to be done by comparing the simulation results with the field observations and measurements, such as measured seabed subsidence or platform subsidence, reservoir compaction observed from radioactive markers, observed well-failure events, time-lapse time-shifts, and so on. In the absence of sufficient subsidence and compaction measurements, the main calibration is conducted by comparing the modelled time-strains from the reservoir geomechanical model with the ones measured from 4D seismic data.

5.3.1 4D seismic calibration

Based on the knowledge learned from Chapter 2, the modelled vertical strain changes from the reservoir geomechanical model for the same period as the 4D seismic vintages can be converted into time-strains via a set of R factors for different formations. The R factors used in this step were taken from the relevant literature in this area (Table 5.4).

Table 5.4: R factors for each formation in BASE case, from published literature (Hatchell and Bourne, 2005b, 2005a; Staples *et al*., 2007b; Angelov, 2009)

Layer No.	Formation	R factors
1	Overburden	5
2	Sele	5
3	Tor	5
4	Hod	20
5	CromerKnoll	5
6	Kimmeridge	5
7-13	Upper Fulmar	2
14-19	Lower Fulmar	2
20	Heather	5
21	Pentland	20
22	Triassic	5
23	Salt	5

By plotting the measured (left) and modelled (right) time-strain profiles using the same colour scale, as shown in Figure 5.6, mismatches are visualized. Apart from the possible depletion signal or measurement error in the Heather shale, which I discussed in Chapter 4, the large time-strain at the base of the overburden Hod chalk, it can be seen that the large extension and depth-varying signals inside the Pentland underburden, and the significant compression signal in Triassic need further matching.

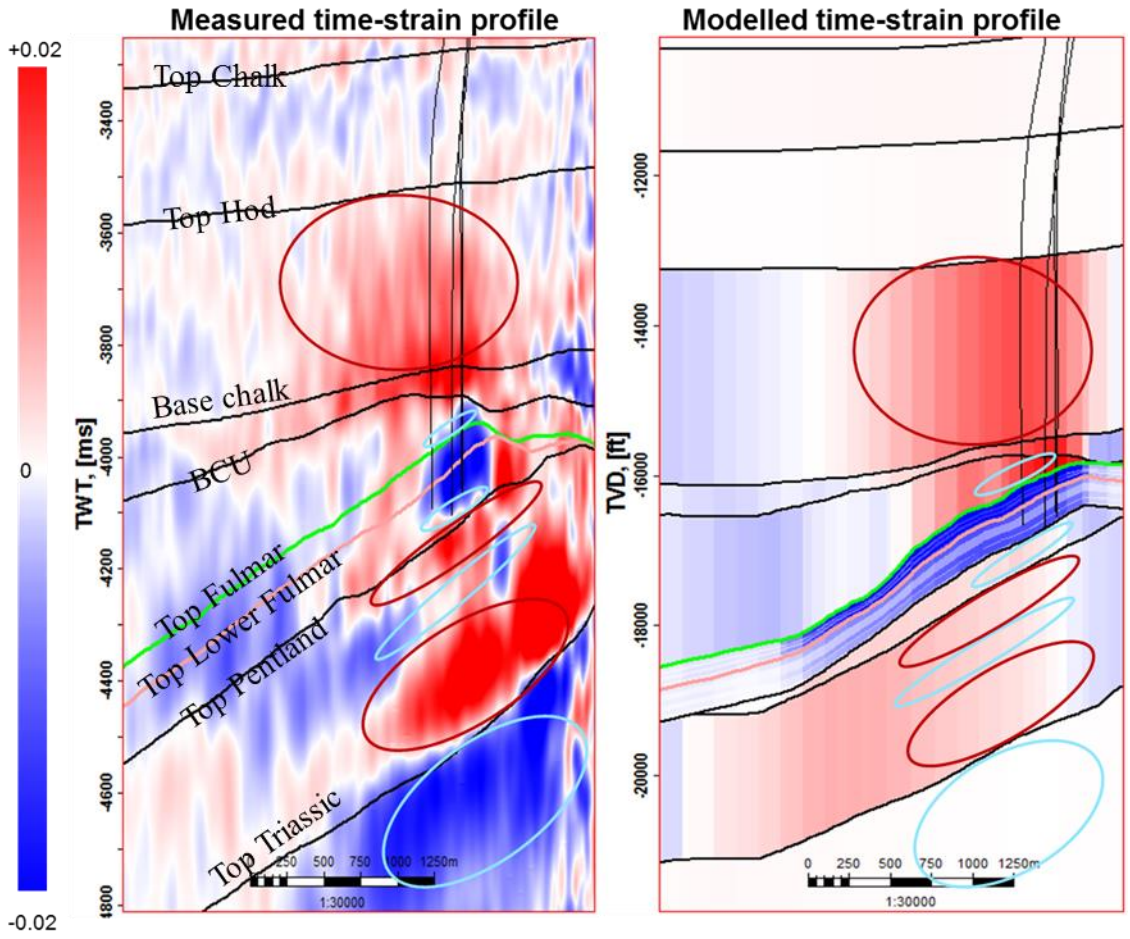

Figure 5.6: A comparison between measured and modelled time-strain profiles. Red circles point out mismatches for extension signals, and blue circles for compression signals. The strong blue signal between green and black horizons is due to pressure depletion during well production.

Comparison of the maps reveals the limitations of the geomechanical model in identifying the lateral variations (Figure 5.7). Good matches have been achieved for overburden formations, as they are widely distributed and have fewer lateral variations in lithology. However, the model failed to match the Fulmar reservoir signals, as the facies varied laterally. Homogeneous properties are populated for each formation; however, the lateral variation is only captured in pressure distribution. However, from the sensitivity study (presented in Appendix A), it was found that the mechanical properties also play a key role in affecting the simulation results, therefore spatially varying properties need to be implemented, which unfortunately cannot be accomplished in current the Petrel reservoir geomechanics simulator.

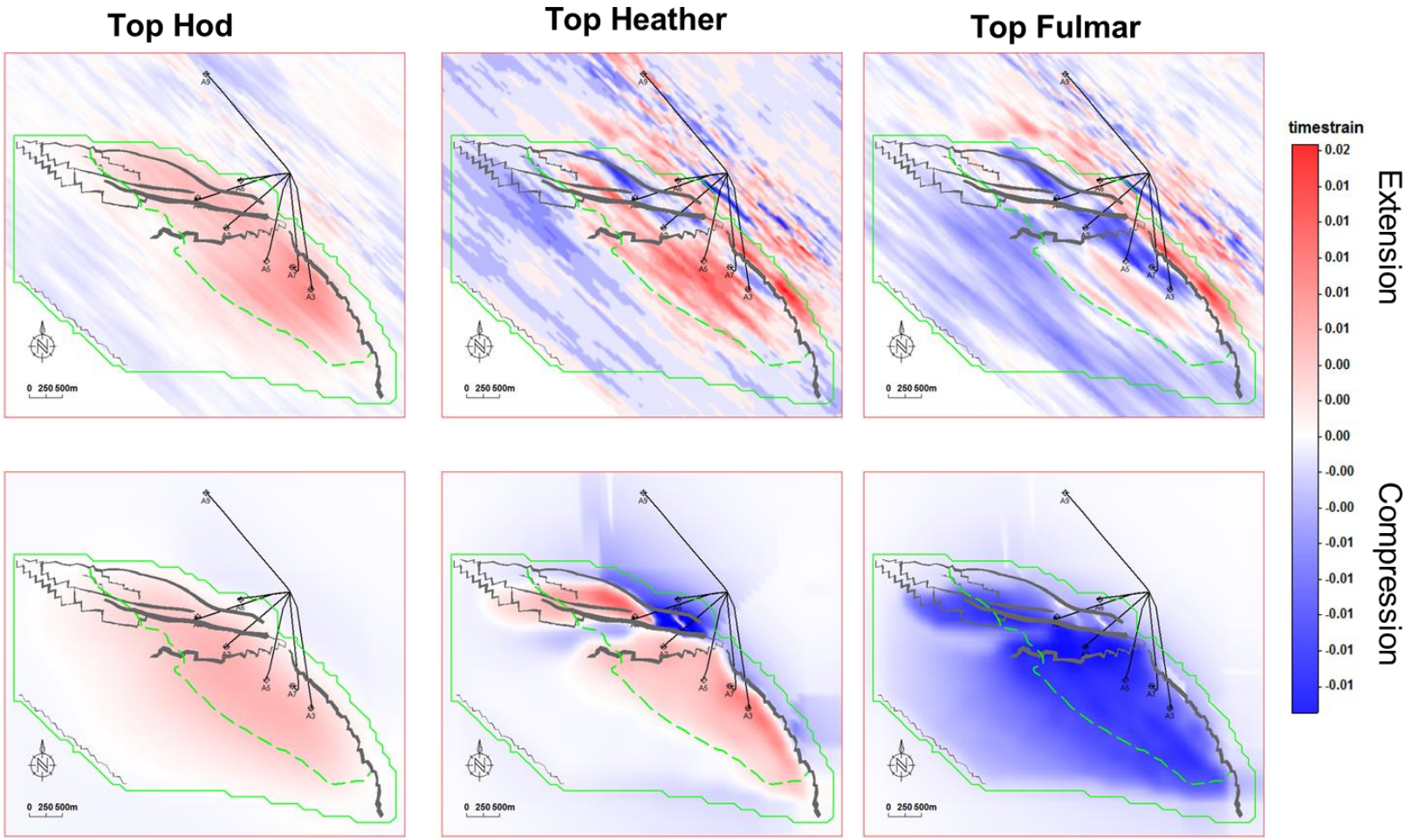

Figure 5.7: Map comparisons for measured (top) and modelled (bottom) time-strains at the Top Hod, Top Heather, and Top Fulmar.

5.3.2 Updating the geomechanical model using geological information

The base model was then updated from a geological perspective, aiming to remove the mismatches identified in the Hod, Pentland, and Triassic formations. A detailed study on the time-shift and time-strain profiles within the overburden Hod will be presented in Chapter 6. The significant mismatch in the lower part of the chalk interval is believed to be induced by the over-pressured gas-bearing stiff chalk in the Hod Geohazard zone. Therefore, a layer with stiffer mechanical properties was added to model this effect.

Due to the huge depth of the Pentland and the Triassic formations in this field area, only one exploration well was drilled into the Pentland, while none of the Shearwater wells has reached the underlying Triassic. The Pentland formation comprises an 1800ft thick sequence of variably stacked fluvial sand channels, crevasse splay and overbank shales and coals. According to the Gamma-ray readings and analogues from adjacent fields, this formation is subdivided into 3 units; the mechanical properties of the top and lower units have been weakened due to the large volume of gas retained within them.

The whole Triassic formation has not yet been penetrated in this field. However, based on its regional distribution, it can be correlated with fields like the Marnock, Heron, and Egret (McKIE and Audretsch, 2005; Erratt *et al.*, 2010). In general, from bottom to top, this formation is comprised of Smith Bank non-marine shales, silty sandstone succession, and continental Skagerrak sandstones. In this case, the strong geomechanical properties assigned to this formation in the base case should not be changed. However, the stresses in this formation are believed to have been distorted due to the Zechstein salt underpinning it.

The layering and mechanical properties, as well as the R factors were then updated, as shown in Table 5.5 and 5.6. The modelled time-strain profile from the updated reservoir geomechanical model finally displays a better match in the Hod and Pentland formations, as can be seen in Figure 5.8.

Table 5.5: Mechanical properties and layering in the geologically updated Shearwater geomechanical model

Layer No.	Formation	Young's Modulus (GPa)			Poisson's Ratio			Bulk Density (g/cm^3)	Porosity
		Low	High	Figure 5.8	Low	High	Figure 5.8		
1 to 4	Nordland and Hordland Group	2	7	5	0.25	0.33	0.31	2.05	0.3
5	Paleocene Claystone/ sele	3	22.7	5	0.25	0.33	0.31	2.385	0.3
6	Tor chalk	26.4	53.3	40	0.25	0.33	0.31	2.636	0.1
7	Hod chalk	11.5	42.6	35	0.25	0.33	0.31	2.583	0.15
8	Hod Geohazard	32.5	46.6	40	0.25	0.35	0.32	2.53	0.1
9	Chalk and Marl - base Creta	3	35	30	0.25	0.33	0.31	2.535	0.12
10	Organic Claystone and Marl	3	12	8	0.25	0.33	0.31	2.506	0.2
11 to 17	Sandstone - Upper Fulmar - Reservoir	4.3	8	6	0.15	0.2	0.16	2.147	0.26
18 to 23	Sandstone - Lower Fulmar - Reservoir	15	16	15	0.2	0.25	0.22	2.355	0.18
24	Lower Heather shale	2	18	10	0.25	0.33	0.3	2.5	0.1
25	Upper Pentland	18.9	37	30	0.1	0.2	0.1	2.4	0.1
26	Mid Pentland	20	36	25	0.15	0.25	0.2	2.4	0.1
27	Lower Pentland	15.5	30	28	0.15	0.25	0.2	2.45	0.1
28	Triassic	20	36	28	0.25	0.33	0.3	2.4	0.1
29	Salt	25.3	36.5	26	0.25	0.25	0.25	1.09	0

Table 5.6: R factors used in the updated case (Hatchell and Bourne, 2005b, 2005a; Staples *et al.*, 2007b; Angelov, 2009)

Layer No.	Formation	R factors
1-4	Overburden	5
5	Sele	5
6	Tor	5
7	Hod	20
8	Hod Geohazard	20
9	CromerKnoll	5
10	Kimmeridge	5
11-17	Upper Fulmar	2
18-23	Lower Fulmar	2
24	Heather	5
25	Upper Pentland	30
26	Mid Pentland	15
27	Lower Pentland	30
22	Triassic	5
23	Salt	5

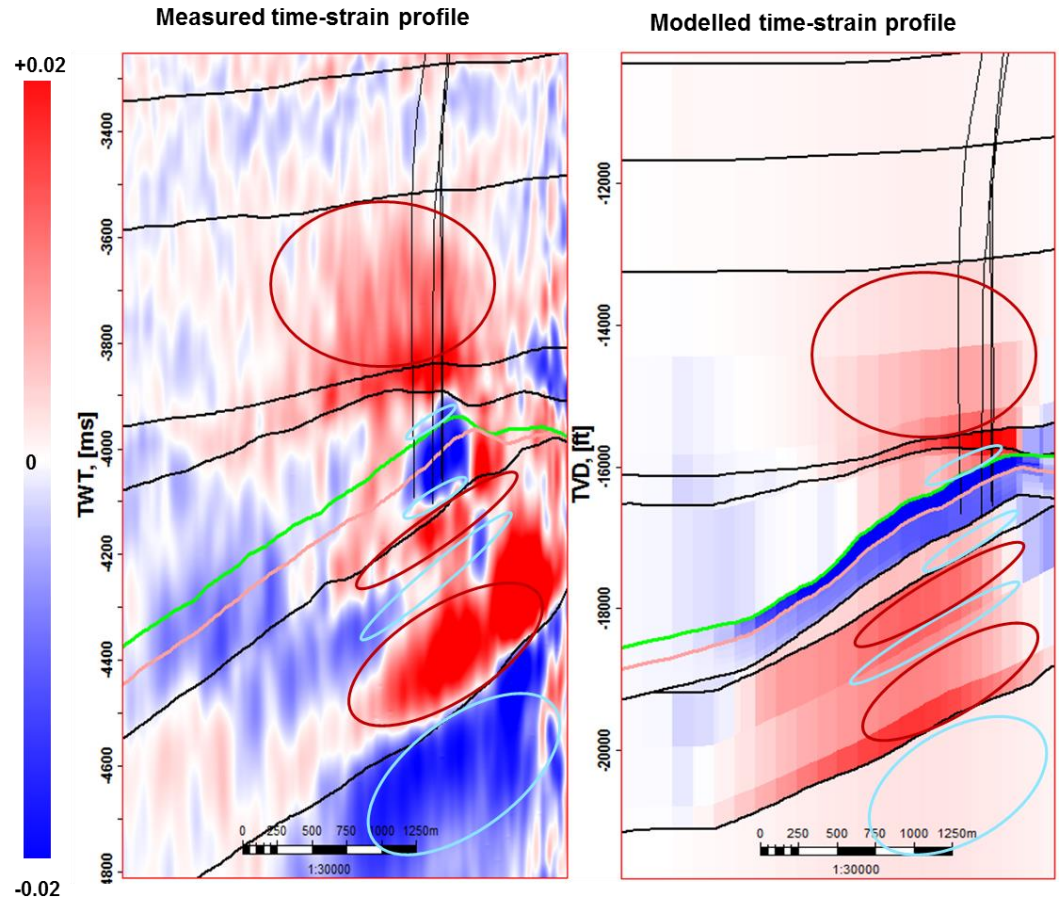

Figure 5.8: Comparison between observed (a) and modelled 4D time-shifts after updating geological information of overburden chalk formations and the underburden Pentland formation.

5.4 Applications of the geomechanical model

With the geomechanical model established, applications could now be carried out, such as the monitoring and prediction of reservoir compaction and subsidence, long-term well-bore integrity, optimization of drilling trajectories and mud weights, and the design of hydraulic stimulation and perforation campaigns (Herwanger *et al.*, 2013).

5.4.1 Evaluation and prediction of well-failure events

The evolutions of three total principal stresses were studied in order to predict well bore stability. Figure 5.9 shows modelled evolutions of the three principal stresses in Heather shale at the well A7 location. It can be seen that dramatic changes occurred just before well failure.

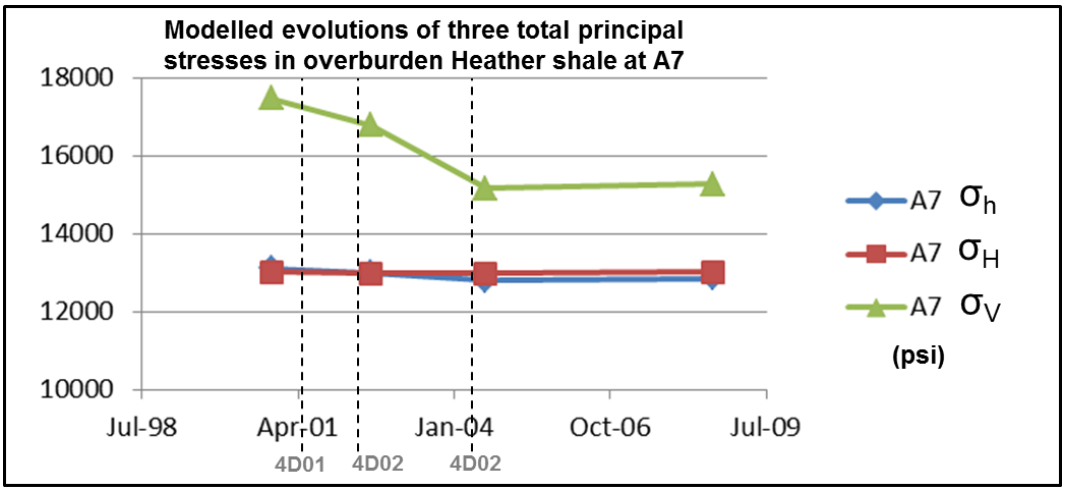

Figure 5.9: Evolution of total principal stresses in overburden Heather shale at well A7.

Figure 5.10 shows that the modelled minimum principal stress changes with depth. There is a significant reduction in minimum total principal stress above the top Fulmar extending into the Hod, indicating that these formations have been mechanically weakened. The minimum total principal stress is often referred to as the 'fracture propagation pressure'. From a safe-drilling point of view, this is the most important stress component that can affect wellbore stability and the drilling window. The model result shows that the areas with the strongest changes are in accordance with well-failure events. Moreover, it shows there is no indication of weakening within the Tor/Ekofisk or any overlying formations.

For the infill drilling, the mud weight should be chosen carefully in order to avoid influencing the mechanical stability of wellbores. If the mud weight is too low for a given wellbore trajectory, borehole breakout may cause the well to collapse. If the mud weight is too high, fluid may be lost into drilling-induced fractures (the fracture gradient is exceeded). These stability problems can be addressed either by setting appropriate mud weights and/or by selecting a wellbore trajectory that allows specific mud weights to be used given the prevailing in-situ stress field and rock strength (Hillis and Nelson, 2005). The risk of breakout development can be assessed in terms of the rock strength (compressive strength, C_0) required to prevent formation breakouts normalized to vertical stress.

Figure 5.11 shows wellbore stability plots for vertical wells in over-pressured Central North Sea area. The risk of forming drilling-induced tensile fractures (DITF) is expressed in terms of the excess mud weight (amount of overbalance with respect to pore pressure) above which DITFs initiate. The maximum mud weight for vertical wells in the same location is calculated, as shown in Figure 5.12.

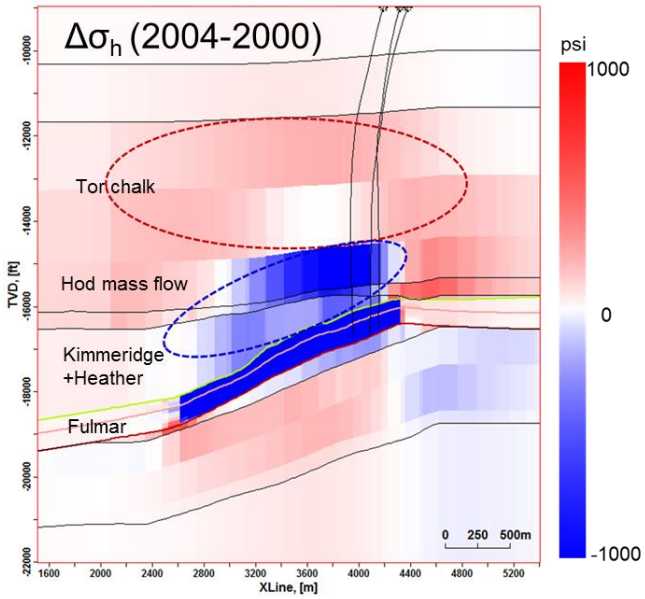

Figure 5.10: Modelled minimum principal stress changes between 2000 and 2004, just before the well-failure events happened.

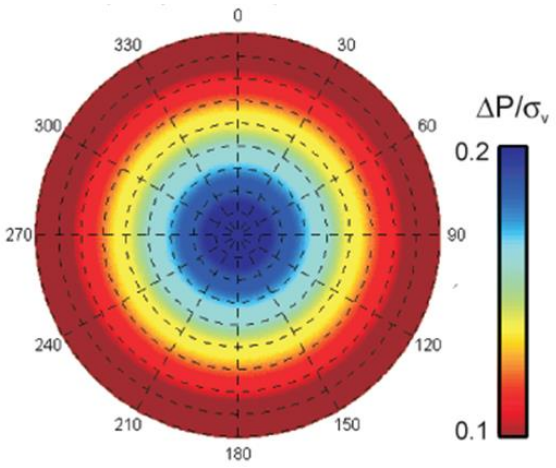

Figure 5.11: Wellbore stability plots for vertical wells in over-pressured Central North Sea. The risk of forming drilling-induced tensile fractures (DITF) is expressed in terms of the excess mud weight (amount of overbalance with respect to pore pressure) above which DITFs initiate (Hillis and Nelson, 2005).

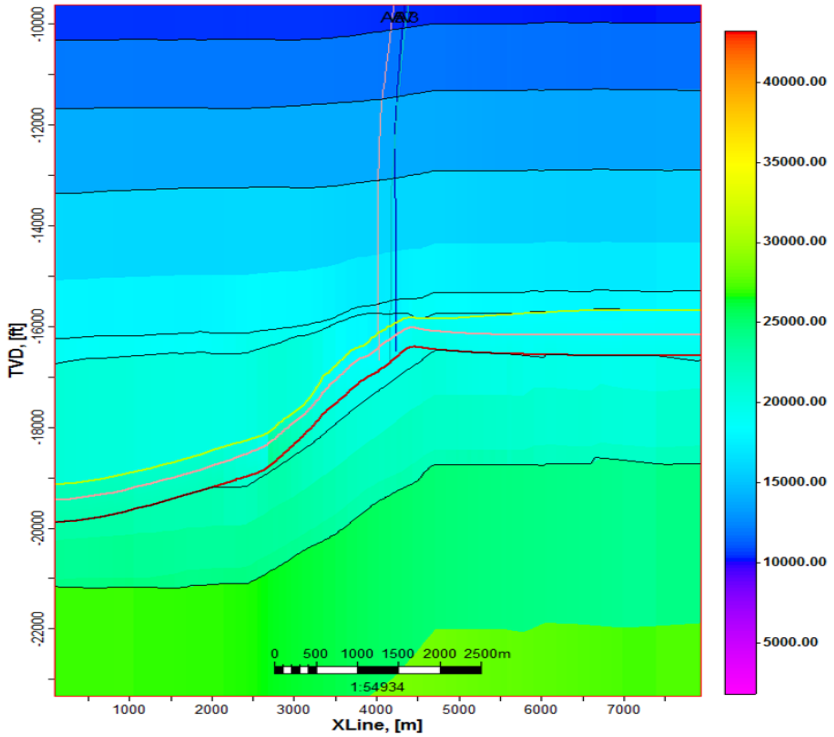

Figure 5.12: Maximum mud weight for vertical well (psi) (According to DITF model in Hillis, 2005)

5.4.2 Evaluating the influence of a dipping structure on lateral/vertical shifts

Figure 5.14 shows measured lateral shifts and modelled lateral shifts in the Base Chalk, Top Fulmar, and Top Triassic formation. Apart from the diverted directions, the magnitudes of the lateral shifts are not significantly comparable in both maps at each location. As demonstrated by Cox and Hatchell (2008) in Figure 5.13, artefacts of vertical and lateral shifts can be introduced if the same velocity model is still used for both the baseline and monitor seismic surveys when the velocity of the monitor survey has been affected by changes in strain. In the case of a dipping structure, the lateral and vertical shifts become interchangeable, as illustrated in Figure 5.15: lateral shifts in the down-dip tend to decrease the apparent vertical shift, and vice versa.

In order to capture the velocity and dipping structure issue, a workflow incorporating 2DFD seismic modelling is suggested in Chapter 7.

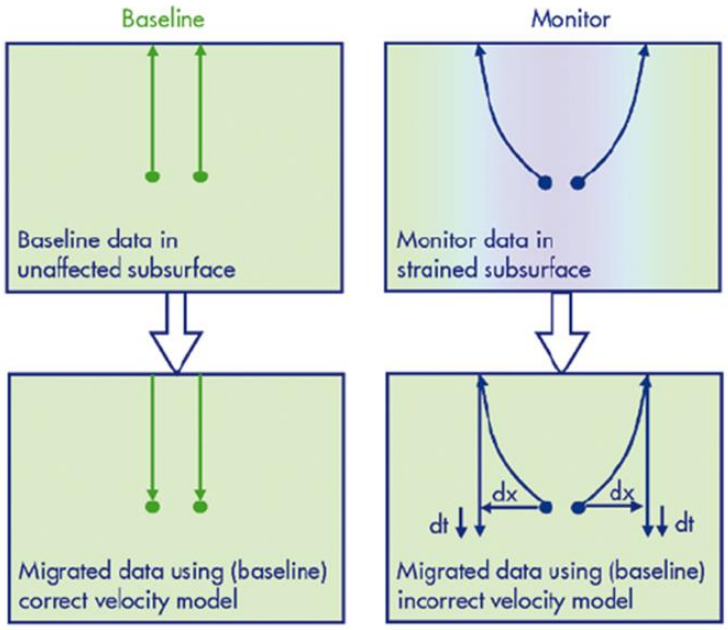

Figure 5.13: Illustration of apparent vertical time shifts induced by strained velocity in the monitor survey (Cox and Hatchell, 2008)

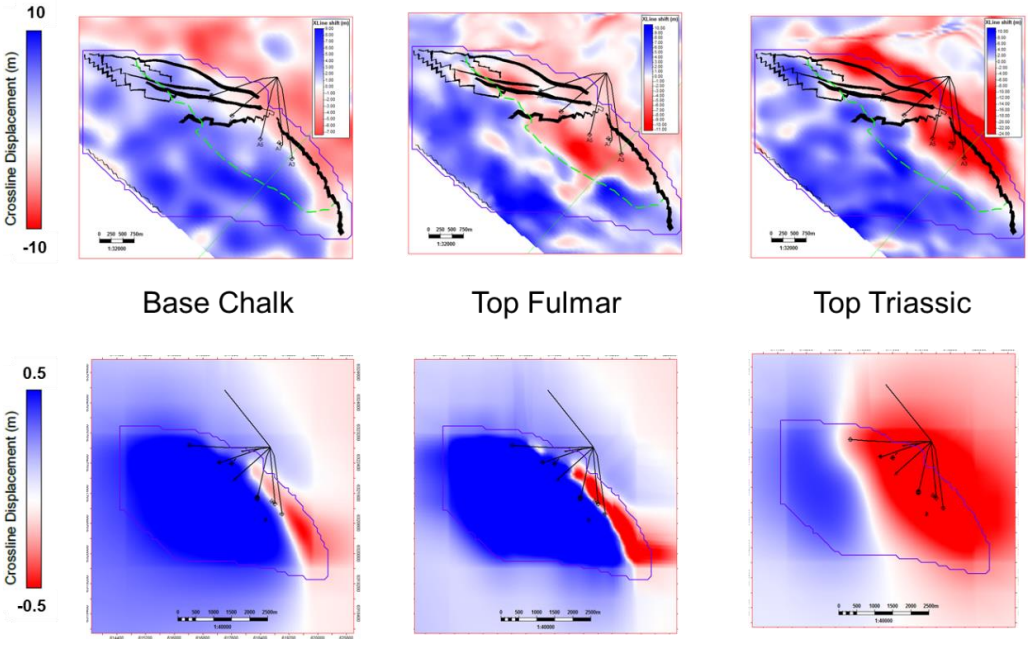

Figure 5.14: Measured (top) lateral shifts and modelled (bottom) lateral shifts at Base Chalk, Top Fulmar, and Top Triassic formation. The magnitude and direction of lateral shifts are not comparable in measured and modelled maps.

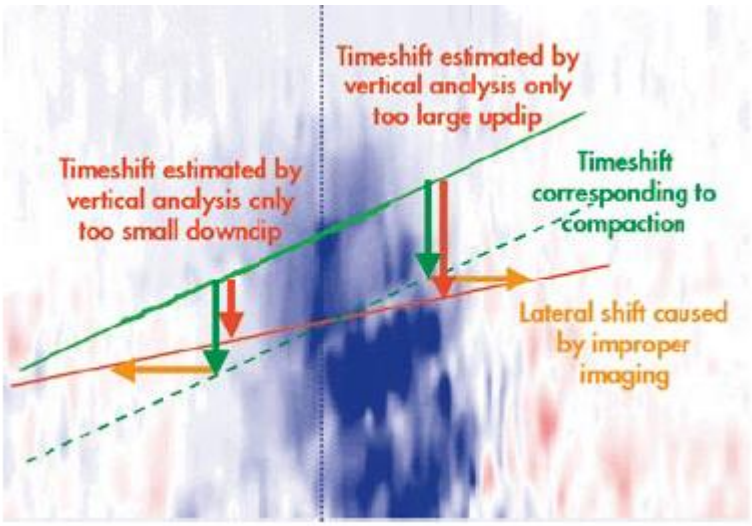

Figure 5.15: The interchangeable lateral and vertical shifts. Downdip lateral shifts decrease the apparent vertical shift. Updip lateral shifts increase the apparent vertical shift (Cox and Hatchell, 2008).

5.5 Summary

This chapter has presented the full process of reservoir geomechanical modelling using Petrel reservoir geomechanics module. Time-shifts have been used as an important tool for calibrating the base model, while geological information has been taken into consideration for the model updating. Based on this process, this study has pushed towards a deeper assessment of mechanical failures, and thus the predictions of well stability during drilling and production. In the final section, the observed and modelled lateral shifts were compared, and the disparities observed are believed to be related to migration.

In this chapter, the calibration was performed by assuming the published R factors to be representative in this field. However, the R factor is also an uncertainty in the modelling, and this requires further estimation and calibration of this parameter. This will be shown in the next chapter.

Chapter 6

Evaluation of the overburden time-shift anomaly in the Shearwater field

This chapter addresses the abnormal overburden time-shift and time-strain distributions observed from the Shearwater field throughout overburden chalks. In this work I explore the potential reasons causing the large time-shift increase within the gas-bearing Hod formation. The prevailing hypotheses include the gas effect and the geomechanical effect. Both effects are modelled for time-shift behaviour and compared to the observations. To model the 4D gas effect, different initial gas saturations are considered, as well as separate scenarios with and without solution gas. With respect to the geomechanical effect, a discussion on the R factor as well as an extra impact contributing to its magnitude is incorporated.

6.1 Introduction

After the verification of the Shearwater time-shift distributions using different calculation methods, in Chapter 4, the abnormal time-shift and time-strain distributions have been observed and confirmed in the lower part of the chalk interval. In order to explore the potential reasons for this phenomenon, this chapter is divided into three parts. Firstly, there is an overview of this time-shift anomaly, and the strategy to solve this is provided. Next, a set of gas modelling cases are conducted, along with a detailed rock physics analysis to evaluate the effects of existing overburden gas on the time-shift measurement. After that, it moves to discussions of the geomechanical effects by considering various magnitudes of R factors. Different realisations of base and monitor traces are modelled through 1D seismic modelling for all the different scenarios, and are taken for time-shift calculations afterwards. The modelled time-shift results are finally compared to the real observations, to determine which one of the two effects is the dominant cause of this abnormal overburden time-shift.

6.2 An overview of the overburden time-shift anomaly

6.2.1 The observation of the abnormal time-shift distribution

In Figure 6.1a, a time-shift map is extracted from one of the calculated time-shift results to display the time-shift changes within the interval from Top Hod formation to Base Chalk formation between the baseline survey (2001) and the monitor survey (2004). It is clear to see that the time-shift changes within this interval are mainly positive and the highest value is measured at around 2.8ms. By plotting this together with available gas penetration logs, which were acquired during well drilling, it is found that large time-shifts usually appear in the locations of wells which encountered large volume of gas in the chalk interval (Figure 6.1a). The observed time-shifts are also converted into time-strains to show instantaneous travel-time differences throughout the overburden (Figure 6.1b). Positive time-strain signals, coloured in red, demonstrate that the reflections on the monitor survey are arriving later than on the baseline survey. This is commonly referred to as velocity slowdown, such as a gas-water contact of the North Sea as presented in Wang, et al. (2002). There are two main intervals displaying slowdown signals: one in

the Hod Formation at the level of the thickest 60ft 'Basal Hod Mass Flow', and another in the upper Herring Formation. Both of them correlate very well with large gas showing in the drilling data. It is widely known that pore fluids strongly influence the seismic properties of rocks. These observations together lead to the first hypothesis, that the existence and/or the perturbation of gas in chalk formations may have an impact on the time-shift measurement. However, before moving to the gas modelling, a detailed review of the characteristics of the chalk formations needs to be carried out, to help understand if other effects such as the geomechanical changes of the rock will contribute to the abnormal time-shift distribution as well.

6.2.2 The characteristics of the Shearwater chalk zone

The Cretaceous chalk zone in the Shearwater field area has a thickness of about 4500 ft (Van Bergen *et al.*, 2013). The entire sequence is further divided into four stratigraphic formations – the Ekofisk, Tor, Hod and Herring formations, with approximate thickness of 350ft, 1650ft, 2300ft, and 350ft respectively. The Ekofisk formation is comprised of interbedded argillaceous chalks and claystones with chert nodules. The underlying Tor formation contains lime Mudstone of uniformly low permeability. Within the Hod formation, a higher percentage of claystone and anomalous units are noted, similarly to those seen in Block 22/29 (Holm *et al.*, 2005), and the clay content is observed to be increasing from the lower part of the Hod formation to the base of the Herring formation. Unlike the high porosity high permeability reservoir chalk in adjacent North Sea fields such as the Valhall and the Ekofisk fields, Shearwater non-reservoir chalk has uniformly low porosity (less than 10%) and extremely low permeability, according to available well-logging and well test data (Van Bergen *et al.*, 2013). Recent lithological and structural studies of the Shearwater chalk interval have been conducted based on analogues from outcrops (e.g. the chalk in Thornwick Bay) and offset wells (e.g. core information from the Stella, Martha and Kessog fields), all of which have highlighted a high degree of lithological heterogeneity, in the form of marl and flint bands (as shown in Figure 6.2). Conjugate fracture sets are also present on the outcrop, and bound by the marl and flint bands (Van Bergen *et al.*, 2013).

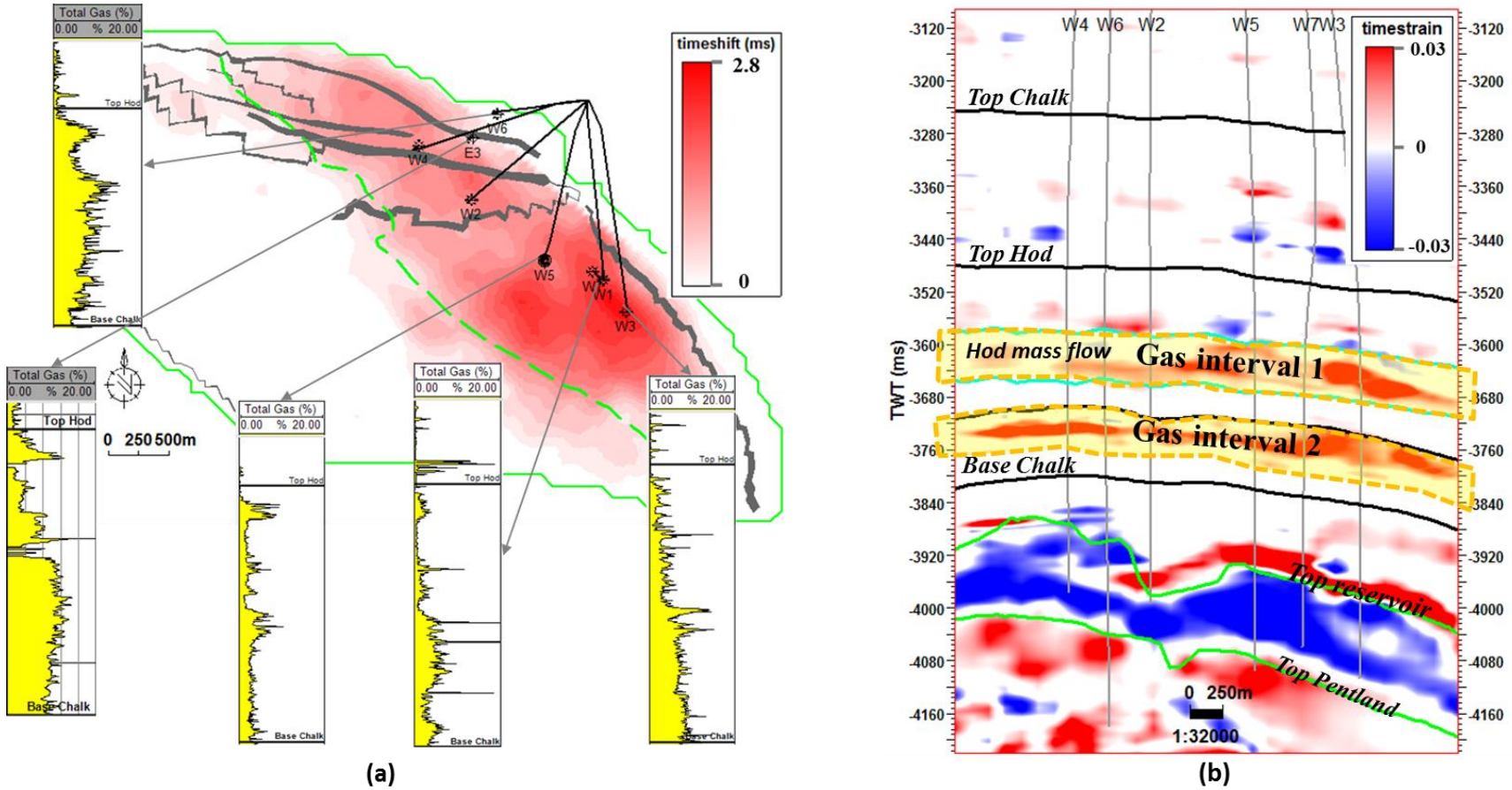

Figure 6.1: (a) The observed time-shift changes between 2001 and 2004 within the interval from the Top Hod formation to the Base Chalk formation, with gas showing logs plotted together. (b) Section view of the time-strain between 2001 and 2004, with two gas zones shaded in yellow.

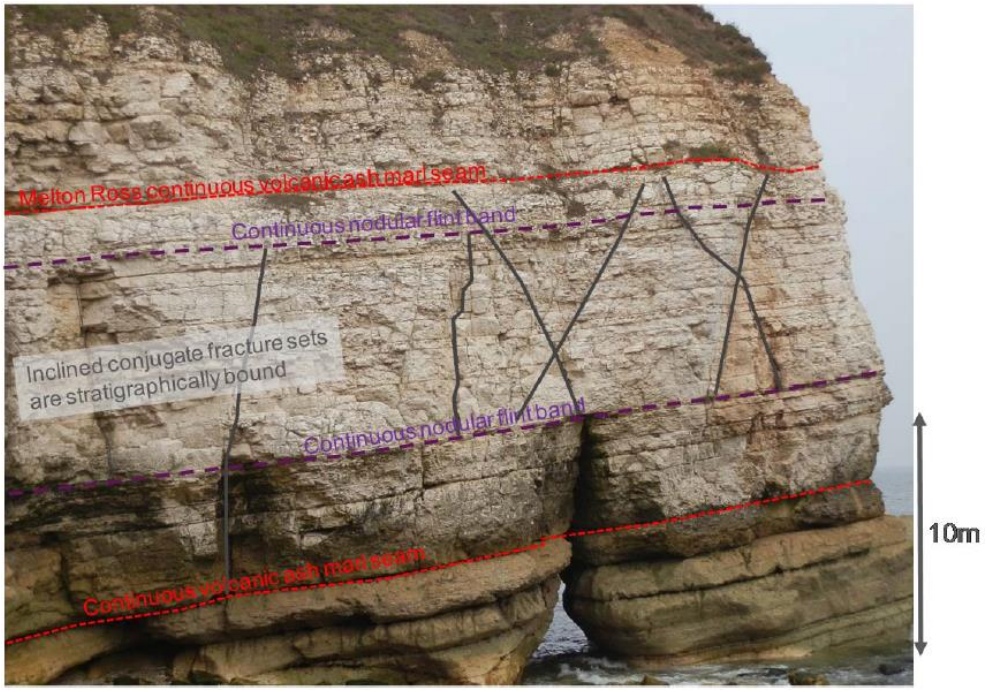

Figure 6.2: An onshore geological analogue of the Shearwater Hod Formation in North Yorkshire (Van Bergen *et al.*, 2013).

The existence of gas in chalk formations has been revealed by pre-production drilling data, which show low volume of gas in the Tor formation and elevated volume throughout the Hod formation, with gas peaks detected in the Hod anomalous zones. A similar gas bearing zone was also encountered in the neighbouring Elgin and Franklin fields operated by Total and is named as the 'Hod Geohazard' due to its impact on drilling and production (Holm *et al.*, 2005). Pressure data gathered from offset wells suggest that the chalk in the Shearwater area is significantly over-pressured, but direct measurements for overpressure are rare (Van Bergen *et al.*, 2013).

Figure 6.3 shows an integrated interpretation of well logs, time-shift, time-strain and lithology. The gas peak zone highlighted in red is interpreted as composed of clean limestones with clay content increase above and below to prevent gas leaking. It shows a good correlation with the large time-shift increase and time-strain.

During production, reservoir compaction has led to stress relaxation in the overburden. Although most of the stress relaxation has taken place in the shale overlying the reservoir,

the velocity sensitivity of chalk especially the gas bearing chalk is believed to be much greater than that of shale. Therefore, the abnormal 4D measurements could also suggest the chalks have been experiencing a complicated form of stress relaxation.

6.2.3 Potential explanations and the workflow of this study

In the absence of any work done previously to study this abnormal time-shift distribution, it is very hard to nail down the reasons, as it could be the effect of the gas saturation changes within chalk formations, or geomechanical reactions of the rock itself, or a combination of both. In order to explore the potential reasons, a 1D layer-based geological model is constructed according to the stratigraphic information of this field, with different elastic properties assigned to each layer accordingly.

The modelling work comes in two parts, the first part is to analyse gas effects, where I investigate velocity sensitivity to different initial gas saturations and saturation changes. Firstly, velocity sensitivity to different gas saturations is explored, following the workflow shown in Figure 6.4. This work is trying to translate changes in pressure and saturation into elastic parameters to help understand the magnitude of 4D signals. Well logs are interpreted and run through rock physics analysis for Vshale, porosity and saturation, followed by the calculations of elastic properties for the base trace. At the same time, stress/pressure changes are modelled from geomechanical modelling processes; Skempton B coefficients, and gas solubility are evaluated to estimate changes in elastic properties. The fluid moduli at different pressures are modelled using Batzle and Wang and mixed to get the two-phase flow fluid moduli. After that, both workflows are combined into Gassmann substitution, and are then forwarded to predict the 4D response for various stress and saturation changes. In the use of Gassmann equations, the sediment of each layer is assumed to be homogeneous, elastic and isotropic, and in pressure equilibrium. It is also assumed that there is no movement of pore fluid across boundaries and that there are no chemical reactions between the fluids and the grains, i.e. shear modulus is constant (Al-Khateb, 2013). Calibrations of elastic moduli have also been conducted using inverse Gassmann and compared to well log data. Synthetic seismograms are computed using velocity and density from previous steps. Finally time-shift is modelled for each scenario and compared to real observations.

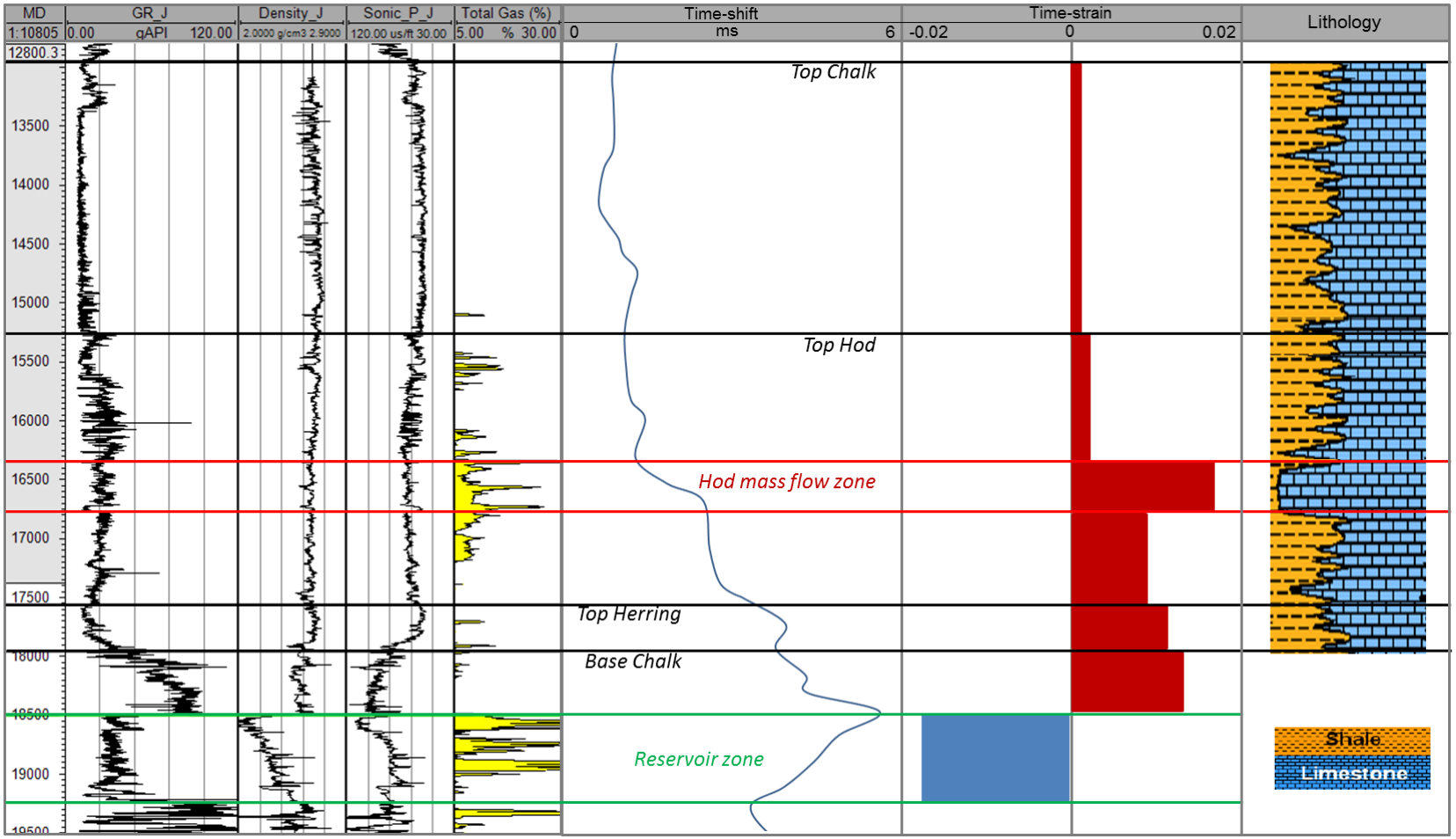

Figure 6.3: A composite plot of the Hod anomalous zone at a well location. The gas peak zone highlighted in red is interpreted as composed of clean limestones with clay content increase above and below to prevent gas leaking. It has a good correlation with the large time-shift increase and time-strain.

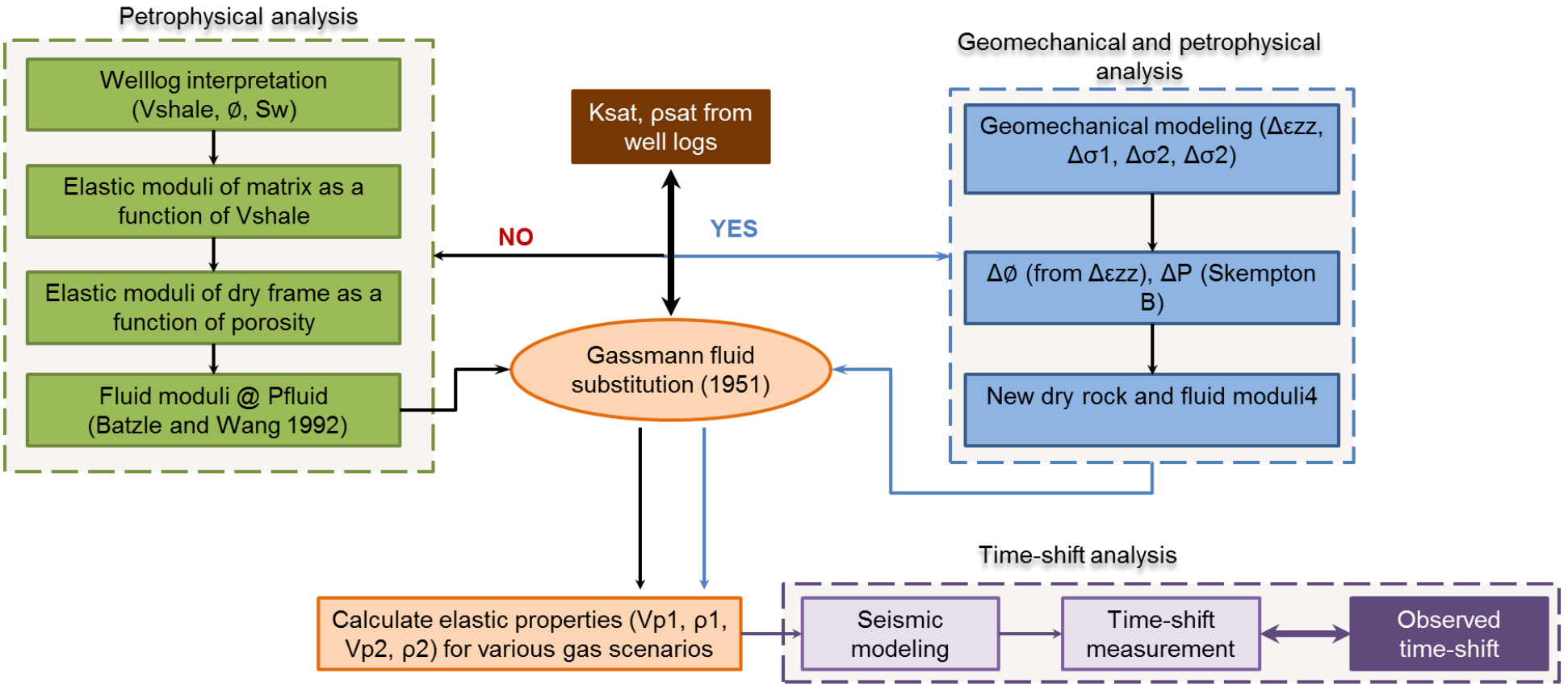

Figure 6.4: The workflow for the modelling of overburden gas effect on time-shift measurement.

The second part is to look at the geomechanical effect on time-shift magnitude, where I evaluate the velocity sensitivity to overburden stretching for different lithology, porosity and fractures. The geomechanical behaviours of different rocks are simplified using R factors (Hatchell and Bourne, 2005b). The workflow for this part of work is shown in Figure 6.5.

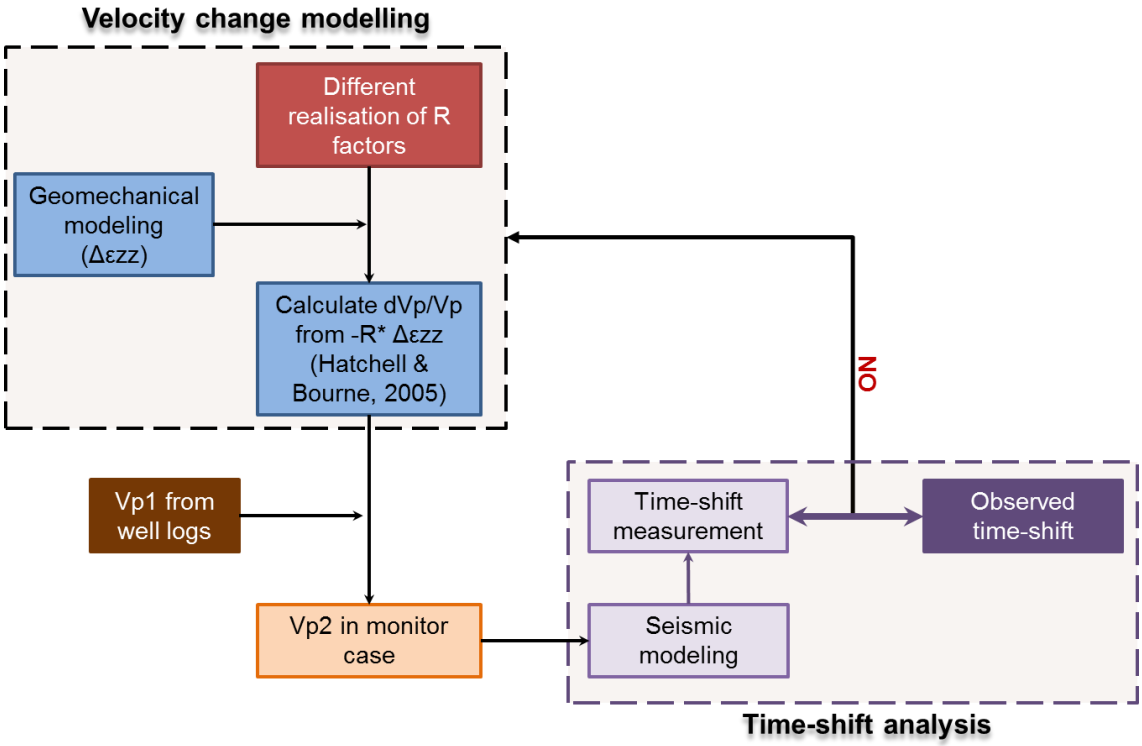

Figure 6.5: The workflow to model the geomechanical effect on time-shift measurements

6.3 Exploring the overburden gas effect on time-shift measurement

6.3.1 Gas modelling scenarios

During the gas effect modelling, two scenarios are considered, as illustrated in Figure 6.6. Due to the fact that gas is widely penetrated within Shearwater chalk formations, free gas is therefore assumed to be initially existing in both scenarios. Unfortunately, there is no direct measurement of fluid saturation within the overburden chalk formations; the range of gas saturation is then modelled between 0 and 1 in both scenarios, to cover all the possibilities. In scenario 1, I assume there is no initial solution gas; so given the small

change in overburden strain, there will not be a significant saturation change. In scenario 2, I assume there is solution gas initially present in the formation water. As pore pressure changes, gas solubility will change; therefore more gas will come out of solution, and this will lead to a change in the gas saturation. A rock physics model is constructed to compute for elastic properties of the gas bearing chalk interval as a function of porosity, pressure and fluid saturation changes.

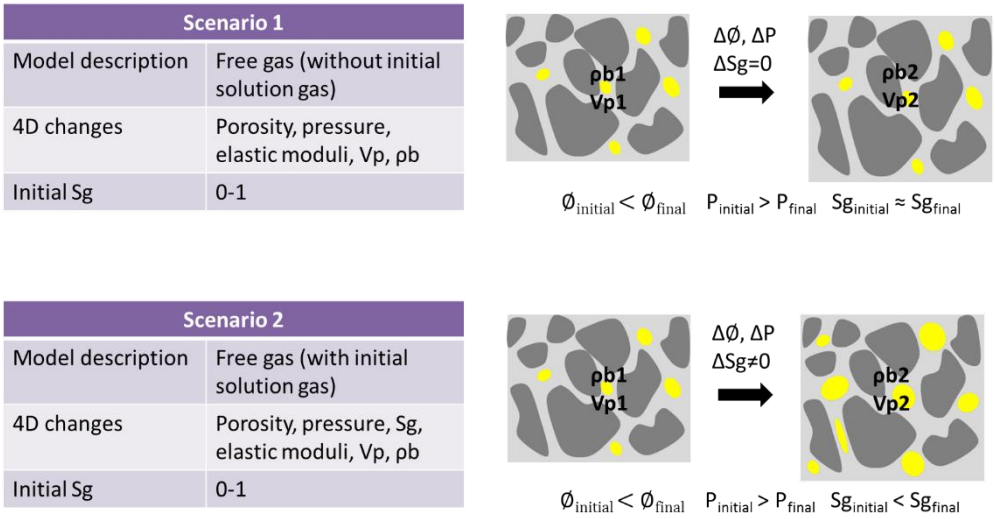

Figure 6.6: A description of the two scenarios in the gas effect modelling.

6.3.2 The rock physics model for the Hod gas zone

Table 6.1 shows the subdivision of the Shearwater chalk interval; the focus of my rock physics modelling is the Hod gas zone.

Table 6.1: The lithology and approximate thickness of Shearwater chalk formations

Name	Approx. Thickness (ft)	Lithology
Ekofisk	350	interbedded argillaceous chalk and claystone with chert nodules
Tor	1650	uniform low permeability limestone
Hod (upper)	1200	chalk, claystone
Hod gas zone	**450**	**clean limestone**
Hod (lower)	650	Limestone (higher clay content)
Herring	350	Limestone (higher clay content

Elastic moduli of the rock matrix

By assuming each constituent is isotropic, linear, and elastic, the simplest Voigt-Reuss-Hill (VRH) average is applied to model the average bulk modulus of the matrix (K_0) as in Eq. 6-1, Eq. 6-2, and Eq. 6-3 (Mavko *et al.*, 2009). More simplified, the matrix density (ρ_m) is calculated from the fractional average (Eq. 6-4).

$$K_{Voigt} = \sum_{i=1}^{N} f_i K_i \quad , \qquad \text{Eq. 6-1}$$

$$K_{Reuss} = \left[\sum_{i=1}^{N} \frac{f_i}{K_i}\right]^{-1} \quad , \qquad \text{Eq. 6-2}$$

$$K_0 = K_{VRH} = \frac{1}{2}\left[K_{Voigt} + K_{Reuss}\right] \quad , \qquad \text{Eq. 6-3}$$

$$\rho_m = \sum_{i=1}^{N} f_i \rho_{mi} \quad , \qquad \text{Eq. 6-4}$$

where K_{Voigt} is the Voigt upper bound of the effective bulk modulus of the matrix, K_{Reuss} is the Reuss lower bound of the effective bulk modulus of the matrix, f_i, K_i, and ρ_m are the volume fraction, the bulk modulus, and the bulk density of the ith mineral grain, respectively.

From well-log interpretations, it is learned that the gas zone is very clean and is mainly composed of limestone with a very small portion of clay in the rock matrix. The volume fraction of limestone and clay in the rock matrix are estimated as approximately 95% and 5% respectively, for each component. The values of mineral moduli have been published widely in the literature (Walls *et al.*, 1998; Japsen *et al.*, 2004; Gommesen *et al.*, 2007; Mavko *et al.*, 2009; Das *et al.*, 2013). The values used in the current model have been modified based on published values for North Sea chalk fields in Mavko *et al.* (2009). Table 6.2 lists all the elastic moduli for each mineral component in my rock physics model. Since a very small overburden extension is assumed in this model, the elastic moduli of the matrix are then assumed to be constant between base and monitor.

Table 6.2: Elastic moduli of each mineral component used in this rock physics model (modified after Mavko et al. 2009). *K*, *G* and ρ denote bulk modulus, shear modulus and density of each mineral respectively.

Elastic properties of minerals		
$K_{limestone}$	GPa	76
K_{clay}	GPa	20.9
$G_{limestone}$	GPa	32
G_{clay}	GPa	6.85
$\rho_{limestone}$	kg/m^3	2650
ρ_{clay}	kg/m^3	2580

Elastic moduli of the dry frame

To model dry frame elastic moduli in a convenient mathematical way, the empirical velocity-porosity model by Nur *et al.* (1998) is adopted. The bulk modulus of the dry rock frame (K_{dry}) is calculated from a linear function, as follows:

$$K_{dry} = K_0 \left(1 - \frac{\phi}{\phi_c}\right), \quad \text{Eq. 6-5}$$

where ϕ_c is the critical porosity.

Therefore, changes in the dry rock frame are derived as follows:

$$\Delta K_{dry} = -K_0 \frac{\Delta\phi}{\phi_c} \quad \text{Eq. 6-6}$$

where $\Delta\phi$ is porosity changes in response to overburden rock stretching. This value will be modelled in the next sub-section.

Table 6.3 gives a list of empirical values of critical porosity which are taken from Nur *et al.* (1998). Table 6.4 shows the initial porosity values for reservoir and non-reservoir rocks which are taken from literature on HPHT non-reservoir chalks (Mallon and Swarbrick, 2008; Swarbrick *et al.*, 2010).

Table 6.3: Empirical values of critical porosity for different rock types (Nur *et al.*, 1998)

Critical Porosity	
limestone	60%
chalk	65%
sandstone	40%

Table 6.4: Initial porosity of reservoir and non-reservoir chalks for Central North Sea fields (Mallon and Swarbrick, 2008; Swarbrick *et al.*, 2010)

Porosity of CNS chalks	
reservoir chalk	0.2 – 0.4
non-reservoir chalk	0.04 – 0.18

Acoustic properties of the fluid

Fluid properties are calculated from Batzle and Wang (1992) equations. As pointed out by Han and Batzle (2002), with the pressure and temperature of Shearwater field (as pointed in Figure 6.7), the existence of gas in brine does not change the elastic properties too much, so the properties for brine in the dissolved gas case are still modelled using the same equations as the dead brine case.

Fluids saturations vary in each scenario (end points using total gas fractions from drilling data). Density and bulk modulus change with temperature, pressure, salinity and gas composition. Brine with dissolved gas (fizz water or live water) is considered as normal brine (dead), according to Han and Batzle (2002).

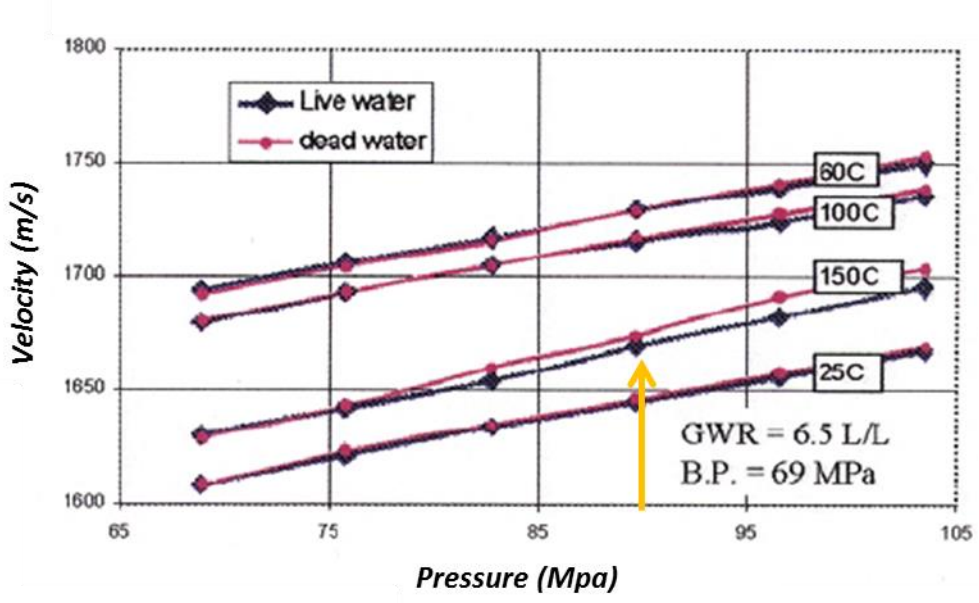

Figure 6.7: Measurements of "live" and "dead" water velocity at different pressure and temperature conditions (Han and Batzle, 2002). Yellow arrow points out the reservoir pressure of the Shearwater field.

The rock physics model for the saturated rock

After all the previous modelling for matrix, dry frame and fluids, the elastic moduli of the saturated rock are modelled using the forward Gassmann equation.

$$K_{sat} = K_{dry} + \frac{(1 - \frac{K_{dry}}{K_0})^2}{\frac{\emptyset}{K_{fl}} + \frac{1 - \emptyset}{K_0} - \frac{K_{dry}}{{K_0}^2}} \qquad \text{Eq. 6-7}$$

The velocity and density of the saturated rock are then calculated. In addition, the initial model is calibrated by comparing the calculated elastic properties against the well logs (

Figure 6.8). The velocity mismatch in the gas zone may due to the under-determined stiffness of this chalk layer or overestimated volume of fluid in the model. In order to get a better match, the mineral and fluid composition, the values of elastic modulus need to be well determined with more information to be acquire in future. After calibration, elastic moduli for mineral and dry rock are updated accordingly and used throughout the following models.

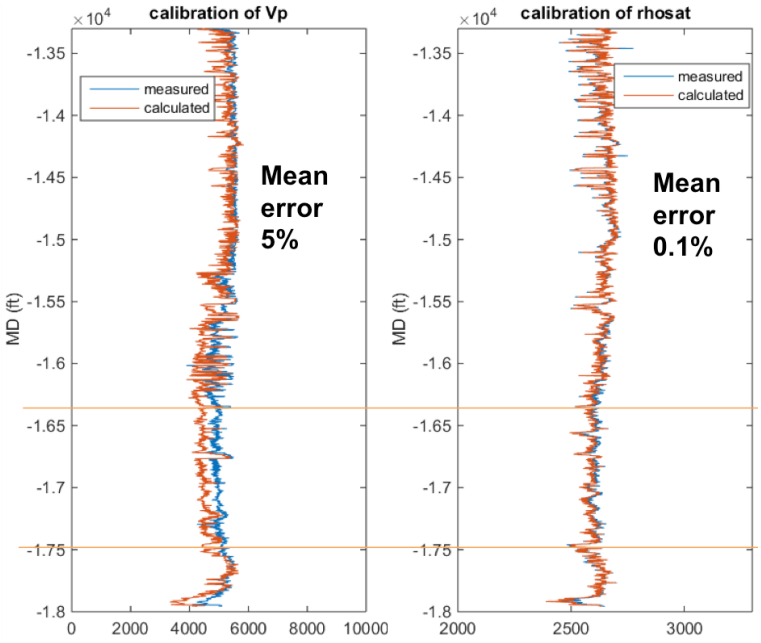

Figure 6.8: Model calibration – (left) calibration of Vp, (right) calibration of bulk density.

6.3.3 Modelling for 4D changes in rock physics properties

Porosity change after overburden stretching

Production-induced reservoir compaction in the Shearwater field has caused the overburden to stretch: as a result the porosity in the overburden rock has changed. The stretch-induced porosity change is calculated by assuming a simple uniaxial stretching of the rock, as illustrated in Figure 6.9. A simple relationship between changes in the vertical strain and the porosity is stated in Eq. 6-8, from which changes in porosity are calculated for the monitor case.

$$\varepsilon_{zz} = \frac{\Delta\emptyset}{1-\emptyset} \quad , \qquad \text{Eq. 6-8}$$

where ε_{zz} represents the vertical strain changes, $\emptyset$ is the original porosity of the rock and $\Delta\emptyset$ is the porosity change in response to overburden stretch.

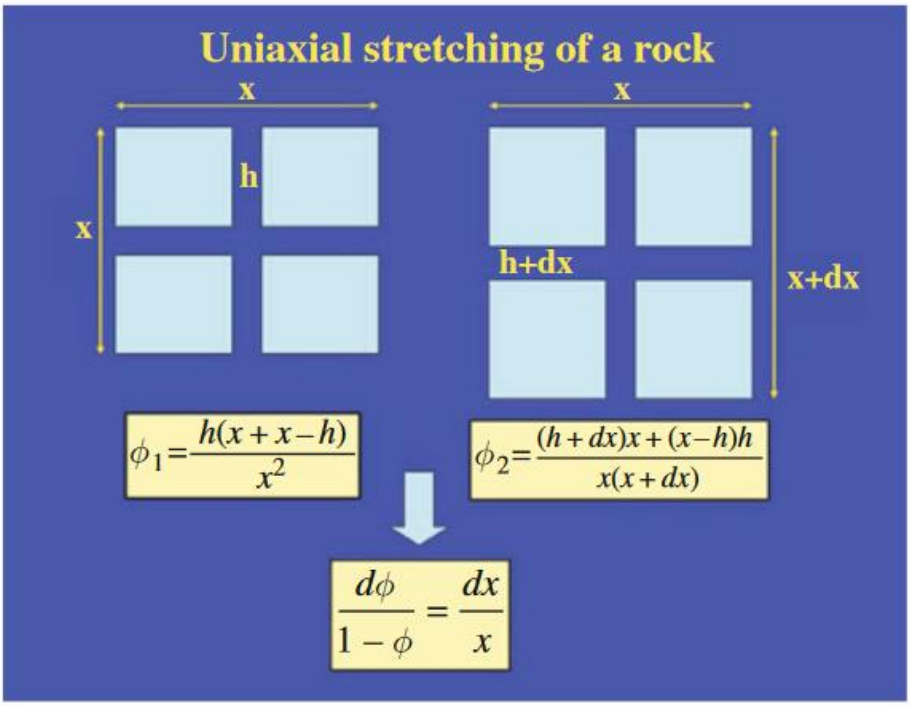

Figure 6.9: An illustraion of uniaxial stretching of a rock (Landrø, 2010). By assuming the rock only stretches in the vertical direction, the porosity change can be derived given the vertical strain change and the initial porosity of the rock.

Changes in pore-pressure and gas solubility

Based on the Skempton B-coefficient equation presented in Chapter 2, the pore pressure is calculated up to 5 MPa.

The composition of the gas in the chalk is unknown, as it is not tested, but it is certainly a wet gas and probably reasonable to assume it is not that different to the Fulmar condensate. Therefore, the Fulmar fluid composition from exploration well 22/30b-11 has been used in this study (Figure 6.10c). The dominant component is methane. As stated by the gas solubility equation in (Dandekar, 2013), the solubility is dependent on both pressure and temperature and gas component. At a given temperature, pressure seems to have a more significant effect on solubility than temperature, at a given pressure. The presence of dissolved solids affects the solubility of gases in water. As the amount of total dissolved solids increases, the solubility decreases. The solubility of light hydrocarbon components increases as pressure increases, and methane has the highest solubility. With

increasing carbon number, the effect of pressure on solubility appears to be minimal. In this modelling, only the methane component is considered.

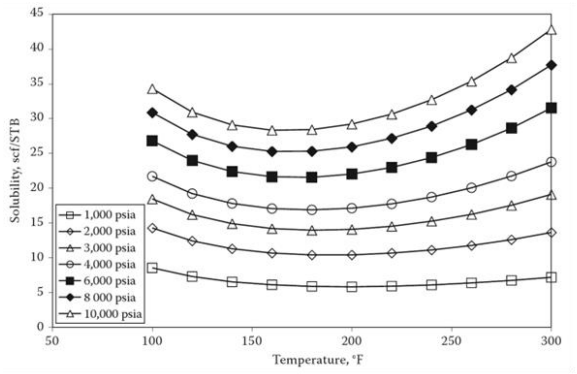

(a)

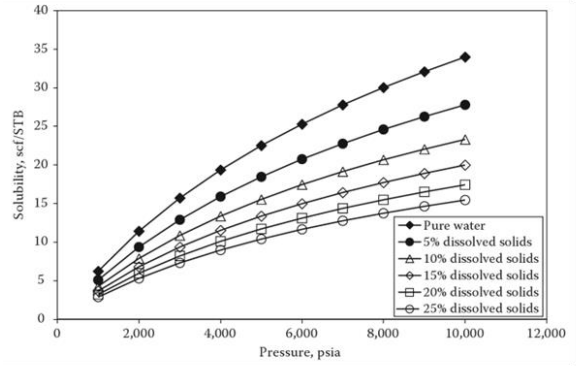

(b)

Extended Composition at 5700 psia 360 °F

Cmpt	Mole %
N2	0.33
CO2	2.88
C1	72.98
C2	7.15
C3	3.35
iC4	0.71
nC4	1.43
iC5	0.64
nC5	0.71
C6	1.11
C7	1.43
C8	1.58
C9	1.13
C10-C11	1.37
C12	0.44
C13	0.41
C14-C15	0.65
C16-C17	0.44
C18-C20	0.457
C21-C24	0.315
C25-C32	0.308
C33-C80	0.18
Total	**100.00**

(c)

Figure 6.10: (a) Solubility changes with temperature for different pressure conditions (Dandekar, 2013). (b) Solubility changes with pressure for different salinity (Dandekar, 2013). (c) Fulmar fluid composition test (provided by Shell).

Velocity changes for different initial gas saturation

The model results show that with the change of pressure, porosity and initial and final gas saturation, changes in velocity are very limited (Figure 6.11). In first scenario, where gas saturation stays constant in base and monitor cases, velocity decreases as a result of porosity and pressure changes; the fractional change only varies between -0.06% to -0.22%. In the second case, when initial gas saturation is very small, velocity is reduced in the monitor case; however, when the initial Sg is larger than the turning point value, velocity starts to increase as gas comes out of solution. The modelled fractional velocity change ranges between -0.19% and 0.02%. These small changes in velocity and thickness are not possible causes of such a large time-shift increase as observed from the 4D data.

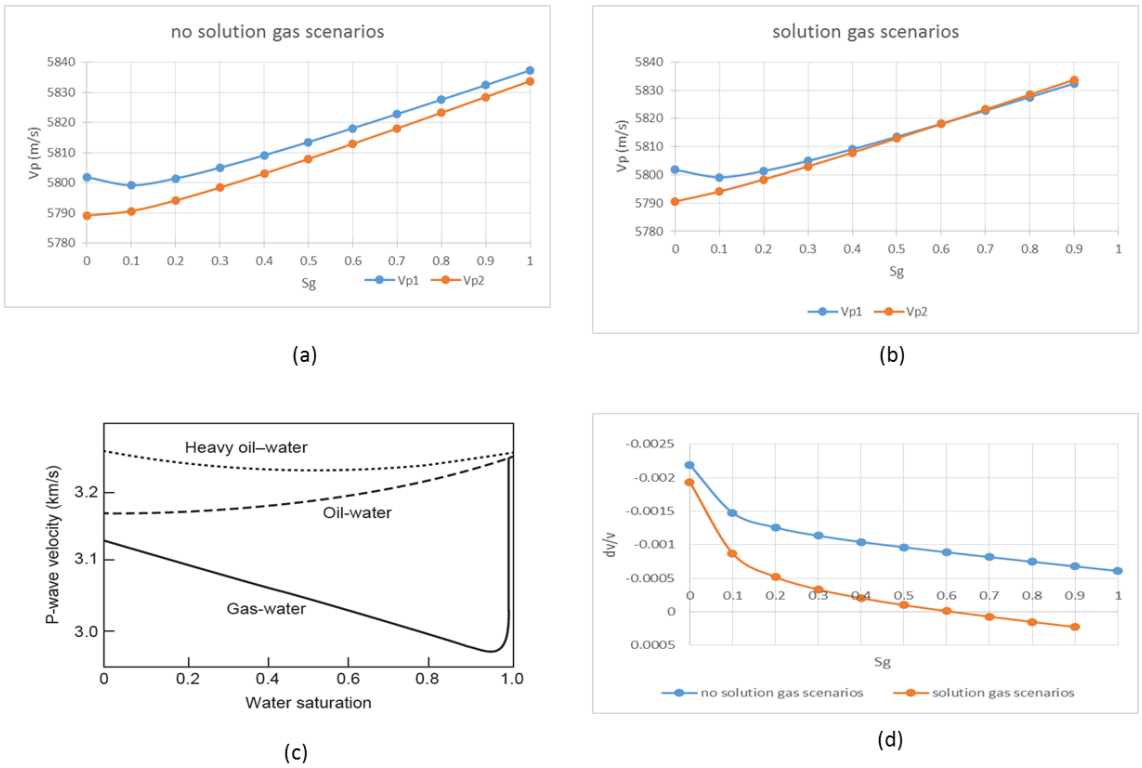

Figure 6.11: 4D changes in Vp with different initial gas saturation

6.3.4 Seismic modelling and time-shift calculation for different gas scenarios

An extracted wavelet from well-tie analysis is used in the 1D seismic modelling for both base and monitor traces. It has a frequency of 17Hz, and was extracted within the reservoir and immediate overburden (Rangel, 2016). Figure 6.12 displays the time-shift result against lithology, total gas reading, modelled seismic traces and observed time-shift between the top and base chalk. The two dashed lines indicate the top and base of the Hod anomalous zone, where a large volume of gas had penetrated. By comparison, the modelled time-shift profiles for various initial gas saturations in both scenarios are all far smaller than the observation. This suggests that the pure gas saturation effect may not be sufficient for creating such an obvious time-shift increase. Thus, the other possible reasons, such as the geomechanical effects, still need to be investigated.

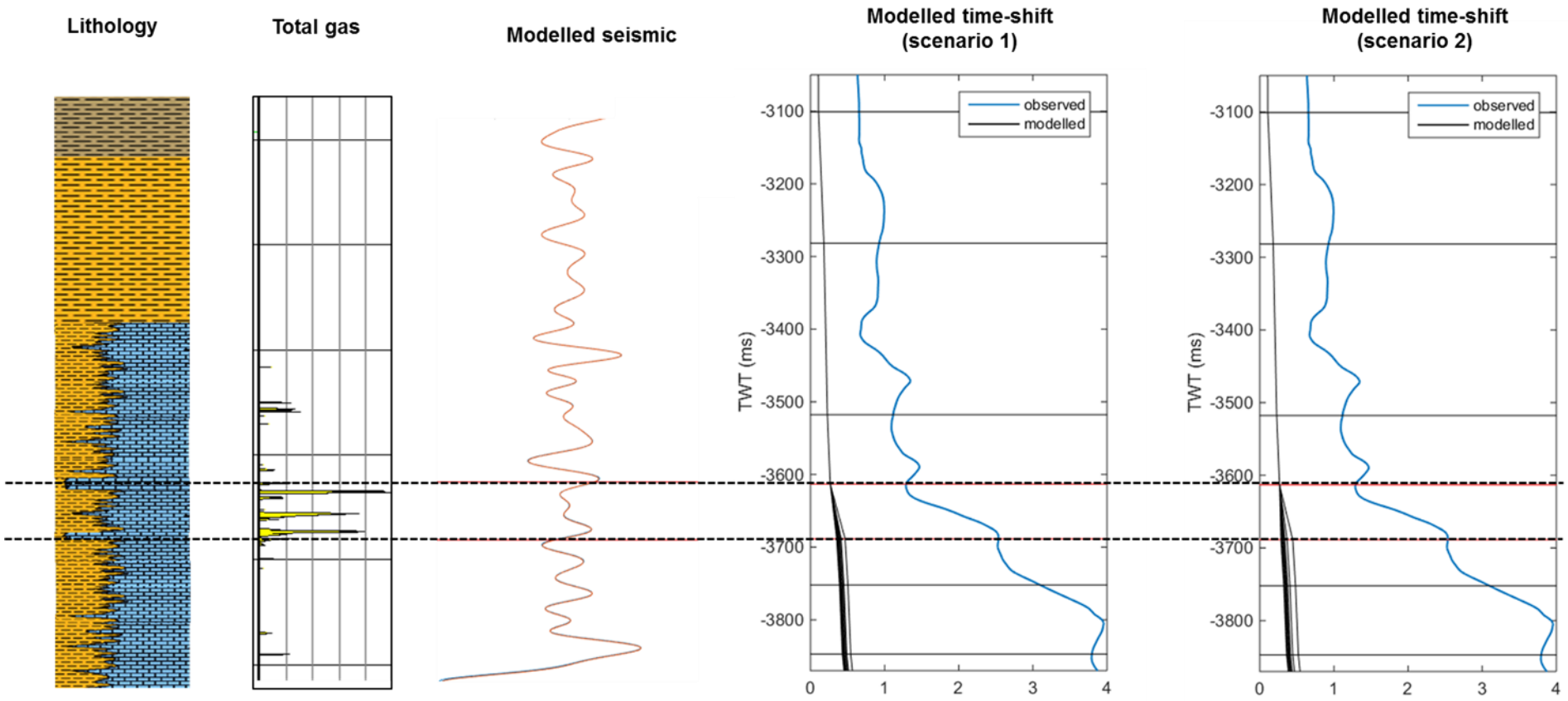

Figure 6.12: Time-shift results of gas effect modelling. The two dashed lines indicate the top and base of the Hod anomalous zone. By comparison, the modelled time-shift profiles for various initial gas saturations in both scenarios are all far smaller than the observation.

6.4 Exploring the geomechanical effect on time-shift measurement

In the modelling of the geomechanical effect on time-shift, the R factor is used. As shown in Chapter 2, there have been quite a lot of measurements to determine the magnitude of this parameter. In the following study, I want to explore a new way to derive this parameter from angle-stack seismic data.

6.4.1 R factors from angle-stack seismic data

The strategy arises based on the work of Landrø and Stammeijer (2004). They suggest a way to discriminate compaction and velocity changes using offset seismic data:

$$(\frac{\Delta t}{t})_N = -\frac{\Delta v}{v}(1 + tan^2\theta_N) + \frac{\Delta z}{z} \quad , \qquad \text{Eq. 6-9}$$

$$(\frac{\Delta t}{t})_F = -\frac{\Delta v}{v}(1 + tan^2\theta_F) + \frac{\Delta z}{z} \quad , \qquad \text{Eq. 6-10}$$

Since the R factor links both of them, it can be calculated subsequently. This equation assumes small changes in thickness and velocity, but it is valid for all angles in the constant-velocity case. Furthermore, isotropy is assumed, so that the vertical and horizontal p-wave velocities change equally and lateral velocity variations are neglected.

In Shearwater, 5 offset data have been provided with different offset ranges, time-shifts and time-strains have been measured, as in Chapter 4. As the reservoir sits quite deep, the dip of the structure appears to be quite shallow, therefore the dip effects are not expected to be very strong. The effective angles (θ) are approximated given the offset and general depth of reservoir. This approximation could bring in some uncertainties in calculation.

Figure 6.13 shows how the R factors are calculated in these layers. Time strains from different offsets are plotted against offset angle, a linear trend line is fitted to get the intercept and the coefficients, which are the normalized thickness and velocity changes respectively. But notice these are a very narrow range of angles, due to the depth of the reservoir, so we do not expect this to be particularly accurate.

In the lower right graph, normalized velocity changes are plotted against normalized thickness changes, here all points in this layer are displayed. From the linear relation, the R factor was then calculated.

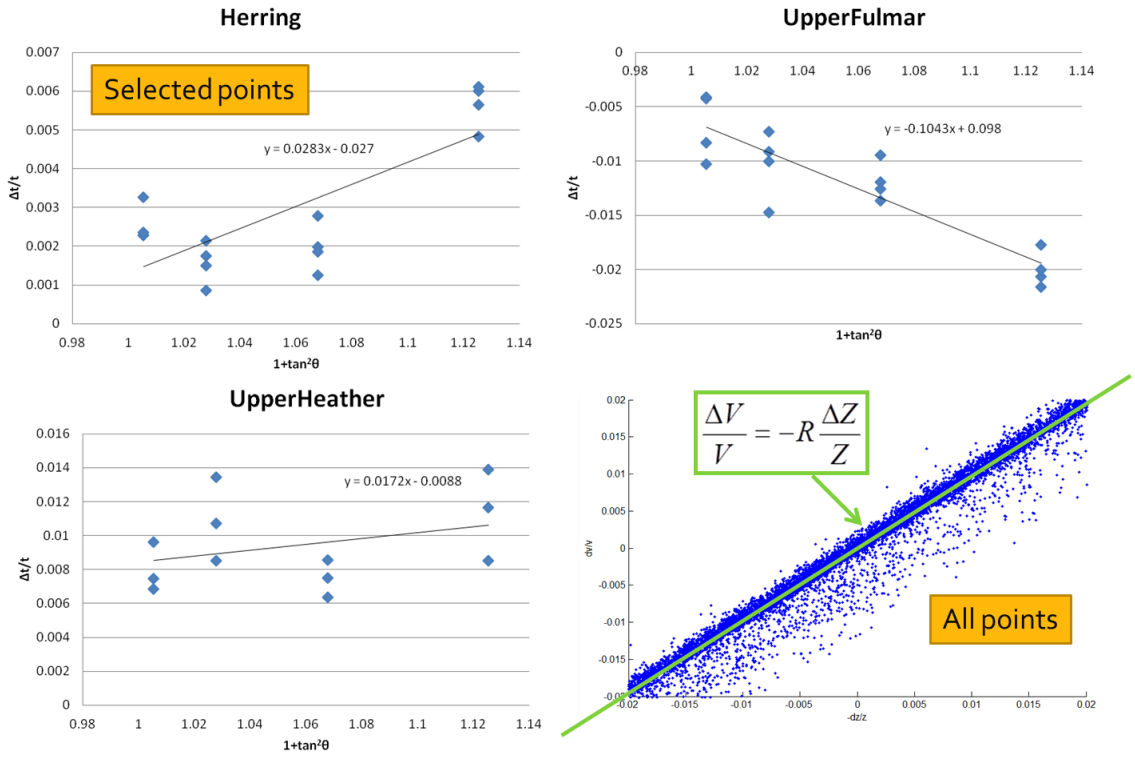

Figure 6.13: Calculating R factors from angle-stack seismic data

In general, this is a layer-based inversion for R factor (Figure 6.14). The input time-strains were provided by averaging the time-strain values in each layer and excluding the outliers at the same time. Table 6.5 shows the arithmetic mean and standard deviations of the results for all formations: they are all very small compared to the literature values and are quite close to unity.

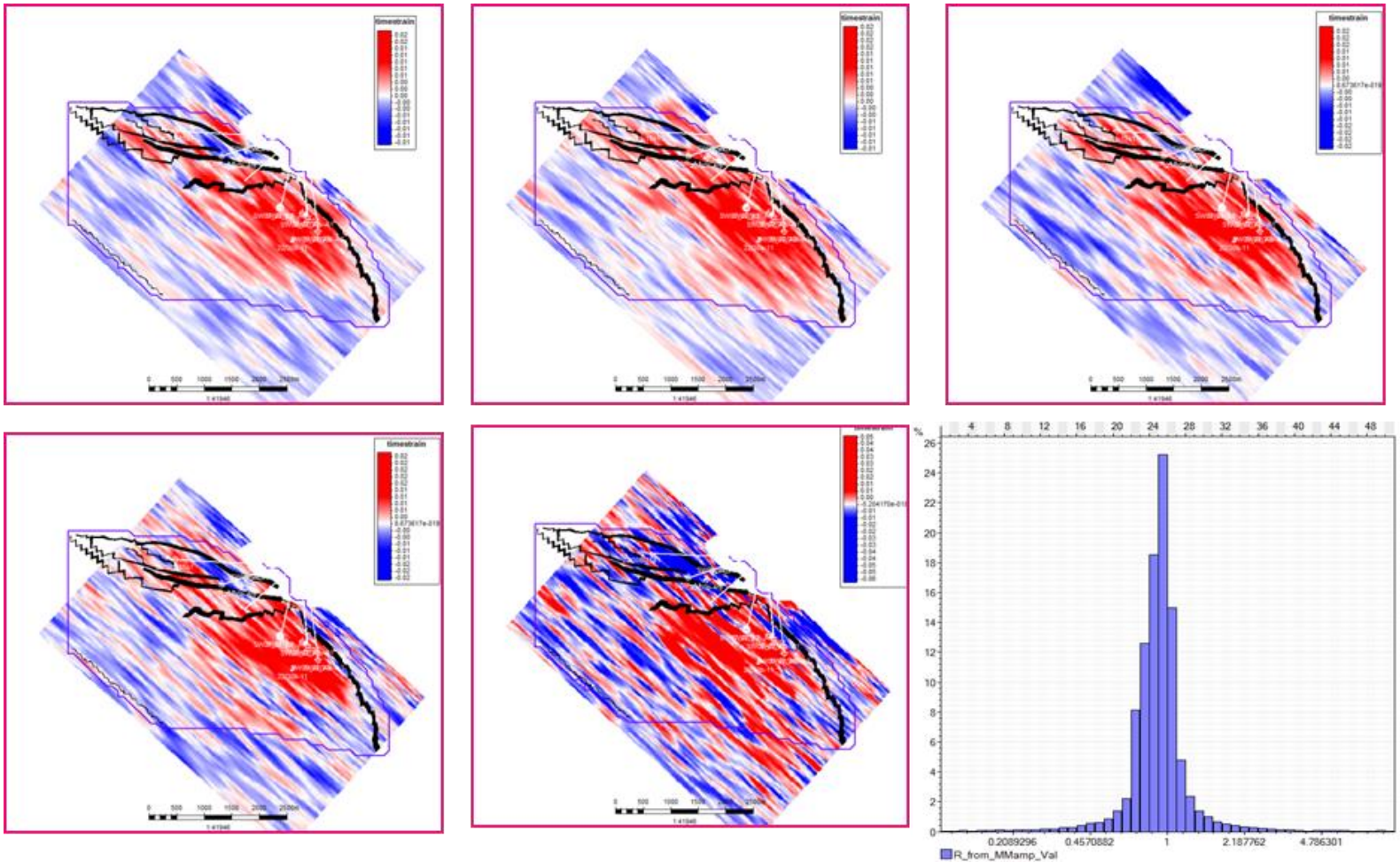

Figure 6.14: Time-strain maps at different formations, illustrating a layer-based method

Table 6.5: R factors from angle-stack seismic data

Formation	Arithmetic average	Standard deviation
Overburden	0.9838	0.1879
Sele	1.0148	0.1656
Ekofisk	0.9626	0.1591
Tor	0.9711	0.1546
Hod	0.9691	0.1537
Hod Mass Flow	0.9655	0.2718
Herring	0.92	0.2672
CromerKnoll	0.9468	0.2688
Kimmeridge	0.9568	0.2035
Heather	0.9719	0.2001
Upper Fulmar	0.9841	0.2133
Lower Fulmar	1.0012	0.2405
Lower Heather	0.9591	0.2295
Upper Pentland	0.9776	0.2091
Mid Pentland	0.9705	0.1969
Lower Pentland	0.9649	0.3368
Triassic	0.9479	0.354
Permian	0.9931	0.2568

There are several uncertainties under this calculation, such as the accuracy of time-shift and time-strain calculations, the non-negligible dip angle, the failure to satisfy the assumptions for Landrø's equation, and so on. However, among them I think that the greatest uncertainty comes from the small offset coverage, which if compared to the very large depth of the reservoir will not give enough variations in $\tan 2\theta$ to validate the calculation.

6.4.2 R factors from the Vp-porosity relation

For a porous material that undergoes uniaxial compaction (and where the compaction of the grain material is ignored), the relative change in the thickness is related to the change in porosity. As presented by Hatchell and Bourne (2005b), it is assumed the seismic velocity is a function of porosity, $V(\varphi)$, so velocity change can be written as a function of

vertical strain and porosity. With the R factor, these equations can be reorganised and R becomes a function of porosity and velocity. Taking the relation between velocity and porosity for chalk formations from sonic and neutron logs, the equation can be further simplified as a function of porosity only. Porosity varies with depth, so the R factor varies with depth (Figure 6.15). In most cases the R-values predicted from these velocity-porosity models are more or less consistent with what is observed for reservoir rock (loading) and much smaller for non-reservoir rock (unloading). Porosity in shearwater chalk formations generally varies from 2% to 10%, so R is between 2.033 and 2.267. These R-values are even smaller than the literature values of around 5 (Hatchell and Bourne, 2005b). Errors could come from well logs, as clay content (clay bound water) and hydrocarbon can exaggerate the readings of porosity. So this vp-Ø correlation needs to be corrected.

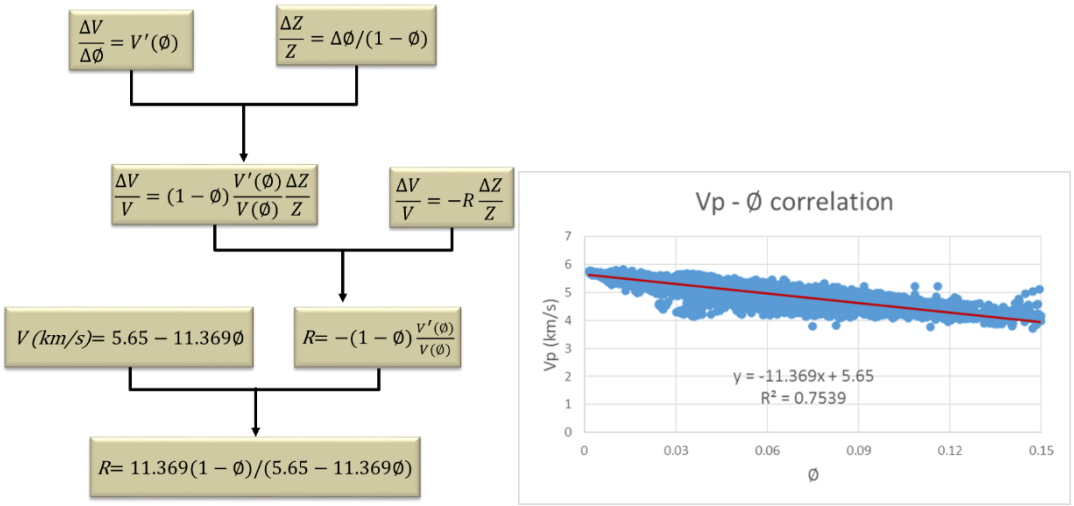

Figure 6.15: Estimating R factors from Vp-porosity relations

Using R factors derived from velocity-porosity relations, the modelled time-shift result, as shown in Figure 6.16 is still not able to match with real observations, which may indicate additional effects, apart from porosity.

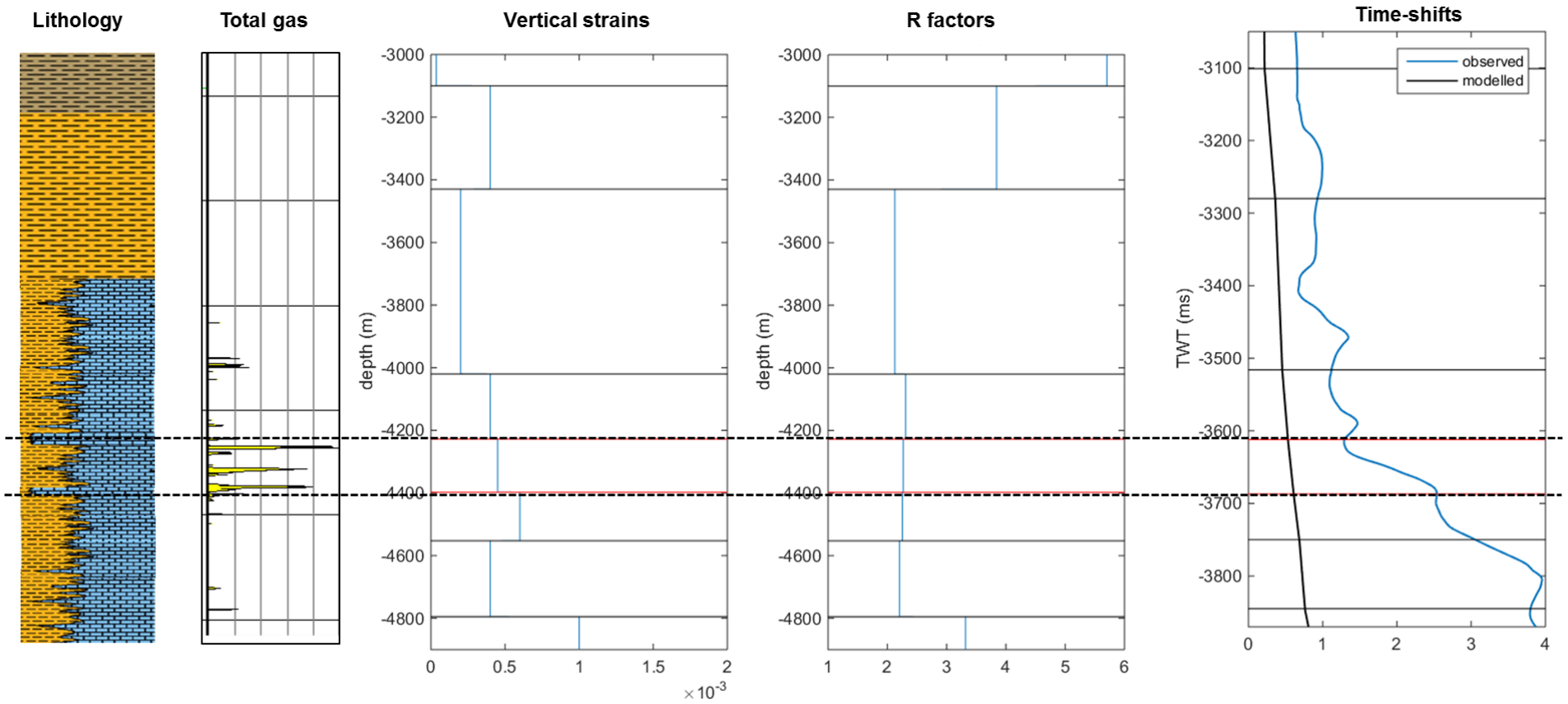

Figure 6.16: Time-shift results using R factors from the Vp-porosity relation

6.4.3 Extra R sensitivity to cracks and different lithology

R factors are predicted using observed time-strain and modelled vertical strain in geomechanical models. A linear regression was applied in a layer-based approach. The results show that in the chalk formations R-values are much higher than porosity predicted R-values, which indicate large changes in velocity as a result of small changes in layer thickness. In the Tor formation, R ranges between 10 and 30, and in the Hod formation, higher R values are expected, between 25 and 55 (Figure 6.17). De Gennaro has performed a similar prediction for Elgin and Franklin fields, which are not far from Shearwater, and chalk formations are interpreted to be widely distributed across these fields. The anomalous zone in Hod is also traceable in these fields. Large R factors of between 25 and 75 were predicted from their study.

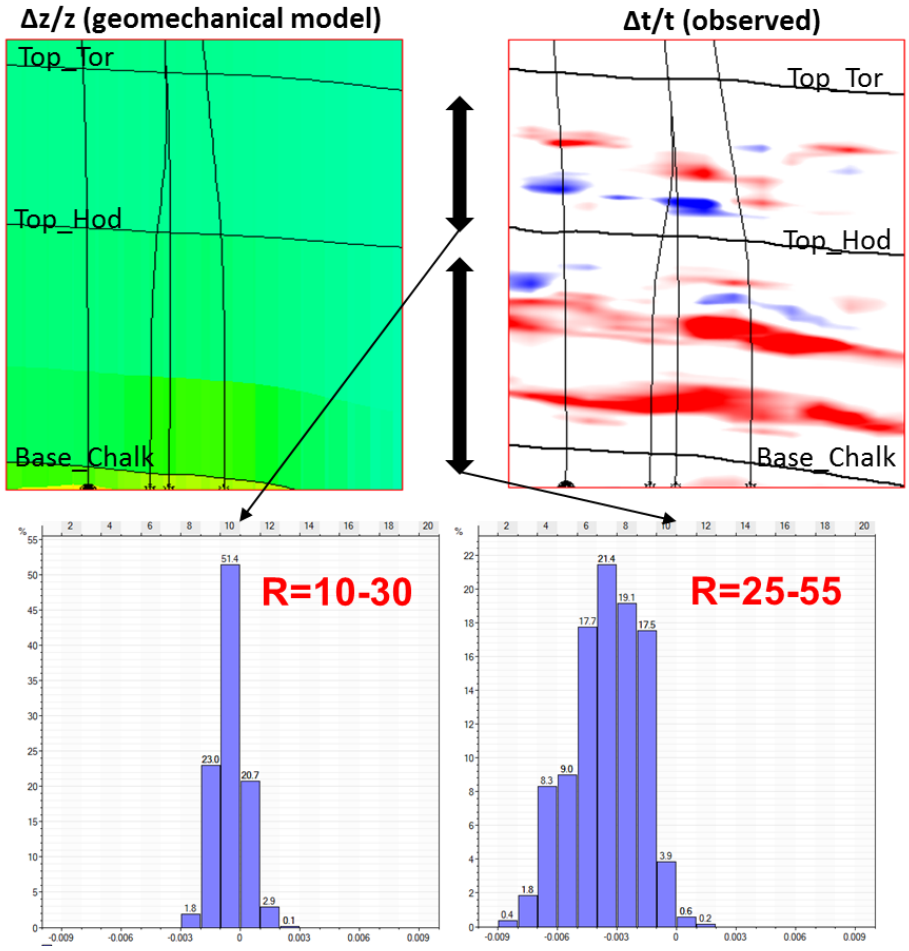

Figure 6.17: Predicted R factors from geomechanical models

There are two facts that are mainly influencing the magnitude of R factors: the first one is the porosity, and the other is the development of fractures. Published studies also show possible additional velocity sensitivity to strain, due to the process of crack opening (Figure 6.18). Geomechanical modeling results show rock expansion, which might promote the opening of natural fractures in the chalk. Core and outcrop analogues show lithological heterogeneity, conjugate fracture sets and vertical joint planes. Horizontal stress might also exist, as the minimum total principal stress vector was in the vertical direction. Fractures existed initially in this area and have been through geomechanical deformations due to production, this will produce a heightened R factor with a magnitude higher than 5. However to fully characterise the development of fractures and to model velocity sensitivity, an integrated interpretation is needed in future.

By using the heightened R factors, the modelled time-shift matches the observations (Figure 6.19).

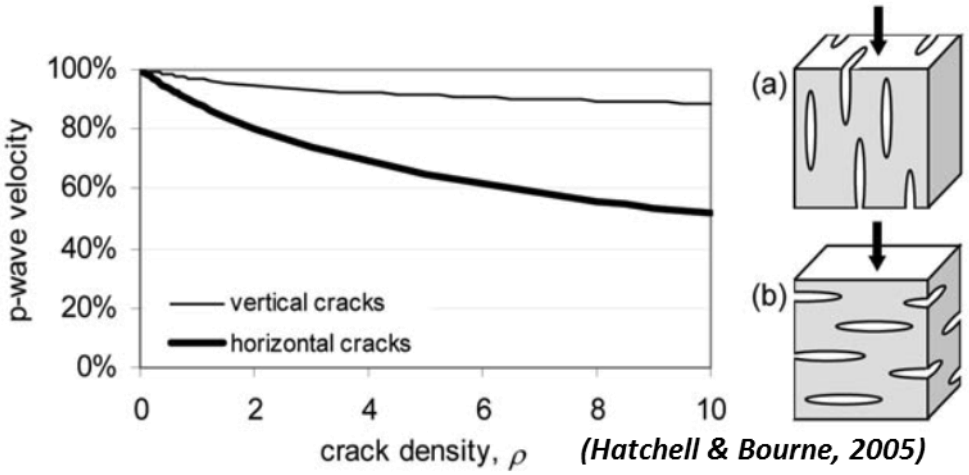

Figure 6.18: Velocity sesitivity to fractures (Hatchell and Bourne, 2005b)

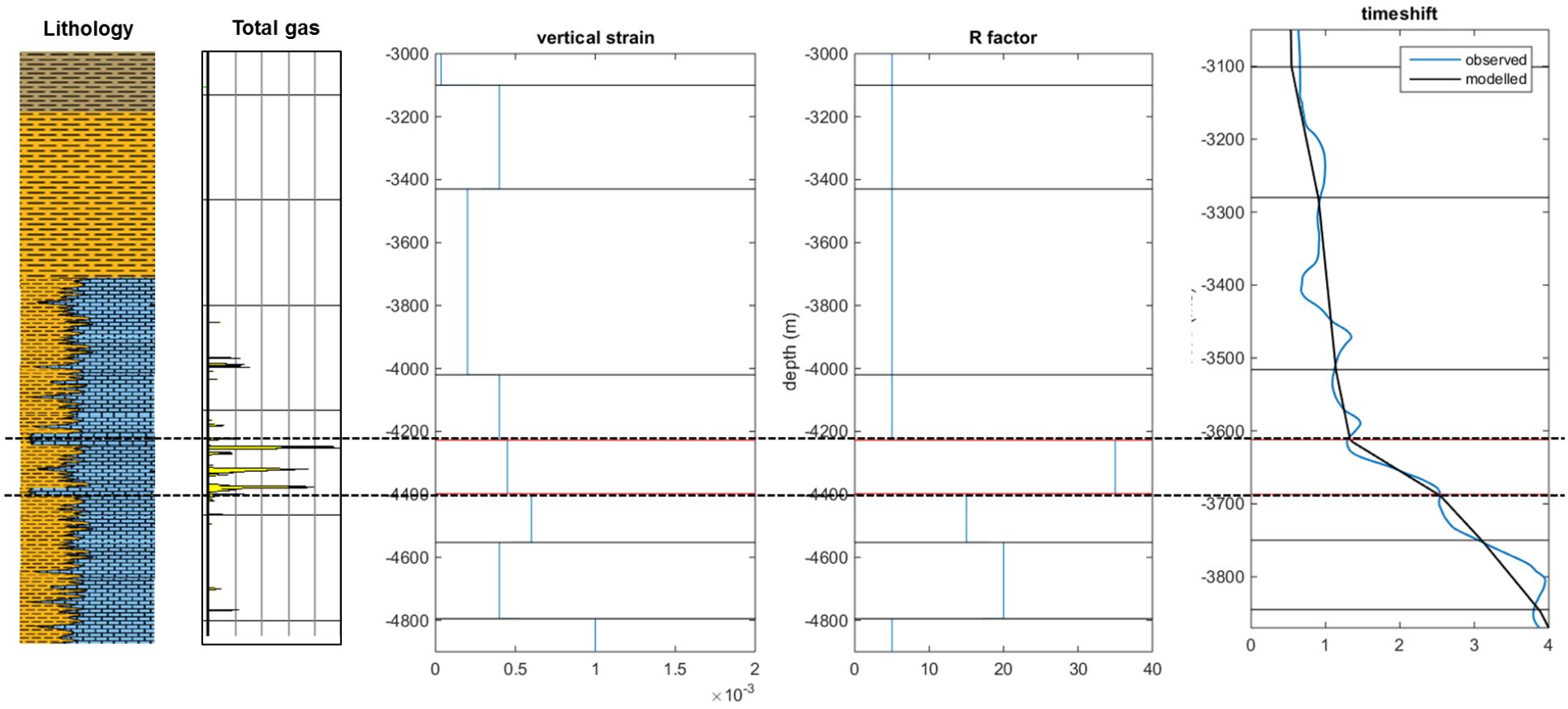

Figure 6.19: Time-shift results using heightened R factors

6.5 Summary

Since it is widely known that pore fluids strongly influence the seismic properties of rocks, and consequently velocity, the existence of gas could be a reason to explain the large measured time-shift increase. The Hod formation contains high percentage of claystone and anomalous units, as widely seen in the Shearwater field, and which are even traceable across the adjacent fields (Holm *et al.*, 2005). Data from drilling reveals background gas throughout the chalks and elevated gas volume (up to 30%) within these anomalous zones. To model the 4D gas effect, I considered different initial gas saturations, as well as separate scenarios with and without solution gas. However, the modelled time-shifts for all the cases considered failed to match the large observations, indicating that the dominant influence on velocity may be perhaps linked to geomechanics.

With respect to geomechanics and time-shift/strain, the R factor is widely used to represent the velocity sensitivity to geomechanical strains. I have shown that, in order to match observations using physical strains from the geomechanical model, an R range of between 20 and 40 is needed within chalk formations. However, if a simple velocity-porosity relation is assumed, the R factor can only range between 2 and 5 for overburden chalk; thus an extra velocity-stress/strain sensitivity linked to the opening of cracks should be considered to heighten R factors (Hatchell and Bourne, 2005b). Geological interpretations, rock physics and geomechanical modeling integration point to the existence of higher R factors, which result in the modelled time-shift matching the observations in the chalk.

To conclude the findings so far: the presence of gas in the overburden chalk has an effect on time-shift, but this effect is small and varies with original gas saturation. The geomechanical effect on time-shift is the dominant effect in the overburden chalk. There is a strong lithology-related variation of the R factors; the presence of cracks or damage, especially in zones of high over-pressure could lead to very high R factors. Large R factors can help explain time-shift observations in the chalk. However further, integrated interpretation is needed to characterise R behaviour as a response to changes in porosity and micro-fractures.

Chapter 7
Conclusions and recommendations for future research

In this chapter, all the work that has been done and lessons that have been learned in this PhD research are summarised. Subsequently, a few suggestions are provided for future research related with this topic together with final remarks about this research.

7.1 Conclusions

This thesis has presented a research study developed around the topic of integrating 4D seismic data into the dynamic characterisation of the Shearwater field. More specifically, it is the time-lapse time-shift, or its derivative time-lapse time-strain, that plays the key role in this research. The aims of this research are to accurately measure the time-lapse time-shift, to resolve various aspects regarding the physical information carried by this attribute, and to use it for updating the geomechanical model to predict future stress and strain changes. Figure 7.1 summarizes the inputs, methods, applications and achievements of this research. The main contributions and general conclusions of this thesis are summarized as follows:

1. Time-shift estimation approaches: a critical comparison of three different time-shift calculation methods was carried out and applied to a set of synthetic and real time-lapse seismic data of various seismic quality and time-shift magnitude.

    - All of the three methods (DHFCC, CLM, and NLI) successfully calculated time-lapse time-shifts from each of the 4D seismic datasets. However, each method showed both advantages and limitations in the comparison test.

    - For calculation of large time-shifts, the DHFCC method was the best and managed to recover stable time-shift profiles, even when dealing with very noisy seismic data. However, the accuracy of the CLM and NLI methods decreased with the increase of noise level in the seismic data.

    - In the case of recovering small time-shifts, DHFCC lost its accuracy, despite still giving a stable result, while, in contrast, NLI and CLM tended to give better results.

    - NLI is the best method for this research, as it generates smooth time-shifts with good accuracy and stable time-strains simultaneously. The resolution of the DHFCC method and the noise suppression ability of the CLM method need to be improved if they are to be considered for future use.

2. General reservoir characterisation of the Shearwater field: a general overview of the geology, production, and 4D seismic data of the Shearwater field was presented, followed by time-shift measurements and time-strain derivation from both full-stack and angle-stack 4D seismic datasets. Interpretations were made by relating to the geology and production patterns.

    - Time-shifts measured from different methods have essentially the same pattern and magnitude. The time shift variation was expected due to it being a compacting reservoir.

    - Four time-strain anomalies were identified in lower chalk, Heather shale, Pentland and Top Triassic, respectively.

    - Time-shifts and time-strains measured from angle-stack seismic data generally increase with the offset trend. Time-shift maps at Top Fulmar show that the increase of time-shift with offset is mainly concentrated in the gas leg around the producing area.

    - Most of the time-shift distribution can be interpreted by linking it to field geology and production.

    - The abnormal time-strain signal in the Heather shale was partially due to the time-shift estimation. Other possibilities such as the shale pressure diffusion could also explain this phenomenon.

3. The reservoir geomechanical modelling: a detailed description of reservoir geomechanical modelling was provided along with model calibration and application.

    - Time-shifts and derived time-strains have been used as important calibration parameters for the constructed RG model.

    - Uncertainties of the RG model arose from elastic properties, initial stress regime, pressure simulations, and R factors.

    - A better match was achieved with integration of geological patterns in the Hod chalk and underburden Pentland.

- Based on the calibrated RG model, stress and strain evolutions can be monitored by analyzing model outputs. This can help to predict future mechanical failures and draw up instructions for the drilling window.

- The observed and modelled lateral shifts did not match either in direction or magnitude. The disparities are linked with dipping structures and inappropriate migration.

4. The Hod time-strain anomaly analysis: an integrated analysis was made to assess the possible reasons for the Hod time-strain anomaly. Two hypotheses – gas effect and geomechanical effect – were modelled to check the time-shift and time-strain responses.

    - Pressure change in the overburden layer can be estimated using the Skempton B-coefficient.

    - Changes in the overburden pressure can lead to gas saturation changes if there is gas originally dissolved in the formation water.

    - Time-shifts induced by gas effects in various gas saturation scenarios failed to match the observed time-shift magnitude. This indicated the dominant influence to be linked with geomechanical effects.

    - R factors estimated from 4D angle-stack seismic data based on Landrø and Stammeijer (2004) are much smaller than expected. The largest uncertainty comes from the small offset coverage, which gives insufficient variations in $\tan^2\theta$ to validate the calculation.

    - R factors recovered using a simple velocity-porosity relation range between 2 and 5 for overburden chalk, which is still smaller than expected. This indicates that an extra velocity-stress/strain sensitivity should be considered to obtain heightened R factors, such as in the case of opening cracks. However, future modelling and calibration of the large R factors are needed, with integration of geological interpretations, rock physics and geomechanical modeling (MacBeth and Mangriotis, 2017).

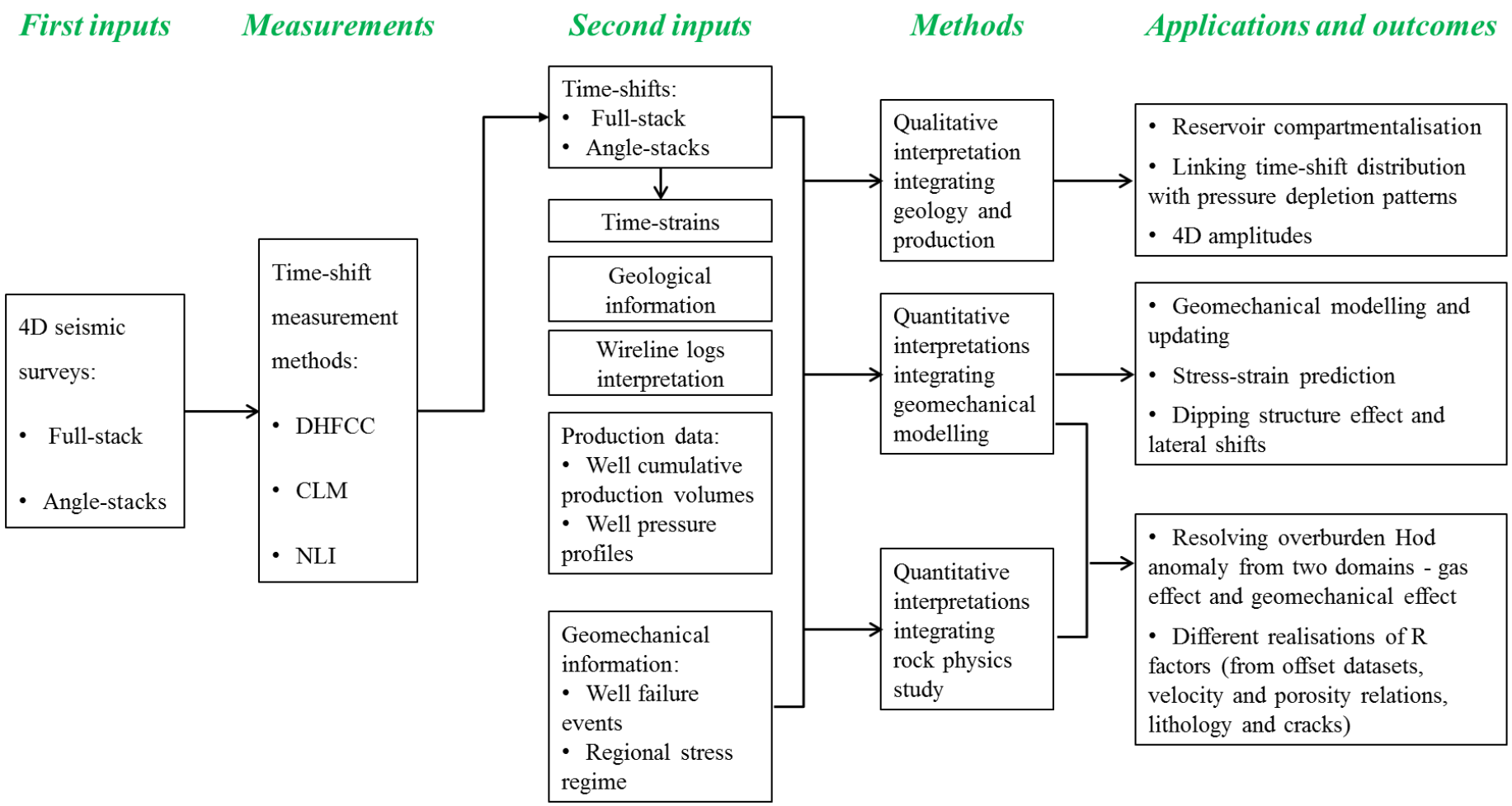

Figure 7.1: A summary diagram showing the inputs, methods, applications and achievements of this research

7.2 Recommendations for future research

7.2.1 The abnormal Triassic signal

During this study, most of the observed unusual time-shift and time-strain distributions which were displayed in Figure 4.9 have been resolved by linking them to geology, production patterns, geomechanical effects or fluid effects. However, the reason for the significant time-strain at the top of the Triassic formation in the deep underburden is still unclear. Two main reasons could be contributing to this sharp signal: the dipping structure effect and the multiples.

The effect of a dipping structure

An illustration of the dipping structure effect on the interchangeable lateral and vertical shifts was provided in section 5.4.2; a seismic modelling should be performed to reveal this effect in more detail. Moreover, the velocity model used for migration of the baseline and monitor seismic surveys could also contribute to the time-shift calculation artefacts, especially when large time-shifts are present. Therefore, an updated velocity model should also be included for the migration of the monitor survey. An example of updating the velocity model using calculated time-lapse time-strains is shown in Appendix B. To include all the effects, I suggest a workflow shown in Figure 7.2, where the original PSDM velocity and the updated velocity from geomechanical modelling are inputs for the 2D finite difference modelling (Amini, 2014). The modelled synthetic seismic gathers for the baseline and monitor surveys are then processed to generate the synthetic post-stack seismic volumes. Finally, time-shift volumes are generated and compared with the observations for the evaluation of dipping structure effects.

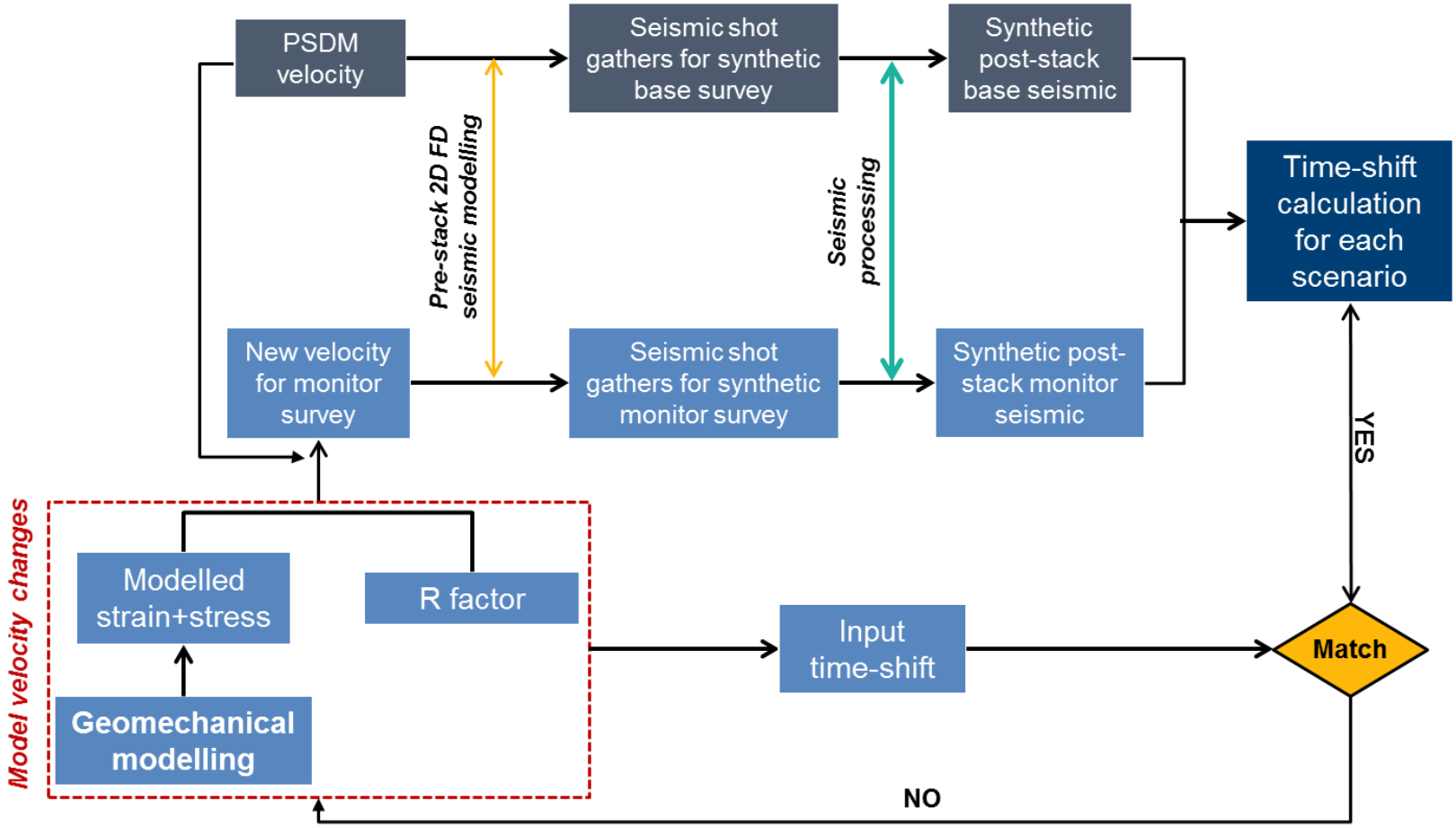

Figure 7.2: The workflow to study dipping structure effects on time-shift calculation using seismic modelling

Effect of multiples on time-shift measurements

Seismic multiples could also be an issue, as they will lead to miss-correlations of seismic events and therefore artificial time-lapse time-shifts. A study by Hatchell *et al.* (2007) provides a way to identify and remove surface multiple effects. However, in Shearwater, internal multiples might be related to the large underburden time-strain anomaly. As concluded by Fehmers (2010), long-path multiples that have similar TWTs to primaries from reflecting horizons far below the reservoir may lead to overestimates of measured time shifts, and the effect of multiples can be significant in the underburden. Seismic modelling with and without multiples incorporating dipping structures can be carried out in future to address the multiple effects on time-shift estimation in this field.

7.2.2 Improving time-shift and time-strain calculation

For a better interpretation and application of time-lapse time-shifts, the measurement techniques need to be improved in order to overcome the shortcomings of current estimations. Alternatively, instead of measuring time-shifts, straightforward time-strain estimation could be a better approach, as this parameter is of more practical value than the time-shift, and the direct measurements can avoid extra noise brought by derivation of time-shifts. Methods suggested by Williamson et al. (2007), Grandi et al. (2009), and Chu et al. (2012) have set good examples for this purpose. Future improvements should focus on decreasing noise and increasing accuracy in time-strain measurements. New time-shift calculations have also been published in recent papers, performed in unconventional ways, such as bringing the calculation into the TT domain (Zabihi Naeini, 2013) and pre-stack domain (Edgar and Blanchard, 2015). However, their applicability, the computation cost, and accuracy need to be further evaluated. Apart from vertical time-shift estimation, normal to reflectors estimation might bring more benefits in dealing with dipping structures, as it reduces the artificial imprints of lateral shifts on the vertical time-shift profile (Figure 7.3) (Thore *et al.*, 2012; Audebert and Agut, 2014).

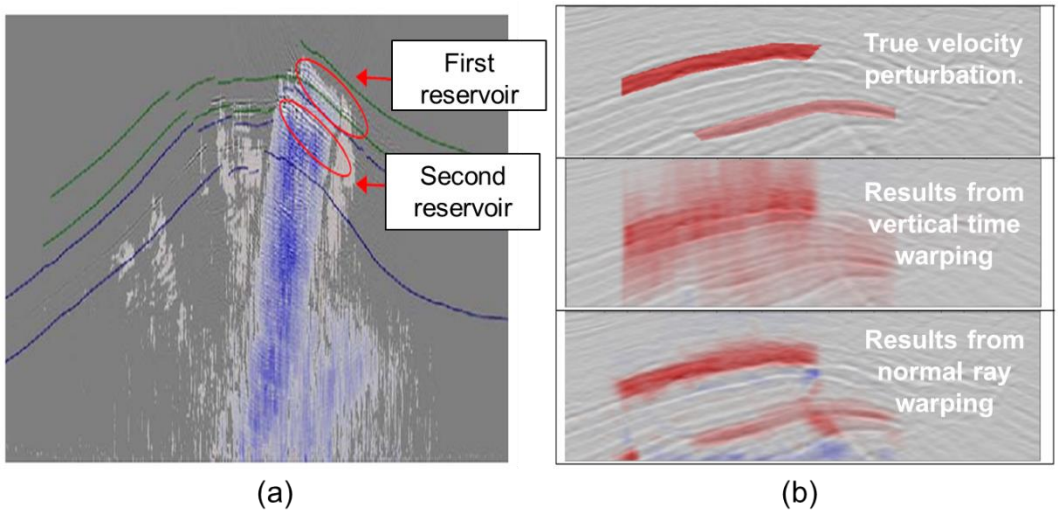

Figure 7.3: The advantages of using normal ray local warping technique: (a) difference between Monitor and Base PSDM images on a synthetic model containing superimposed dipping reservoirs; (b) a comparison among true velocity perturbation, results from classical vertical time warping, and results from normal ray local warping (Audebert and Agut, 2014).

7.2.3 Updating the geomechanical model

Further updating of mechanical properties and model calibrations needs to be carried out for the RG model. Rock mechanical tests are strongly required, and triaxial tests are much more important than uniaxial tests, as they can capture the real behaviour of the rock. Although the simulated pressure from reservoir simulator has information of faults imprinted, it is still better to include the discontinuity modelling in the RG model for more accurate estimation of fault reactivation and other potential geomechanical deformations. To do this, a good characterisation of faults and fractures are essential to construct a valid model for each field. Other software for geomechanical modelling (such as the GEM module in CMG) could also be tried out to avoid the limitations in the Petrel RG module, such as its imperfection in revealing the lateral variation, and to reach a fully coupled reservoir simulation and geomechanical modelling.

7.2.4 R factor

As one of the most important bridges between 4D seismic and geomechanics, the magnitudes of R factors in different locations need to be defined wisely. The behaviour of the R factor should differ for loading and unloading processes. Apart from simple

approximations from rock property trends, new models for defining the strain sensitivity of seismic velocity should be considered; a good example is given by MacBeth and Mangriotis (2017) where they suggest a new model for determining R factor at vertical and non-vertical incidence as a function of lithology and strain polarity.

7.2.5 Investigating more potential 4D seismic applications

Going back to the discussion on the changing global energy landscape at the beginning of my thesis, it can be suggested that, instead of focusing on the petroleum industry only, 4D seismic should also explore its way into other aspects of the energy field. The interesting thing is that some studies have already been initiated for dynamic monitoring of geologic sites, conducting CO2 injection and storage to mitigate the issue of greenhouse gases. Other possible applications could also be made in the area of renewables, such as the exploitation of geothermal fields. However, this will be open to questions in the future.

7.3 Final Remarks

My PhD research as presented in this thesis has been developed from optimizing attribute measurements, to ask relevant scientific questions based on the observations, and to resolve these questions, as well as to give suggestions for future research. The topic of integrating 4D seismic data into dynamic characterisation for HPHT reservoirs is indeed challenging but intriguing, and the work that I have done has managed to address some of the challenges confronted. Nevertheless, my hope is that this research can inspire further studies towards better dynamic reservoir characterisations of complex fields like Shearwater by integrating 4D seismic with other disciplines, such as geomechanics, geology and rock physics, which will contribute towards the reduction of potential risks during development of these fields.

Appendix A: A sensitivity study on reservoir geomechanical modelling

This appendix shows a sensitivity study on reservoir geomechanical modelling in order to evaluate the impact of each parameter on modelled vertical strain results. The main parameters included in this sensitivity study are Young's modulus, Poisson's ratio, density, porosity, and pressure change (Eq. A-1). Perturbations of +/- 10% from the base case (Table A.1) are performed to each of the parameters.

$$\varepsilon_{zz} = f(E, \upsilon, \rho, \emptyset, \Delta P) \qquad \text{Eq. A-1}$$

Table A.1: base case parameters, elastic properties are collected from literature, pressure is taken from the reservoir simulation results

Layer No.	Formation	Young's modulus, E	Poisson's Ratio	*Bulk Density, ρ*	Porosity	pressure
		Mpsi	*v*	g/cm^3	ft^3/ft^3	
1 to 2	Nordland and Hordland Group	0.41	0.31	2.05	0.30	
3 to 4	Nordland and Hordland Group	0.70	0.31	2.25	0.30	
5	Paleocene Claystone/ sele	1.31	0.31	2.39	0.30	
6	Tor chalk	4.57	0.31	2.64	0.10	
7	Hod chalk	4.93	0.31	2.58	0.15	
8	Hod Geohazard	6.24	0.33	2.53	0.10	
9	Chalk and Marl - base Creta	4.93	0.31	2.54	0.12	
10	Organic Claystone and Marl	1.64	0.33	2.51	0.20	
11 to 17	Sandstone - Upper Fulmar - Reservoir	0.68	0.16	2.15	0.26	
18 to 23	Sandstone - Lower Fulmar - Reservoir	1.81	0.22	2.36	0.18	
24	lower Heather shale	1.45	0.3	2.50	0.10	
25	Upper Pentland	5.22	0.1	2.40	0.10	
26	Mid Pentland	4.00	0.2	2.40	0.10	
27	Lower Pentland	2.74	0.2	2.45	0.10	
28	triassic	3.19	0.25	2.40	0.10	
29	salt	4.35	0.25	1.09	0.00	
30	Underburden	3.26	0.25	2.60	0.10	

The modelled vertical strains (ε_{zz}) within the overburden, reservoir, and underburden in each simulation case is compared to the result from base case to determine the sensitivity of each parameter. The RMSD value for each parameter is calculated by Eq. A-2.

$$RMSD = \sqrt{\frac{1}{n}\sum_{i=1}^{n}((\varepsilon_{zz})_i - (\varepsilon_{zz})_{base})^2} \qquad \text{Eq. A-2}$$

As displayed in Figure A.1, it is found that the most controlling parameters are pressure change, young's modulus, and Poisson's ratio. Changes of these parameters within the reservoir result in the largest impact on model results within all of the three intervals (overburden, reservoir, and underburden). Moreover, changes of these parameters tend to create the largest impact inside the reservoir.

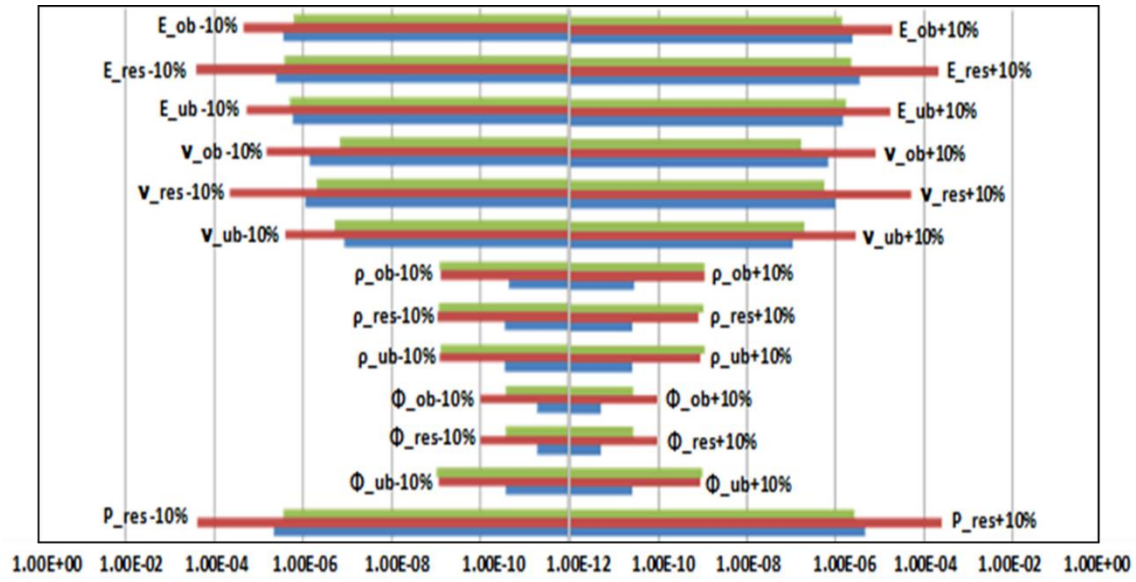

Figure A.1: The sensitivity diagram in logarithmic scale, showing the influence of each parameter on modelled vertical strains in different layers

Appendix B: Updating the velocity model

In this appendix, the process of updating velocity model using time-lapse seismic attributes is presented.

In the practice of current seismic processing, both seismic baseline and monitor are migrated using the same base velocity model, however, by definition, this will introduce time-shift artefacts to the monitor as in reality the velocity is changing with time. Therefore, time-shift calculated from the baseline and monitor migrated using the same velocity model will contain an error component. In the case where large velocity change is existing, the velocity model for monitor survey should be updated.

As time-strain can be decomposed into a vertical strain component and a fractional change in velocity (Landrø and Stammeijer, 2004):

$$\frac{\Delta t}{t} \approx \frac{\Delta z}{z} - \frac{\Delta v}{v} \qquad \text{Eq. B-1}$$

In the case of no significant reservoir compaction, such as when reservoir rock is stiff or pressure is well maintained, the fractional thickness changes (vertical strains) will be much smaller than the fractional velocity changes. Therefore, the following approximation is made:

$$\frac{\Delta t}{t} \approx -\frac{\Delta v}{v} \qquad \text{Eq. B-2}$$

And the velocity change is calculated as:

$$\Delta v \approx -v\frac{\Delta t}{t} \ , \qquad \text{Eq. B-3}$$

where v is the initial velocity model.

The new velocity model, v_2, is then expressed as:

$$v_2 = v + \Delta v \approx v(1 - \frac{\Delta t}{t}) \ , \qquad \text{Eq. B-4}$$

As discussed in chapter 2 and 3, the time-strain can be derived from measured time-shift or directly inverted by methods like Lie (2011) and Williamson *et al.* (2007). An example of updating the velocity model is shown in Figure B.1.

For highly compacted reservoirs, this approximation is no longer valid. However, velocity changes could still be approximated following Eq. 2-7 (Hatchell and Bourne, 2005b). The vertical strain is then converted into fractional velocity changes using R factor. The velocity change becomes:

$$\Delta v \approx -vR\varepsilon_{zz} \ , \qquad \text{Eq. B-5}$$

And the new velocity model can be estimated:

$$v_2 = v + \Delta v \approx v(1 - R\varepsilon_{zz}) \ , \qquad \text{Eq. B-6}$$

where the vertical strain, ε_{zz}, can be modelled in reservoir geomechanical model.

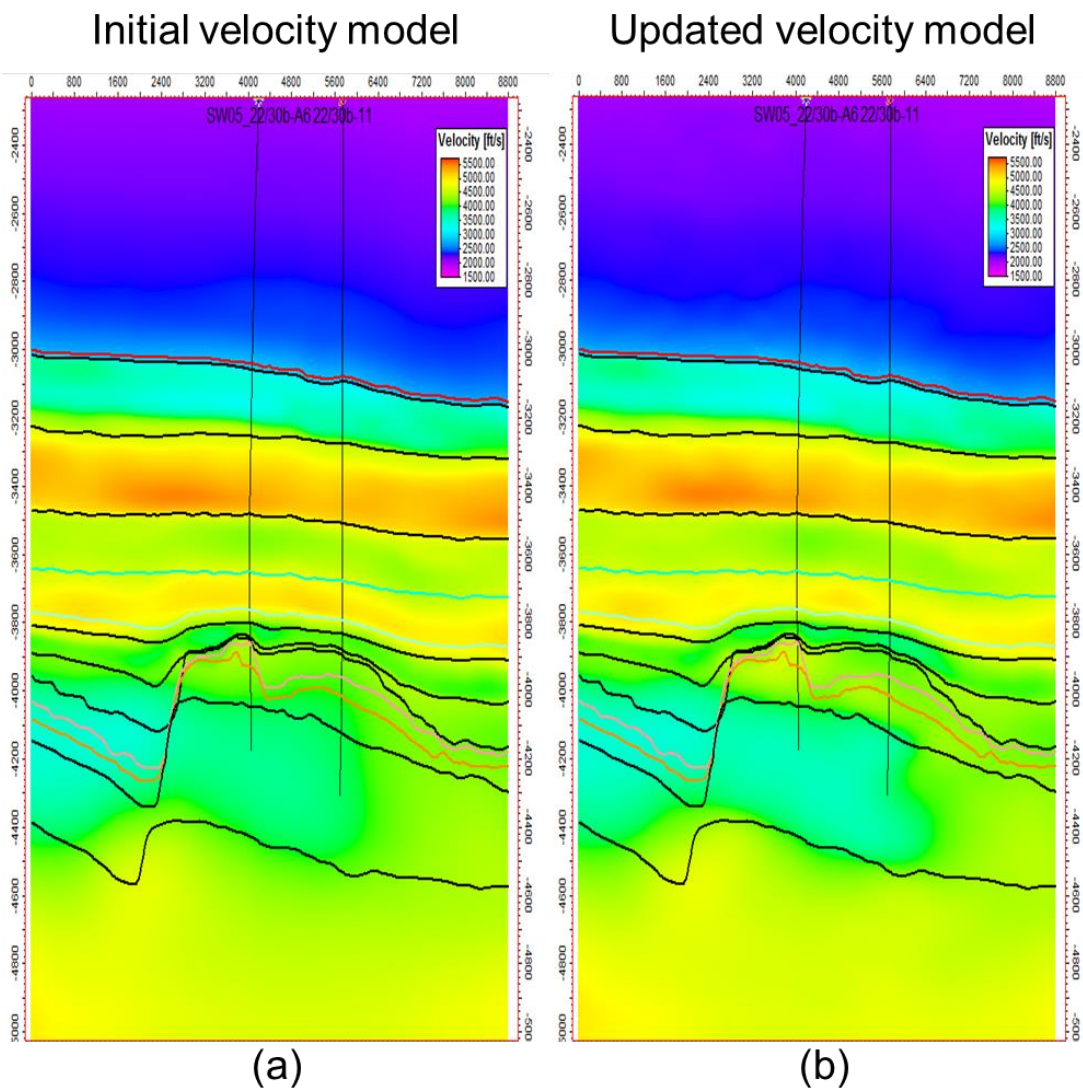

Figure B.1: (a) initial velocity model; (b) updated velocity model using time-strain

References

Aarre, V. (2006). Estimating 4D velocity changes and contact movement on the Norne field. In: *SEG/New Orleans 2006 Annual Meeting*, 2006, New Orleans, p.3115–3119.

Aarre, V. (2007). Estimating 4D velocity changes and contact movement on the Norne field. In: *2007 Offshore Technology Conference*, 2007, Houston, p.OTC 19049. [Online]. Available at: doi:10.1190/1.2370175.

Addis, M. a. (1997). The Stress-Depletion Response Of Reservoirs. In: *SPE Annual Technical Conference and Exhibition*, 1997. [Online]. Available at: doi:10.2118/38720-MS.

Al-Khateb, N. (2013). A look into Gassmann ' s Equation. *Integration geoConvention 2013*.

Alsos, T., Osdal, B. and Høiås, A. (2009). The Many Faces of Pressure Changes in 4D Seismic at the Svale Field and Its Implication on Reservoir Management. In: *71st EAGE Conference & Exhibition*, (June 2009), 2009, p.1–5.

Amini, H. (2014). *A pragmatic approach to simulator-to-seismic modelling for 4D seismic interpretation*. Heriot-Watt University.

Angelov, P. V. (2009). *4D seismic reservoir characterization, integrated with geo-mechanical modelling*. Delft University of Technology.

Audebert, F. A. and Agut, C. A. (2014). Retrieval of 4D Perturbations by Application of Warping in Depth Imaging Contexts. In: *76th EAGE Conference & Exhibition 2014*, 2014, p.We P06 04.

Baird, T., Fields, T., Drummond, R., Mathison, D., Langseth, B., Martin, A., Silipigno, L. and Chasse, B. (1998). High-Pressure, High-Temperature Well Logging, Perforating and Testing. *Oilfield Review*, p.50–67.

Batzle, M. and Wang, Z. (1992). Seismic properties of pore fluids. *Geophysics*, 57 (11), p.1396–1408. [Online]. Available at: doi:10.1190/1.1443207.

Beck, L. M. (2015). Shell Shearwater Project. *The Oil and Gas Industry Conference, 2015*, Aberdeen, UK.

Behrens, R., Condon, P., Haworth, W., Bergeron, M., Wang, Z. J., Ecker, C. and Ramon, S. (2001). 4D Seismic Monitoring of Water Influx at Bay Marchand: The Practical Use of 4D in an Imperfect World. In: *2001 SPE Annual Technical Conference and Exhibition*, 2001, New Orleans, Louisiana, p.SPE 71329. [Online]. Available at: doi:10.2118/79961-PA.

Van Bergen, P., De Gennaro, S., Fairhurst, F., Hurry, R., Concho, M., Watson, J., Sturgess, L. and Bevaart, M. (2013). Shearwater - Securing the Chalk - Effects of Depletion of a HPHT Reservoir on Chalk Overburden. In: *SPE Offshore Europe Oil and Gas Conference and Exhibition 2013*, 2013, Aberdeen, UK, p.SPE 166574. [Online]. Available at: doi:10.2118/166574-ms.

Bertrand, A., Buizard, S. and Grandi, A. (2014). Ekofisk life-of-field seismic: Operations and 4D processing. *The Leading EdgeLeading Edge*, February (33), p.142–148. [Online]. Available at: doi:10.1190/tle33020142.1.

Bertrand, A., Folstad, P. G., Grandi, A., Jeangeot, G., Haugvaldstad, H., Lyngnes, B., Midtun, R. and Haller, N. (2013). The Ekofisk Life of Field Seismic (LoFS) System - Experiences and Results after Two Years in Operation. In: *75th EAGE Conference & Exhibition incorporating SPE EUROPEC 2013*, 2013, London, UK.

Bourne, S. J. and Hatchell, P. J. (2007). Monitoring reservoir compaction by joint inversion of seafloor subsidence and time-lapse seismic timeshift data. *Society of Petroleum Engineers 69th European Association of Geoscientists and Engineers Conference and Exhibition 2007 Securing the Future*, 4 (June 2007), p.2518–2522.

BP. (2017). 2017 Energy Outlook. *BP Statistical Review of World Energy*. [Online]. Available at: doi:10.1017/CBO9781107415324.004.

Bruno, M. S. (2002). Geomechanical and Decision Analyses for Mitigating Compaction-Related Casing Damage. *Society of petroleum engineers*, 17 (September), p.179–188. [Online]. Available at: doi:10.2118/79519-PA.

Buizard, S., Bertrand, A., Nielsen, K. M., de Pierrepont, S., Grandi, A., Hoeber, H., Oexnevad, G. and Gresillaud, A. (2013). Ekofisk Life of Field Seismic: 4D Processing. In: *75th EAGE Conference & Exhibition incorporating SPE EUROPEC 2013*, (June), 2013, London, UK.

Calvert, M. a., Vagg, L. D., Lafond, K. B., Hoover, a. R., Ooi, K. C. and Herbert, I. H. (2014). Insights into sweep efficiency using 4D seismic at Halfdan field in the North Sea. *The Leading Edge*, 33 (2), p.182–187. [Online]. Available at: doi:10.1190/tle33020182.1.

Carstens, H. (2009). Using 4D Seismic. *geoexpro*, 6 (5).

Cayley, G. T. (1987). Hydrocarbon migration in the central North Sea. In: Parker, J. R. (ed.) Petroleum Geology of Northwest Europe. Geological Society, London, 549-555.

CGG. (2013). *Shearwater 4D Processing Report*.

Chambefort, M. (2013). 4D time-shift interpretation for the Shearwater field. *28th Meeting of the Edinburgh Time Lapse Project*.

Chu, D., Burger, J. and Medema, G. (2012). Using time strain volume for improved 4D interpretation: Methods and case studies. In: *74th EAGE Conference & Exhibition incorporating SPE EUROPEC 2012*, 2012, Copenhagen, Denmark, p.Y017. [Online]. Available at: doi:10.1190/1.3628071.

Corzo, M., Macbeth, C. and Barkved, O. (2013). Estimation of pore-pressure change in a compacting reservoir from time-lapse seismic data. *Geophysical Prospecting*, 61 (5), p.1022–1034. [Online]. Available at: doi:10.1111/1365-2478.12037.

Cox, B. and Hatchell, P. (2008). Straightening out lateral shifts in time-lapse seismic. *First Break*, 26 (5), p.93–98.

Dandekar, A. Y. (2013). *Petroleum Reservoir Rock and Fluid Properties, Second Edition*.

Das, A., Roy, B., Folstad, P. G., Lyngnes, B., Smith, B. and Grandi, A. (2013). A rock physics modelling workflow for compacting chalk reservoirs: Ekofisk Case study. In: *2nd international workshop on rock physics*, 2013, Southampton.

DeBruijn, G., Skeates, C., Greenaway, R., Southampton, E., Harrison, D., Parris, M., James, S., Mueller, F., Ray, S., Riding, M., Temple, L. and Wutherich, K. (2008). High-Pressure, High-Temperature Technologies. *Oilfield Review*, p.46–60.

Dusseault, M. B., Bruno, M. S. and Barrera, J. (2001). Casing Shear: Causes, Cases, Cures. *SPE Drilling & Completion*, (June), p.98–107.

Edgar, J. A. and Blanchard, T. D. (2015). Estimating Overburden Velocity Changes from Pre-stack Time Shifts Using Linear Tomography. In: *77th EAGE Conference & Exhibition 2015 – Workshops programme*, 2015, Madrid, p.WS02–A04.

Erratt, D., Thomas, G. M., Hartley, N. R., Musum, R., Nicholson, P. H. and Spisto, Y. (2010). North Sea hydrocarbon systems: some aspects of our evolving insights into a

classic hydrocarbon province. *Petroleum Geology Conference Series*, 7, p.37–56. [Online]. Available at: doi:10.1144/0070037.

Erratt, D., Thomas, G. M. and Wall, G. R. T. (1999). The evolution of the Central North Sea Rift. In: *Petroleum Geology of Northwest Europe: Proceedings of the 5th Conference*, 1999, London: the Geological Society, p.63–82.

Falahat, R. (2012). *Quantitative monitoring of gas injection , exsolution and dissolution using 4D seismic*. Heriot-Watt University.

Fan, L., Harris, B. W., Jamaluddin, a J., Mott, R., Pope, G. a and Whitson, C. H. (2006). Understanding Gas-Condensate Reservoirs. *Oilfield Review*, p.14–27.

Fehmers, G. (2010). How Compaction Causes Misaligned Multiples and False Time Shifts in Time-lapse Seismic. *first break*, 28 (June 2010), p.35–40.

Fehmers, G. C., Hunt, K., Brain, J. P., Bergler, S., Kaestner, U., Schutjens, P. M. and Burrell, R. V. (2007). Curlew D – Pushing the boundaries of 4D Depletion Signal in a Gas Condensate Field , UK Central North Sea. In: *EAGE 69th Conference & Exhibition*, 2007, London, UK, p.P074.

Fjaer, E., Holt, R. M., Horsrud, P., Raaen, A. M. and Risnes, R. (2008). *Petroleum related rock mechanics 2nd edition*. [Online]. Available at: doi:10.1016/0148-9062(93)92632-Z.

Fletcher, J. (Bp). (2004). What Do Petroleum Engineers Expect from Time Lapse Seismic, and Do Geophysicists Answer the Right Questions? *SPE/EAGE Joint Workshop*.

Folstad, P. G. (2010). Monitoring of the Ekofisk Field. *Geo ExPro*, 7 (3), p.72–76.

Fuck, R., Bakulin, A. and Tsvankin, I. (2009). Theory of traveltime shifts around compacting reservoirs: 3D solutions for heterogeneous anisotropic media. *Geophysics*, 74 (1), p.D25. [Online]. Available at: doi:10.1190/1.3033215.

Fuck, R. F., Bakulin, A. and Tsvankin, I. (2007). Time-lapse traveltime shifts above compacting reservoirs: 3D solutions for prestack data. In: *SEG 2007 Annual Meeting*, 2007, San Antonio. [Online]. Available at: doi:10.1190/1.2793079.

Gaarenstroom, L., Tromp, R. a. J., de Jong, M. C. and Brandenburg, a. M. (1993). Overpressures in the Central North Sea: implications for trap integrity and drilling safety. In: *Petroleum Geology Conference series 1993*, 4, 1993, p.1305–1313. [Online]. Available at: doi:10.1144/0041305.

Gabrielsen, R. H. (1984). Long-lived fault zones and their influence on the tectonic development of the southwestern Barents Sea. *Journal of the Geological Society*, 141 (4), p.651–662. [Online]. Available at: doi:10.1144/gsjgs.141.4.0651.

Garcia, A. (2011). *Dynamic reservoir characterization from overburden time-lapse strains*. Heriot-Watt University.

Garcia, A., Macbeth, C., Grandi, A., Total, E. and Uk, P. (2010). Time-shift inversion for dynamic reservoir characterization in the Elgin field. In: *SEG Denver 2010 Annual Meeting*, 2010, p.4175–4179.

De Gennaro, S., Schutjens, S., Frumau, M., Fuery. M., Ita, J. and Fokker, P. (2010). The Role of Geomechanics In the Development of an HPHT Field. In: *American Rock Mechanics Association*, 2010, Salt Lake City, Utah, p.ARMA 10–450.

Ghaderi, A. and Landrø, M. (2009). Estimation of thickness and velocity changes of injected carbon dioxide layers from prestack time-lapse seismic data. *Geophysics*, 74 (2), p.O17–O28. [Online]. Available at: doi:10.1190/1.3054659.

Gilham, R., Hercus, C., Evans, A. and De Haas, W. (2005). Shearwater (UK Block 22/30b): managing changing uncertainties through field life. *Petroleum Geology Conference series 2005,* 6, p.663–673. [Online]. Available at: doi:10.1144/0060663.

Glass, A. (2005). High pressure , high temperature developments in the United Kingdom Continental Shelf. *UKCS.*

Gommesen, L., Fabricius, I. L., Mukerji, T., Mavko, G. and Pedersen, J. M. (2007). Elastic behaviour of North Sea chalk: A well-log study. *Geophysical Prospecting*, 55 (3), p.307–322. [Online]. Available at: doi:10.1111/j.1365-2478.2007.00622.x.

Gowland, S. (1996). Facies characteristics and depositional models of highly bioturbated shallow marine siliciclastic strata: an example from the Fulmar Formation (Late Jurassic), UK Central Graben. *Geological Society, London, Special Publications*, 114 (1), p.185–214. [Online]. Available at: doi:10.1144/gsl.sp.1996.114.01.09.

Grandi, A., Wauquier, S., Cumming, H. and Deplanté, C. (2009). Quantitative 4D time lapse characterisation: three examples. In: *SEG Houston 2009 International Exposition and Annual Meeting*, 2009, Houston, USA, p.3815–3819. [Online]. Available at: doi:10.1190/1.3255662.

Greaves, R. J. and Fulp, T. J. (1987). Three-dimensional seismic monitoring of an enhanced Oil recovery process. *Geophysics*, 52 (9), p.1175–1187.

Gubbins, D. (2004). *Time Series Analysis and Inverse Theory for Geophysicists*. [Online]. Available at: doi:10.1198/tech.2005.s291.

Guilbot, J. and Smith, B. (2002). 4-D constrained depth conversion for reservoir compaction estimation: Application to Ekofisk Field. *The Leading Edge*, 21 (3), p.302–308. [Online]. Available at: doi:10.1190/1.1463782.

Guzman, J. D. L. T. (2011). *Shearwater 4D Time and Lateral Shift Analysis*. Imperial College London.

Hajnasser, Y. (2012). *The implications of shale geomechanics and pressure diffusion for 4D interpretation*. (October), Heriot-Watt University.

Hale, D. (2007). A method for estimating apparent displacement vectors from time-lapse seismic images. In: *SEG/San Antonio 2007 Annual Meeting*, 2007, p.2939–2943.

Hale, D. (2009). A method for estimating apparent displacement vectors from time-lapse seismic images. *Geophysics*, 74 (5), p.V99. [Online]. Available at: doi:10.1190/1.3184015.

Hall, S. A., MacBeth, C. A., Barkved, O. I. and Wild, P. (2002). Time-lapse seismic monitoring of compaction and subsidence at Valhall through crossmatching and interpreted warping of 3D streamer and OBC data. In: *72nd SEG Annual International Meeting*, 2002, Salt Lake City, Utah, p.1696–1699. [Online]. Available at: doi:10.1190/1.1817004.

Hall, S. a., MacBeth, C., Barkved, O. I. and Wild, P. (2005). Cross-matching with interpreted warping of 3D streamer and 3D ocean-bottom-cable data at Valhall for time-lapse assessment. *Geophysical Prospecting*, 53 (2), p.283–297. [Online]. Available at: doi:10.1111/j.1365-2478.2004.00470.x.

Haller, N. (2012). Introduction to Seismic Reservoir Characterisation at Ekofisk field. *ConocoPhillips*.

Han, D.-H. and Batzle, M. (2002). Fizz water and low gas-saturated reservoirs. *The Leading Edge*, 21 (4), p.395. [Online]. Available at: doi:10.1190/1.1471605.

Hatchell, P. . and Bourne, S. . (2005a). Measuring reservoir compaction using time-lapse timeshifts. In: *SEG/Houston 2005 Annual Meeting*, 2005, Houston. [Online]. Available at: doi:10.1190/1.2148230.

Hatchell, P. and Bourne, S. (2005b). Rocks under strain : Strain-induced time-lapse time shifts are observed for depleting reservoirs. *The Leading Edge*, p.1222–1225.

Hatchell, P. J., Van Den Beukel, A., Molenaar, M. M., Maron, K. P., Kenter, C. J., Stammeijer, J. G. F., Van Der Velde, J. J. and Sayers, C. M. (2003). Whole earth 4D: Reservoir monitoring geomechanics. In: *73rd SEG Meeting, Dallas, USA*, 2003, Dallas, USA. [Online]. Available at: doi:10.1190/1.1817532.

Hatchell, P. J., Jorgensen, O., Gommesen, L. and Stammeijer, J. (2007). Monitoring Reservoir Compaction From Subsidence And Time-lapse Timeshifts In the Dan Field. In: *2007 SEG Annual Meeting*, 2007, San Antonio. [Online]. Available at: doi:10.1190/1.2793062.

Hatchell, P. J., Kawar, R. S. and Savitski, a a. (2005). Integrating 4D seismic , geomechanics and reservoir simulation in the Valhall oil field . In: *EAGE 67th Conference & Exhibition*, 2005, Madrid, p.C012.

Hawkins, K. (2008). Defining the extent of the compacting Elgin reservoir by measuring stress-induced anisotropy. *First Break*, 26 (10), p.81–88.

Hawkins, K., Howe, S., Hollingworth, S., Conroy, G., Ben-Brahim, L., Tindle, C., Taylor, N., Joffroy, G. and Onaisi, A. (2007). Production-induced stresses from time-lapse time shifts: A geomechanics case study from Franklin and Elgin fields. *The Leading Edge*, 26 (5), p.655. [Online]. Available at: doi:10.1190/1.2737105.

Herwanger, J. and Horne, S. (2005). Linking geomechanics and seismics : Stress effects on time-lapse multicomponent seismic data. In: *EAGE 67th Conference & Exhibition*, (June), 2005, Madrid, p.C011.

Herwanger, J. V. and Horne, S. A. (2009). Linking reservoir geomechanics and time-lapse seismics: Predicting anisotropic velocity changes and seismic attributes. *Geophysics*, 74 (4), p.W13–W33. [Online]. Available at: doi:10.1190/1.3122407.

Herwanger, J. V. and Koutsabeloulis, N. (2011). Seismic geomechanics: How to build and calibrate geomechanical models using 3D and 4D seismic data. EAGE Publications.

Herwanger, J. V., Mohamed, F. R., Newman, R. B. and Vejbæk, O. V. (2013). Time-lapse seismic data-calibrated geomechanical model reveals hydraulic fracture re-orientation. In: *SEG Houston 2013 Annual Meeting*, 2013, Houston, USA, p.4949–4953. [Online]. Available at: doi:10.1190/segam2013-0947.1.

Hettema, M. H. H., Schutjens, P. M. T. M., Verboom, B. J. M. and Gussinklo, H. J. (1998). Production-Induced Compaction of Sandstone Reservoirs: The Strong Influence of Field Stress. In: *SPE European Petroleum Conference*, (August), 1998, p.547–554. [Online]. Available at: doi:10.2118/50630-MS.

Hillis, R. R. and Nelson, E. J. (2005). In situ stresses in the North Sea and their applications: petroleum geomechanics from exploration to development. In: *Petroleum Geology: North-West Europe and Global Perspectives—Proceedings of the 6th Petroleum Geology Conference*, 2005, Geological Society, London, p.551–564.

Hodgson, N. (2009). *Inversion for reservoir pressure change using overburden strain measurements determined from 4D seismic*. Heriot-Watt University.

Hodgson, N., MacBeth, C., Duranti, L., Rickett, J. and Nihei, K. (2007). Inverting for reservoir pressure change using time-lapse time strain: Application to Genesis Field, Gulf

of Mexico. *The Leading Edge*, 26 (5), p.649. [Online]. Available at: doi:10.1190/1.2737104.

Holm, G., E, T., K, P. U., Owens, J., Shell, U. K. L., Page, G., Ritchie, A. and Hughes, B. (2005). The Hod Geohazard : A Unique Overpressured Interval — Cooperation in I ts Recognition , Evaluation , and Risk Mitigation. In: *SPE Offshore Europe Oil and Gas Conference and Exhibition 2005*, 2005, Aberdeen, UK, p.SPE 96383.

Holm, G. M. (1998). Distribution and origin of overpressure in the Central Graben of the North Sea. *Abnormal pressures in hydrocarbon environments*, 70, p.123–144.

Hudson, T., Regel, B., Bretches, J., Condon, P., Rickett, J., Cerney, B., Inderwiesen, P. and Ewy, R. (2006). Preliminary Results of the Genesis Field Time-Lapse - Seismic Project , Gulf of Mexico. In: *2006 Offshore Technology Conference*, 2006, Houston.

Japsen, P., Bruun, a., Fabricius, I. L., Rasmussen, R., Vejbaek, O. V., Pedersen, J. M., Mavko, G., Mogensen, C. and Hoier, C. (2004). Influence of porosity and pore fluid on acoustic properties of chalk: AVO response from oil, South Arne Field, North Sea. *Petroleum Geoscience*, 10 (4), p.319–330. [Online]. Available at: doi:10.1144/1354-079303-586.

Johnstad, S. E., Uden, R. and Dunlop, K. N. B. (1993). Seismie reservoir monitoring over the Oseberg field. *first break*, 11 (5), p.177–185.

Johnston, D. H. (2013). *Practical Applications of Time-lapse Seismic Data*.

Kanu, C., Toomey, A., Hodgson, L., Gherasim, M., L'Heureux, E., Du, B. and Zhang, Q. (2016). Evaluation of time-shift extraction methods on a synthetic model with 4D geomechanical changes. *The Leading Edge*, 35 (10), p.888–893. [Online]. Available at: doi:10.1190/tle35100888.1.

Kfoury, M. (2012). *Kristin HPHT Gas Condensate Field: challenges, remedial actions & strategy to improve hydrocarbon reserve*.

Kloosterman, H. J., Kelly, R. S., Stammeijer, J., Hartung, M., Waarde, J. Van and Chajecki, C. (2003). Successful application of time-lapse seismic data in Shell Expro' s Gannet Fields, Central North Sea, UKCS. *Analysis*.

Koster, K., Gabriels, P., Hartung, M. and Verbeek, J. (2000). Time-lapse seismic surveys in the North Sea and their business impact. *The Leading Edge*, p.286–293.

Kragh, E. and Christie, P. (2002). Seismic repeatability, normalized rms, and predictability. *THE LEADING EDGE*, (July), p.640–647.

Kudarova, A., Hatchell, P., Brain, J. and Macbeth, C. (2016). Offset-dependence of production-related 4D time-shifts: real data examples and modeling. In: *SEG International Exposition and 87th Annual Meeting*, 2016, Houston, Texas, p.5395–5399. [Online]. Available at: doi:10.1190/segam2016-13611549.1.

Kwakwa, K. a, Batchelor, a S. and Clark, R. C. (1991). Assessment of the Mechanical Stability of High-Angle Wells in Block 22 / 11 , Nelson Field Discovery. *Society of Petroleum Engineers*.

Landa, J., Meadows, M., Thacher, C., Waddle, R. and Williams, N. (2015). *Map-Based Estimation of Reservoir Pressure and Saturation from 4D Seismic with a Data-Driven Procedure Approaches for Pressure-Saturation Inversion from 4D Seismic Model-Driven Inversion Approach*.

Landrø, M. (2001). Discrimination between pressure and fluid saturation changes from marine multicomponent time-lapse seismic data. *Geophysics*, 66 (3), p.836–844. [Online]. Available at: doi:10.1190/1.1620633.

Landrø, M. (2010). 4D seismic. In: K. Bjørlykke (ed.), *Petroleum Geoscience: From Sedimentary Environments to Rock Physics*, Springer, p.427–444. [Online]. Available at: doi:10.1007/978-3-642-02332-3.

Landrø, M. and Janssen, R. (2002). Estimating compaction and velocity changes from time-lapse near and far offset stacks. In: *Expanded Abstract: 64th EAGE Conference & Exhibition, Euro. Asso. Geo. Eng.*, 2 (May), 2002, p.P036.

Landrø, M. and Stammeijer, J. (2004). Quantitative estimation of compaction and velocity changes using 4D impedance and traveltime changes. *Geophysics*, 69 (4), p.949–957.

Lasocki, J., Guemene, J.-M., Hedayati, A., Legorjus, C. and Page, W. M. (1999). The Elgin and Franklin fields: UK Blocks 22/30c, 22/30b and 29/5b. *Petroleum Geology Conference series 1999*, 5, p.1007–1020. [Online]. Available at: doi:10.1144/0051007.

Li, L., Chen, Z., Mu, Y. and Chen, X. (2004). Short note: 4D seismic time differences extracted from pre-stack seismic data. *Journal of Geophysics and Engineering*, 1, p.143–146. [Online]. Available at: doi:10.1088/1742-2132/1/2/006.

Li, X., Mitchum, F. L., Bruno, M., Pattillo, P. D. and Willson, S. M. (2003). Compaction, Subsidence, and Associated Casing Damage and Well Failure Assessment for the Gulf of Mexico Shelf Matagorda Island 623 Field. In: *SPE Annual Technical Conference and Exhibition*, 2003, Denver, p.SPE 84553. [Online]. Available at: doi:10.2118/84553-ms.

Lie, E. O. (2011). Constrained Timeshift Estimation. In: *73rd EAGE Conference & Exhibition incorporating SPE EUROPEC 2011*, 2011, Vienna, Austria, p.G038.

Lumley, D. E. (2004). Business and technology challenges for 4{D} seismic reservoir monitoring. *The Leading Edge*, 23 (11), p.1166–1168.

MacBeth, C., Ji, L. and Mondal, D. (2012). The use, value and measurement of time-shifts: a guided discussion. *27th Technical meeting report of the Edinburgh Time-Lapse Project.*

MacBeth, C. and Mangriotis, M. (2017). The potential of post- and pre-stack time-shifts for reservoir monitoring. *36th Technical meeting report of the Edinburgh Time-Lapse Project.*

MacBeth, C., Mangriotis, M. and Hatchell, P. (2016). Evaluation of the spurious time-shift problem. In: *34th Technical meeting report of the Edinburgh Time-Lapse Project*, 2016, Heriot-Watt University.

Maldonado, B., Arrazola, A. and Morton, B. (2006). Ultra deep HPHT Completions: Classification, Design Methodologies, and Technical Challenges. In: *2006 Offshore Technology Conference*, 2006, Texas, p.OTC 17927.

Mallon, a. J. and Swarbrick, R. E. (2008). Diagenetic characteristics of low permeability, non-reservoir chalks from the Central North Sea. *Marine and Petroleum Geology*, 25 (10), p.1097–1108. [Online]. Available at: doi:10.1016/j.marpetgeo.2007.12.001.

Marsh, J., Bagley, G., Lewis, A., McGarrity, J., Nash, T., Parr, R., Saxby, I. and Whitcombe, D. (2001). The use of 4D seismic in reservoir management. In: *EAGE 63rd Conference & Technical Exhibition*, 2001, Amsterdam, p.F – 01.

Martin, K. and Macdonald, C. (2010). The Schiehallion Field : Applying a Geobody Modelling Approach to Piece Together a Complex Turbidite Field. In: *7th European Production and Development Conference*, 2010, Aberdeen, UK.

Mavko, G., Mukerji, T. and Dvorkin, J. (2009). *The Rock Physics Handbook, Second Edition*. [Online]. Available at: doi:http://dx.doi.org/10.1017/CBO9780511626753.

McKIE, T. and Audretsch, P. (2005). Depositional and structural controls on Triassic reservoir performance in the Heron Cluster, ETAP, Central North Sea. In: *Petroleum Geology: North-West Europe and Global Perspectives – Proceedings of the 6th Petroleum Geology Conference*, 2005, p.285–297. [Online]. Available at: doi:10.1144/0060285.

Meadows, M. (2001). Enhancements to Landrø's method for separating time-lapse pressure and saturation changes. In: *SEG Int'l Exposition and Annual Meeting*, 2001, San Antonio, Texas. [Online]. Available at: doi:10.1190/1.1816433.

Nagel, N. B. (2001). Compaction and subsidence issues within the petroleum industry: From Wilmington to Ekofisk and beyond. *Physics and Chemistry of the Earth, Part A: Solid Earth and Geodesy*, 26 (1-2), p.3–14. [Online]. Available at: doi:10.1016/S1464-1895(01)00015-1.

Nickel, M., Schlaf, J. and Sonneland, L. (2001). New tools for 4D Seismic Analysis in Carbonate reservoirs. In: *SEG Int'l Exposition and Annual Meeting*, 2001, San Antonio, Texas.

Nickel, M. and Sønneland, L. (1999). Non-rigid matching of migrated time-lapse seismic. In: *SEG 1999 Expanded Abstracts*, 1999.

Nottvedt, a., Gabrielsen, R. H. and Steel, R. J. (1995). Tectonostratigraphy and sedimentary architecture of rift basins, with reference to the northern North Sea. *Marine and Petroleum Geology*, 12 (8), p.881–901. [Online]. Available at: doi:10.1016/0264-8172(95)98853-W.

Nur, A., Mavko, G., Dvorkin, J. and Galmudi, D. (1998). Critical porosity: A key to relating physical properties to porosity in rocks. *The Leading Edge*, 17 (3), p.357. [Online]. Available at: doi:10.1190/1.1437977.

Olden, P., Corbett, P., Westerman, R., Somerville, J., Smart, B. and Koutsabeloulis, N. (2001). Modeling combined fluid and stress change effects in the seismic response of a producing hydrocarbon reservoir. *The Leading Edge*, 20 (10), p.1154–1163. [Online]. Available at: doi:10.1190/1.1486773.

Onaisi, A., Fiore, J., Rodriguez-Herrera, A., Koutsabeloulis, N. and Selva, F. (2015). Matching stress-induced 4D seismic time-shifts with coupled geomechanical models. In: *49th US Rock Mechanics / Geomechanics Symposium*, 2015, San Francisco, p.ARMA 15–801.

Pedersen, L., Ryan, S., Sayers, C., Sonneland, L. and Hafslund Veire, H. (1996). Seismic Snapshots for Reservoir Monitoring. *Oilfield Review*, 8 (4), p.32–43.

Rangel, R. (2016). *The impact of shale pressure deiffusion on 4D seismic interpretation*. Heriot-Watt University. [Online]. Available at: doi:10.1002/fut.

Rattey, R. P. and Hayward, A. B. (n.d.). *Sequence stratigraphy of a failed rift system: the Middle Jurassic to Early Cretaceous basin evolution of the Central and Northern North Sea*.

Rawson, P. F. and Riley, L. a. (1982). Latest Jurassic-Early Cretaceous events and the 'late Cimmerian unconformity' in North Sea area. *American Association of Petroleum Geologists Bulletin*, 66 (12), p.2628–2648.

Reinecker, J., Heidbach, O. and Mueller, B. (2003). The 2003 release of the World Stress Map. www.world-stress-map.org.

Rickett, J., Duranti, L., Hudson, T. and Hodgson, N. (2006). Compaction and 4-D time strain at the Genesis Field. In: *SEG/New Orleans 2006 Annual Meeting*, 2006, New Orleans, USA, p.3215–3219.

Rickett, J., Duranti, L., Hudson, T., Regel, B. and Hodgson, N. (2007). 4D time strain and the seismic signature of geomechanical compaction at Genesis. *The Leading Edge*, 26, p.644. [Online]. Available at: doi:10.1190/1.2737103.

Rickett, J. and Lumley, D. E. (2001). Cross-equalization data processing for time-lapse seismic reservoir monitoring: Acase study from the Gulf of Mexico. *Geophysics*, 66 (4), p.1015–1025.

Røste, T., Landrø, M. and Hatchell, P. (2007). Monitoring overburden layer changes and fault movements from time-lapse seismic data on the Valhall Field. *Geophysical Journal International*, 170 (3), p.1100–1118. [Online]. Available at: doi:10.1111/j.1365-246X.2007.03369.x.

Røste, T., Stovas, A. and Landrø, M. (2005). Estimation of layer thickness and velocity changes using 4D prestack seismic data. In: *EAGE 67th Conference & Exhibition*, 2005, Madrid, p.C010. [Online]. Available at: doi:10.1190/1.2335657.

Røste, T., Stovas, A. and Landrø, M. (2006). using 4D prestack seismic data. *Geophysics*, 71 (6).

Sayers, C. M. and Schutjens, P. M. T. M. (2007). An introduction to reservoir geomechanics. *The Leading Edge*, 26 (5), p.597. [Online]. Available at: doi:10.1190/1.2737100.

Segall, P. (1989). Geology Earthquakes triggered by fluid extraction Earthquakes triggered by fluid extraction. *Geology*, 17 (October), p.942–946. [Online]. Available at: doi:10.1130/0091-7613(1989)017<0942:ETBFE>2.3.CO;2.

Shadravan, A. and Amani, M. (2012). HPHT 101 - What every engineer or geoscientist should know about high pressure high temperature wells. In: *SPE Kuwait International*

Petroleum Conference and Exhibition, 2012, Kuwait, p.SPE 163376. [Online]. Available at: doi:10.2118/163376-ms.

Shell. (2013). *Shearwater volumes naming*.

Shell. (2015). *Shearwater key facts*.

Smith, S., Tsvankin, I. and Phenomena, W. (2012). Feasibility of inverting compaction-induced traveltime shifts for reservoir pressure. In: *SEG Las Vegas 2012 Annual Meeting*, (2), 2012, Las Vegas, p.1–6.

Sønneland, L., Veire, H. H., Raymond, B., Signer, C., Pedersen, L., Ryan, S. and Sayers, C. (1997). Seismic reservoir monitoring on Gullfaks. *The Leading Edge*, 16 (9). [Online]. Available at: doi:10.1190/1.1487188.

Stammeijer, J., Van Der Velde, J. J., Hatchell, P. ., Van Den Beukel, A. and Molenaar, M. M. (2004). Integrating 4D seismic and geomechanics : a case study. In: *EAGE 66th Conference & Exhibition*, 2004, Paris, p.A038.

Staples, R., Ita, J., Burrell, R. and Nash, R. (2007a). Monitoring pressure depletion and improving geomechanical models of the Shearwater Field using 4D seismic. *The Leading Edge*, 26 (5), p.636–642. [Online]. Available at: doi:10.1190/1.2737120.

Staples, R., Ita, J., Nash, R., Hague, P. and Burrell, R. (2007b). Using 4D Seismic Data and Geomechanical Modelling to Understand Pressure Depletion in HPHT Fields of the Central N Sea. In: *EAGE 69th Conference & Exhibition*, 2007, London, p.A025.

Staples, R., Stammeijer, J., Jones, S., Brain, J., Smit, F., Hatchell, P. and Ep, S. I. (2006). Time-Lapse (4D) Seismic Monitoring - Expanding Applications. *2006 CSPG-CWLS Convention*, p.181–189.

Sulak, R. M. and Danielsen, J. (1989). Reservoir Aspects of Ekofisk Subsidence. *Journal of Petroleum Technology*, 41 (7), p.709–716. [Online]. Available at: doi:10.2118/17852-pa.

Swarbrick, R. E., Lahann, R. W., O'Connor, S. a. and Mallon, a. J. (2010). Role of the Chalk in development of deep overpressure in the Central North Sea. *Petroleum Geology: From Mature Basins to New Frontiers—Proceedings of the 7th Petroleum Geology Conference*, p.493–507. [Online]. Available at: doi:10.1144/0070493.

Thore, P., De Verdiere, C. and McManus, E. (2012). Estimation of 4D signal in complex media : A Fast Track approach. In: *SEG L*, 2012, Las Vegas.

Tian, S. (2014). *Closing the Loop By Engineering Consistent 4D Seismic To Simulator Inversion*. Heriot-Watt University.

Tigrek, S. and Hatchell, P. (2006). Reservoir Compaction Quantification Using Geomechanical Inversion of Timelapse Timeshifts. In: *EAGE 68th Conference & Technical Exhibition*, 2006, Vienna.

Tolstukhin, E., Lyngnes, B. and Sudan, H. . (2012). Ekofisk 4D Seismic - Seismic History Matching Workflow. In: *EAGE Annual Conference & Exhibition incorporating SPE Europec*, (June), 2012, Copenhagen, Denmark, p.4–7. [Online]. Available at: doi:10.2118/154347-ms.

Tura, a, Barker, T., Cattermole, P. and Collins, C. (2005). Monitoring primary depletion reservoirs using amplitudes and time shifts from high-repeat seismic surveys. *The Leading Edge*, p.1214–1221. [Online]. Available at: doi:10.1190/1.2149620.

Tura, A. and Lumley, D. (1999). Estimating pressure and saturation changes from time-lapse AVO data. In: *SEG 1999 Expanded Abstracts*, 1999.

Vaziri, H. H., Allam, R. D., Kidd, G. a, Bennett, C. L., Grose, T. D., Robinson, P. a and Malyn, J. (2006). Sanding: A Rigorous Examination of the Interplay Between Drawdown, Depletion, Startup Frequency, and Water Cut. *SPE Production & Operations*, 21 (4), p.pp. 430–440. [Online]. Available at: doi:10.2118/89895-pa.

Walls, J. D., Dvorkin, J. and Smith, B. a. (1998). Modeling seismic velocity in Ekofisk chalk. In: *1998 SEG Expanded Abstracts*, 1998. [Online]. Available at: doi:10.1190/1.1820055.

Wang, Y., Worthington, M. H. and Pratt, R. G. (2002). Decomposition of structural amplitude effect and AVO attributes: Application to a gas-water contact. *Pure and Applied Geophysics*, 159 (6), p.1305–1320. [Online]. Available at: doi:10.1007/s00024-002-8683-1.

Whitcombe, D. N., Paramo, P., Philip, N., Toomey, A., Redshaw, T. and Linn, S. (2010). The Correlated Leakage Method - It's Application to Better Quantify Timing Shifts on 4D Data. In: *72nd EAGE Conference & Exhibition incorporating SPE EUROPEC 2010*, (June 2010), 2010, p.B037.

Williamson, P., Cherrett, A. and Sexton, P. (2007). A new approach to warping for quantitative time–lapse characterisation. In: *69th EAGE Conference & Exhibition*, 2007, London, UK.

Winefield, P., Gilham, R. and Elsinger, R. L. (2005). Plumbing the depths of the Central Graben: towards an integrated pressure, fluid and charge model for the Central North Sea HPHT play. *Petroleum Geology Conference series 2005*, 6, p.1301–1316. [Online]. Available at: doi:10.1144/0061301.

Wong, M. Y. (2016). A Comparison of Towed Streamer and LoFS Time Shift Information. *34th Meeting of the Edinburgh Time Lapse Project*.

Wong, M. Y., MacBeth, C. and Bertrand, A. (2015). Engineering Consistent Constraints for the Inversion of Changes in Pressure and Saturation on Ekofisk. In: *77th EAGE Conference & Exhibition 2015 – Workshops programme*, 2015, Madrid.

Yilmaz, O. and Doherty, S. (2001). *Seismic Data Analysis: Processing, Inversion, and Interpretation of Seismic Data*. [Online]. Available at: doi:10.1190/1.9781560801580.

Zabihi Naeini, E. (2013). TT domain time shift estimation. *75th EAGE Conference & Exhibition incorporating SPE EUROPEC 2013*, (June 2013), p.10–13.

Zimmer, M. A. (2003). *Seismic velocities in unconsolidated sands: Measurements of pressure, sorting, and compaction effects*. Stanford University.